SCUOLA DOTTORALE IN INGEGNERIA
SEZIONE DI SCIENZE DELL'INGEGNERIA CIVILE

CICLO XXV

Physical and numerical modelling of landslide-generated tsunamis at a conical island: generation, propagation and early warning

Dottorando:
Ing. Alessandro Romano _____

Tutor:
Prof. Leopoldo Franco _____

Coordinatore:
Prof. Leopoldo Franco _____

Collana delle tesi di Dottorato di Ricerca
In Scienze dell'Ingegneria Civile
Università degli Studi Roma Tre
Tesi n° 39

A Lei...

"If I have seen further it is by standing on the shoulders of Giants"

Sir Isaac Newton, Physicist

Acknowledgements

I would like to thank prof. Leopoldo Franco and dr. Giorgio Bellotti. They have guided me during these three years with patience and care, encouraging my work and inciting me to do my best. I really don't know how to thank you, hoping that my work can live up to their guidance and hoping that these few words can testify how much I appreciated their assistance.
Furthermore, I would like to thank prof. Paolo De Girolamo that gave me the possibility to participate at the experimental campaign carried out during the PRIN 2007. I would like to warmly thank dr. Marcello Di Risio and dr. Matteo Gianluca Molfetta (i.e., the fellowship of the island) wherewith I carried out the experiments at Bari. I can not forget the period on which we carried out the experiments, and this is due to their help and, more important, to their friendship. Thank you! Moreover, I would like to thank dr. Riccardo Briganti for the helpful discussions and suggestions who he gave me during the PhD.
A special thank is due to my mother Elisa and my father Sebastiano, who have never failed to lend their support. I hope they know how much they are important for me. A particular thank is for Eleonora, my love. She has been near to me from the beginning of the PhD. During these years she has been (and she is) a costant guidance and a dear mate. I hope that she can know what she represents for me. This work is dedicated to Her.
Finally, I would like to thank the friends that I have known since I was child (Roberto, Novella, Giordano, Valerio, Raffella, Valentino, Luigi, Matilde, Giulia, Daniele, Valeria, Ambra, Valerio and Andrea) and those ones that I have known during these three years (Elisa, Claudia, Antonio, Pietro, Michele, Ali). Thank you to all of you!

Abstract

Tsunamis are natural phenomena that can produce devastating effects for life and human activities. They can be generated mainly by earthquakes or landslides. As far as tsunamis generated by landslides that occur directly at the coast are concerned, it has to be noted that the gererated waves can propagate both seaward than along the shoreline itself. Therefore, several scientific and engineering issues arise. Indeed, the waves can be trapped by the bathymetry, inundating the coast itself for long distances. Furthermore, the waves that propagate seaward can reach the facing coasts (if any) with devastating effects.

In this work landslide-generated tsunamis that occur at the flanks of a conical island have been studied. New laboratory experiments have been carried out in a large wave tank to gain insight on tsunami generation and propagation mechanisms. The data collected during these new experiments are intended to be a benchmark dataset for validating analytical and numerical models. This has been achieved using a new acquisition technique, that allowed to obtain a large number of repetitions for each experiment along with a high spatial resolution of the measurements. The results of the new experiments are herein presented and discussed in depth. A detailed analysis of wave generation is provided. The influence of the landslide thickness is evaluated, since two different landslide models have been used during the experiments. The repeatibility of the experiments is statistically quantified. Moreover, the features of the generated waves, both near the generation area and around the island, are described.

Given the large number of time series collected around the island, a study of the spatial structure of the wave field has been carried out, and it is presented in this work. The k-f analysis has been applied in order to identify the dispersion relation followed by the waves that propagate along the shoreline (i.e., run-up). Furthermore, this technique allowed to study in detail the physics of wave propagation around the island. The relevance of each wave mode, which occurs during the propagation, is then adequately discussed.

Furthermore, aiming at improving the tsunamis early warning systems in the far field (TEWS), the application of a numerical model, which is based on the mild-slope equation (MSE) solved in the frequency domain, is presented. The method proposed herein takes advantage of an inversion technique which can be used in real time to reconstruct the tsunami waveform in the far-field. The method is effective in reconstructing the free surface elevation time series during the tsunami event. Consequentely, this technique seems to be suitable to improve the tsunamis early warning systems.
Finally, aiming at providing experimental tools to study the propagation phenomena of tsunamis, it is shown in this work a simple approach to improve the generation technique of solitary waves in experimental tests. Solitary waves are often used in laboratory experiments to study the propagation and the interaction with the coasts of tsunamis. A correction technique, that aims at minimizing the discrepancies between the experimental profile and the theoretical one, is herein presented. The technique is shown in the Appendix of this work.

Sommario

Le onde di maremoto (tsunami) sono fenomeni naturali che possono causare effetti catastrofici per la vita e le attività umane. Tali onde vengono generalmente generate da terremoti sottomarini o da frane. Gli tsunami generati da frane che avvengono in diretta corrispondenza della linea di costa sono caratterizzati da onde che si propagano sia lungo la costa stessa che ne ha visto la generazione, sia verso il mare aperto. Tali fenomeni sono oggetto di studio e dibattito sia da un punto di vista scientifico che ingegneristico. Le onde generate possono subire infatti fenomeni di intrappolamento ad opera della batimetria, inondando dunque la costa per considerevoli distanze. Inoltre, le onde che si irradiano verso il mare aperto possono raggiungere, con effetti devastanti, le aree costiere posizionate di fronte all'area di generazione.
In questo lavoro viene proposto lo studio degli tsunamis generati da frane che avvengono sulle pendici di un'isola di forma circolare. Sono stati condotti, in una grande vasca modelli, nuovi esperimenti di laboratorio per approfondire la conoscenza dei meccanismi di generazione e propagazione di tali onde di maremoto. La grande quantità di dati collezionata durante la campagna sperimentale mira dunque a costituire un benchmark per la validazione di modelli analitici e numerici. Ciò è possibile grazie all'innovativa tecnica di acquisizione utilizzata che ha consentito di ottenere, per ciascun esperimento, un gran numero di ripetizioni e, concordemente, una grande risoluzione spaziale delle misure. I risultati di questa nuova campagna sperimentale sono presentati e discussi nell'ambito di questo lavoro, ove viene inoltre fornita una dettagliata analisi della generazione delle onde di maremoto. Inoltre, grazie all'utilizzo di due differenti modelli di frana durante gli esperimenti, è stato possibile valutare l'influenza dello spessore di frana in termini di onde generate. Si noti inoltre che la ripetibilità degli esperimenti è stata oggetto di quantificazione statistica. Per di più, il grande numero di misure ha permesso di affrontare quantitativamente lo studio delle caratteristiche delle onde di maremoto sia vicino all'area di generazione che attorno alle coste dell'isola.

Viene inoltre presentato lo studio condotto circa l'identificazione della struttura spaziale del campo d'onda generato; ciò è stato possibile grazie all'elevata risoluzione spaziale delle misure. L'analisi k-f è stata applicata per identificare la relazione di dispersione seguita dalle onde che si propagano lungo la linea di costa (run-up). Tale tecnica ha inoltre consentito di studiare in dettaglio la fisica della propagazione attorno all'isola. Ciò ha permesso di valutare la rilevanza dei modi d'onda che si manifestano nei meccanismi di propagazione.
Inoltre, con lo scopo di fornire strumenti di miglioramento ai sistemi di allerta in campo lontano per la prevenzione dai maremoti (TEWS), viene mostrata l'applicazione di un modello numerico basato sulla risoluzione nel dominio della frequenza dell'equazione di mild-slope (MSE). Il metodo presentato si basa sull'utilizzo di una tecnica di inversione che viene utilizzata per ricostruire in tempo reale la forma d'onda del maremoto in campo lontano. Come mostrato nel presente lavoro, il metodo risulta efficace nel ricostruire la serie temporale di elevazione della superficie libera durante l'evento di maremoto. Di conseguenza, il metodo proposto risulta essere utilizzabile per migliorare i sistemi di allerta rapida per la prevenzione dagli tsunamis.
Infine, con l'intento di fornire uno strumento per lo studio sperimentale dei meccanismi di propagazione degli tsunami, viene mostrato in questo lavoro un semplice approccio per migliorare le tecniche di generazione di onde solitarie in esperimenti di laboratorio. Le onde solitarie sono infatti spesso usate per studiare i fenomeni di propagazione e di interazione con la costa delle onde di maremoto. In questo lavoro si propone una tecnica di correzione che mira a minimizzare le differenze tra il profilo sperimentale e teorico delle onde solitarie generate. Tale tecnica viene mostrata nell'Appendice di questo lavoro.

Contents

1 Introduction **3**

2 Landslide-generated tsunamis: state of the art **7**
2.1 Preface 7
2.2 Introduction 7
2.3 Landslide-generated tsunamis: generation and propagation mechanisms 10
2.4 Tsunamis generated by subaerial landslides: wave features . . 11
2.5 Tsunamis generated by submerged landslides: wave features . 13

3 Description of the experimental setup **15**
3.1 The 3D physical model 15
3.2 Instruments and acquisition techniques 19

4 Data analysis of the new 3D experiments: a benchmark data set **25**
4.1 Introduction 25
4.2 Landslide motion 26
4.3 Experimental findings and discussion 31
4.3.1 Time series analysis 31
4.3.2 Repeatibility 42
4.3.3 Wave features 50
4.3.4 Wave periods and arrival times 63
4.4 Preliminary concluding remarks 66

5 Wave propagation around the island: wavenumber-frequency analysis for detecting spatial structures of the wave field **67**
5.1 Introduction 67
5.2 Wavenumber-frequency analysis (k-f) 70
5.3 Description of the k-f features 72
5.3.1 Spatial sampling issues: 1D k-f 74

5.3.2 Spatial sampling issues: 2D k-f 80
5.4 Results and discussion 94
5.4.1 The one-dimensional k-f 94
5.4.2 The two-dimensional k-f 101
5.5 Concluding remarks 111

6 Numerical modelling of landslide-generated tsunamis: an inversion technique to improve tsunami early warning systems (TEWS) 113
6.1 Preface 113
6.2 Introduction 114
6.3 Description of the numerical model 116
6.3.1 Boundary conditions 122
6.4 Description of the physical model 122
6.5 Real-time tsunami inversion 125
6.5.1 Numerical simulations 125
6.5.2 Inversion using the correct landslide scenario 126
6.5.3 Effect of uncertainties on the landslide scenario 128
6.5.4 Real-time inversion 131
6.6 Discussion and conclusions 132

7 Concluding remarks 135

A Laboratory generation of solitary waves: an inversion technique to improve available methods 139
A.1 Preface 139
A.2 Introduction 139
A.3 Solitary waves generation techniques: a brief overview 141
A.4 The correction technique 143
A.5 Experimental set-up 145
A.6 Results and discussion 145
A.7 Concluding remarks 150

List of Figures

1.1 Pictures of hystorical landslide-generated tsunamis. 4

1.2 Left panel: numerical snapshot of the tsunami that occurred during the Pleistocene at Tenerife, Canary Islands, Spain [*Giachetti et al.*, 2011]. Right panel: numerical snapshot of the tsunami that occurred at Stromboli, Aeolian Islands, Italy in 2002 [*La Rocca et al.*, 2004]. 5

2.1 Sketch of landslide-generated impulse waves. [*Di Risio et al.*, 2010]. 9

3.1 Sketch of the wave tank. 16

3.2 Left panel: picture of the conical island in the wave tank. Right panel: sketch of the physical model (plan view). 16

3.3 Left panel: plan view of the Stromboli island (South Thyrrenian Sea). Right panel: Sketch of the physical model. 17

3.4 Pictures of the Sciara del Fuoco (Stromboli island) and the slide placed on the conical island model. 18

3.5 Sketch of the landslide models. 19

3.6 Side view of the conical island: detail of the movable steel frame. 20

3.7 Sketch of the measurement points. 21

3.8 Name and position of the instruments (WG = wage gauges, RG =run-up gauges, US = ultrasonic sensors). 22

3.9 Pictures of the conical island and of the instruments used. . . 23

4.1 Example of the image analysis for tracking landslide motion: each panel shows the landslide at a given time-step after the release; the white diamond marker identifies the position of the seaward edge of the landslide. 28

4.2 Left panel: space traveled. Middle panel: velocity. Right panel: acceleration. In each panel the round marker identifies th time at which the landslide hits the water, while the square one identifies the time at which the motion becomes completely submerged. 29
4.3 Run-up time series (i^{th}−release). 31
4.4 Zero-crossing analysis of the run-up time series (i^{th}−release). Note: gray markers identify the beginning of the tsunamis; red lines identify the odd waves in the packet; blue lines identify the even waves in the packet; vertical gray dashed lines identify the time at which the tsunami begins (left line) and the time at which the fifth wave ends (right line) respectively. 32
4.5 Free surface elevation time series collected by the moving arm at $\vartheta = 0°$ (upper panels), and zero-crossing analysis (lower panels). Note: the symbols have the same notation of that in Figure 4.4. 34
4.6 Free surface elevation time series collected by the moving arm at $\vartheta = 15°$ (upper panels), and zero-crossing analysis (lower panels). Note: the symbols have the same notation of that in Figure 4.4. 35
4.7 Free surface elevation time series collected by the moving arm at $\vartheta = 30°$ (upper panels), and zero-crossing analysis (lower panels). Note: the symbols have the same notation of that in Figure 4.4. 36
4.8 Free surface elevation time series collected by the moving arm at $\vartheta = 45°$ (upper panels), and zero-crossing analysis (lower panels). Note: the symbols have the same notation of that in Figure 4.4. 37
4.9 Free surface elevation time series collected by the moving arm at $\vartheta = 60°$ (upper panels), and zero-crossing analysis (lower panels). Note: the symbols have the same notation of that in Figure 4.4. 38
4.10 Free surface elevation time series collected by the moving arm at $\vartheta = 90°$ (upper panels), and zero-crossing analysis (lower panels). Note: the symbols have the same notation of that in Figure 4.4. 39
4.11 Free surface elevation time series collected by the moving arm at $\vartheta = 180°$ (upper panels), and zero-crossing analysis (lower panels). Note: the symbols have the same notation of that in Figure 4.4. 40

4.12 Sketch of the available sensors for both LS1 (left panel) and LS2 (right panel). 41
4.13 Superposition of all the run-up time series (LS1). 44
4.14 Superposition of all the run-up time series (LS2). 45
4.15 Upper panel: maximum induced tsunami run-up and minimum draw-down around the island as a function of s'. Lower panels: run-up and draw-down of the first four waves respectively. Note: positive values of s' refer to LS1, while negative ones refer to LS2. 46
4.16 Run-up and draw-down of the first four waves respectively: statistical estimate of the experimental repeatibility. Black points identify run-up and draw-down. Blue lines refer to the mean values calculated over the whole set of available landslide releases, for each run-up gauge. Red lines represent the confidence intervals. Note: positive values of s' refer to LS1, while negative ones refer to LS2.. 47
4.17 Free surface elevation around the island at several time steps from the landslide release. Note: in order to magnify the features of the wave propagation, different color scales have been used for each panel. 50
4.18 Comparison between the run-up and draw-down generated by the two landslide models. Upper panel: maximum induced tsunami run-up and minimum draw-down around the island as a function of s'. Lower panels: run-up and draw-down of the first four waves. Note: red markers refer to LS1, while green ones refer to LS2). 52
4.19 Comparison between the maximum wave crest and trough amplitudes (red and green empty markers) of the first wave, measured at several radial distances r as a function of the angle ϑ, and run-up and draw-down (red and green solid markers). 53
4.20 Comparison between the maximum wave crest and trough amplitudes (red and green empty markers) of the second wave, measured at several radial distances r as a function of the angle ϑ, and run-up and draw-down (red and green solid markers). 54
4.21 Comparison between the maximum wave crest and trough amplitudes (red and green empty markers) of the third wave, measured at several radial distances r as a function of the angle ϑ, and run-up and draw-down (red and green solid markers). 55

4.22 Experimental identification of the limit between "near-field" and "far-field" for the first (upper panels), second (middle panels) and third wave (lower panels). Note: left panels refer to the wave crests, while right ones refer to the wave troughs. Blue dashed lines identify the theoretical limit as from *Lynett and Liu* [2005]. 56

4.23 Spatial distribution of crest and trough amplitudes around the island. Left panels: first wave. Right panels: second wave. Upper panels: wave crests. Lower panels: wave troughs. Note: colorbars are expressed in mm. 57

4.24 Comparison between experimental data of wave crest and trough amplitudes of the first wave, generated by LS1, as a function of the angular distance ϑ and the fitting ones. . . . 58

4.25 Fitting parameters of the equation (4.12) as a function of the radial distance r. Left panel: parameter η_0 estimated for wave crest a trough. Left panel: parameter B estimated for wave crest (diamond markers) and trough (square markers). . 59

4.26 Free surface elevation time series collected by means of the moving arm at three angular positions ($\vartheta = 0, 10, 20°$) and at four radial distances ($r = 2.57, 3.07, 3.47, 3.87m$). 60

4.27 Spatial distribution of crest and trough amplitudes around the island. Left panels: third wave. Right panels: fourth wave. Upper panels: wave crests. Lower panels: wave troughs. Note: colorbars are expressed in mm. 61

4.28 Spatial distribution of maximum crest (left panel) and mimimum trough (right panel) amplitudes around the island. Note: colorbars are expressed in mm. 62

4.29 Spatial distribution of maximum "wave height" (i.e., envelope of the maximum and minimum free surface elevation) around the island, evaluated in terms of absolute value (left panel) and percentage (right panel). 62

4.30 Period of the first four run-up waves. Note: red markers refer to LS1, while green ones refer to LS2. 63

4.31 Mean arrival times of the run-up waves along the shoreline as a function of s'. Note: lower black markers refer to the time at which the tsunami begins; red markers identify the time at which the maximum of the packet occurs; upper black markers identify the time at which the fifth wave ends 64

4.32 Individual wave periods of the first three waves measured by the moving arm and the run-up gauges. Note : black points refer to the wave periods of the waves measured by the moving arm, while the solid markers (green and red) refer to the wave periods of the run-up waves. 65

5.1 Array smoothing functions for four array apertures D. Note: the number of sensors is fixed and equal to 30. 75

5.2 Steered response power spectra. The gray line identifies the linear waves dispersion relation. Note: the number of sensors is fixed and equal to 30. 76

5.3 Array smoothing function for four arrays made-up of different numbers of sensors (i.e., several spatial lag d_{min}). Note: the aperture of the array D is fixed. 77

5.4 Steered response power spectra. Note: the aperture of the array D is fixed. 78

5.5 Steered response power spectra of four test wave signals. Upper left panel: wave signal characterized by one frequency component. Upper right panel: characterized by two frequency components. Lower left panel: wave signal characterized by three frequency components. Lower right panel: solitary wave that propagate in space. Note: gray lines identify the wave dispersion relations. 80

5.6 Left panel: contour plot of the free surface elevation at $t = 1.0$ s, measured by a square-shaped array; white markers identify the sensors that form the array, while blue arrows identify the propagation direction of the waves. Note: the sensors are equally-spaced. Right panel: ASF. 81

5.7 SPRS evaluated at the two carrier frequencies of the wave signal, as a function of the wavenumber scalar components. Note: gray dashed lines identify the theoretical values of the wavenumber scalar components. 82

5.8 Left panel: contour plot of the free surface elevation at $t = 1.0$ s, measured by a square-shaped array; white markers identify the sensors that form the array, while blue arrows identify the propagation direction of the waves. Note: the sensors are not equally-spaced. Right panel: ASF. 83

5.9 SPRS evaluated at the two carrier frequencies of the wave signal, as a function of the wavenumber scalar components. Note: gray dashed lines identify the theoretical values of the wavenumber scalar components. 84

5.10 Left panel: contour plot of the free surface elevation at $t = 1.0$ s, measured by a diamond-shaped array; white markers identify the sensors that form the array, while blue arrows identify the propagation direction of the waves. Note: the sensors are equally-spaced. Right panel: ASF. 85

5.11 SPRS evaluated at the two carrier frequencies of the wave signal, as a function of the wavenumber scalar components. Note: gray dashed lines identify the theoretical values of the wavenumber scalar components. 86

5.12 Left panel: contour plot of the free surface elevation at $t = 1.0$ s, measured by a circle-shaped array; white markers identify the sensors that form the array, while blue arrows identify the propagation direction of the waves. Note: the sensors are not equally-spaced. Right panel: ASF. 87

5.13 SPRS evaluated at the two carrier frequencies of the wave signal, as a function of the wavenumber scalar components. Note: gray dashed lines identify the theoretical values of the wavenumber scalar components. 87

5.14 Synthetic SRPS. Note: the black lines identify the linear wave dispersion relation. 88

5.15 Left panel: contour plot of the free surface elevation at $t = 0.02$ s (radiated waves); white markers identify the sensors that form the array, while blue arrows identify the propagation direction of the waves. Right panel: ASF. 89

5.16 SPRS evaluated at the carrier frequency of the wave signal. Left panel: SPRS as a function of the wavenumber scalar components in cartesian coordinates. Right panel: SPRS as a function of the wavenumber scalar components in polar coordinates. 90

5.17 Left panel: contour plot of the free surface elevation at $t = 0.02$ s (trapped waves); white markers identify the sensors that form the array, while blue arrows identify the propagation direction of the waves. Right panel: ASF. 91

5.18 SPRS evaluated at the carrier frequency of the wave signal. Left panel: SPRS as a function of the wavenumber scalar components in cartesian coordinates. Right panel: SPRS as a function of the wavenumber scalar components in polar coordinates. 92

5.19 Left panel: contour plot of the free surface elevation at $t = 0.02$ s (partially radiated and partially trapped waves); white markers identify the sensors that form the array, while blue arrows identify the propagation direction of the waves. Right panel: ASF. 93

5.20 SPRS evaluated at the carrier frequency of the wave signal. Left panel: SPRS as a function of the wavenumber scalar components in cartesian coordinates. Right panel: SPRS as a function of the wavenumber scalar components in polar coordinates. 93

5.21 Run-up time series (thin black lines) for nine wave gauges (from the top to the bottom). Each panel contains several run-up time series (one for each repetition of the same experiment). The envelopes (thick black line), obtained for each run-up gauge, are also proposed in each plot. 95

5.22 Steered response power spectrum obtained by means of the one-dimensional k-f analysis and several dispersion relations (black dashed line: linear waves for $h = 0.8$ m; upper thick black line: 1st-order edge waves; lower thick black line: 0th-order edge waves; thin black line: 0th-order edge waves for curvilinear shoreline; gray dashed lines: linear waves for different values of water depth). 96

5.23 Wave spectral amplitudes (thin black lines) for nine wave gauges (from the top to the bottom). Each panel contains several spectral amplitudes (one for each repetition of the same experiment). In each panel the averaged values of the mean frequency (averaged over all the repetitions), are marked by the dashed lines. 98

5.24 Left panel: Comparison between the theoretical phase celerities (black dot markers) and the estimated ones (gray markers) of the first three waves. Right panel: Comparison between the theoretical edge waves celerities (black dot markers) and the mean values (evaluated at an intermediate position of each couple of neighbouring gauges) of the estimated celerities of the first three waves (gray dot markers). Note: The overlined symbols in the legend are mean values. 99

5.25 Comparison between the theoretical group celerities (black dot markers) and the estimated ones (gray diamond markers). 101

5.26 Left panels: Sketch of the used sensors for the two-dimensional k-f analysis. Right panels: Synthetic steered response power spectrum obtained for the four array geometries. Note: The line styles of the dispersion relations plotted are the same of those described in Figure 5.22. 102

5.27 Steered response power spectra, obtained from the first array geometry, evaluated at four selected frequencies in the k_r-k_s^* plane (left panels) and in the k_x-k_y plane (right panels). Horizontal black dashed lines: alongshore wavenumbers of the 0th- and 1st-order edge waves. Vertical black thin dashed lines: radial wavenumbers as from the linear wave theory dispersion relation. Note: the same color scaling is used for all the plots. 104

5.28 Steered response power spectra, obtained from the second array geometry, evaluated at four selected frequencies in the k_r-k_s^* plane (left panels) and in the k_x-k_y plane (right panels). Horizontal black dashed lines: alongshore wavenumbers of the 0th- and 1st-order edge waves. Vertical black thin dashed lines: radial wavenumbers as from the linear wave theory dispersion relation. Note: the same color scaling is used for all the plots. 105

5.29 Steered response power spectra, obtained from the third array geometry, evaluated at four selected frequencies in the k_r-k_s^* plane (left panels) and in the k_x-k_y plane (right panels). Horizontal black dashed lines: alongshore wavenumbers of the 0th- and 1st-order edge waves. Vertical black thin dashed lines: radial wavenumbers as from the linear wave theory dispersion relation. Note: the same color scaling is used for all the plots. 107

5.30 Steered response power spectra, obtained from the fourth array geometry, evaluated at four selected frequencies in the k_r-k_s^* plane (left panels) and in the k_x-k_y plane (right panels). Horizontal black dashed lines: alongshore wavenumbers of the 0th- and 1st-order edge waves. Vertical black thin dashed lines: radial wavenumbers as from the linear wave theory dispersion relation. Note: the same color scaling is used for all the plots. 108
5.31 Measured angles δ_{rs}, frequency function, between the wavenumber scalar components (k_s^*-k_r) at which the maximum value of the SRPS occur at a given frequency. 110

6.1 Skecth of the plan view layout of the laboratory experiments (measures in m). 123
6.2 Picture of the landslide and island models. 124
6.3 Layout of the laboratory gauges positions. 124
6.4 Sketch of the numerical domain from *Cecioni and Bellotti* [2010b]. The numbers 2.07, 4.47 and 8.00 express the radii in meters of the undisturbed shoreline, the island base at the tank bottom, and the external circular boundary respectively. 125
6.5 Comparison of the numerical result (red solid line) with the experimental time series (black dashed line) at the control gauge 24S. Each plot refers to a different gauge (12S, 20S, 7S and 15S) used for the inversion. 127
6.6 Comparison of the numerical result (red solid line) with the experimental registration (black dashed line) at the control gauge 24S. Numerical model prediction is performed adopting gauge 7S as the inversion gauge, and using pre-event numerical computations carried out with 4 tentative landslide volumes. V_{cls} is the volume of the so called correct landlide scenario. 128
6.7 Comparison of the numerical result (red solid line) with the experimental records (black dashed line) at the control gauge 24S, using inversion gauge 7S. Numerical model prediction is performed using pre-event numerical computations carried out with 4 tentative landslide motion directions. The angle β measures the difference between the correct landslide scenario and that used in the computations. $\beta = 0^o$ represents the correct landslide scenario, i.e. that representing the experiments. 129

6.8 Tsunami inversion using scenarios computations with wrong landslide velocity; inversion from gauge 7S, results checked against records at gauge 24S. Red solid lines refer to numerical results, black dashed lines to experimental time series. v_{cls} is the velocity of the so called correct landslide scenario. 130

6.9 Sample computations of real-time inversion using partial input time series at gauge 7S; results checked against records at gauge 24S. 132

6.10 Predicted maximum surface elevation at gauge 24S, using as input partial time series of length t_{known}; horizontal dashed line represents the reference experimental result at gauge 24S. 133

A.1 Left panel: solitary waves profile for several wave nonlinearities and for a given water depth. Right panel: paddle law of motion according to the method developed by *Guizien and Barthélemy* [2002]. 143

A.2 Sketch of the experimental set-up (left panel) and picture of the wave maker installed on the wave flume (right). 145

A.3 Left panel: comparison between the paddle laws of motion for three wave nonlinearities (grey lines: initial law of motion; red lines: corrected law of motion). Right panel: comparison between the water free surface elevation (black lines: theoretical profile; grey lines: initial profile; red dots: corrected profile). Note: the experimental free surface elevation time series used in the correction technique have been measured at the wave gauge n. 3 (i.e., $x_{WG3} = 4.00$ m). 147

A.4 Left panel: comparison between the spectral amplitudes for three wave nonlinearities (black lines: spectrum of the theoretical profile; grey lines: spectrum of the initial profile; red dots: spectrum of the corrected profile). Right panel: comparison between the spectral differences (grey lines: spectral difference between the theoretical profile and the initial one; red lines:spectral difference between the theoretical profile and the icorrected one). Note: the experimental free surface elevation time series used for the correction technique have been measured at the wave gauge n. 3 (i.e., $x_{WG3} = 4.00$ m). 148

A.5 Left panel: peak coefficient. Middle panel: shape coefficient. Right panel: global coefficient. Note: circle markers identify the coefficient calculated for the initial profiles, while the diamond markers are those calculated for the corrected ones. Note: the experimental free surface elevation time series used in the correction technique have been measured at the wave gauge n. 3 (i.e., $x_{WG3} = 4.00$ m). 149
A.6 Peak coefficient (left panel), shape coefficient (middle panel), global coefficient (right panel) against the number of iteration N, for a given wave nonlinearity. Note: circle markers identify the coefficient calculated for the initial profiles, while the diamond markers are those calculated for the corrected ones. The experimental free surface elevation time series used in the correction technique have been measured at the wave gauge n. 3 (i.e., $x_{WG3} = 4.00$ m). 150

List of Tables

3.1 Landslide models physical parameters. Note: subscript $(\cdot)_M$ refers to model values, while subscript $(\cdot)_P$ refers to prototype ones. 18
3.2 Sensors position and naming. 23

4.1 Landslide models physical and hydrodynamics parameters. . . 30
4.2 Mean values and confidence intervals of run-up (LS1). 48
4.3 Mean values and confidence intervals of draw-down (LS1). . . 48
4.4 Mean values and confidence intervals of run-up (LS2). 49
4.5 Mean values and confidence intervals of draw-down (LS2). . . 49

5.1 Position and wave parameters at each run-up gauge. 100

6.1 Angular and radial position of sea level gauges: the point where the landslide impacts the water is taken as the origin, and the angular position is taken counterclockwise from the landslide motion direction (see Figure 6.3). 125

Chapter 1

Introduction

Tsunamis are transient perturbations of the water free surface elevation that propagate with high celerities for long distances. These waves are characterized by large periods and, potentially, large wave heights. Tsunamis can be generated by submarine earthquakes, by landslides (subaerial, submerged or partially submerged), by submarine explosions, by meteorite impacts, and by sudden changes of the atmospheric pressure (meteotsunamis). Regardless of the mechanisms that generate these waves, their effects can be disastrous. Many devastating events have indeed occurred in the past. Earthquake-generated tsunamis are probably more known, rather than those generated by landslides. However, it has to be mentioned that the latter caused well-known calamities in the past (see Figure 1.1). The largest known induced tsunamis run-up (about 524 m) is due to the large landslide that occurred at Lituya Bay, Alaska, in 1958 (see upper left panel of the Figure 1.1, *Miller* [1960]).

This work aims at gaining insight on the physics of landslide-generated tsunamis that occur at the flank of a conical island. The problem at hand is quite interesting, both from a scientific than from an engineering point of view, since many issues arise. Small volcanic islands are often characterized by steep unstable flanks, where landslides are likely to occur (see lower left panel of the Figure 1.1). Flank instabilities may lead to landslide generation, which sliding and entering the water (if subaerial), cause tsunamis. When a landslide occurs directly at a water boundary the generated impulse waves propagate both seaward (i.e., radiating waves) than alongshore (i.e., trapped or partially trapped waves), as qualitatively shown in Figure 1.2. In that regard, field measurements (e.g., *Tinti et al.* [2005]), along with laboratory experiments (e.g., *Di Risio et al.* [2009b]), have shown that the tsunami event that occurred at Stromboli in 2002 (South Thyrrenian Sea,

(a) *Lituya Bay, Alaska, 1958.*

(b) *Vajont Valley, Italy, 1963.*

(c) *Stromboli Island, Italy, 2002.*

(d) *Damages at Stromboli Island, Italy, 2002.*

Figure 1.1: Pictures of hystorical landslide-generated tsunamis.

Italy) caused the largest damages along the coast of the island itself, i.e., the tsunami reached those areas which are naturally sheltered by the tsunami source. Furthermore, the small distances imply early wave arrival along the coast of the island. Thus, little times are available for spreading effective alarms. Given the above, it is essential to properly identify the physics of the waves that propagate around the island in order to design effective tsunamis early warning systems (TEWS). Moreover, the waves that leave the generation area radiating seaward may reach other coasts, which can placed also at large distances, with devastating effects. Thus, it is fundamental to identify and to numerically reconstruct the propagating waves in order to estimate the magnitude and the arrival times of the waves themselves and, consequentely, to spread an alarm before that the facing coasts are reached by the tsunamis.

To reach these purposes both physical and numerical models have been used

and they are shown in this work. The research presented herein, starts from the experimental study carried out by *Di Risio et al.* [2009b] that has provided a detailed analysis of the tsunamis run-up at the coast of a conical island, focusing on subaerial landslides. A new experimental campagin, aiming at providing a benchmark dataset for validating theoretical models, has been recently carried out. The new experimental results are in depth shown in this work. These experiments are characterized by a large numbers of measurements with a high-spatial resolution (i.e., comparable with that of a numerical model output), since an innovative acquisition technique, described by *Molfetta et al.* [2010], has been used. Furthermore, two landslide models, of different size, have been used.

The new measurements allowed to study in detail the features of the landslide-generated tsunamis that occur at a conical island. As shown in the following chapters, a detailed analysis of the waves that both radiate seaward and propagate around the island has been carried out. Then, the results are discussed in depth. Moreover, the large number of measurements allowed to estimate statistically the repeatibility of the experiments (i.e., confidence intervals of the benchmark dataset are provided). This aspect is essential to provide a benchmark dataset aiming at validating theoretical models. The high space-resolution measurements allowed to apply the so-called wavenumber-frequency analysis aiming at identifying the dispersion relation followed by the waves that propagate alongshore. Furthermore, a

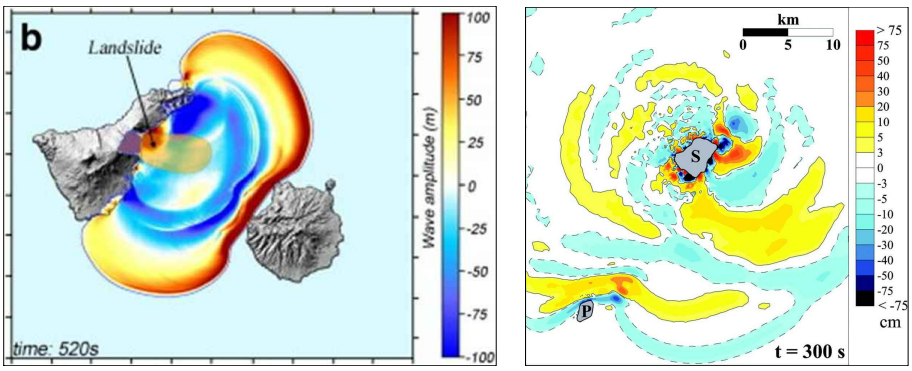

(a) *Tenerife, Canary Islands, Spain.*

(b) *Stromboli, Aeolian Islands, Italy.*

Figure 1.2: Left panel: numerical snapshot of the tsunami that occurred during the Pleistocene at Tenerife, Canary Islands, Spain [*Giachetti et al.*, 2011]. Right panel: numerical snapshot of the tsunami that occurred at Stromboli, Aeolian Islands, Italy in 2002 [*La Rocca et al.*, 2004].

quantitative analysis of the spatial wave modes around the island is provided and discussed. Finally, it is shown the application of a numerical model based on the Mild Slope Equation, as described by *Bellotti et al.* [2008], aiming at improving tsunamis early warning systems. An inversion technique has been used to reconstruct in real-time the tsunamis wave form in the far-field. Detailed discussions on the real-time application of the method and on the uncertainties of the initial landslide scenario to be used are provided.

This work is structured as follows. After this introduction the next chapter provides a brief review of the state of the art. The following chapters describe the experimental set-up and the experimetal results (i.e., the benchmark dataset). Then the study of the spatial wave modes is provided in a separated chapter. After this, a chapter that describes the numerical model aiming at improve the tsunami early warning systems follows. Concluding remarks close the work. Finally, the description of a correction technique to improve the generation of solitary waves in laboratory experiments is given in the Appendix.

Chapter 2

Landslide-generated tsunamis: state of the art

2.1 Preface

Tsunamis in general, and landslide-generated tsunamis in particular, have been widely studied in past researches. Many authors dealt with the problem of impulse waves generation, propagation and interaction with the coast. Different approaches can be found in the scientific literature: analytical, numerical and experimental ones. In this chapter a brief overview of the main scientific works dealing with landslide-generated tsunamis is given. An exhaustive dissertation of the topic discussed in this chapter can be found in the work of *Di Risio et al.* [2010].

2.2 Introduction

When either subaerial or submerged landslides occur, the displacements at water body boundaries generate transient free surface perturbations. The involved phenomena are quite different with respect to those related to earthquake-generated tsunamis. In the case at hand, the tsunami source, i.e. the landslide, takes place on both larger temporal-, and smaller spatial-scale. Indeed, the deformations are of the order of hundreds of meters and the generated waves are different from those induced by submarine earthquakes. Landslide tsunamis tend to be a local phenomenon, although extreme [*Synolakis et al.*, 2002].
Among the first researches on the topics it has to be mentioned the work of *Mallet and Mallet* [1858], that argued how the impulse waves genaration can be related not only to earthquakes but to submerged landslides as well.

Many devastating ladnslide-generated tsunamis events happened in the past; most of these have been described in scientific works. Among the main hystorical events it has to be mentioned the tsunamis occurred at Lituya Bay (Alaska, July 9, 1958; e.g. *Miller* [1960]). In this case a huge subaerial landslide entered the water and generated the highest known tsunamis run-up; it has been estimated to be up to 524 m. Furthermore, it has to be mentioned the tsunami generated by submarine landslide close to the Sissano Lagoon (Papua Nuova Guinea, July 17, 1998; e.g. *Synolakis et al.* [2002]). Altough the induced tsunamis run-up was not very large (i.e., 15 m) more than 2100 people were killed. As far as enclosed basins (e.g., lakes and reservoirs) are concerned devastating tsunamis have been observed. The event of Vajont Valley (Italy, October 9, 1963; e.g. *Panizzo et al.* [2005b]) is one of the biggest. In this case a subaerial landslide entered the water in the Vajont reservoir. The generated impulse waves caused a run-up of almost 235 m. The following overtopping of the reservoir dam caused the flooding of the village of Longarone with crushing effects: 1901 people were killed.
Following the description of *Di Risio et al.* [2010], the phenomena related to landslide-generated tsunamis can be qualitatively separated in four phases; each of these is characterized by its own physics. The phases are listed as follows:

- a solid or granular mass starts to move from one of the boundaries of a water body;
- an impulsive perturbation is generated as a consequence of the interaction with the water surface;
- the generated perturbation propagates into the water body;
- the propagated perturbation interacts with water body boundaries (i.e., coastlines).

The tsunamis generation, propagation and interaction with the coast mechanisms are schematically represented in Figure 2.1. The figure also shows the changes in terms of both physics and wave features, as the generation mechanism varies (i.e., subaerial, partially submerged or totally submerged landslide).
In the present work subaerial landslides are considered; thus, we focus mainly on this kind of generation mechanisms. When a subaerial landslide hits the water boundary and, consequently, enters the water, the sliding mass interacts with the water body and transfers its energy to it; a tsunami is then triggered. As shown in the next chapters, *Lynett and Liu* [2005] argued that

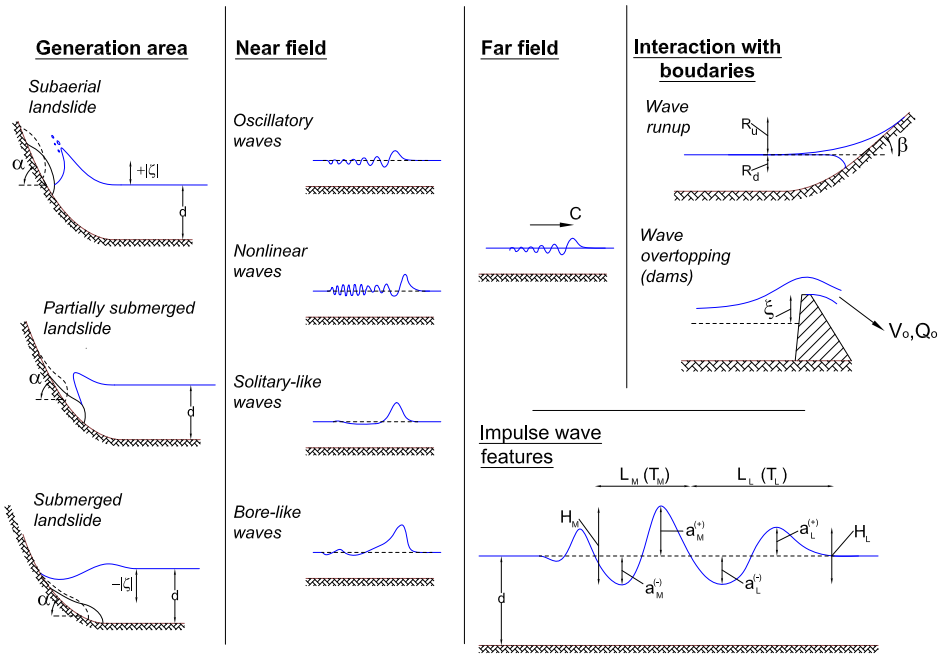

Figure 2.1: Sketch of landslide-generated impulse waves. [*Di Risio et al.*, 2010].

there is a distinction between the wave features in the so-called "near-field" and "far-field". In the "near-field" the wave features are mainly related to the characteristics of the landslide (i.e., volume, velocity, underwater travel time, density, porosity, shape, etc.). In other words, the wave features in the"near-field" are related to the initial conditions. As the generated waves propagate away from the generation area, both radiating seaward and propagating alongshore, other mechanisms dominate the wave features in the "far-field" (i.e., frequency and directional dispersion, refraction and diffraction, leaking and trapping of energy, etc.). Furthermore, as the propagating waves reach a water boundary, complex phenomena take place (i.e., run-up/draw-down, flooding, etc.).

When the landslide occurs directly at the water body boundaries, impulse waves both radiate seaward and propagate alongshore. The complex interaction that exists between the generation and the propagation mechanisms has therefore to be taken into account. In such case trapped waves can be triggered by the source of the tsunami and propagate along the coast by inducing large wave run-up observed in some real cases [*Ursell*, 1952; *Liu and Yeh*, 1996; *Liu et al.*, 1998; *Johnson*, 2007]. It is worth to highlight that this topic is in depth analyzed in the present work, as shown in chapter 5.

This chapter is structured as follows. After this introduction, the next section describes the main generation and propagation mechanisms of the landslide-generated tsunamis. Then an overview of the tsunamis generated by subaerial landslides is provided and a brief description of the impulse waves generated by submerged landslides closes the chapter.

2.3 Landslide-generated tsunamis: generation and propagation mechanisms

In this section a brief dissertation on the landslide-generated tsunamis generation and propagation mechanisms is given. The first study on the impulse waves generation in physical models is due to *Russell* [1844]. This author, aiming at reproducing solitary waves, used a vertical falling square-shaped box in a wave flume in order to generate transient perturbations of the free surface elevation. *Russell* [1844] showed by means of experimental tests that a solitary wave of a certain wave height H that propagates on a constant depth h travels with constant celerity $c = \sqrt{g(H+h)}$. Many authors used the so-called "Scott Russell wave generator" aiming at reproducing impulse waves in experimental facilities (e.g., *Wiegel et al.* [1970]; *Noda* [1970]; *Panizzo et al.* [2002]; *Di Risio and Sammarco* [2008]).
Furthermore, to simulate impulse waves generated by landslides moving paddle systems have been employed in the past (e.g., *Noda* [1970]; *Miller* [1970]). Wave paddles are still used to generate cnoidal, solitary and N-shaped waves in both two- and three-dimensional experiments (e.g., *Goring* [1978]; *Synolakis* [1990]; *Guizien and Barthélemy* [2002]; *Malek-Mohammadi and Testik* [2010]; *Romano et al.* [2013]). These kind of waves are quite useful to study the propagation and the interaction with the coast mechanisms of tsunamis, especially those genearated by earthquakes.
Nevertheless, the above mentioned methods are mainly effective in studying the tsunamis propagation and inundation phenomena; the energy exchange problem between the landslide and the water (i.e., the so-called "water entry problem") is not well addressed. Many researches, aiming at gaining insight on the impulse waves generation due to ideal landslides (i.e., solid boxes sliding down inclines and entering the water), have been carried out (e.g., *Wiegel et al.* [1970]; *Watts* [1998, 2000]; *Watts et al.* [2000]; *Walder et al.* [2003]; *Panizzo et al.* [2005a]; *Enet and Grilli* [2007]). Note that in these case, the shape of the landslide is defined a priori; furthermore, both the porosity and the deformation of the landslide are not reproduced in the mentioned works. *Watts et al.* [2005] investigated numerically the influence

that the shape of a submerged landslide can lead, in terms of generated wave features; they found that the higher the spreading of Gaussian shape, the lower the amplitude of the generated waves. Furthermore, *Watts et al.* [2005] pointed out that as far as submerged landslides are concerned, then the semi-elliptical-shaped rigid body represents the worst case scenario in terms of generated wave height. Finally, if subaerial landslides are considered, *Ataie-Ashtiani and Nik-Khah* [2008] suggested that landslide shape does not significatively affect the generated waves.

2.4 Tsunamis generated by subaerial landslides: wave features

As far as subaerial landslides are concerned, a clear, although qualitative, description of the generation physics has been provided by *Liu et al.* [2005], *Di Risio et al.* [2009a] and *Di Risio et al.* [2010]. The latter authors stated that "When landslide enters the water body, it pushes ahead the fluid and a leading positive seaward radiating wave is generated. Once the landslide becomes totally submerged, the water is initially depressed by generating a trailing wave through. Strong alongshore free surface gradients occur in the generation area resulting in converging flows that collide and rebound along the centreline of the landslide. The rebound is the responsible of a large positive wave radiating offshore".
Several researches have been carried out aiming at shedding light on the features of the generated waves. Among these it has to be mentioned the work of *Kamphuis and Bowering* [1970]. Based on experimental results they proposed a dimensional analysis devoted at evaluating the influence and the relationship f between the dependent quantities (in dimensionless form Π), as follows:

$$\Pi = f\left(F, M, G, X, S, t, \sqrt{\frac{g}{h}}, \gamma, \alpha, p\right), \tag{2.1}$$

where F is the landslide Froude number ($F = u_s/\sqrt{gh}$), M is the dimensionless two-dimensional landslide volume, G the specific gravity, X the dimensionless propagation distance, t the time, g the gravitational acceleration, γ the landslide slope front, α the slope angle of the incline and p the landslide porosity. The experimental results, according with the above mentioned analysis, highlighted that the maximum generated wave height H_M is strongly affected by the dimensionless volume M and the landslide Froude number F. Furthermore, it is shown that the leading wave period

T_l is mainly influenced by the dimensionless propagation distance X (i.e., frequency dispersion occurs).
More recently, *Walder et al.* [2003], by performing experimental investigations using solid landslides, pointed out that the dimensionless underwater travel time τ (as analytically confirmed by *Di Risio and Sammarco* [2008]), the dimensionless landslide volume M, the landslide Froude number F and the slope of the incline α have a great influence on the generated waves. More specifically, *Walder et al.* [2003] demonstrated that the tsunamis wave height increases as the underwater travel time decreases. *Panizzo et al.* [2005a] performed three-dimensional experiments, using a regular-shaped rigid body sliding along an incline that generated waves in a wave tank, aiming at evaluating the influence of the incline slope α. They demonstrated that the wave height increases as the incline slope decreases.
It has to be mentioned that most of the works cited so far mainly aim at studying the features of the waves that, leaving the generation area, radiate seaward. But as earlier mentioned, when a tsunamis, which is generated by a landslide that occurs directly at the water boundary, is triggered, also waves that propagate alongshore takes place. The physics of the wave propagation alongshore is dominated by complex phenomena (i.e., refraction, diffraction, reflection, etc.). In a qualitative way it is possible to state that the wave propagation alongshore is intimately related to the so-called "tsunamis trapping mechanisms". In this work this topic is of particular interest and it is treated in a dedicated chapter (i.e., chapter 5). Given this, just a brief overview of the main literature works is provided in this chapter.
The first studies on the tsunamis propagation alongshore have been carried out in the last decades. Many authoritative experimental, numerical and analytical studies have been addressed the propagation of the lanslide-generated waves both along straight coasts (e.g., *Yeh* [1985]; *Chang* [1995]; *Liu and Yeh* [1996]; *Liu et al.* [1998]; *Lynett and Liu* [2005]; *Sammarco and Renzi* [2008]; *Di Risio et al.* [2009a]; *Renzi and Sammarco* [2012]; *Seo and Liu* [2013]) and around circular islands (e.g., *Yeh et al.* [1994]; *Tinti and Vannini* [1994, 1995]; *Cho and Liu* [1999]; *Liu et al.* [2005]; *Di Risio et al.* [2009b]; *Renzi and Sammarco* [2010]). As in depth shown in chapter 5, edge waves (i.e., trapped waves) dominate the wave propagation along the shore, when a straight beach is considered. More complex is the physics of the wave propagation alongshore as far as a circular island is concerned, as pointed out by *Renzi and Sammarco* [2010]. The latter authors demonstrated that in a polar-symmetric topogaphy a perfect wave trapping is not possible.
Since the present work mainly aims at extending and improving the works of *Di Risio et al.* [2009a] and *Di Risio et al.* [2009b], it could be helpful to

recall the main issues addressed in these two works. *Di Risio et al.* [2009a] carried out a series of experiments in a three-dimensional wave tank aiming at reproducing landslide-generated tsunamis at a straight beach. The experimental layout was similar to that simulated numerically by *Lynett and Liu* [2005], although the beach was steeper. The landslide model was a semi-elliptical rigid body (note that the model is the same one that has been used by *Di Risio et al.* [2009b] and it is one of the two landslide models that have been used for the experiments described in this work). Both partially submerged and subaerial landslides have been tested during the experiments. The experimental layout allowed to observe the near field wave pattern, just landward to the landslide, and the propagation alongshore of the leading wave before the sidewalls reflection contaminated the induced waves. During the experiments secondary run-up peaks were observed and the maximum run-up was located at about two times the landslide width away the centreline of the landslide rather than directly landward the landslide. *Di Risio et al.* [2009b] were aimed at reproducing impulse waves propagation around a conical island, similar to that of *Briggs et al.* [1995], placed at the centre of a large wave tank. As mentioned, the landslide model was exactly the same used by *Di Risio et al.* [2009a]. Only subaerial landslides have been tested. During the experiments, the induced run-up along the coast was measured by means of special gauges directly embedded into the island flanks. The authors found that the higher the undisturbed shoreline radius, the higher the induced run-up. The large dimensions of the wave tank allowed to observe the propagation of waves along the whole circular coastline and dispersive features of wave packets were observed, being the maximum run-up induced by the first wave near the generation area, by the second wave up to a curvilinear distance alongshore equal to about 8 times the landslide width, then the third wave induces the maximum run-up and so on.

2.5 Tsunamis generated by submerged landslides: wave features

As highlighted by *Di Risio et al.* [2010], the features of the tsunamis generated by submerged landslides are quite different with respect to those generated by subaerial ones. Since in the following chapters tsunamis generated by submerged landslides are not considered, just a brief description of this phenomena is given.

Watts [1998] demonstrated that the features of the generated waves are intimately related to the landslide motion, especially if the landslide starts to move when it is completely submerged. *Enet and Grilli* [2007], by performing three-dimensional experiments in a wave tank, pointed out that submerged landslides cause a depression of the free surface elevation above the initial position of the landslide; this implies that a rebound takes place. Thus, the waves leave the generation area as a leading elevation N-wave that radiate seaward [*Tadepalli and Synolakis*, 1994] followed by small trailing waves. Moreover, the generated waves propagate alongshore as well, inundating the coast (i.e., run-up/draw-down occurs). Furthermore, *Enet and Grilli* [2007] demonstrated the importance of the so-called initial acceleration and terminal velocity of the landslide.

Chapter 3

Description of the experimental setup

3.1 The 3D physical model

As introduced in chapter 1, this work aims at describing the physics of landslide-generated tsunamis that occur at the coast of a conical island. In order to gain insight on this topic, laboratory experiments have been carried out on a large scale physical model. In this chapter a detailed description of the experimental setup is given.

The experiments have been carried out in a large wave tank (50 m long, 30 m wide, 3 m deep) at the Research and Experimentation Laboratory for Coastal Defence of Polytechnic of Bari (LIC, Italy). The Figure 3.1 shows the sketch of the wave tank. The physical model consists of a truncated conical island (base diameter equal to 8.90 m, maximum height equal to 1.20 m, see Figure 3.2) made up of PVC sheets (thickness 0.01 m) sustained by a rigid steel frame. The island is placed at the centre of the tank in order to obtain an appropriate distance from the tank walls; indeed, the walls when are reached by radiating waves induce spurious reflected waves that contaminate the experimental domain. The water depth was kept constant to 0.80 m. The slope (α) of the island flanks is of $\cot\alpha = 3$ (i.e. 1 vertical, 3 horizontal) to reproduce the typical slope of volcanic islands where landslides are likely to occur (i.e. Stromboli Island, Southern Tyrrhenian Sea, Italy, *Tinti et al.* [2005]). One of the island flanks reproduces a slide that allows landslide model to slide along the island and to enter the water; thus tsunamis can be triggered. Notwithstanding the physical model reproduces a geometry as general as possibile, it is interesting to highlight that the conical island could be a schematized (and idealized) reproduction of the

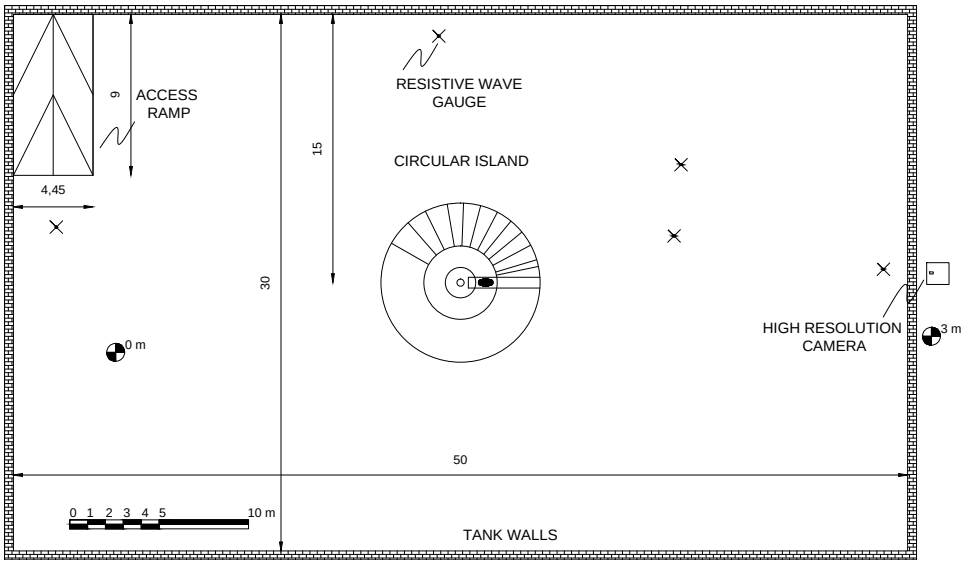

Figure 3.1: Sketch of the wave tank.

Stromboli Island (see Figure 3.3), if a Froude law scale 1:1000 is considered. Accordingly the slide along the island flanks can be seen as a reproduction of the Sciara del Fuoco (see Figure 3.4).
In order to simulate the effect of landslides, past studies were carried out by using solid boxes falling vertically (Scott Russell's wave generator, *Russell* [1845]) or sliding along inclines with different shapes (semi-elliptical, triangular, parallelepiped) with deformable sand bags and with granular materials (a complete review is provided in the work of *Di Risio et al.* [2010]). When a solid landslide model is used, its shape has to be defined preliminarily, and

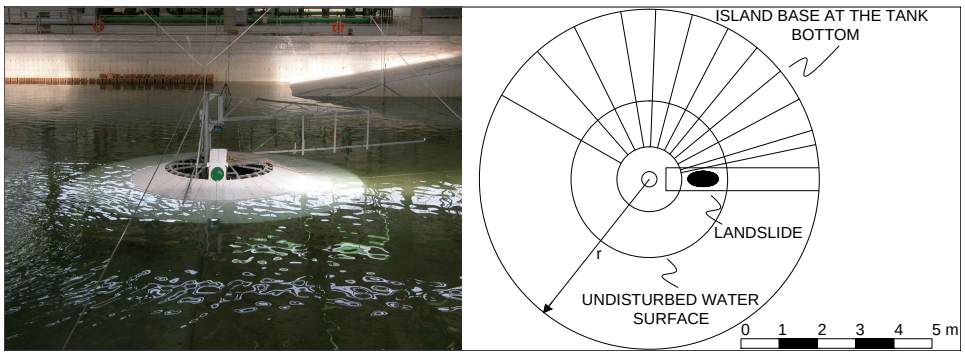

Figure 3.2: Left panel: picture of the conical island in the wave tank. Right panel: sketch of the physical model (plan view).

the deformations and porosity of real landslides are not reproduced in the model. *Grilli and Watts* [2003] and *Watts et al.* [2005] found that, in the case of underwater landslides, the higher the spreading of a Gaussian shape, the lower the amplitude of generated waves, at least for underwater landslides. Then, *Watts et al.* [2005] indicate that semi-elliptical shaped rigid body represents the worst case scenarios, at least for underwater landslides [*Watts*, 2000; *Enet and Grilli*, 2007; *Di Risio et al.*, 2009a, b]. Then, as in *Di Risio et al.* [2009a, b], solid landslide models, shaped as a half of an ellipsoid, have been used (Figure 3.5).

In a reference frame with the origin placed at the centre of the ellipsoid, the landslide model is described by the following equation:

$$x^2/a^2 + y^2/b^2 + z^2/c^2 = 1 \tag{3.1}$$

where x is the coordinate directed along the incline, y the coordinate parallel to the undisturbed shoreline and z is the orthogonal distance from island flank. The axis a (orthogonal to the undisturbed shoreline) is equal to 0.40 m (landslide length $2a = 0.80$ m), the axis b (parallel to the undisturbed shoreline) is equal to 0.20 m (landslide width $2a = 0.40$ m). During the experiments two different landslide models have been used (see Figure 3.5). The first one (hereinafter referred to as LS1) is characterized by a thickness of 0.05 m (c=0.05 m). The LS1 volume is then equal to $V = 0.0084$ m^3. The thickness of the second landslide model (hereinafter referred to as LS2)

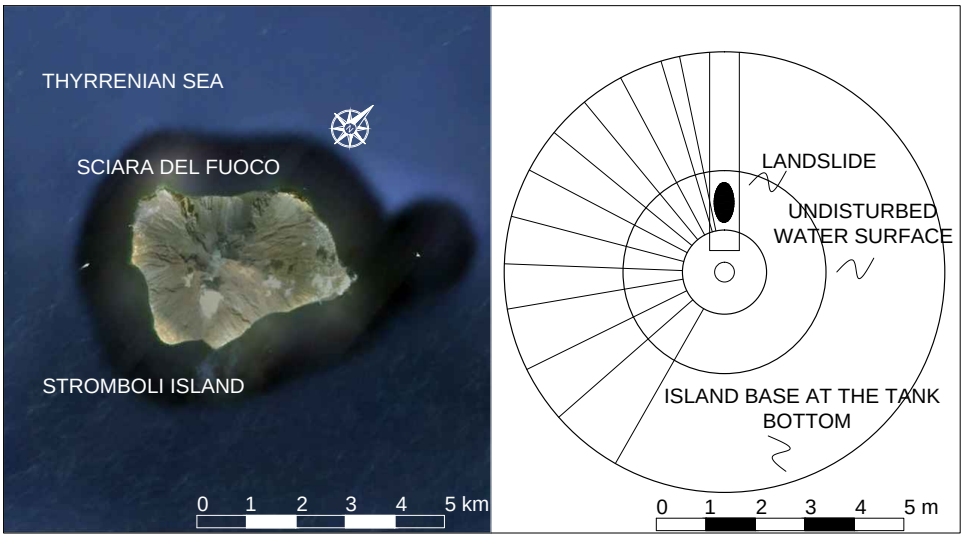

Figure 3.3: Left panel: plan view of the Stromboli island (South Thyrrenian Sea). Right panel: Sketch of the physical model.

is 0.10 m (c=0.10 m) and the volume $V = 0.0168$ m^3. The density of the landslide models was kept constant to 1.83 kg/m^3 for a total mass of about 15.4 kg and 31.7 kg for LS1 and LS2 respectively (see Table 3.1). The landslide models are made up of PVC covered by an exterior layer of fiberglass. The flat bottom, in contact with the island flank, is made up of steel. In order to constrain the landslide to move along a fixed line a steel T frame is welded to the landslide bottom (see Figure 3.5).

(a) *Detail of Sciara del Fuoco: rock fall.*

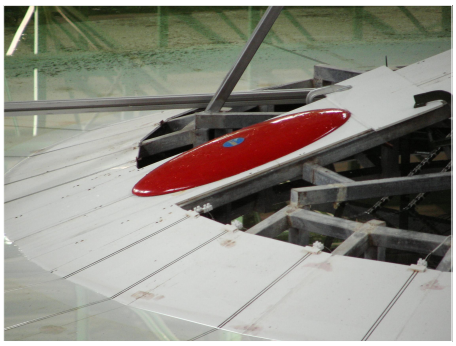

(b) *Detail of the slide along the conical island.*

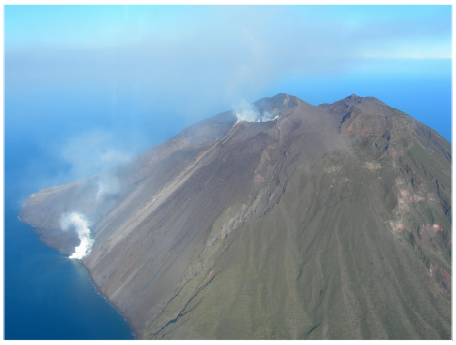

(c) *Aerial view of Sciara del Fuoco.*

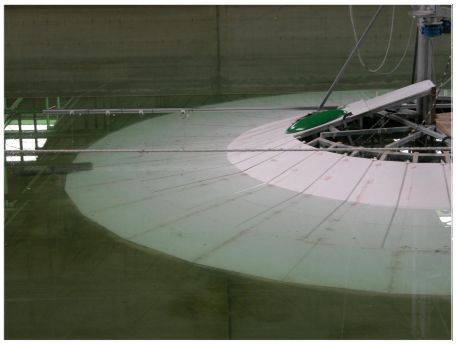

(d) *Lateral view of the conical island and the slide.*

Figure 3.4: Pictures of the Sciara del Fuoco (Stromboli island) and the slide placed on the conical island model.

Landslide model	V_M (dm^3)	M_M (kg)	ρ_M (kg/m^3)	V_P (m^3)	M_P (kg)	ρ_P (kg/m^3)
LS1	8.40	15.4	1.83	8.4E+06	15.4E+06	1.83
LS2	16.80	31.7	1.83	16.8E+06	30.7E+06	1.83

Table 3.1: Landslide models physical parameters. Note: subscript $(\cdot)_M$ refers to model values, while subscript $(\cdot)_P$ refers to prototype ones.

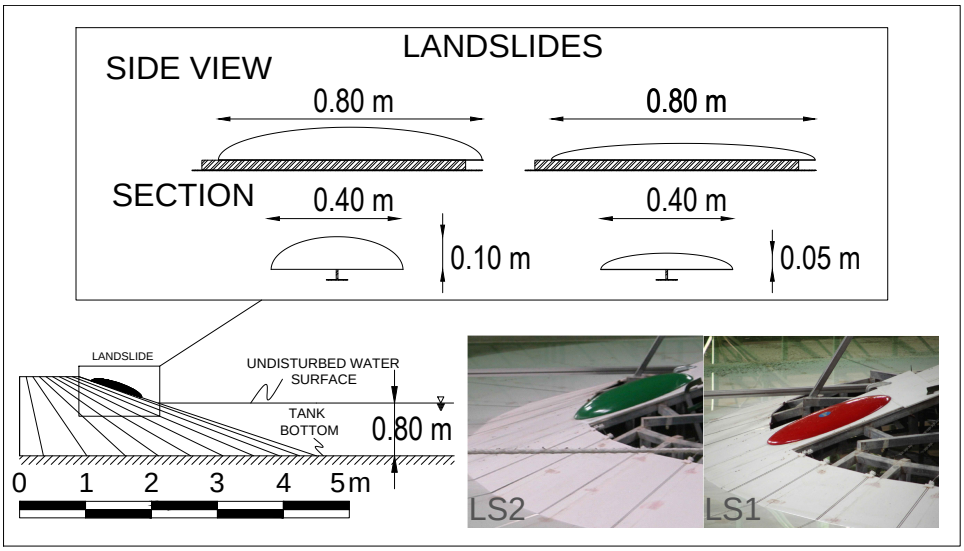

Figure 3.5: Sketch of the landslide models.

3.2 Instruments and acquisition techniques

The experiments aim at measuring the waves generated by the landslide model that slides down the island flank. Then landslide motion and water surface elevation data have to be recorded. A high-resolution camera was placed on a steel frame placed just outside of the wave tank, directly in front of the generation area (see panel (a) of the Figure 3.9). The digital images collected by means of the video-camera have been used to reconstruct the landslide motion, as detailed in the next chapter.

For what concerns the free surface elevation measurements new 3D experiments have been performed aiming at providing a benchmark data set for validating theoretical models of landslide-generated tsunamis. In order to reach this purpose it is essential to have both a large number of free surface elevation measurements, with a spatial resolution as high as possible, both a large number of repetitions for each experiment. Of course this it would imply a large number of instruments. Indeed, the idea of this experimental campaign is to use few instruments; some of these are fixed in space (to check the repeatibility of the experiments) while some others are placed on a moving frame (to measure the whole wave pattern around the island). As described in the following, this method allows to obtain a high-space reso-

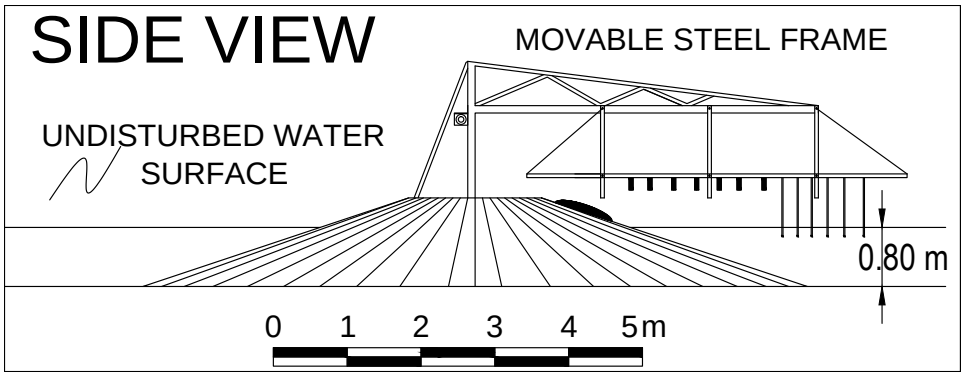

Figure 3.6: Side view of the conical island: detail of the movable steel frame.

lution measurements data set while minimizing the number of instruments. In order to measure the free surface elevation time series around the conical island wave gauges (hereinafter referred to as WG), ultrasonic water level sensors (hereinafter referred to as US) and run-up gauges (hereinafter referred to as RG) were employed. Some of the instruments were kept fixed in space (i.e., RG and nine WG), some others were placed on a steel frame (i.e., US and six WG) that can rotate around the island centre spanning a half of the island (see Figures 3.6, 3.7, and 3.8). This "movable" system allows to collect the free surface time series along cross-shore sections, starting from the axis along which the landslide moves (θ =0°) up to the rear side of the island (θ =180°). For each test, the landslide is placed at starting position and the movable steel frame moved to the correct angular position, then the acquisition process begins, the landslide model is released and the tsunami is generated. Typically the acquisition process is stopped about 50 s after the release of the landslide, when the waves reflected at the side walls had completely contaminated the wave field. The procedure was repeated for each position of the movable frame, from θ =0° up to θ =180° every 5°, for a total of 37 landslide releases. As described in the next chapter the fixed sensors were used to check the repeatability of the tests; the sensors placed on the movable frame were used to measure the whole wave pattern around the island. In particular:

- 12 run-up gauges (RG) were embedded directly into the PVC of the island flanks in order to measure the shoreline displacements time series;
- 9 wave gauges (WG) were placed in fixed position near the generation area and in the far field;

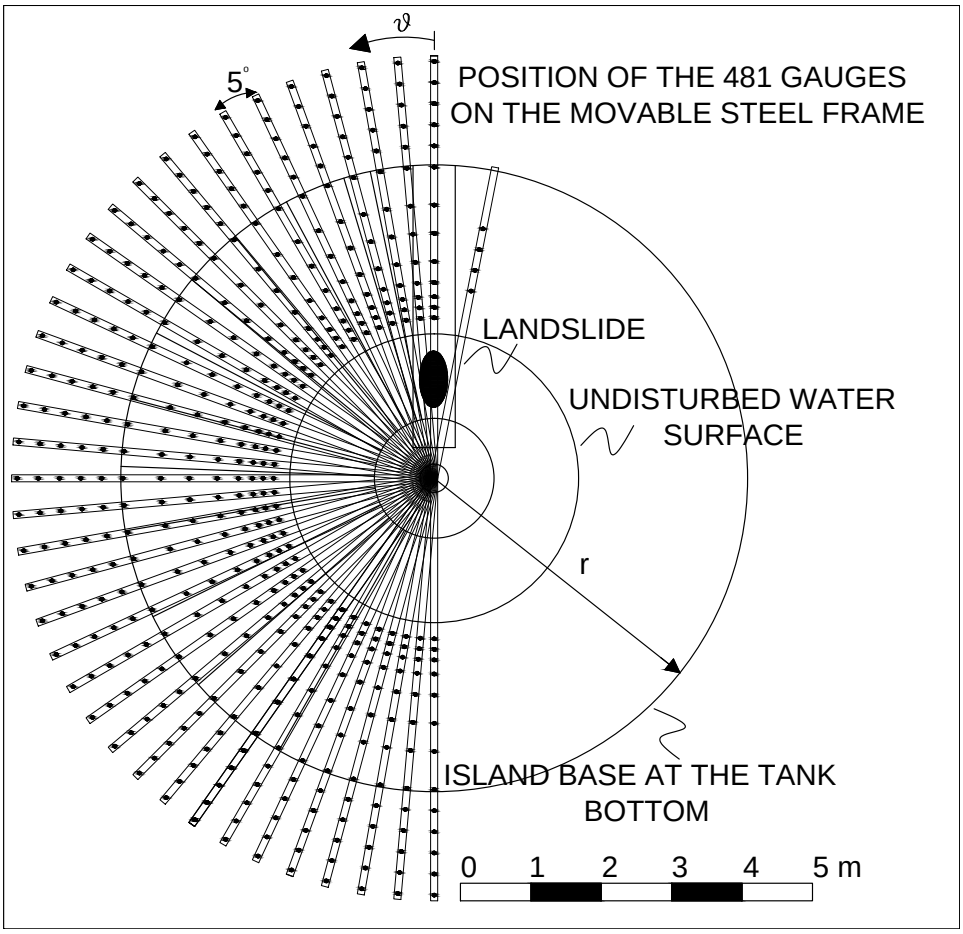

Figure 3.7: Sketch of the measurement points.

- 7 ultrasonic (US) sensors were placed on the movable frame;
- 6 wave gauges (WG) were placed on the movable frame;

Table 3.2 summarizes the sensors position and naming. All the signals have been acquired with a sampling frequency of 200 Hz. The acquisition process has required three different National Instruments boards. Furthermore, in order to syncronize the measurements collected by the boards, a Labview software has been used to trigger simultaneously the data acquisition.

Once the repeatability of the tests has been addressed, the whole data set (37 landslide releases) corresponds to a single test with 497 sensors. This measurements spatial resolution (comparable to numerical results, e.g. *Montagna et al.* [2011]) allows to characterize the wave pattern around the island in great detail.

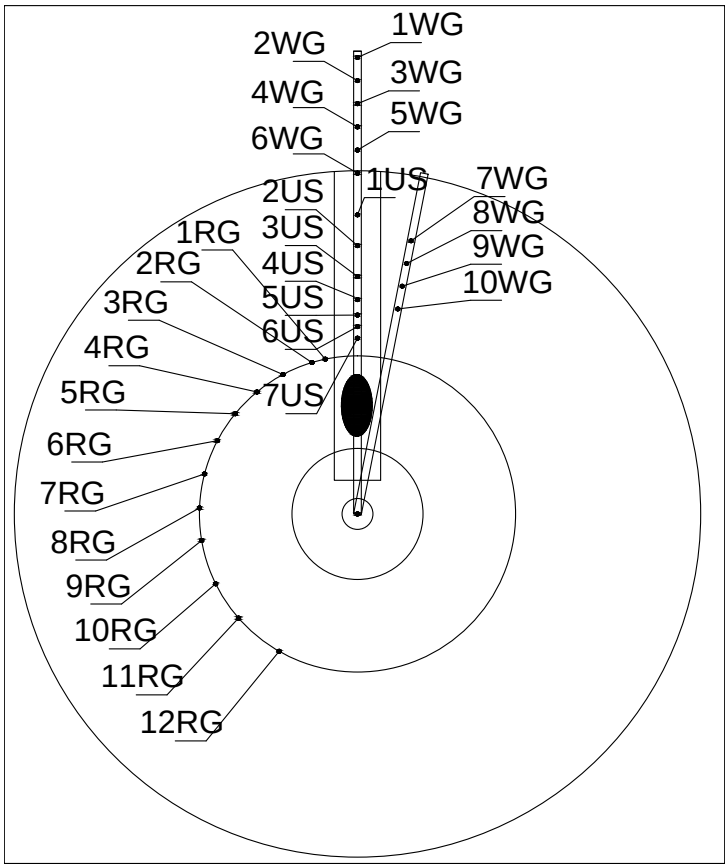

Figure 3.8: Name and position of the instruments (WG = wage gauges, RG =run-up gauges, US = ultrasonic sensors).

Wave Gauges			Runup Gauges		Ultrasonic Sensors		
Sensor name	Radial Position (R) (m)	Angular Position (θ) (°)	Sensor name	Angular Position (θ) (°)	Sensor name	Radial Position (R) (m)	Angular Position (θ) (°)
7WG	4.53	7.9	1RG	14.5	1WG	5.92	0 to 180 by 5
8WG	4.08	8.9	2RG	20.6	2WG	5.62	0 to 180 by 5
9WG	3.66	10.0	3RG	34.3	3WG	5.32	0 to 180 by 5
10WG	3.13	11.9	4RG	47.6	4WG	5.02	0 to 180 by 5
			5RG	60.2	5WG	4.72	0 to 180 by 5
			6RG	72.9	6WG	4.42	0 to 180 by 5
			7RG	86.3	1US	3.88	0 to 180 by 5
			8RG	98.7	2US	3.48	0 to 180 by 5
			9RG	111.5	3US	3.08	0 to 180 by 5
			10RG	125.2	4US	2.78	0 to 180 by 5
			11RG	138.6	5US	2.58	0 to 180 by 5
			12RG	151.6	6US	2.43	0 to 180 by 5
					7US	2.28	0 to 180 by 5

Table 3.2: Sensors position and naming.

(a) *High-resolution camera.*

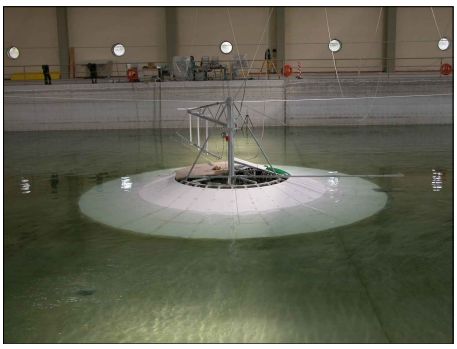

(b) *Lateral view of the conical island.*

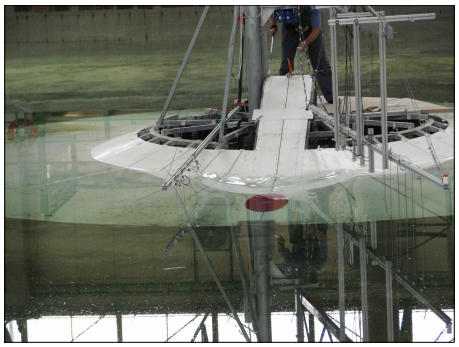

(c) *Moving and fixed arms with sensors.*

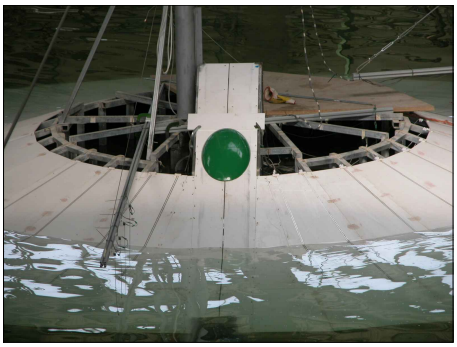

(d) *Run-up gauges.*

Figure 3.9: Pictures of the conical island and of the instruments used.

Chapter 4

Data analysis of the new 3D experiments: a benchmark data set

4.1 Introduction

In this chapter a detailed description of the new experimental results is given. As stated in chapter 3, new measurement techniques have been used to describe in detail the features of the waves that propagate offshore and those that propagate along the shoreline. In order to achieve measurements with a high spatial resolution, a new special movable acquisition system has been employed, along with a series of fixed wave gauges. Each experiment has been repeated 37 times, changing for each repetition the position of the movable gauges, devoted at measuring the water surface elevation around the island. Few surface elevation gauges and several fixed run-up gauges measure the waves at identical positions: these instruments provide 37 time series for each experiment, allowing an in depth statistical analysis of the experimental repeatability. The high-space resolution and the large number of the measurements have been used for defining a benchmark data set for the development/calibration/validation of analytical and numerical models of tsunamis generated by landslides.
This chapter is structured as follows. The next section provides the measurements and the analysis of the landslide motion; the following section illustrates a detailed analysis of the free surface elevation time series

4.2 Landslide motion

The proper description of the landslide kinematic is a crucial point when experimental data are intended to be used as benchmark test case for mathematical/analytical models validation. The governing equation of landslide motion has been widely used in past researches in the case of submerged landslides (e.g. *Pelinovsky and Poplavsky* [1996]; *Watts* [1998]). In the followings the methodology, used to estimate the parameters needed to reproduce the observed landslide motion in the case of subaerial landslides, is illustrated.
During the subaerial phase, the motion is governed by the following equation:

$$m\frac{d^2s}{dt^2} = mg\left(\sin\alpha - C_n\cos\alpha\right), \tag{4.1}$$

where m is the landslide mass, s the landslide displacements, t the elapsed time, g the gravity acceleration, α the slope angle, C_n the Columbic friction coefficient. Then, if landslide displacements are measured and velocities estimated by numerical differentiation, the Columbic friction coefficient can be estimated by the following relationship:

$$C_n = \left(\frac{1-u_0^2}{2gz_0}\right)\tan\alpha, \tag{4.2}$$

where u_0 indicates the landslide velocity when it hits the free surface and z_0 the dropping height, measured along the vertical direction. After the landslide hits the free surface a transition phase occurs, during which the landslide motion is affected by the complex interaction between the landslide and the fluid flow, related to the water entry problem. When the landslide becomes totally submerged, then buoyancy and drag forces act on it. During the underwater travel the landslide motion is governed by the following equation:

$$\begin{aligned}(m + C_m m_0)\frac{d^2s}{dt^2} &= (m - m_0)\,g\left(\sin\alpha - C_n\cos\alpha\right) + \\ &\quad + \frac{1}{2}C_d\rho A\left(\frac{ds}{dt}\right)^2\end{aligned} \tag{4.3}$$

where C_m is the added mass coefficient, m_0 is the displaced water mass, A is the main cross section of the moving landslide perpendicular to the direction of motion, ρ is the water density. The global drag coefficient C_d describes both form drag and skin friction:

$$C_d = \frac{C_F A_w}{A} + C_D \tag{4.4}$$

where C_D, C_F and A_w are the form drag coefficient, the skin friction coefficient and the wetted surface respectively.
For LS1 *Di Risio et al.* [2009a] performed a detailed analysis of the landslide motion on the basis of acceleration measurements collected by means of an accelerometer placed into the landslide model.
Due to the different scale of the experiments the landslide motion was reconstructed on the basis of the analysis of a series of digital images collected by means of a high resolution videocamera (images frequency acquisition equal to 25 Hz). Then the landslide motion were measured on the basis of its displacements rather than on the basis of its accelerations, i.e. direct acceleration measurements have not been collected during the new experiments. Of course, it is possible to compute the landslide acceleration by double numerical differentiation of displacements. However the double differentiation can lead to unacceptable errors on acceleration estimation. Then we used a different approach to infer the dynamical coefficients. In particular, the Coulumbic friction coefficient was calculated on the basis of estimated velocity, whilst the added mass and the global drag coefficients were estimated directly from the observed landslide displacements.
In the case of submerged landslides the theoretical solution of (4.3) is (e.g. *Watts* [1998]):

$$s(t) = \frac{u_t^2}{a_0} log \left[\cosh \left(\frac{a_0 t}{u_t} \right) \right] + s_0 \tag{4.5}$$

where a_0 is the initial acceleration and u_t is the terminal velocity that the landslide reaches when the gravity action is balanced by the boyancy, friction and drag forces. For submerged landslides, the initial acceleration a_0 can be directly inferred from (4.3) by imposing the velocity to be zero at the initial time:

$$a_0 = \frac{(m - m_0)g(\sin\alpha - C_n \cos\alpha)}{m + C_m m_0}. \tag{4.6}$$

Similarly, the terminal velocity is the (constant) velocity at which the landslide moves with a nil force resultant (i.e. $d^2s/dt^2 = 0$):

$$u_t^2 = \frac{2(m - m0)g(\sin\alpha - C_n \cos\alpha)}{C_d \rho A}. \tag{4.7}$$

It has to be stressed that the solution (4.5) with a_0 and u_t provided by (4.6) and (4.7) respectively, is valid only when the landslide motion starts when it is totally submerged. However such a solution can be used also in the case of subaerial landslide if different initial conditions are considered. Indeed equation (4.3) is valid for the submerged phase for both subaerial and submerged landslide. When the transition phase ends, the landslide motion

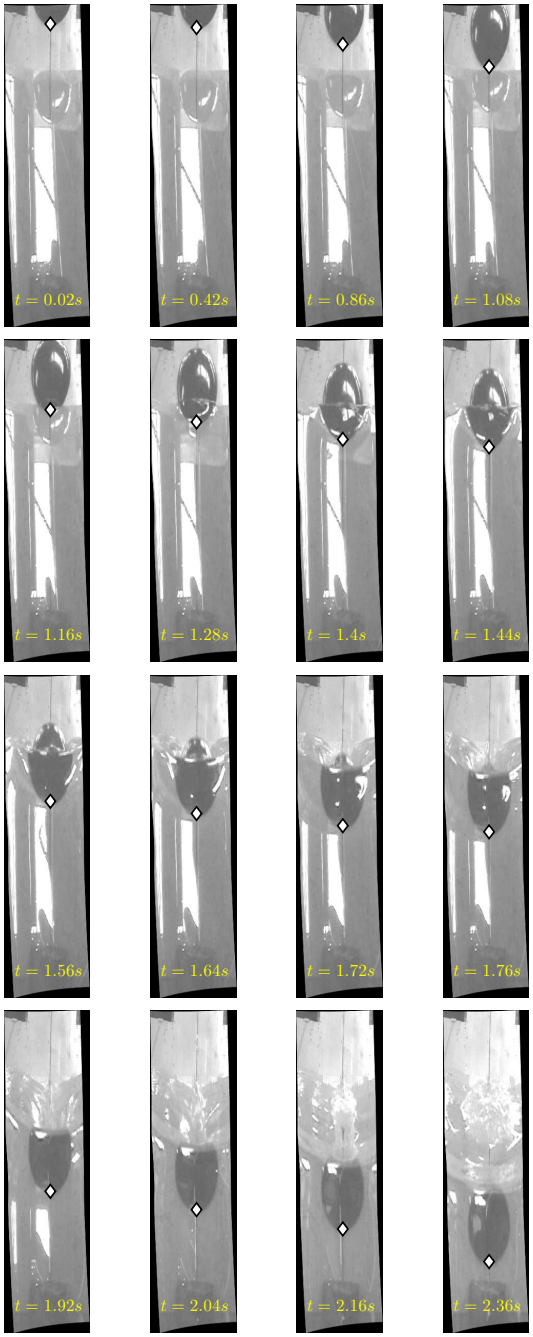

Figure 4.1: Example of the image analysis for tracking landslide motion: each panel shows the landslide at a given time-step after the release; the white diamond marker identifies the position of the seaward edge of the landslide.

is governed by equation (4.3) and the initial velocity is equal to u_0^*. In the case of subaerial landslides, the solution in the underwater phase ($t > t_0^*$, being t_0^* the instant when the transition phase ends) can be expressed as follows:

$$s(t) = \frac{u_t^2}{a_0^*} \log \left\{ \cosh \left[\left(\frac{a_0^*}{u_t} \right) (t - t_0^*) + \right. \right. \\ \left. \left. + \tanh^{-1} \left(\frac{u_0^*}{u_t} \right) \right] \right\} \tag{4.8}$$

Here the acceleration a_0^*, provided again by equation (4.8), is not the initial acceleration of the real landslide, but that of a kind of "equivalent submerged landslide" that reaches the velocity u_0^* at instant $t = t_0^*$. It has to be noticed that terminal velocity of the "dummy" equivalent submerged landslide is equal to that one of the real subaerial landslide.
In order to estimate the values of u_t and a_0^* it is possible to use a least square optimization technique based on observed landslide displacements.
During experimental tests, as anticipated in the previous chapter, a digital high-resolution camera was employed to collect images of falling landslides. Then, the collected images were rectified based on a series of points whose positions in space were measured by means of a high precision topographic total station. All the images where used to reconstrct the instantaneous position of the landslide from which the displacement time series is defined. By means of image analysis techniques based on the colour recognition in rectified pictures, it was possible to track the position of the lanslide for each frame (see Figure 4.1).

The velocity was estimated by numerical evaluation of the time derivative of landslide displacements, needed to estimate the impact velocity u_0

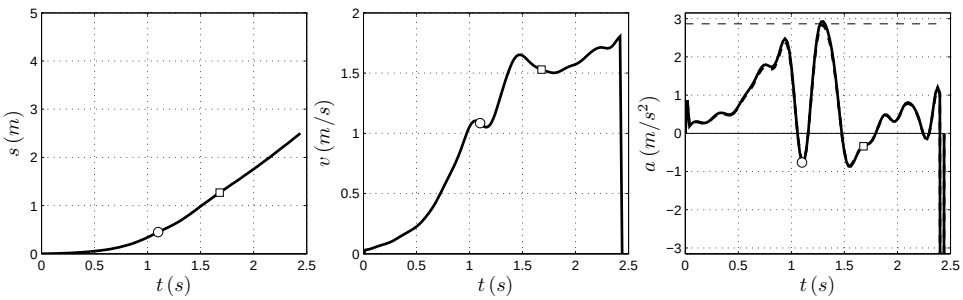

Figure 4.2: Left panel: space traveled. Middle panel: velocity. Right panel: acceleration. In each panel the round marker identifies th time at which the landslide hits the water, while the square one identifies the time at which the motion becomes completely submerged.

and then to estimate the value of Columbic friction coefficient. During the subaerial phase, the velocity increases up to the impact velocity. Then the transition phase occurs and the landslide motion is affected by the water-solid interaction. Then the transition phase ends and the submerged phase starts until the landslide hits the tank bottom.
The falling height z_0 was kept constant during the experiments (z_0= 0.14 m), then the value of impact velocity (almost the same for all the tests) was used to estimate the Columbic friction coefficient. Data analysis showed that C_n is equal to 0.194±0.014. In order to estimate the values of C_d and C_m, the landslide displacements time series related to underwater phase were used. In particular, the terminal velocity u_t and initial acceleration a_0^* are inferred by means of non linear least square optimization (Gauss-Newton method) aimed at minimizing the deviation between the computed, given by equation (4.8), and observed displacements. The use of relationships (4.6) and (4.7) allows to estimate the values of the drag coefficient C_d and added mass coefficient C_m. Obtained results are synthetized in Table 4.1 for both LS1 and LS2 landslide models.
The theoretical landslide velocity $v(t)$ can be defined by the time derivative of solution (4.8):

$$v(t) = u_t \tanh\left[\frac{a_0^*}{u_t}(t - t_0*) + \tanh^{-1}\left(\frac{u_0^*}{u_t}\right)\right] \tag{4.9}$$

The theoretical value of added mass coefficient C_m can be estimated by using the strip theory (e.g. *Enet and Grilli* [2007]; *Newman* [1989]). In the case of semi ellipsoid landslide model it reads:

$$C_m = \frac{2bc^2\pi}{3V} \tag{4.10}$$

The theoretical value of C_m are equal to 0.249 and 0.499 for LS1 and LS2 respectively. Furthermore the estimated value of C_d for LS1 can be compared with the results of *Di Risio et al.* [2009a, b] who obtained $C_d \approx 0.40$.

Landslide model	V (dm^3)	Mass (kg)	Density (kg/m^3)	Added Mass (kg)	Drag Coefficient ()	Terminal velocity (m/s)
LS1	8.40	15.4	1.83			
LS2	16.80	31.7	1.83		0.421±0.009	1.713 ± 0.018

Table 4.1: Landslide models physical and hydrodynamics parameters.

4.3 Experimental findings and discussion

This section describes the experimental results in terms of free surface elevation collected around the conical island and wave run-up at its coast. In particular, once the repeatibility of the tests is addressed, the data are analyzed in order to describe the wave features around the island.

4.3.1 Time series analysis

All the time series collected during the experiments have been analyzed in the time-domain by means of a zero-crossing analysis (hereinafter ZC). When a tsunamis time series is considered, ZC analysis is more appropriate than a spectral one. Tsunamis are unsteady phenomena; this aspect is not perfectly in line with the hypothesis of the spectral analysis in the frequency domain (i.e., periodicity of the signal). However, also spectral analysis has been successfully used in this work to identify meaningful properties of the waves; but, in order to catch the properties of each single wave in the tsunamis packet, ZC is supposed to be more effective. Furthermore, ZC allows to better catch the properties of the analyzed time series in the time-domain

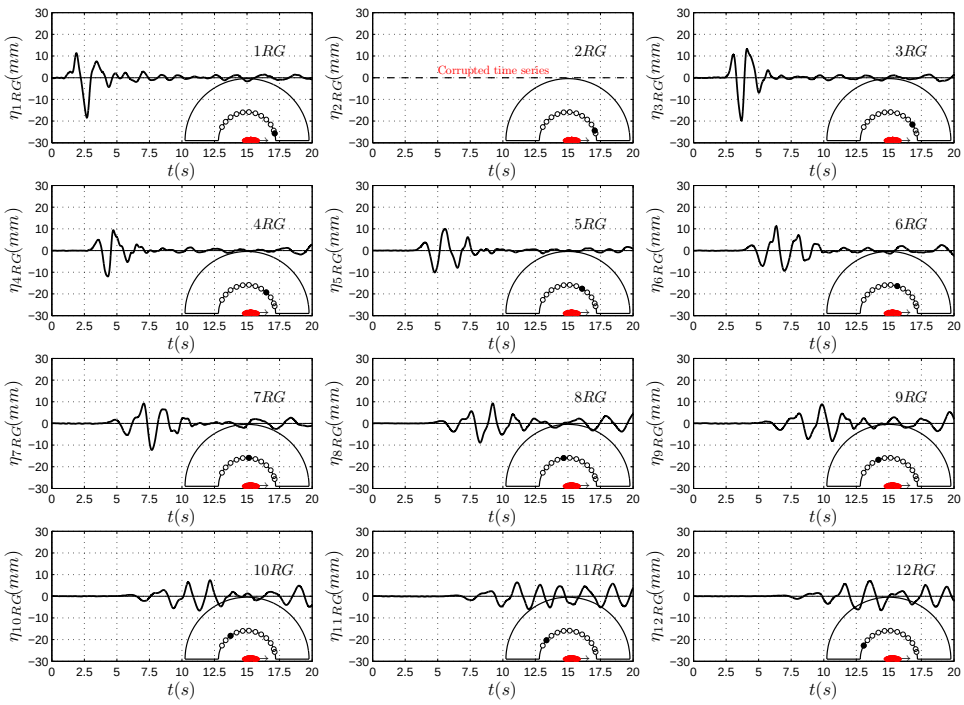

Figure 4.3: Run-up time series (i^{th}−release).

(i.e., arrival time of the first wave, arrival time of the maximum wave of the packet, periods of first waves of the group, etc.), which are of high scientific and technical interest to describe the features of the wave packet.
Each time series has been processed with zero-crossing analysis in order to obtain:

- "Beginning" of the tsunamis (i.e., time at which the first crest takes place at each wave gauge);
- Free surface elevation of the maximum crests and minimum troughs of the generated waves;
- Wave periods of the generated tsunamis;

To obtain the above mentioned wave properties all the signals have been analyzed by means of an automatic ZC algorithm, which has been fully devel-

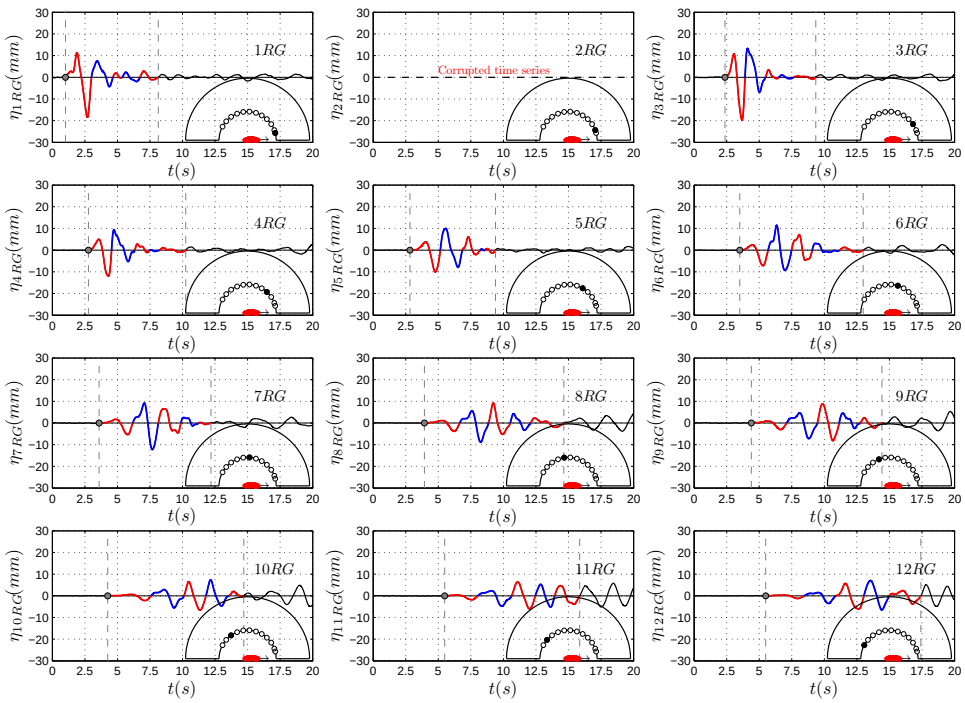

Figure 4.4: Zero-crossing analysis of the run-up time series (i^{th}−release). Note: gray markers identify the beginning of the tsunamis; red lines identify the odd waves in the packet; blue lines identify the even waves in the packet; vertical gray dashed lines identify the time at which the tsunami begins (left line) and the time at which the fifth wave ends (right line) respectively.

oped at the University of Roma Tre. The algorithm has been widely tested; it is found that it is very effective in identifying each wave of the packet and, even more important, the "beginning" of the tsunamis. To detect the beginning of the tsunamis two checks have been simultaneously implemented in the algorithm: the first one identifies the time at which the signal reaches and exceeds an amplitude treshold, while the second one analyzes the signal by calculating the Fast Fourier Transform (FFT) on a window that grows in duration; when the maximum spectral amplitude reaches and exceeds a given treshold and the peak frequency becomes less than a frequency treshold, the beginning of the tsunamis is uniquely identified. The Figure 4.3 shows the time series collected by means of the run-up gauges (RG), related to the ith-release of the landslide. Each panel refers to a different RG; the position of the sensor along the shoreline is showed, for each panel, by the sketch in the right low corner of the graphs. Figure 4.4 shows the results of the ZC, which has been applied to the time series represented in Figure 4.3. Figure 4.4 shows the behavior of the detection algorithm. Gray markers identify the beginning of the tsunamis; red and blue lines identify the odd and even waves respectively, that form the tsunamis packet. Note that only the first five waves have been represented in the plots; this is due to that the wave packet consists of less than five waves, especially in the so-called "near-field". When each wave of the group has been identified, the algorithm allows to obtain the properties of these (i.e., maximum crest, minimum trough and wave period, etc.).

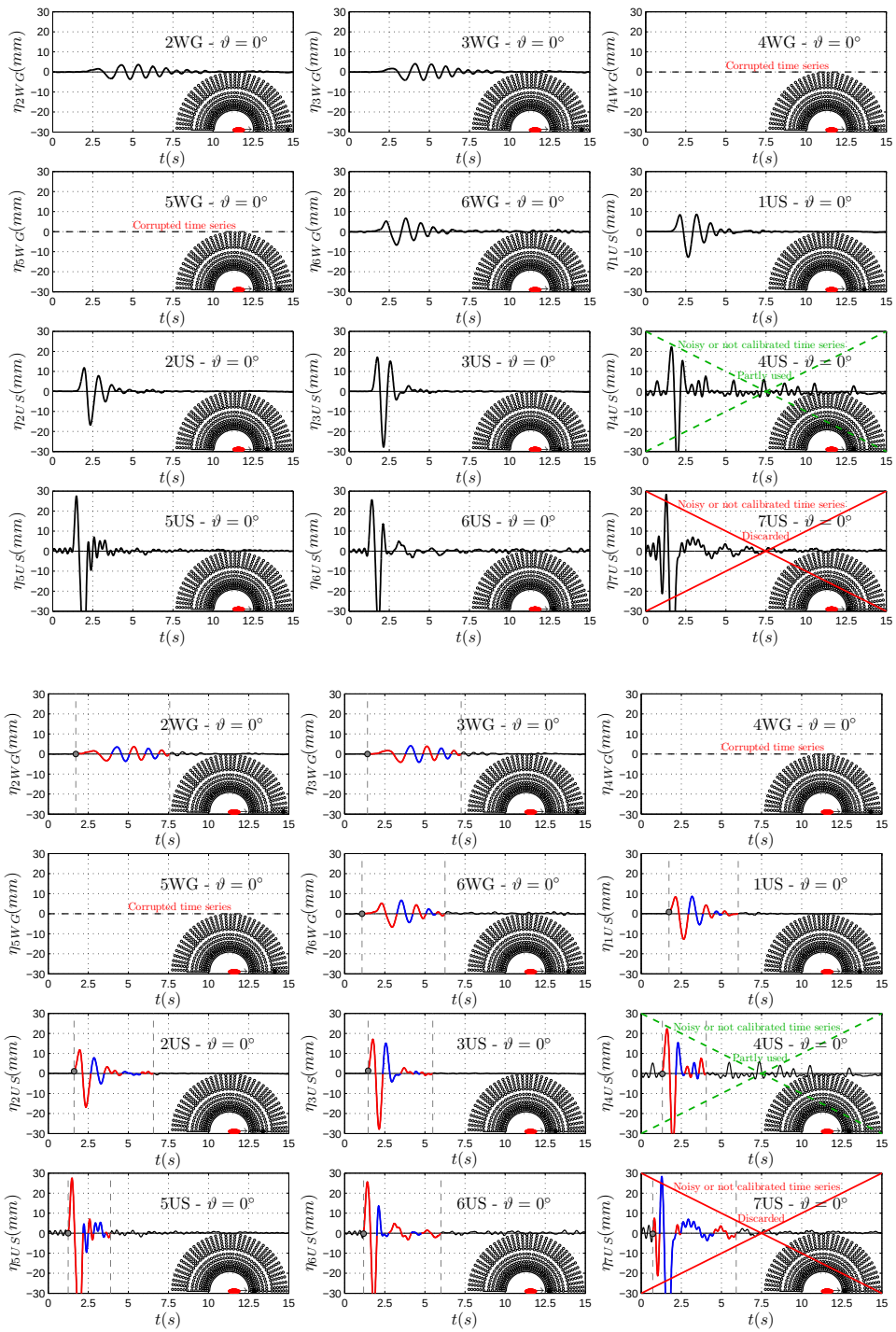

Figure 4.5: Free surface elevation time series collected by the moving arm at $\vartheta = 0°$ (upper panels), and zero-crossing analysis (lower panels). Note: the symbols have the same notation of that in Figure 4.4.

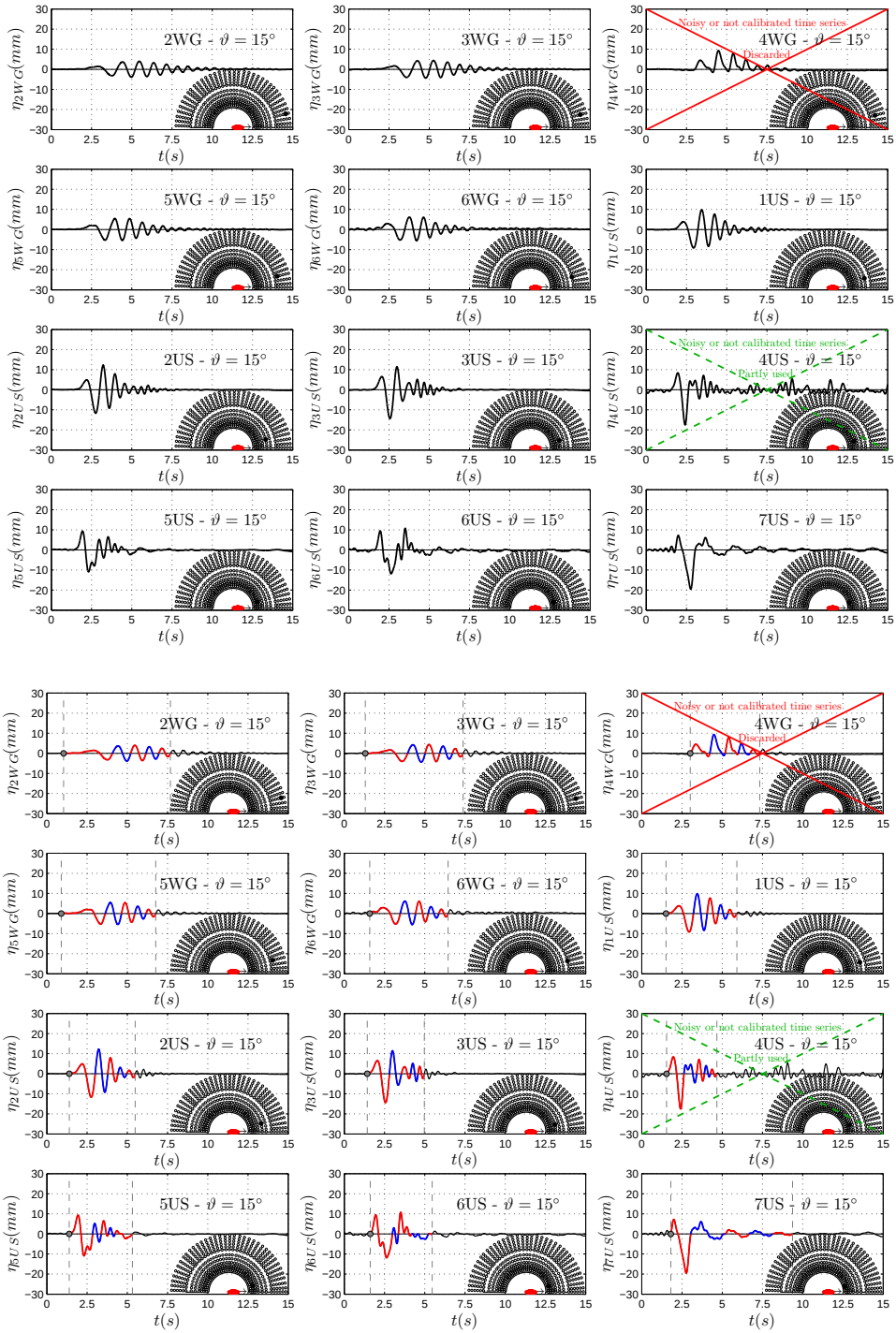

Figure 4.6: Free surface elevation time series collected by the moving arm at $\vartheta = 15°$ (upper panels), and zero-crossing analysis (lower panels). Note: the symbols have the same notation of that in Figure 4.4.

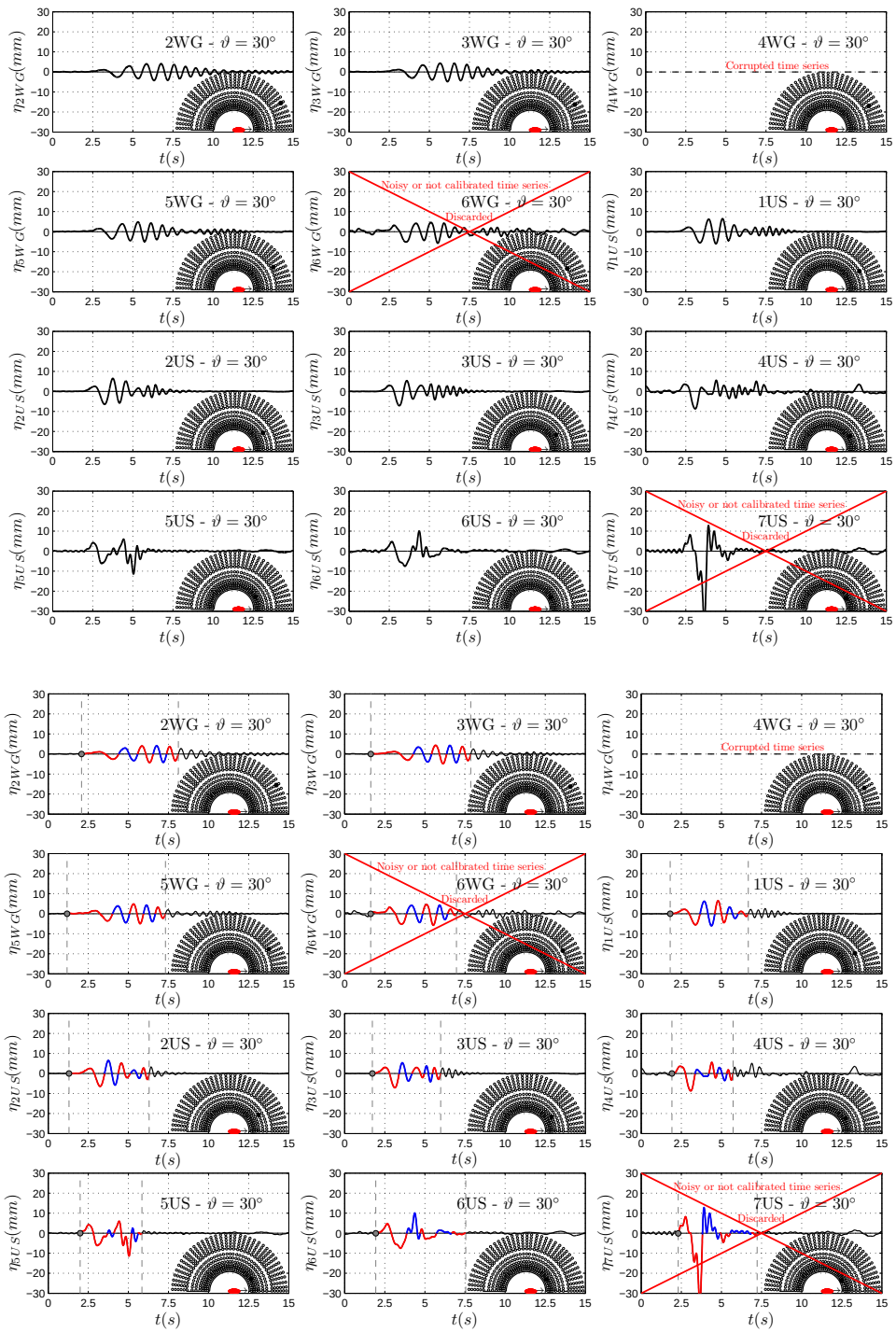

Figure 4.7: Free surface elevation time series collected by the moving arm at $\vartheta = 30°$ (upper panels), and zero-crossing analysis (lower panels). Note: the symbols have the same notation of that in Figure 4.4.

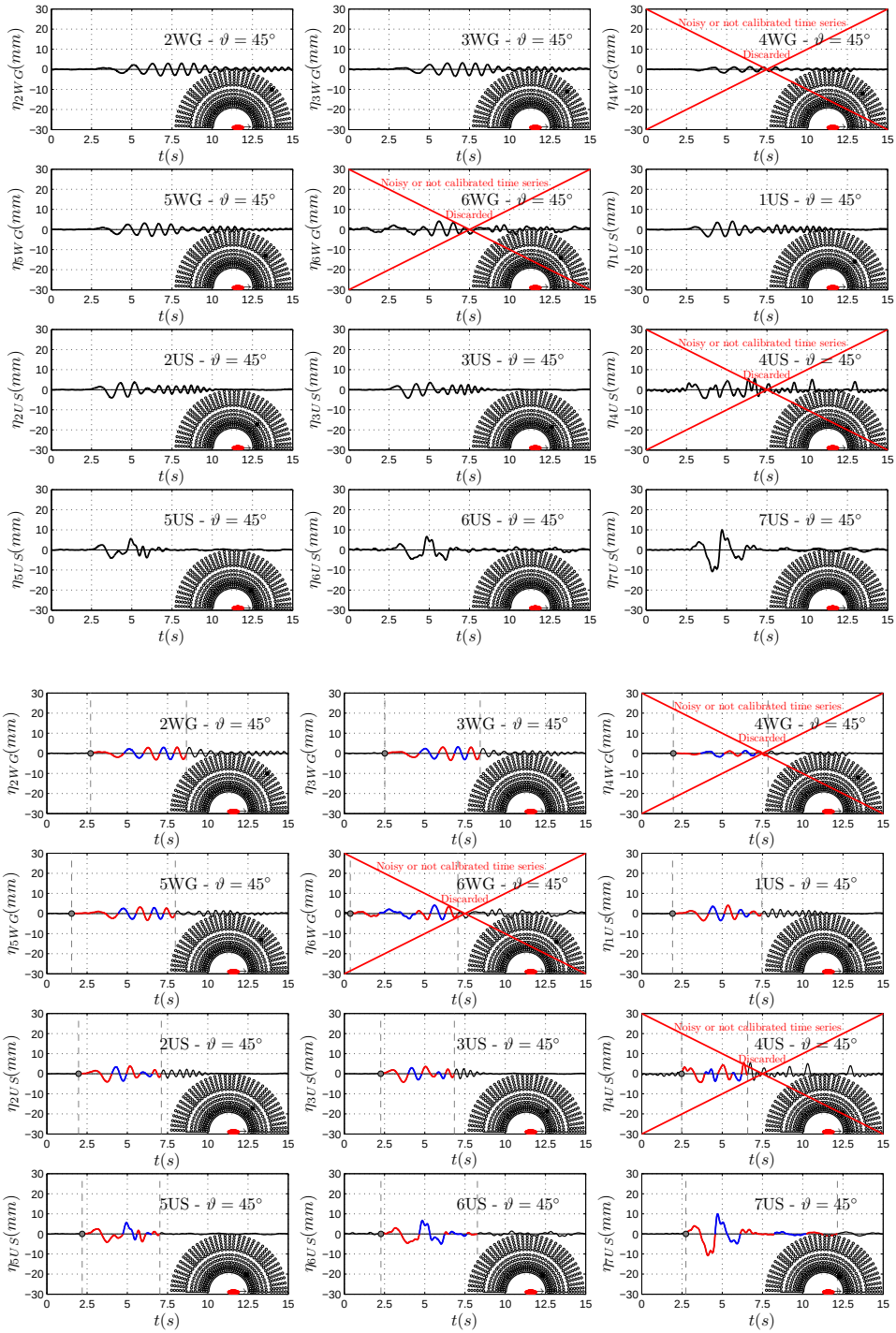

Figure 4.8: Free surface elevation time series collected by the moving arm at $\vartheta = 45°$ (upper panels), and zero-crossing analysis (lower panels). Note: the symbols have the same notation of that in Figure 4.4.

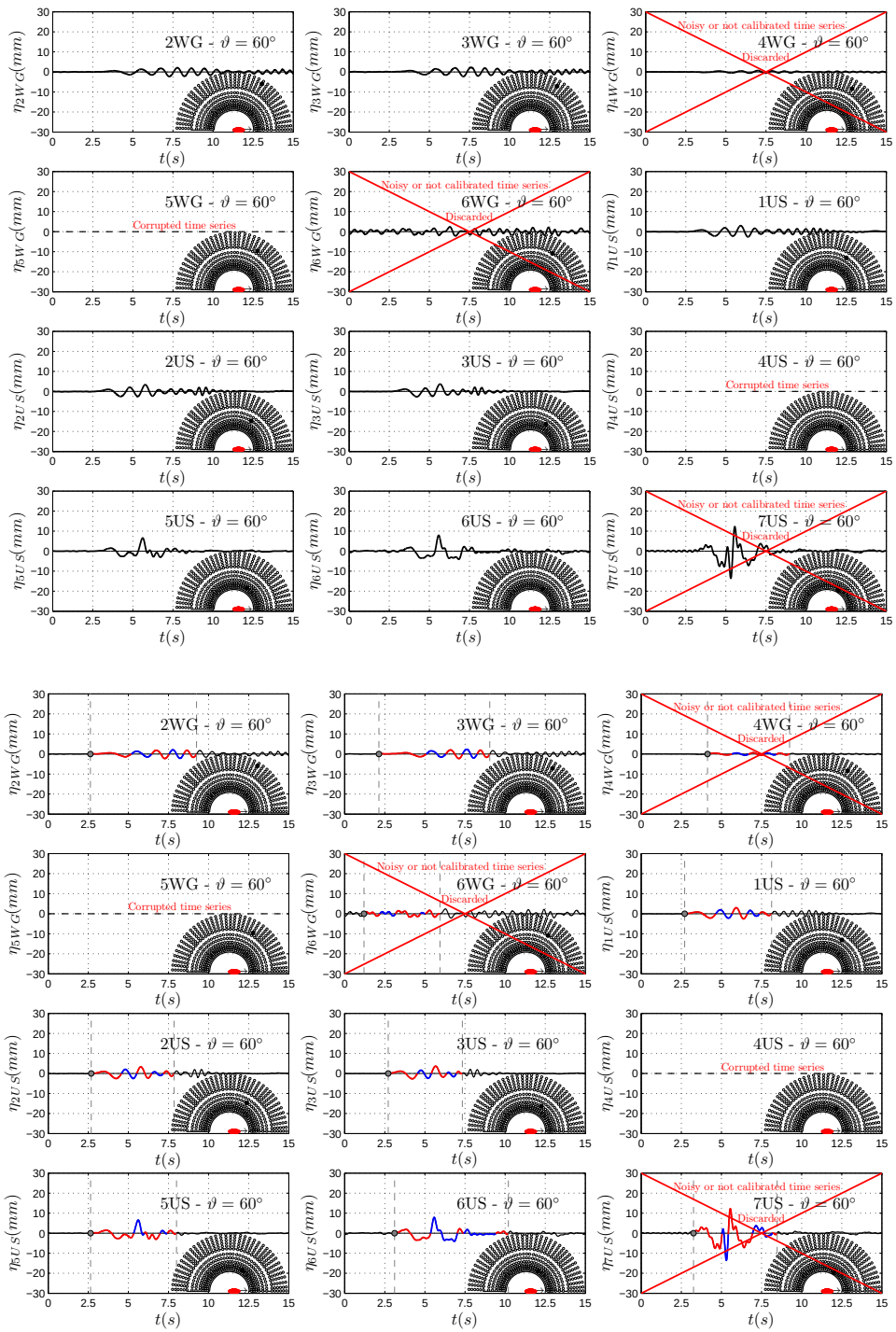

Figure 4.9: Free surface elevation time series collected by the moving arm at $\vartheta = 60°$ (upper panels), and zero-crossing analysis (lower panels). Note: the symbols have the same notation of that in Figure 4.4.

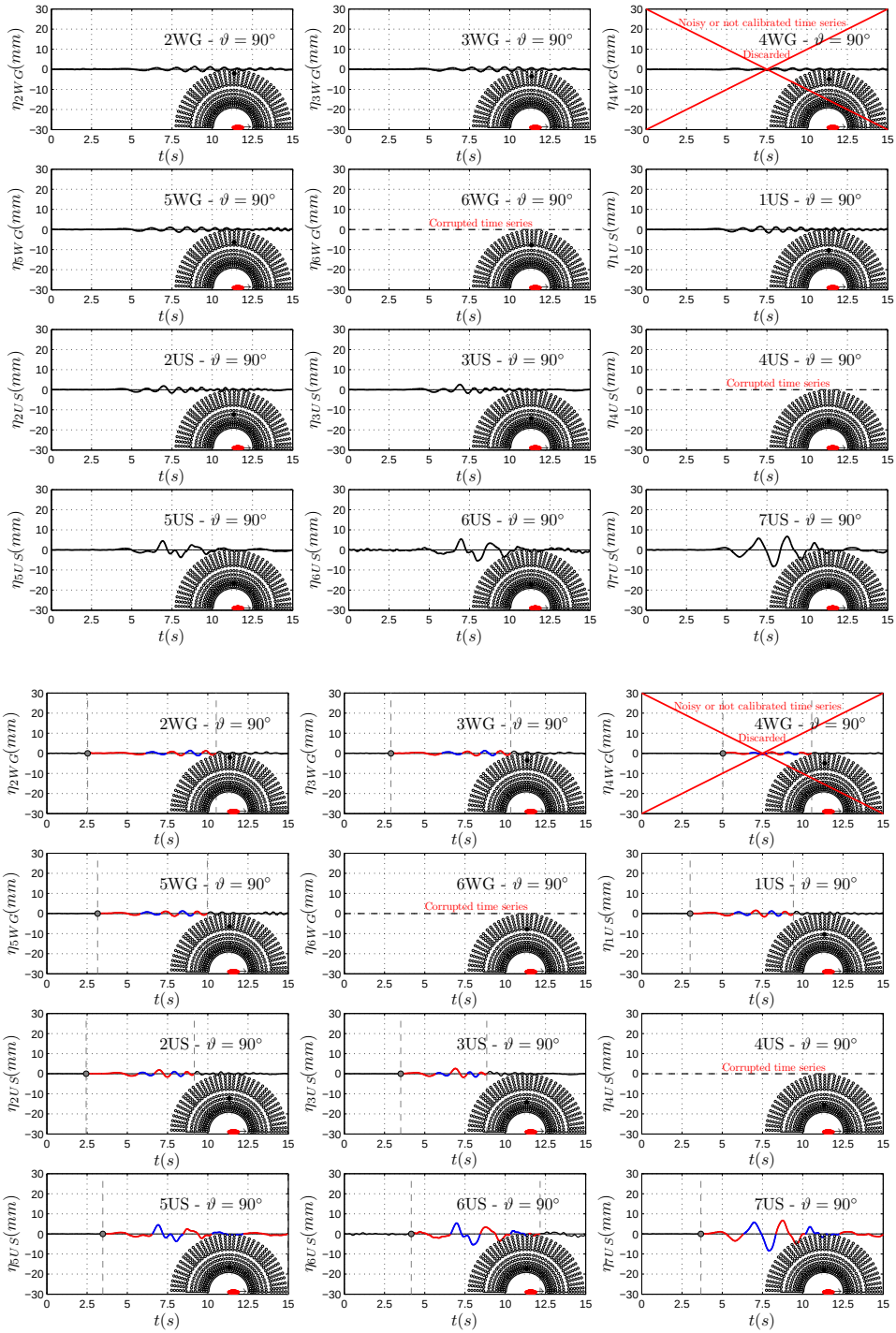

Figure 4.10: Free surface elevation time series collected by the moving arm at $\vartheta = 90°$ (upper panels), and zero-crossing analysis (lower panels). Note: the symbols have the same notation of that in Figure 4.4.

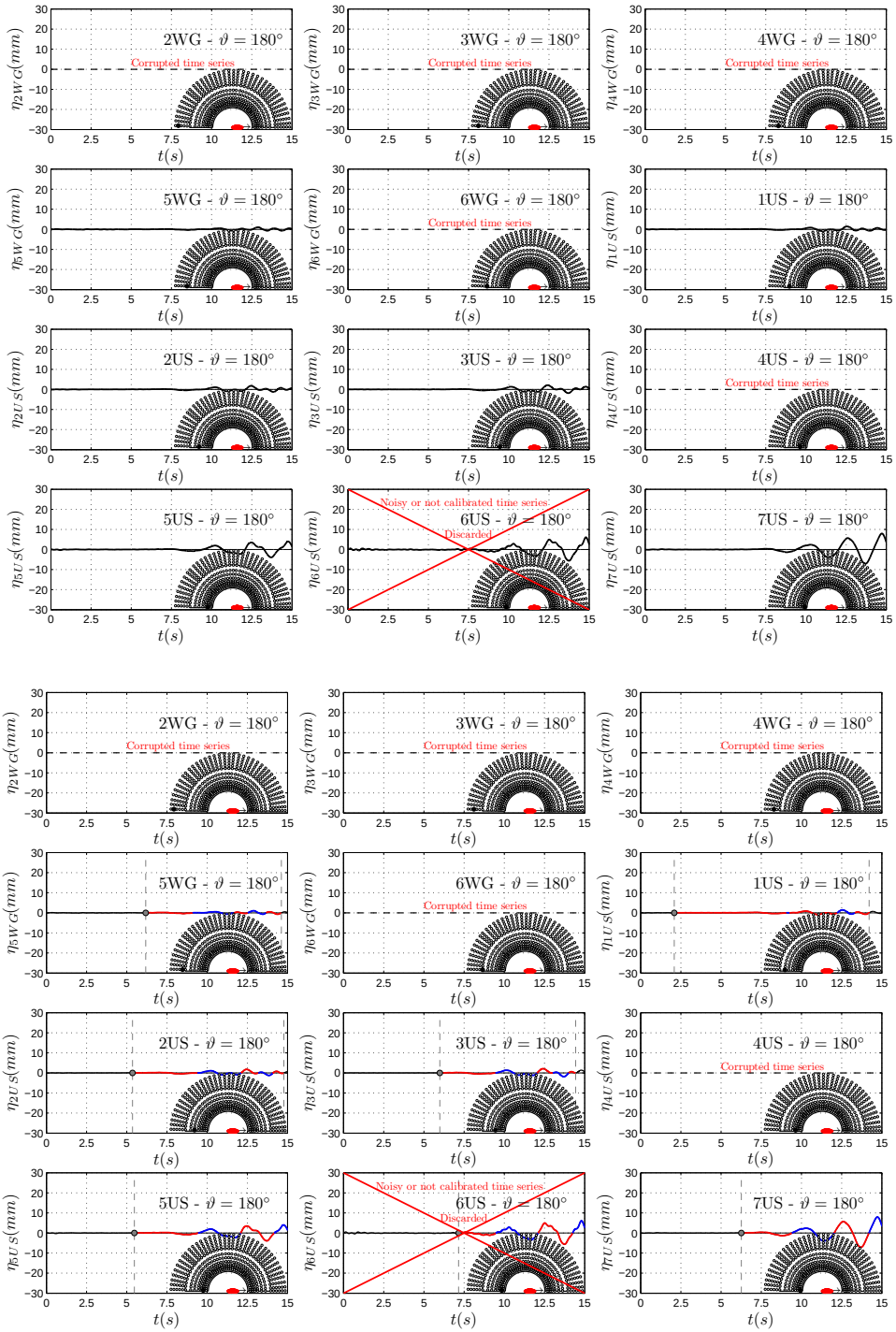

Figure 4.11: Free surface elevation time series collected by the moving arm at $\vartheta = 180°$ (upper panels), and zero-crossing analysis (lower panels). Note: the symbols have the same notation of that in Figure 4.4.

The Figures 4.5, 4.6, 4.7, 4.8, 4.9, 4.10 and 4.11 show the free surface elevation time series collected by means of the moving arm (upper panel), and the ZC of the same time series (lower panel), at several angular positions ($\vartheta = 0°$, $15°$, $30°$, $45°$, $60°$, $90°$ and $180°$ respectively). Furthermore, the position at which each time series has been collected is shown in the sketch, placed in the lower right corner of each sub-panel; the solid black markers identify the position of the generic wave gauge at the ith-release of the landslide. It is remarkable to highlight that moving away from the generation area (i.e., both r and ϑ increase) wave amplitudes become smaller and smaller. Frequency dispersion seems to play a role during the wave propagation; this aspect will be quantitatively addressed in the following. The algorithm seems to be still effective in detecting the wave properties. Furthermore in this post-processing phase it was possible to discard totally or partially the corrupted time series. Several time series were considered to be too much noisy for using these in zero-crossing results; thus they have been discarded. Otherwise some of these were considered to be noisy enough for not being used in zero-crossing results, but not too much noisy for being used in catching the waves propagation properties (as showed in the followings chapters). In the figures mentioned above the totally discarded time series are identified by the red cross, the so-called partially discarded ones are identified by the green dashed cross, while the missing ones (i.e. so-called corrupting time series in the plots) are identified by black dashed lines. Figure 4.12 shows the available sensors, i.e. the free surface elevation

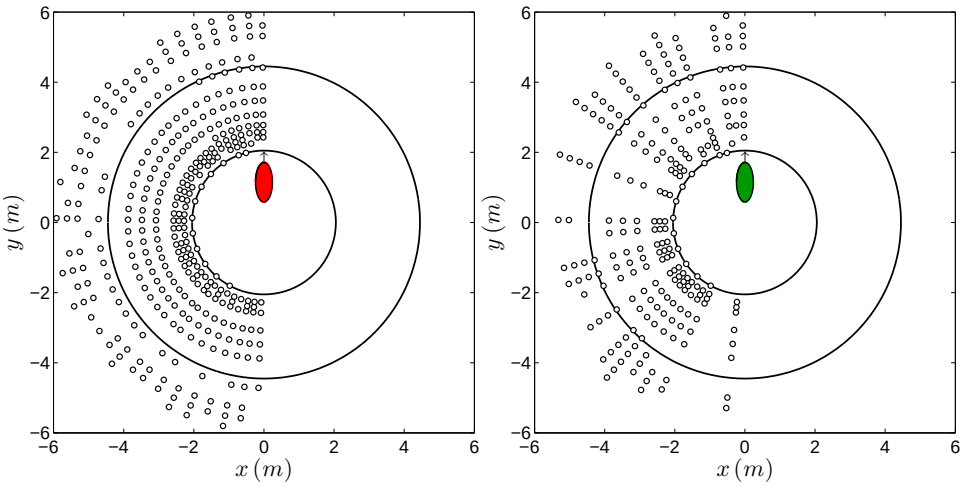

Figure 4.12: Sketch of the available sensors for both LS1 (left panel) and LS2 (right panel).

time series that have been considered not to be discarded, for both LS1 (left panel) and LS2 (right panel). A great number of instruments are available for LS1; conversely, as far as LS2 is considered a great number of instruments have been discarded.

4.3.2 Repeatibility

As described in chapter 3, some of the deployed sensors were kept in a fixed position in order to verify the experiments repeatibility. The fixed gauges were placed directly embedded on the conical island flank (RGs) and close to the generation area (WGs). To check the experiments repeatibility the tsunamis time series collected by the RGs have been used.
In Figures 4.13 and 4.14 the superpositions of all the run-up time series, measured for each landslide release, are plotted. Each panel of the figures refers to the measurements collected by a different RG. Figure 4.13 refers to the LS1 experiments, while Figure 4.14 refers to the LS2 ones. From a qualitative point of view it is possible to state that the experiments have, globally, a good repeatability (both for LS1 and LS2). Comparing the signals represented in Figures 4.13 and 4.14 it is prominent that the waves generated by LS1 are more repeatable than the ones generated by LS2. Despite this, some features of both tsunamis shows a poor repeatability (e.g., the second wave), as quantitatively showed in the following.
Figure 4.15 shows the results of standard zero-crossing analysis on the run-up time series collected by means of RGs. The upper panel shows the maximum induced tsunami run-up (positive values) and minimum draw-down (negative values) all around the island as a function of the dimensionless distance s' from generation area, defined as follows

$$s' = \frac{r_0 \vartheta}{b}, \tag{4.11}$$

where $r_0 = 2.05$ m is the radial distance that identifies the undisturbed shoreline, ϑ is the angular position around the island and $b = 0.40$ m is the landslide width. Positive values of s' refer to experimental results observed for LS1, negative ones to LS2 data. The four lower panels of Figure 4.15 show ZC results for the first four waves of the generated wave packet. The markers refer to the first (circles), the second (squares), the third (diamonds) and the fourth (triangles) wave respectively. The markers used in the upper panel for maximum run-up and minimum draw-down identify which wave of the packet induces it.
The experiments repeatibility, is addressed in the Figure 4.16. Each panel shows the statistical parameters of run-up and draw-down of the first four

waves, as a function of the dimensionless distance s'. The individual experimental data are represented as black points, their mean values are identified by blue segments and the confidence intervals (i.e., 95% confidence level) are identified by red segments. Mean values and confidence intervals, evaluated at each run-up gauge for both LS1 and LS2, are listed in Tables 4.2, 4.3, 4.4 and 4.5.

The quantitative analysis of the experimental repeatability confirms as it has been previously mentioned qualitatively: the repeatibility of the experiments is satisfactory. Both tsunamis generated by LS1 and LS2 models show confidence intervals that are close to mean values, especially for the first wave. However, it is clearly observable that when the wave run-up, or wave draw-down, reaches its maximum, the repeatibility deteriorates. This aspect was already highlighted by *Di Risio et al.* [2009b]. Therefore, it is confirmed that small differences in the landslide energetic features (i.e., drop height) can lead to some differences in terms of maximum run-up and minimum draw-down, i.e. on the envelope amplitude. The differences in envelope amplitude increase with increasing volume. It has to be stressed that this aspect is intimately related to the dispersive features of the generated waves that propagates along the coastline. Furthermore it can be observed that:

- the confidence intervals of wave run-up are wider than the confidence interval of wave draw-down;
- the confidence intervals are wider for the larger landslide model (i.e., LS2).

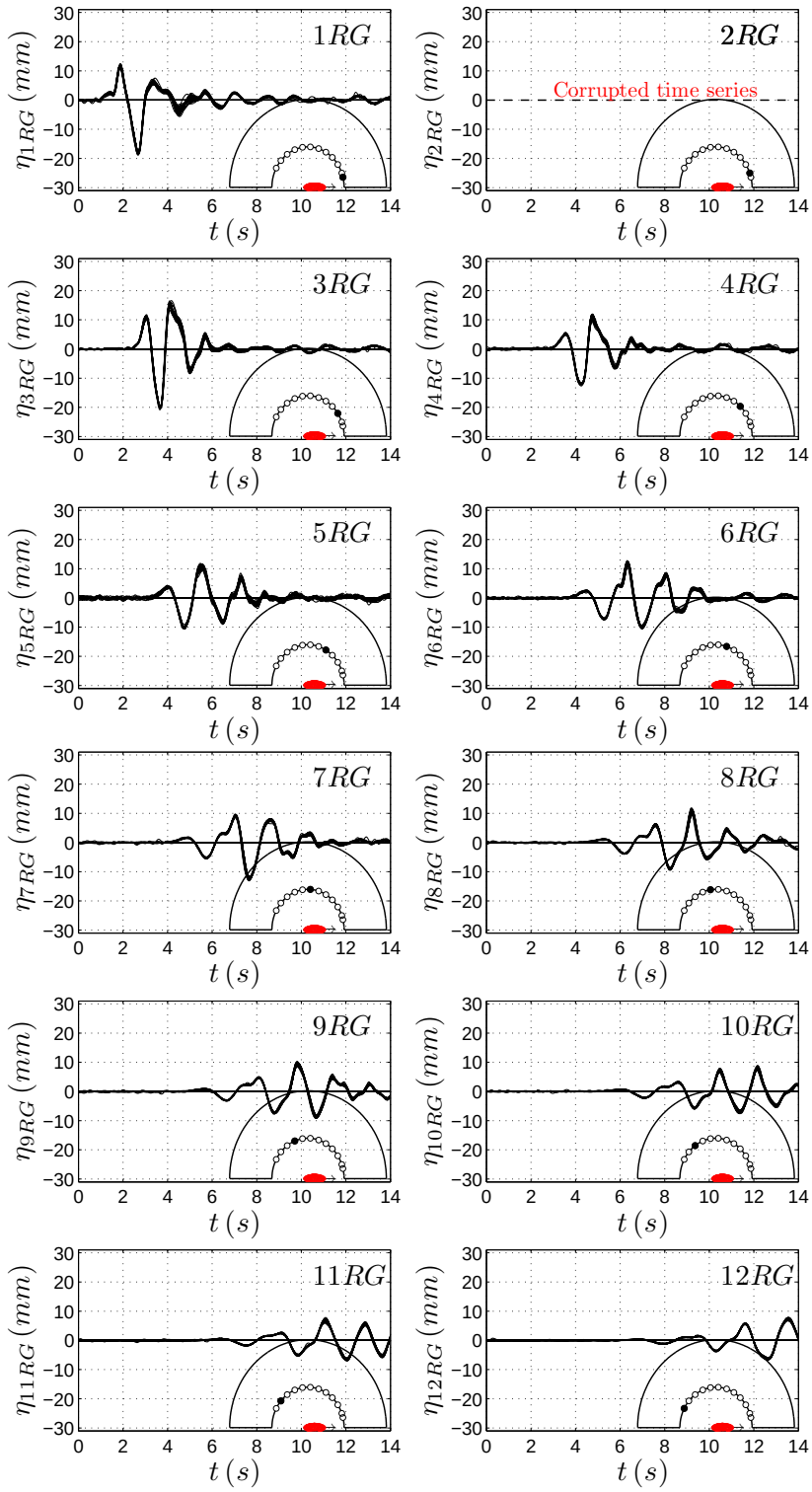

Figure 4.13: Superposition of all the run-up time series (LS1).

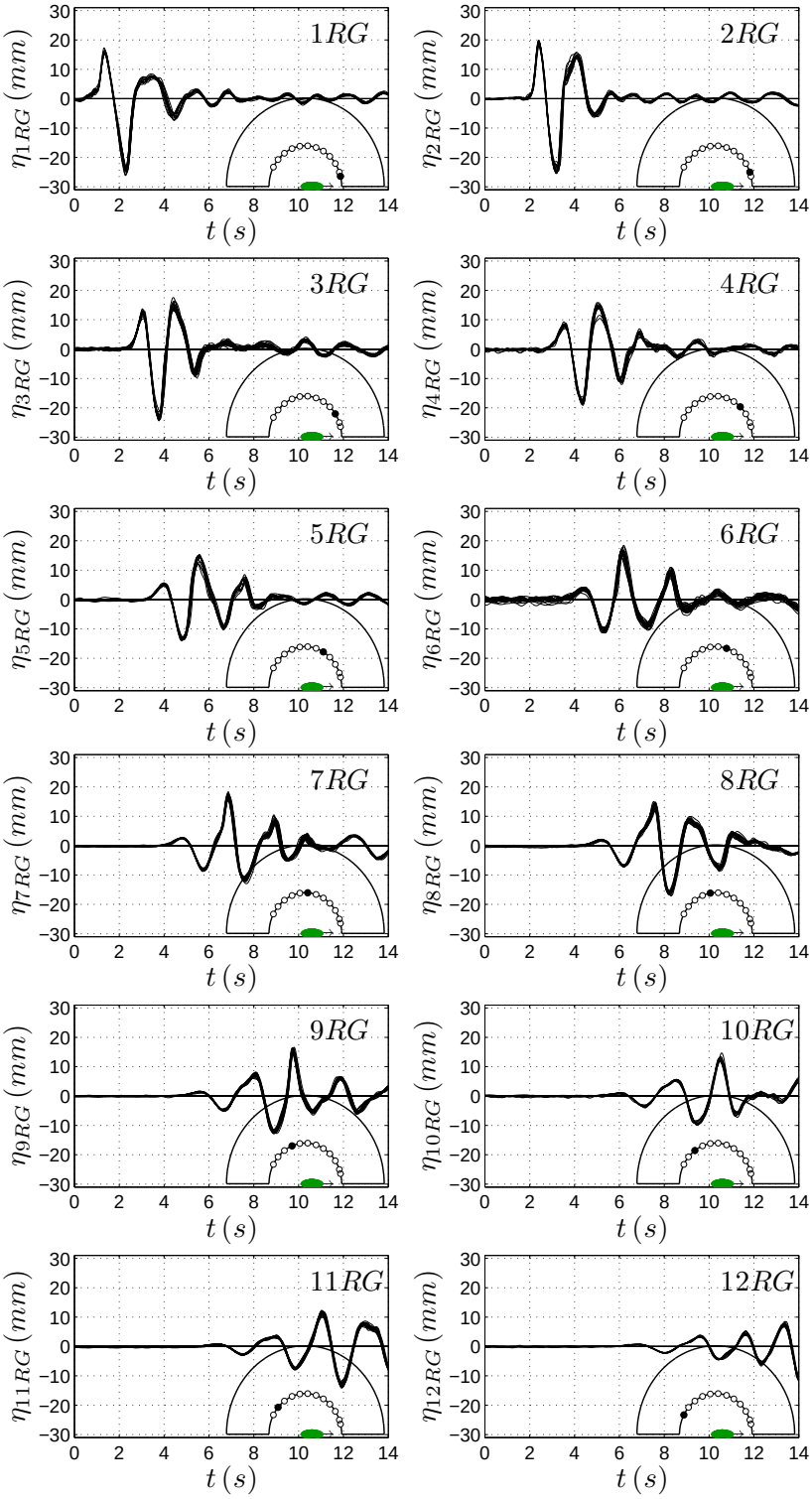

Figure 4.14: Superposition of all the run-up time series (LS2).

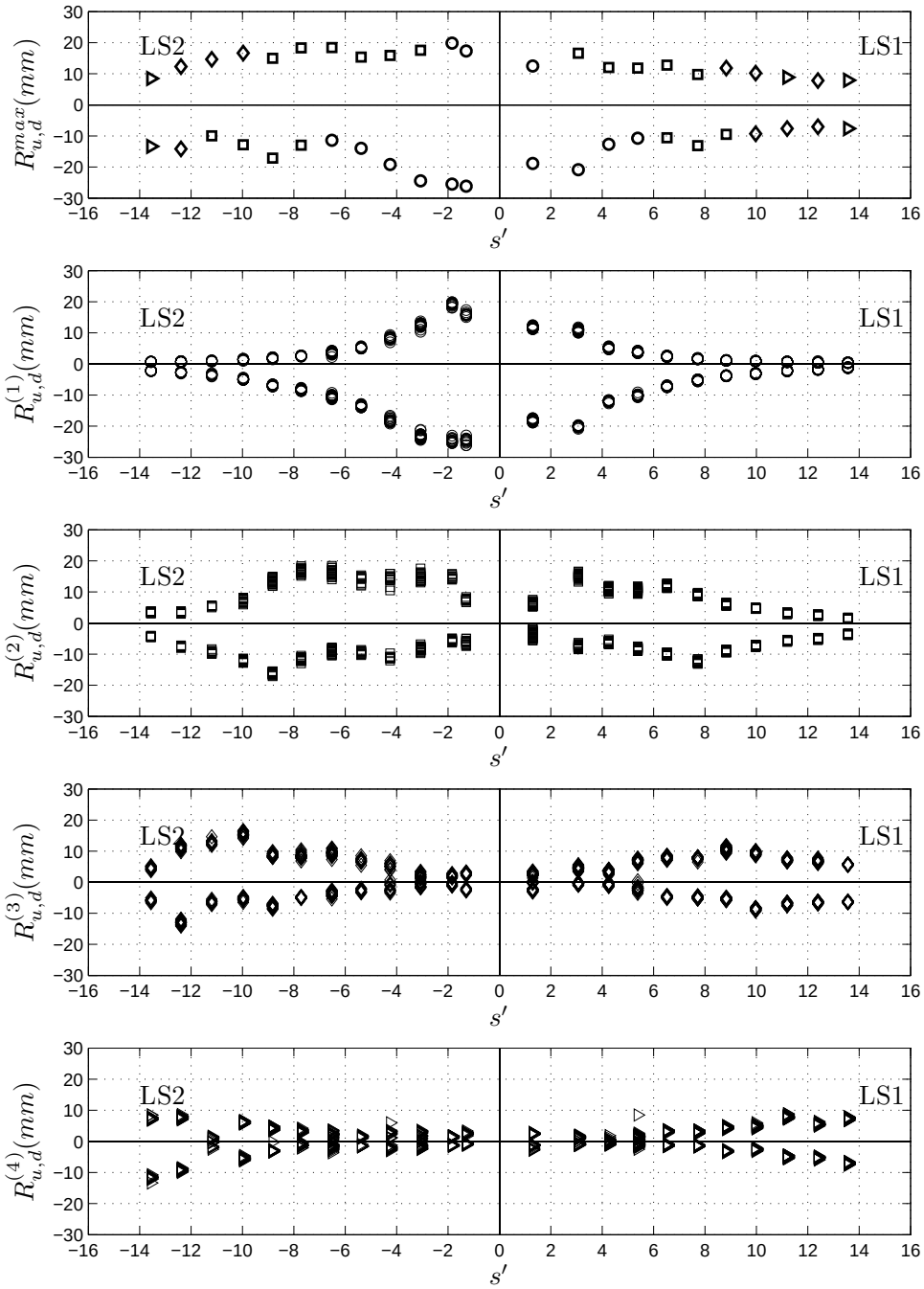

Figure 4.15: Upper panel: maximum induced tsunami run-up and minimum draw-down around the island as a function of s'. Lower panels: run-up and draw-down of the first four waves respectively. Note: positive values of s' refer to LS1, while negative ones refer to LS2.

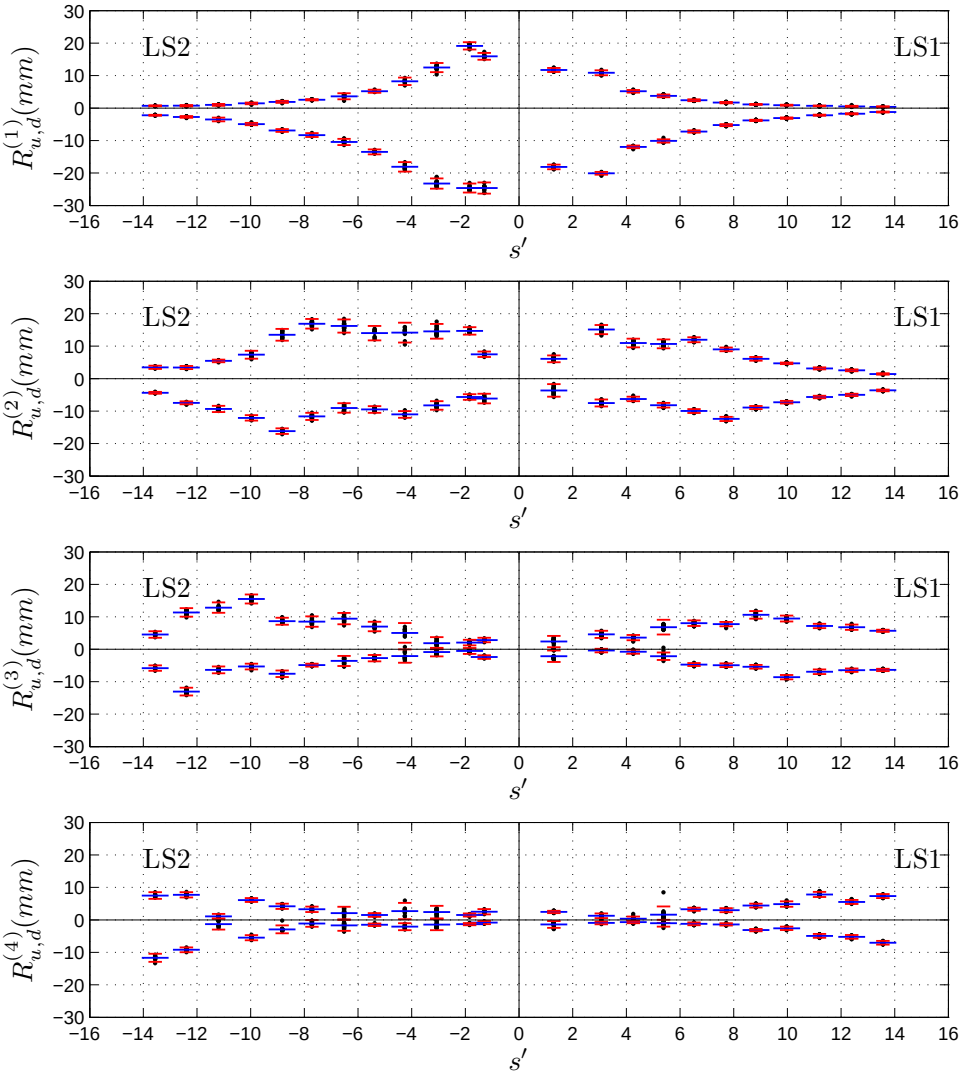

Figure 4.16: Run-up and draw-down of the first four waves respectively: statistical estimate of the experimental repeatibility. Black points identify run-up and draw-down. Blue lines refer to the mean values calculated over the whole set of available landslide releases, for each run-up gauge. Red lines represent the confidence intervals. Note: positive values of s' refer to LS1, while negative ones refer to LS2..

LS1								
GAUGES	$\overline{R}_u^{(1)}$ (mm)	95% CI (mm)	$\overline{R}_u^{(2)}$ (mm)	95% CI (mm)	$\overline{R}_u^{(3)}$ (mm)	95% CI (mm)	$\overline{R}_u^{(4)}$ (mm)	95% CI (mm)
1RG	11.73	± 0.62	6.10	± 1.04	2.38	± 1.74	2.44	± 0.36
2RG	-	± -	-	± -	-	± -	-	± -
3RG	10.88	± 0.76	15.09	± 1.41	4.58	± 1.10	1.26	± 0.70
4RG	5.16	± 0.41	10.96	± 1.32	3.58	± 0.82	0.34	± 0.66
5RG	3.74	± 0.42	10.69	± 1.35	6.81	± 2.29	1.59	± 2.53
6RG	2.41	± 0.28	11.95	± 0.74	8.02	± 0.85	3.27	± 0.49
7RG	1.67	± 0.21	8.98	± 0.57	7.75	± 0.66	3.00	± 0.61
8RG	1.13	± 0.14	6.09	± 0.56	10.59	± 1.16	4.41	± 0.59
9RG	0.89	± 0.13	4.69	± 0.25	9.44	± 0.90	4.87	± 0.83
10RG	0.67	± 0.13	3.13	± 0.31	7.16	± 0.68	7.82	± 0.78
11RG	0.49	± 0.19	2.55	± 0.29	6.79	± 0.82	5.51	± 0.63
12RG	0.38	± 0.14	1.43	± 0.21	5.68	± 0.32	7.35	± 0.62

Table 4.2: Mean values and confidence intervals of run-up (LS1).

LS1								
GAUGES	$\overline{R}_d^{(1)}$ (mm)	95% CI (mm)	$\overline{R}_d^{(2)}$ (mm)	95% CI (mm)	$\overline{R}_d^{(3)}$ (mm)	95% CI (mm)	$\overline{R}_d^{(4)}$ (mm)	95% CI (mm)
1RG	-18.14	± 0.72	-3.60	± 1.94	-2.10	± 1.76	-1.40	± 1.04
2RG	-	± -	-	± -	-	± -	-	± -
3RG	-20.08	± 0.44	-7.50	± 1.07	-0.40	± 0.54	-0.90	± 0.42
4RG	-11.95	± 0.39	-6.20	± 0.70	-0.70	± 0.61	-0.60	± 0.37
5RG	-10.11	± 0.50	-8.10	± 0.72	-2.10	± 1.14	-1.00	± 1.04
6RG	-7.20	± 0.34	-9.90	± 0.59	-4.70	± 0.45	-1.20	± 0.44
7RG	-5.20	± 0.31	-12.40	± 0.64	-4.90	± 0.57	-1.30	± 0.35
8RG	-3.70	± 0.21	-8.90	± 0.49	-5.30	± 0.55	-3.10	± 0.35
9RG	-3.10	± 0.20	-7.20	± 0.40	-8.50	± 0.66	-2.50	± 0.52
10RG	-2.20	± 0.18	-5.60	± 0.37	-6.90	± 0.70	-4.90	± 0.62
11RG	-1.70	± 0.16	-5.00	± 0.37	-6.40	± 0.52	-5.20	± 0.57
12RG	-1.20	± 0.15	-3.60	± 0.25	-6.30	± 0.35	-7.00	± 0.56

Table 4.3: Mean values and confidence intervals of draw-down (LS1).

LS2								
GAUGES	$\overline{R}_u^{(1)}$ (mm)	95% CI (mm)	$\overline{R}_u^{(2)}$ (mm)	95% CI (mm)	$\overline{R}_u^{(3)}$ (mm)	95% CI (mm)	$\overline{R}_u^{(4)}$ (mm)	95% CI (mm)
1RG	15.94	± 1.05	7.48	± 0.84	2.83	± 0.68	2.51	± 0.82
2RG	19.14	± 1.12	14.69	± 1.12	2.05	± 0.88	1.48	± 0.47
3RG	12.48	± 1.40	14.55	± 2.26	1.87	± 1.87	2.38	± 1.92
4RG	8.24	± 1.13	14.14	± 3.05	5.03	± 3.02	2.71	± 2.49
5RG	5.19	± 0.48	13.99	± 2.21	6.98	± 1.46	1.49	± 0.56
6RG	3.62	± 0.93	16.20	± 2.03	9.42	± 1.74	2.08	± 1.92
7RG	2.56	± 0.20	16.87	± 1.48	8.52	± 1.59	3.25	± 0.84
8RG	1.90	± 0.30	13.500	± 1.81	8.63	± 1.07	4.17	± 0.81
9RG	1.44	± 0.25	7.36	± 1.21	15.50	± 1.38	6.11	± 0.60
10RG	0.96	± 0.28	5.46	± 0.40	12.82	± 1.61	1.09	± 0.72
11RG	0.72	± 0.22	3.43	± 0.47	11.33	± 1.31	7.72	± 0.82
12RG	0.68	± 0.13	3.47	± 0.50	4.55	± 0.99	7.49	± 1.01

Table 4.4: Mean values and confidence intervals of run-up (LS2).

LS2								
GAUGES	$\overline{R}_d^{(1)}$ (mm)	95% CI (mm)	$\overline{R}_d^{(2)}$ (mm)	95% CI (mm)	$\overline{R}_d^{(3)}$ (mm)	95% CI (mm)	$\overline{R}_d^{(4)}$ (mm)	95% CI (mm)
1RG	-24.63	± 1.71	-6.10	± 1.48	-2.40	± 0.55	-0.80	± 0.46
2RG	-24.62	± 1.36	-5.60	± 0.85	-0.50	± 0.90	-1.20	± 0.33
3RG	-23.23	± 1.57	-8.20	± 1.30	-0.80	± 1.32	-1.40	± 1.72
4RG	-18.08	± 1.45	-11.03	± 1.00	-2.10	± 2.06	-2.10	± 1.06
5RG	-13.50	± 0.76	-9.50	± 1.03	-2.70	± 0.98	-1.50	± 0.38
6RG	-10.43	± 0.95	-9.00	± 1.46	-3.60	± 1.54	-1.60	± 1.67
7RG	-8.30	± 0.58	-11.62	± 1.08	-4.80	± 0.43	-1.10	± 1.03
8RG	-6.90	± 0.41	-16.17	± 0.84	-7.50	± 1.02	-2.90	± 1.21
9RG	-4.90	± 0.34	-12.09	± 0.84	-5.30	± 0.87	-5.40	± 0.80
10RG	-3.40	± 0.57	-9.30	± 0.95	-6.30	± 1.04	-1.20	± 1.71
11RG	-2.70	± 0.27	-7.40	± 0.46	-13.05	± 1.20	-9.20	± 0.73
12RG	-2.20	± 0.14	-4.30	± 0.27	-5.80	± 0.84	-11.68	± 1.25

Table 4.5: Mean values and confidence intervals of draw-down (LS2).

4.3.3 Wave features

Once the experimental repeatibility has been quantitatively estimated, by analyzing the data of the fixed gauges (i.e., RGs), it is possible to use the measurements collected by the sensors placed on the moving arm. These allow to analyze the free surface elevation time series in the whole experimental domain, given the high spatial resolution of the measurements themselves. Furthermore, the high density of the measurements in proximity of the shoreline allows to better understand the trapping mechanisms of tsunamis that,

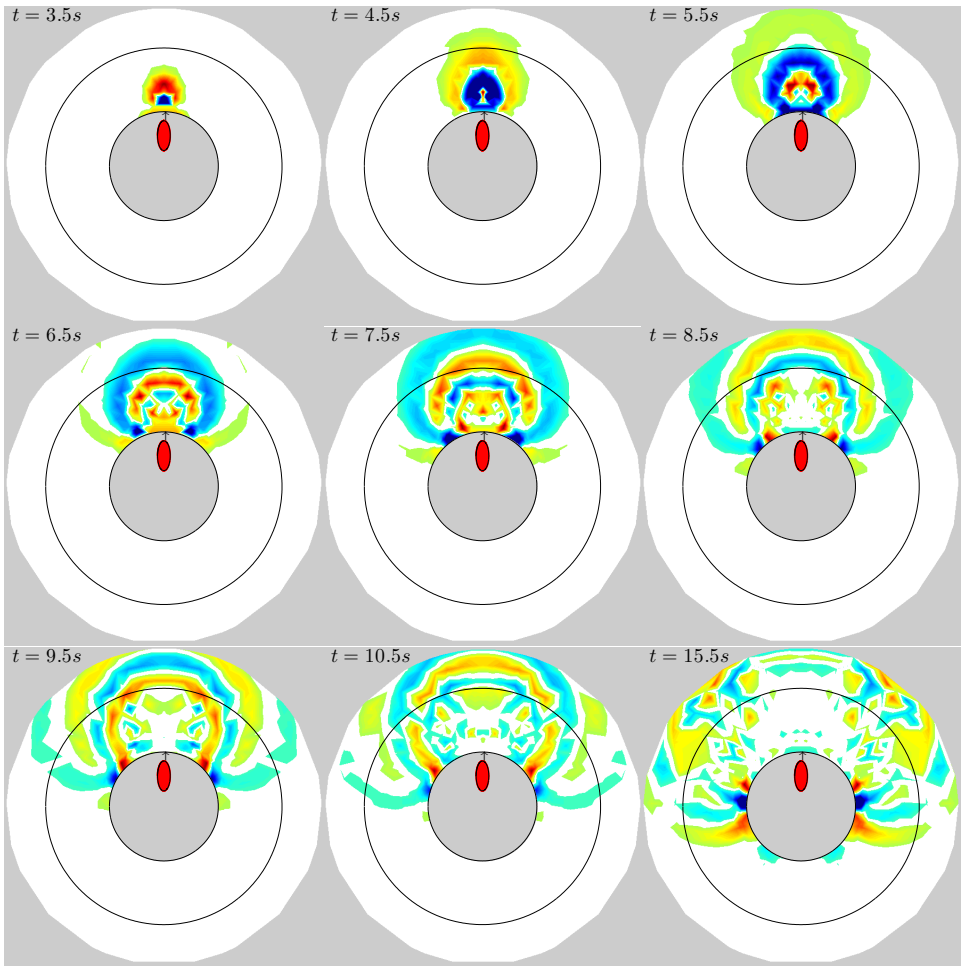

Figure 4.17: Free surface elevation around the island at several time steps from the landslide release. Note: in order to magnify the features of the wave propagation, different color scales have been used for each panel.

as shown, propagate around the coast of the island. In the Figure 4.17 the free surface elevation contour plots, evaluated at several time steps since the landslide has been released, are represented. Each contour plot has been obtained by linearly interpolating the free surface elevation, collected around the island, at a given time step. It is shown that the spatial resolution of the measurements is high enough to describe in depth the tsunamis propagation around the island (both alongshore and in deep water area).
Figure 4.17 clearly shows that in the first phases, after the landslide impact, the waves mainly propagate seaward (i.e., radiating waves), while, as the time increases, it seems clear that the tsunami propagates alongshore and inundate the island coast. This suggests that tsunamis trapping mechanisms, due to bathymetry, play a fundamental role in the propagation/inundation phenomena. A detailed study of the physics of the propagation around the island will be addressed in the next chapter. Finally, the high spatial resolution measurements provide an effective tool for gaining insight on the wave propagation phenomena.

Run-up: volume influence

During the experiments two landslide models have been used, thus an analysis aiming at evaluating the influence of landslide volume on the generated waves has been carried out and presented in Figure 4.18. The upper panel shows the maximum induced tsunamis run-up (red markers refers to the run-up induced by LS1, while the green ones refers to the run-up induced by LS2) and minimum draw-down all around the island as a function of the dimensionless distance s' from generation area ($s' = r_0\theta/b$). The four lower panels show the run-up and draw-down of the first four waves obtained by ZC. The influence of landslide volume is almost clear: the larger the volume, the larger the induced run-up and draw-down (in absolute value). However, it has to be stressed that although the thickness of the LS2 is twice than the LS1 the induced tsunamis run-up is not two times larger. Consistently with *Di Risio et al.* [2009b] and *Lynett and Liu* [2005], the maximum run-up and the minimum draw-down (upper panel in Figure 4.18) first increase close to the generation area and then they decrease as the distance from the generation area grows. An extended region is observed to be characterized by almost constant maximum wave run-up (i.e., 4<s'<10) and minimum wave draw-down (i.e., 4<s'<10). *Lynett and Liu* [2005] numerically demonstrated that the wave propagation in this area (i.e., far field) is dominated by the so-called edge-waves [*Ursell*, 1952], as shown in the following chapter.
Furthermore, by analyzing the individual waves of the run-up packet other

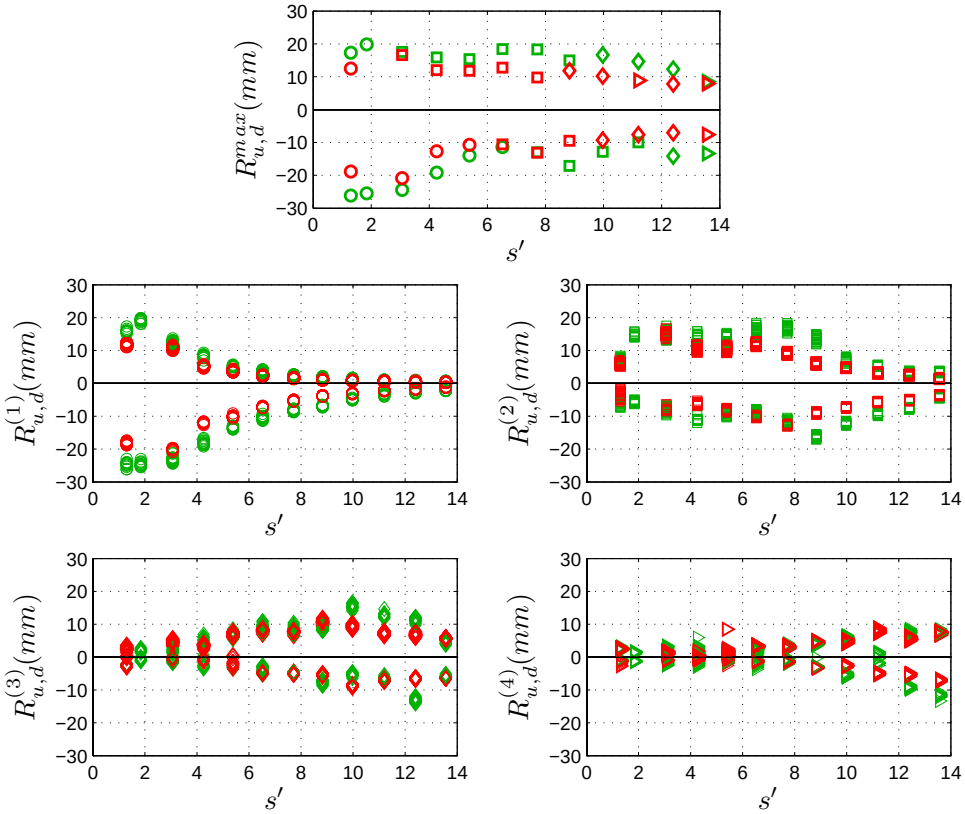

Figure 4.18: Comparison between the run-up and draw-down generated by the two landslide models. Upper panel: maximum induced tsunami run-up and minimum draw-down around the island as a function of s'. Lower panels: run-up and draw-down of the first four waves. Note: red markers refer to LS1, while green ones refer to LS2).

features can be observed. As far as the first wave is concerned (see left upper panel of the Figure 4.18), a significant difference between the run-up (and draw-down) induced by the two landslides can be seen only near the generation area (i.e., 0<s'<2); as the distance from the generation area grows the run-up amplitudes, generated by the two landslides, tend to become similar (in absolute value). As far as the second wave is concerned (see right upper panel of the Figure 4.18), it is possible to observe that the main differences, between the ZC results of LS1 and LS2, occur quite far from the generation area (i.e., 6<s'<10), while in the remaining areas the ZC results are similar. Analogous features can be seen if the third wave is considered.

Wave field around the island

As far as the free surface elevation time series collected around the island are concerned a more complete picture of the overall wave field can be depicted. Figures 4.19, 4.20, 4.21 show maximum wave crest and trough amplitudes of the first (circle markers), second (square markers) and third (diamond markers) wave respectively, measured at different radial distances (r) from the undisturbed shoreline, as a function of the angular position (ϑ). Solid markers indicate the data measured at the shoreline (i.e., run-up and draw-down). Red markers refer to the experiments carried out by using LS1, while green ones refer to the ones carried out by using LS2. The angular position ϑ is used instead of dimensionless variable s' ($= r\vartheta/b$), as for constant ϑ (i.e., cross section) the value of s' is not constant.

As far as the first wave is concerned (see Figure 4.19), it can be observed that the maximum wave crest and trough amplitude is observed in front of the generation area (at $r = 2.57$ m for LS1 and at $r = 2.77$ m for LS2). Furthermore, the maximum crest and trough amplitude occurs at $\vartheta = 0°$. As the angular distance from the generation area increases (i.e., $\vartheta > 15 - 20°$), it can be seen that for fixed angular position the maximum crest and trough

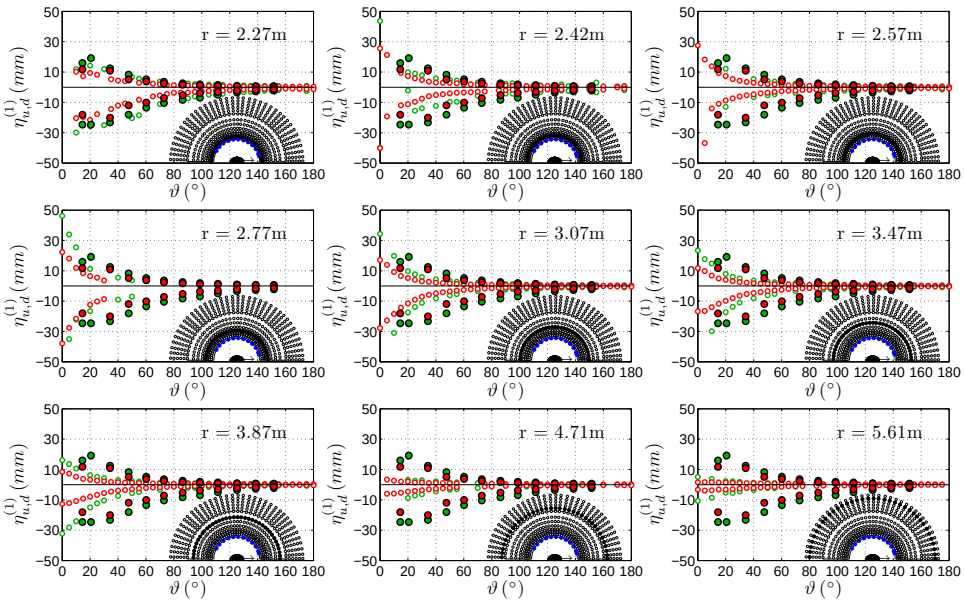

Figure 4.19: Comparison between the maximum wave crest and trough amplitudes (red and green empty markers) of the first wave, measured at several radial distances r as a function of the angle ϑ, and run-up and draw-down (red and green solid markers).

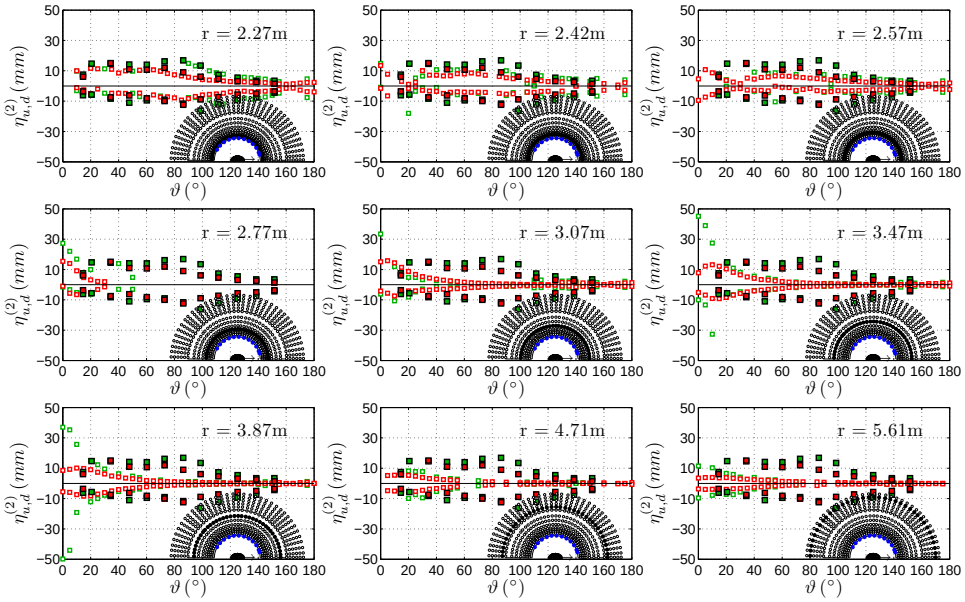

Figure 4.20: Comparison between the maximum wave crest and trough amplitudes (red and green empty markers) of the second wave, measured at several radial distances r as a function of the angle ϑ, and run-up and draw-down (red and green solid markers).

amplitude occurs at the island coast ($r = r_0$). Moreover, as the distance from the coast (i.e., r), or the distance from the generation area (i.e. $r\vartheta$), increases the wave crest and trough amplitudes decrease monotically.

Similarly, by considering the second wave (see Figure 4.20), the maximum wave amplitudes occur in front of the generation area and, as the angular distance from the generation area increases (i.e., $\vartheta > 15 - 20°$), for fixed angular position the maximum wave amplitudes occur at the coast ($r = r_0$). However a more detailed inspection reveals that there is a spatial shift of the amplitudes, i.e. the maximum wave amplitudes at the coast ($r = r_0$) occur at higher values of angular position than those at which occur the ones observed as moving away from the coast (i.e., $r > r_0$). Moreover, the maximum amplitudes are not a monotonic function of angular position (like the first wave crest and trough amplitudes are), since they reach the maximum value far from the generation area.

A similar behavior is found also when the third wave is considered (Figure 4.21). In this case the maximum wave amplitudes, which occur at the shoreline ($r = r_0$), take place far from the generation area. Therefore, these features suggest that the overall wave propagation around the island seems

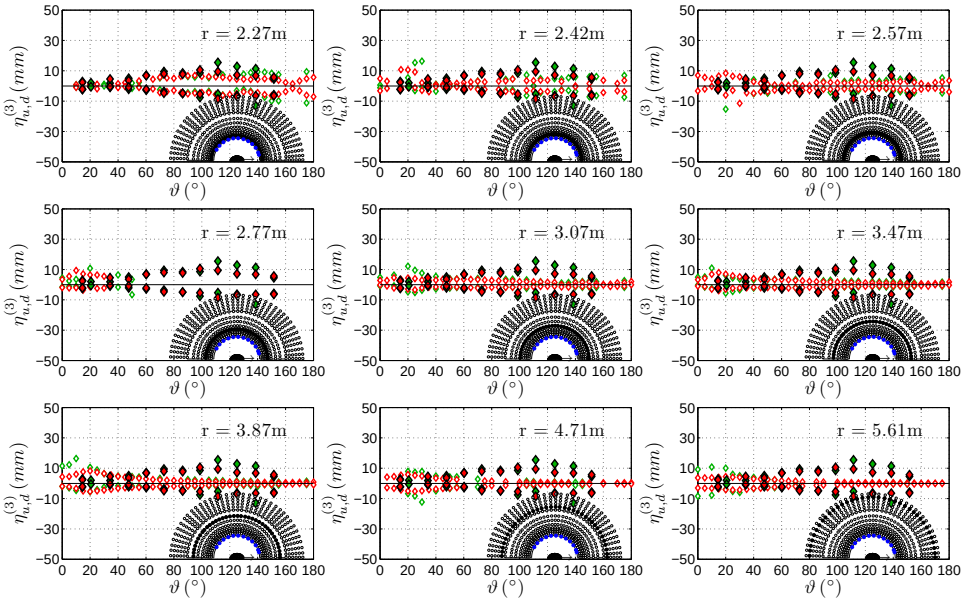

Figure 4.21: Comparison between the maximum wave crest and trough amplitudes (red and green empty markers) of the third wave, measured at several radial distances r as a function of the angle ϑ, and run-up and draw-down (red and green solid markers).

to be governed by frequency dispersion, as pointed out by *Di Risio et al.* [2009b], and wave trapping mechanisms.

Furthermore the Figures 4.19, 4.20, 4.21 can be heuristically used for the experimental identification of the areas on which the wave trapping mechanisms become noticeable. *Lynett and Liu* [2005] argued that, for a straight coast, the "near-field" is commonly identified as the region on which the wave field is dominated by source-specific waves, while the "far-field" is defined as the region along the shoreline on which edge waves become important, i.e., where trapped or almost-trapped wave modes become significant. This split-up is of particular interest along the shoreline (both from a scientific than from a technical point of view), since the comprehension of the propagation/inundation mechanisms is essential in order to design and realize an early warning system. The experimental identification of the areas on which the wave trapping mechanisms are noticeable is showed in the Figure 4.22. The beginning of these areas has been identified as the angular position ϑ at which the maximum run-up and draw-down amplitude is greater than the maximum wave crest and trough amplitude measured in front of the coastline, evaluated at the same angular position. This limit has been iden-

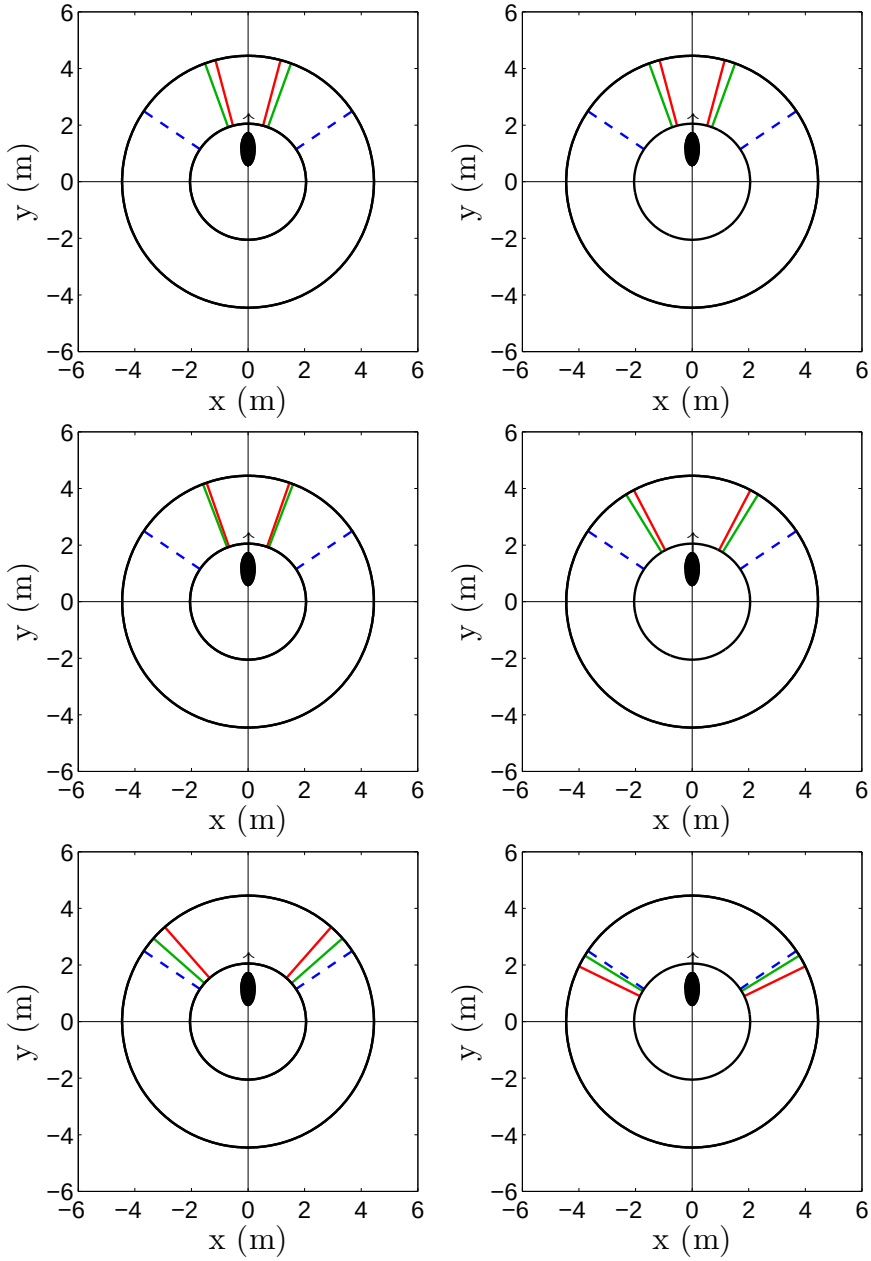

Figure 4.22: Experimental identification of the limit between "near-field" and "far-field" for the first (upper panels), second (middle panels) and third wave (lower panels). Note: left panels refer to the wave crests, while right ones refer to the wave troughs. Blue dashed lines identify the theoretical limit as from *Lynett and Liu* [2005].

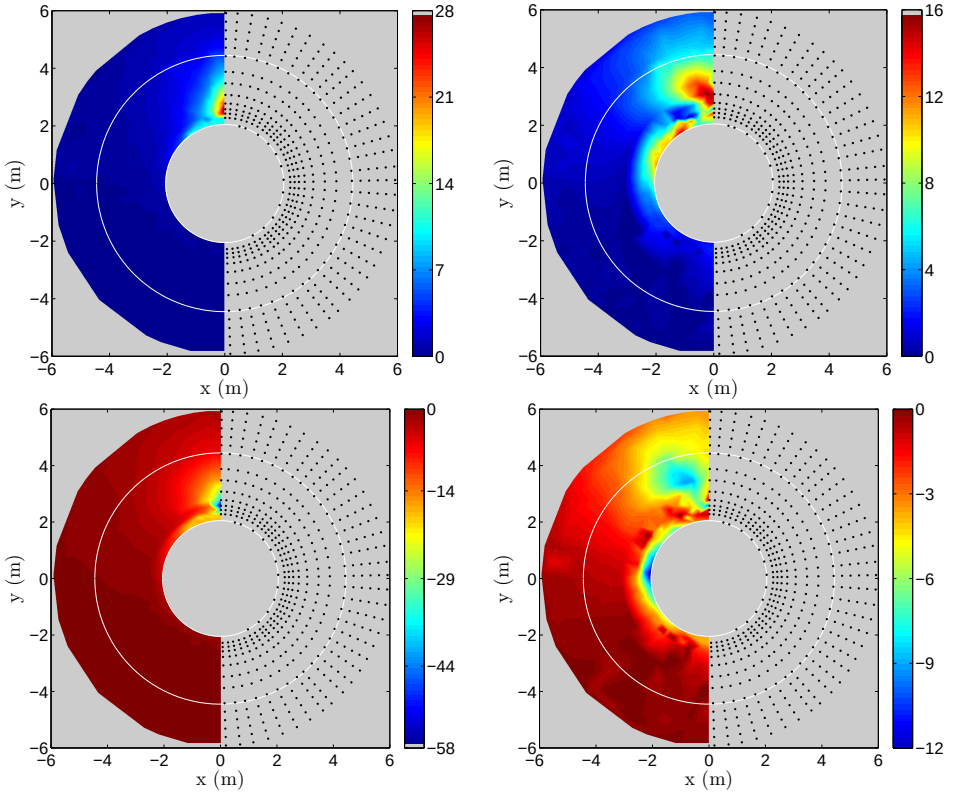

Figure 4.23: Spatial distribution of crest and trough amplitudes around the island. Left panels: first wave. Right panels: second wave. Upper panels: wave crests. Lower panels: wave troughs. Note: colorbars are expressed in mm.

tified for the wave crest (left panels) and trough (right panels) of the first three waves of the packet (upper panels: first wave, middle panels: second wave, lower panels: third wave), and of course for both the landslide models (red lines refer to LS1, while green ones refer to LS2). It has to be noticed that the above mentioned experimental limit, in terms of the dimensionless abscissa s', varies from 1.3 (when the first wave is considered) to 5.7 (when the third wave is considered). These values are in line with those found by *Lynett and Liu* [2005] for a straight coast (represented by the blue dashed lines in the Figure 4.22).

A more detailed description of wave pattern can be addressed by looking at the spatial distribution of crest and trough amplitudes around the island. Figure 4.23 shows the spatial distribution of the wave crest (upper panels) and trough amplitudes (lower panels) of the first (left panels) and second wave (right panels) obtained by linearly interpolating the experimental data

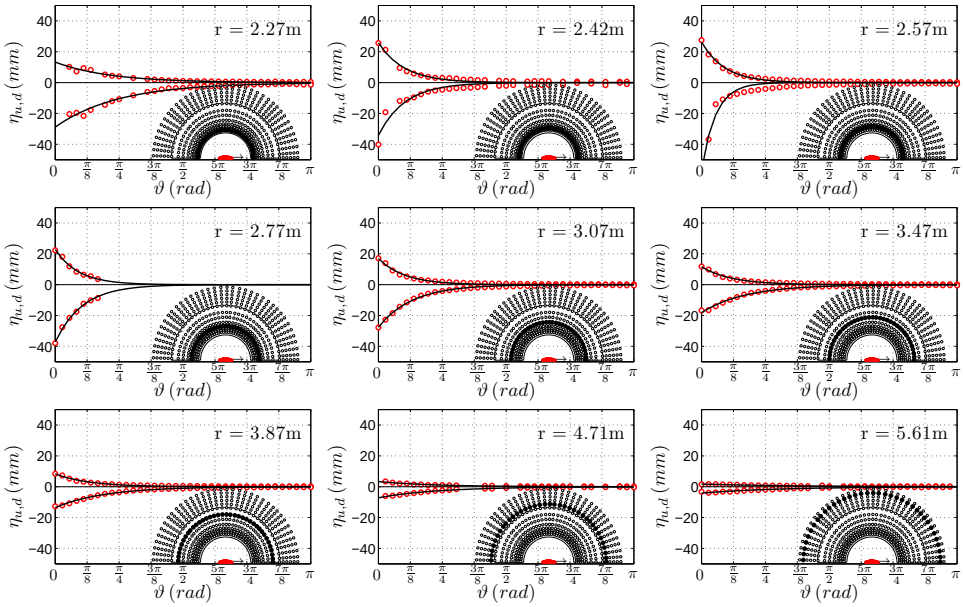

Figure 4.24: Comparison between experimental data of wave crest and trough amplitudes of the first wave, generated by LS1, as a function of the angular distance ϑ and the fitting ones.

obtained by using LS1. As far as the wave crest and trough amplitudes of the first wave are concerned (left panels), the highest amplitudes occur in front of the generation area, as pointed out by the Figure 4.19. Furthermore in Figure 4.23 it is shown that the energy of the first wave (both wave crest and trough) seems to be channelled in a direction that is parallel to the one along which the landslide travels, while as the angular distance ϑ from the generation area grows the wave crest and trough amplitudes rapidly decrease.

To better gain insight on these features, Figure 4.24 shows the wave crest and trough amplitudes of the first wave, generated by LS1, as a function of the angular distance ϑ (note that the experimental data are the same of those showed in Figure 4.19). Given the fast decay of the wave amplitudes for increasing ϑ, an exponential function is supposed to be suitable to describe the evolution of the first wave with the angular distance. This function is defined as follows

$$\eta_{u,d}(r,\vartheta) = \eta_0(r)e^{-B(r)\vartheta}, \tag{4.12}$$

where both η_0 and B are function of the radial distance r. The experimental data (both wave crest and trough amplitudes) have been processed by means

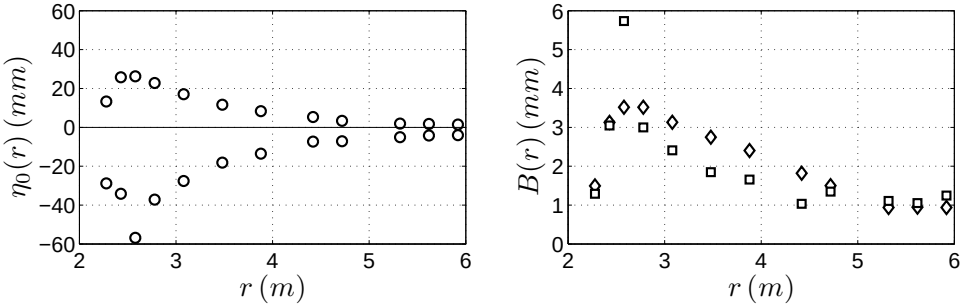

Figure 4.25: Fitting parameters of the equation (4.12) as a function of the radial distance r. Left panel: parameter η_0 estimated for wave crest a trough. Left panel: parameter B estimated for wave crest (diamond markers) and trough (square markers).

of a Gauss-Newton non-linear optimization method to estimate the fitting parameters of the equation (4.12). The results of the fitting are represented in Figure 4.24 with black lines, while experimental data are identified by red markers. The fitting parameters of the equation (4.12) are shown in the Figure 4.25 as a function of the radial distance r. It is worth to highlight that neither η_0 nor B are monotonic functions. Given that a good agreement is found when comparing the experimental data with the fitting ones, saving for low radial distances, we can state that the first landslide-generated tsunamis wave is strongly directive, i.e. maximum wave crest and trough amplitudes occur in front of the generation area and, as ϑ increases the above mentioned quantities rapidly decrease.

By observing the spatial structure of the second wave (right panels of the Figure 4.23) other interesting features can be catched. As shown in Figures 4.23 and 4.24, the maximum amplitude of the first wave crest occurs close to the impact point, while the trailing first wave trough amplitude and, in particular, second wave crest and trough amplitudes occur at increasing distance, in front of the generation area. This aspect can be catched in more details looking at the time series collected close to the generation area. Along the directions close to the one along which the landslide travels (i.e., $\theta = 0°$, left panels, and $\theta = 10°$, middle panels, of Figure 4.26), the first wave exhibits the highest crest and trough amplitudes close to the impact point. As the distance increases the crest and trough amplitudes of the second waves become the highest. Actually the first wave crest and trough can be interpreted as a near-field effect of the wave generation, being the crest generated by the piston-like generation mechanism occuring when the landslide enters the water and the trough generated by the rebound of

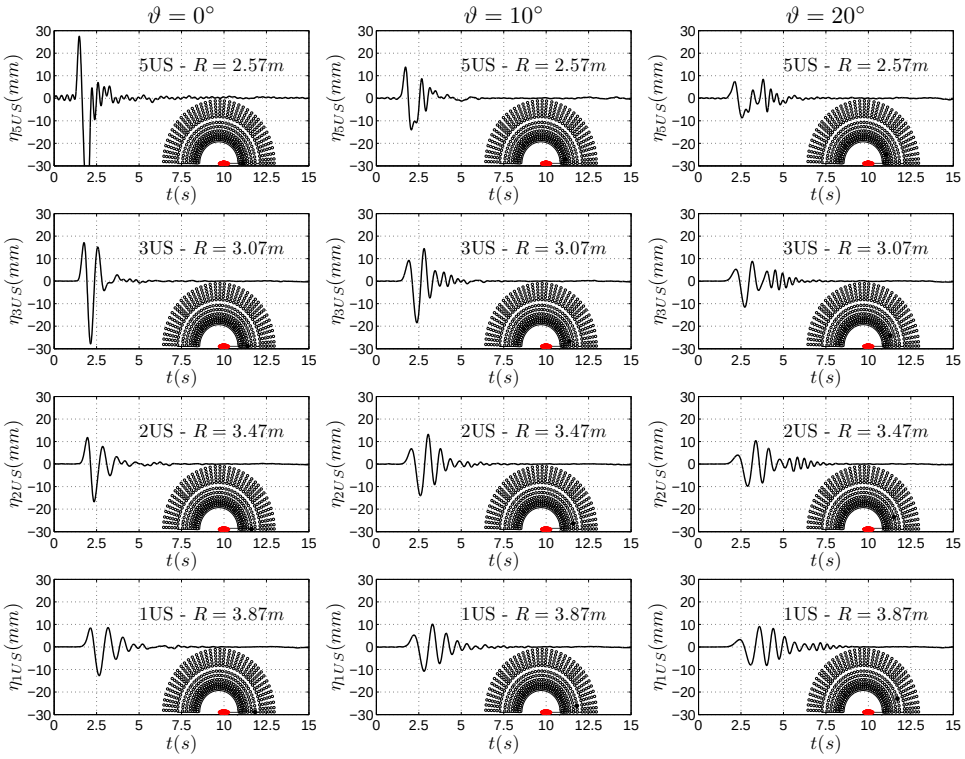

Figure 4.26: Free surface elevation time series collected by means of the moving arm at three angular positions ($\vartheta = 0, 10, 20°$) and at four radial distances ($r = 2.57, 3.07, 3.47, 3.87m$).

water and by the interaction of landslide tail with the free surface. As θ increases (i.e., $\theta = 20°$, right panels of Figure 4.26) the effects of the generation mechanism becomes less important and the wave pattern is governed by propagation mechanisms. It is important to stress that only when the propagation mechanisms become important, the maximum amplitudes occur at the coast as already observed in the case of straight coast by *Lynett and Liu* [2005] and *Di Risio et al.* [2009a]. This is due to frequency dispersion which characterizes the propagation of the seaward radiated waves as well as the propagation of the ones that travel alongshore. Indeed, by observing the second wave (right panels), a large part of energy seems to be trapped by the bathymetry at the shoreline. The maximum amplitudes of the second wave crest and trough occur along the shoreline as the distance (ϑ) from the generation area grows. Furthermore, it is evident a spatial shifting between the position at which the maximum wave crest occurs with respect to the one at which the minimum trough takes place. As pointed out by *Di Risio*

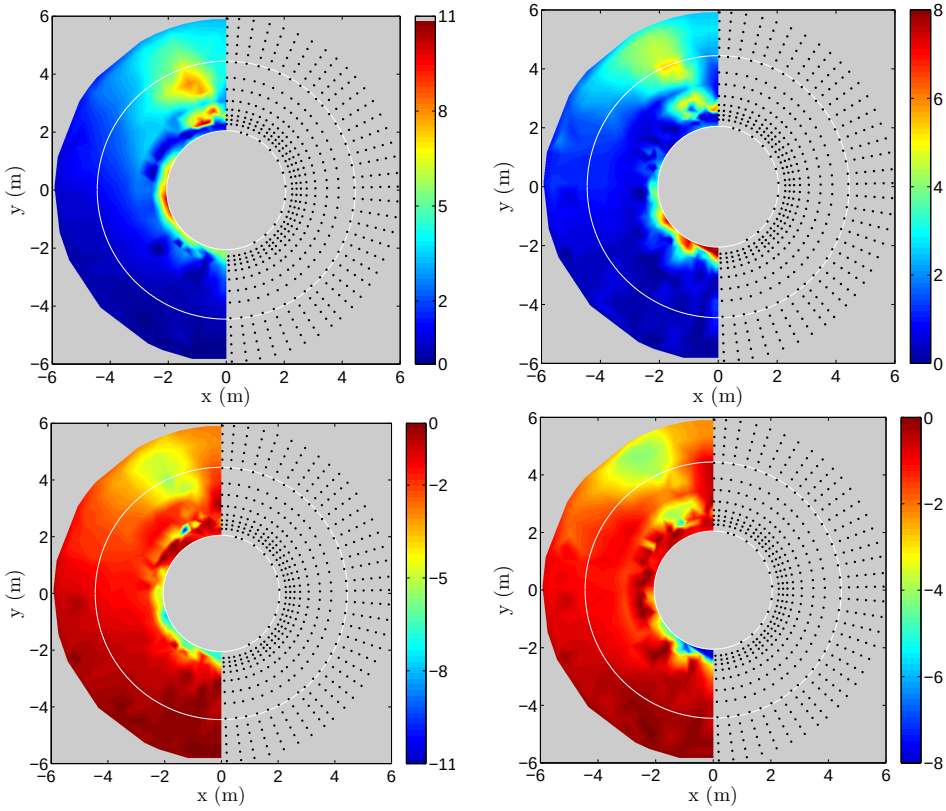

Figure 4.27: Spatial distribution of crest and trough amplitudes around the island. Left panels: third wave. Right panels: fourth wave. Upper panels: wave crests. Lower panels: wave troughs. Note: colorbars are expressed in mm.

et al. [2009b] this is clearly due to frequency dispersion, that dominate the propagation phenomena along the coastline.

Trapping and frequency dispersion phenomena are confirmed, and even emphasized, if one takes into account Figure 4.27. This figure shows the spatial distribution of the wave crest (upper panels) and trough amplitudes (lower panels) of the third (left panels) and fourth wave (right panels) obtained by linearly interpolating the experimental data obtained by using LS1. The third and the fourth waves exhibit their maximum values at the shoreline. The maximum wave crest and trough amplitude of the fourth wave occurs as the angular position ϑ, from the generation area, is almost 180° (i.e., the rear side of the island).

Finally, to better gain insight on the wave crest and trough amplitudes features around the island the Figures 4.28 and 4.29 are presented. Figure 4.28 shows the contour plot of the maximum wave crests (left panel) and the min-

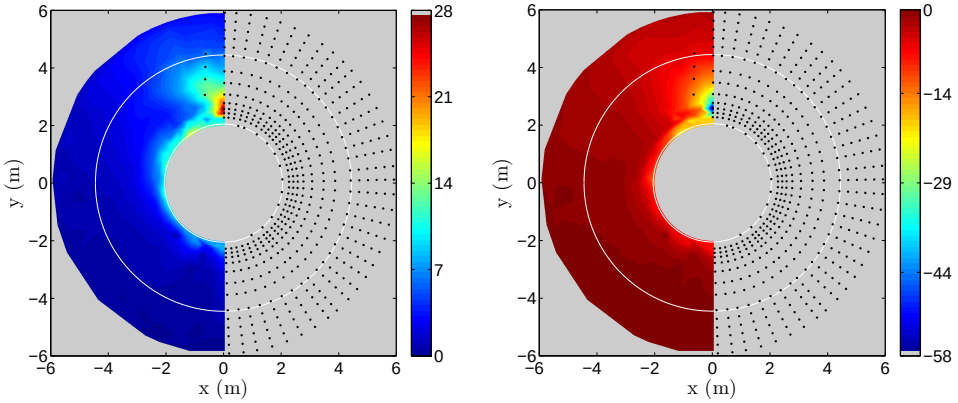

Figure 4.28: Spatial distribution of maximum crest (left panel) and mimimum trough (right panel) amplitudes around the island. Note: colorbars are expressed in mm.

imum wave troughs (right panel). Figure 4.29 shows the contour plot of the maximum "wave height" around the island, evaluated in terms of absolute value (left panel) and percentage (right panel). The maximum wave height around the island has been obtained as the sum of the maximum wave crest and trough amplitudes. Note that it is not to be intended as the height of the maximum wave of the tsunami packet, rather it has to be intended as the envelope of the maximum and minimum free surface elevation. It is worth to highlight that in the right panel of the Figure 4.29 also the contour lines of the wave height have been provided. These are indeed very useful to

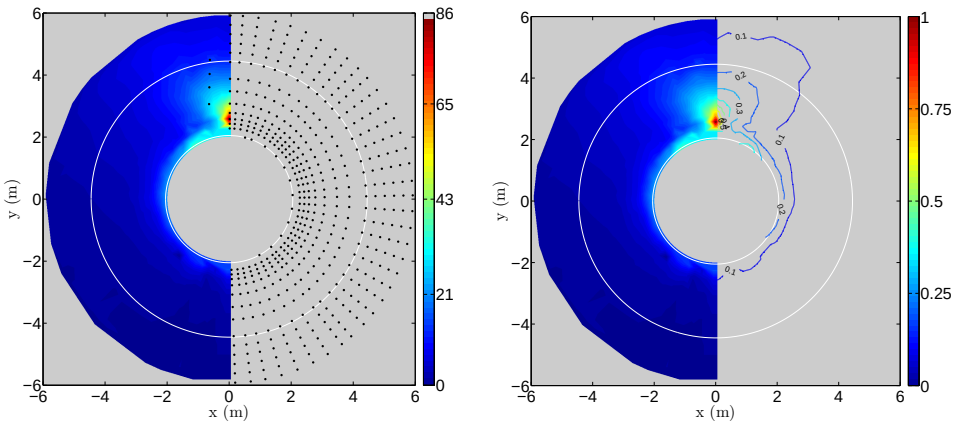

Figure 4.29: Spatial distribution of maximum "wave height" (i.e., envelope of the maximum and minimum free surface elevation) around the island, evaluated in terms of absolute value (left panel) and percentage (right panel).

evaluate, although in a qualitative manner, the wave trapping around the island. The contour lines show that when the angle ϑ is equal to 90° the 20% of the wave height is still present at the shoreline. While, when the angle ϑ is equal to 180° this quantity decreases up to the 10%.

4.3.4 Wave periods and arrival times

The wave periods have been estimated by means of both time domain (zero-crossing analysis) and frequency domain (spectral analysis) standard tecniques.

As far as the run-up time series are considered, Figure 4.30 shows the period of the first four run-up waves as a function of the dimensionless distance s'. Red markers refer to LS1, while green ones refer to LS2. It is worth to cite that wave periods, generated by both landslide models, are quite similar, especially if the first two waves are considered (upper panels). Indeed, this aspect is no longer surprising, since past researches (e.g., *Wiegel* [1955]) demonstrated that landslide-generated tsunamis wave period is mainly affected by the landslide length and the slope of the beach, rather than the thickness of the slide. Furthermore it has to be noticed that wave periods tend to slowly grow as the distance from the generation area increases.

It is also interesting to evaluate the mean arrival times of the run-up waves along the shoreline. Arrival times are showed in Figure 4.31 as a function

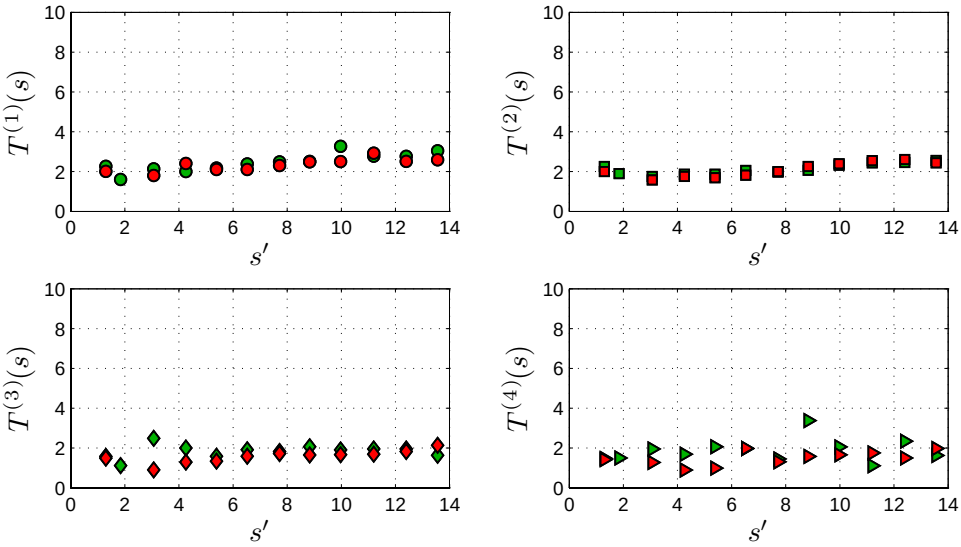

Figure 4.30: Period of the first four run-up waves. Note: red markers refer to LS1, while green ones refer to LS2.

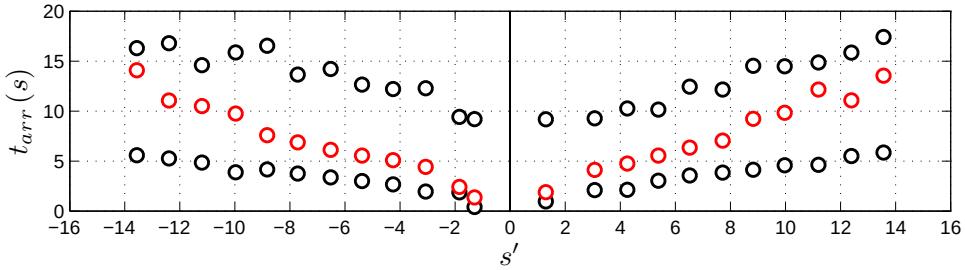

Figure 4.31: Mean arrival times of the run-up waves along the shoreline as a function of s'. Note: lower black markers refer to the time at which the tsunami begins; red markers identify the time at which the maximum of the packet occurs; upper black markers identify the time at which the fifth wave ends

of the dimensionless distance s'. Positive values of s' refer to experimental results observed for LS1, negative ones are referred to LS2 data. For each run-up gauge (i.e., at a fixed value of s') the lower black markers identify the time at which the tsunami begins, the red markers identify the time at which the maximum of the packet occurs, and finally the upper black markers identify the time at which the fifth wave ends. It is worth to highlight that as s' increases the time at which the maximum of the wave packet occurs, increases as well; in particular this arrival time tends to move from the arrival time of the first wave toward the ones of the following waves (i.e., second, third, etc.). This feature confirm that frequency dispersion is prevalent in wave propagation alongshore.

As far as the individual first three waves of the generated train are concerned, Figure 4.32 shows the wave periods of the waves measured by means of both the moving arm and the run-up gauges, as a function of the dimensionless variable s'. The black points refer to the wave periods of the waves measured by the moving arm, while the solid markers (green and red) refer to the wave periods of the run-up waves. It is almost clear that the first wave period, even if rather dispersed, increases as the distance from generation area grows. The periods of the trailing waves exhibit lower dispersion and it is possible to observe clear differences between radiating waves period and the period of the waves that propagate along the coast of the island, with the former lower than the latter. It can be argued that two different wave system occurs and each of them obeys to their own dispersion relation.

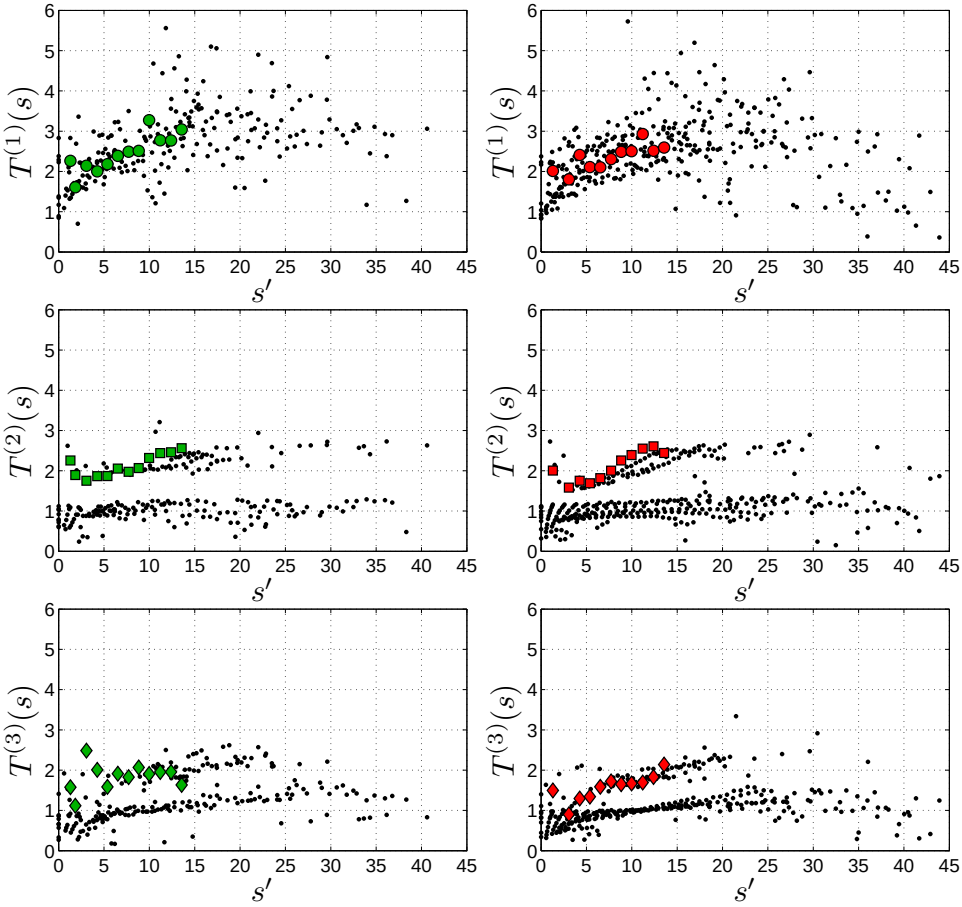

Figure 4.32: Individual wave periods of the first three waves measured by the moving arm and the run-up gauges. Note : black points refer to the wave periods of the waves measured by the moving arm, while the solid markers (green and red) refer to the wave periods of the run-up waves.

4.4 Preliminary concluding remarks

In this chapter the results of a new set of three-dimensional experiments reproducing tsunamis generated by subaerial landslides sliding down the flank of a conical island have been showed. The new experimental investigation was carried out by employing a special movable system that allows to achieve high spatial resolution, comparable to the resolution of numerical results. Then, the experimental data are intended to be useful to gain insight about the physical phenomenon at hand and to be used as a benchmark for mathematical models validation. A detailed analysis of landslide motion were performed and hydrodynamic coefficients were estimated on the basis of observed landslide displacements in order to provide reliable tools to define boundary conditions useful for models validation. Furthermore a measure of the data uncertainty was estimated.
Experimental analysis on free surface elevation shows that near the impact point the wave features are dependent upon the near-field wave generation process and the highest wave amplitude occurs in front of the impact point. When propagation mechanisms become the governing phenomena, the highest wave amplitudes occur at the coast. It is almost clear that two different system of waves are generated. The first one propagates along the coast, the second one radiates offshore. Wave periods, celerities and lengths of the two system are rather different. Close to the coast wave periods are higher and wave celerities are lower if compared to the radiating waves. The landslides thickness affects significantly only wave amplitudes, whilst wave periods show little dependence upon landslide thickness.

Chapter 5

Wave propagation around the island: wavenumber-frequency analysis for detecting spatial structures of the wave field

5.1 Introduction

The experimental results shown in chapter 4 suggest that tsunamis trapping mechanisms can play a role during the propagation along the island coast. The knowledge of trapping mechanisms is essential to adequately catch the physics of the problem and to properly design effective early warning systems. In this chapter an analysis of the physics of the propagation of landslide-generated tsunamis around a conical island is provided. As shown, we focus on the experimental identification of the dispersion relation followed by the propagating waves.
As far as landslide generated-tsunamis are concerned, the wave generation is likely to occurr in shallow water regions, thus the interaction between the waves and the sloping sea bottom plays immediately a relevant role. The waves can be refracted by the interaction with the bottom, and trapping mechanisms, like those typical of edge waves, can occur. Trapping phenomena of tsunamis have been observed in nature on the basis of measurements, in analytical and numerical models, in laboratory experiments, as briefly reviewed in the following.

As far as field measurements are concerned, *Gonzalez et al.* [1995] showed that the 25 April 1992 Cape Mendocino earthquake generated a tsunami characterized by both coastal trapped edge waves and non-trapped tsunami modes. Coastal tide-gauge signals were consistent with the 0th-order edge waves mode. *Neetu et al.* [2011] observed from tide-gauge records collected during the 27 November 1945 Makran tsunami, that large waves persisted along the Makran coast and at Karachi for several hours after the arrival of the first wave. Also *Yamazaki and Cheung* [2011], on the basis of measurements and numerical tools, found that, during the 2010 Chile tsunami, trapped waves occured along the coastline. The tsunami firstly propagated away from the rupture zone in radial direction; then the continental slope refracted and trapped the waves, initially as progressive edge waves on the shelf and, after reflection at headlands and continental shelf boundaries, a number of standing and partial standing wave systems occurred along the coast. Tsunami can also be trapped when, coming from offshore, propagate toward the coast, as pointed out by *Fujima et al.* [2000]. Similar trapping mechanisms were also reported during the 2009 Samoa tsunami by *Roeber et al.* [2010].

Evidences of edge waves tsunamis can also be found in analytical, numerical and laboratory models. *Sammarco and Renzi* [2008], and later *Renzi and Sammarco* [2012], demonstrated that landslides occurring at a straight sloping coast generate waves that travel along the shoreline as edge waves; their analytical method suggests that perfect wave trapping occurs. *Lynett and Liu* [2005], by applying a numerical model to reproduce landslide tsunamis at a coast, found that edge waves dominate the physics of the run-up in the far field. The occurrence of trapped modes in the far-field, where edge waves dominate the wave pattern, can lead to secondary run-up peaks (even larger than the peak immediatly landward of the slide).

As far as laboratory models investigations are concerned, *Yeh* [1985], and few years later *Chang* [1995], have performed experiments reproducing edge waves generated at the coast of a straight coast, by using the same experimental set-up. A special wave paddle hinged offshore and swinging in the longshore direction, was used to generate edge waves packets. *Liu and Yeh* [1996] described the generation theory of such laboratory set-up; it was found that the wave field is dominated by the 0th-order edge waves mode. *Liu et al.* [1998] applied spectral analysis to the same laboratory records and found a combination of several progressive edge waves modes. They pointed out that these waves are frequency dispersive (as demonstrated by *Yeh* [1987]) and that 0th-order mode dominate in the lower frequency range, while higher modes dominate in higher frequencies. *Di Risio et al.* [2009a]

carried out a series of three-dimensional experimental works aimed at reproducing the generation of impulsive waves by semi-elliptical landslides sliding down along a straight sloping coast. Based on experimental findings, they confirmed that landslide-generated waves, which propagate along the shoreline, are frequency dispersive and remain trapped near the coast itself.
The research cited so far, mainly deals with edge waves at plane and straight coasts. As far as non rectilinear coast is concerned, *Smith and Sprinks* [1975] showed, by using the asymptotic solution of *Smith* [1974], that trapping phaenomena, in general, and edge waves in particular, can occur at a conical island. *Tinti and Vannini* [1994, 1995] studied the wave trapping mechanism around a conical island using an analytical model. Similarly to the work of *Smith and Sprinks* [1975], *Tinti and Vannini* [1994, 1995] considered waves coming from offshore, i.e. not generated directly at the coast. It was found that a local system of edge waves, rotating around the island, can develop. *Renzi and Sammarco* [2010], using an analytical model, demonstrated that landslide tsunamis, generated at the coast of a conical island, propagate along the coastline in a form similar to that of edge waves. However they are not perfectly trapped by the bathymetry, as indeed happens for a straight coast [*Sammarco and Renzi*, 2008], and the energy gradually radiates toward the open sea. It is important to stress that *Renzi and Sammarco* [2010] do not identify which edge wave mode is prevalent in the wave propagation alongshore, and no explicit frequency dispersion relation is provided by their theory.
The knowledge of the trapping mechanisms of tsunamis by the bathymetry, is of special scientific and technical interest. First, the trapping mechanism governs the celerity at which the waves propagate along the coast. Second, trapping mechanisms can induce high waves along the coast, also at very large distances from the tsunamigenic source, since the wave energy does not radiate toward the open sea. Third, the effect of the bathymetry can induce the waves to travel around small islands, attacking areas geographically sheltered by the tsunami [*Smith and Sprinks*, 1975; *Briggs et al.*, 1995; *Tinti and Vannini*, 1994, 1995; *Renzi and Sammarco*, 2010].
In this chapter we focus on identifying the propagation and trapping mechanisms of the landslide-generated tsunamis that are triggered directly at the coast of a conical island. In order to shed light on these phenomena we apply the so-called wavenumber-frequency analysis (hereinafter k-f), which allows to evaluate the properties of a geophysical signal, measured by a spatial array of sensors, in the wavenumber-frequency plane.
The k-f has been used, although not frequently, to study coastal phenomena. *Huntley et al.* [1981] used the k-f, deploying 42 sensors over an area of 0.26

km^2, on a natural beach in California; they were able to identify progressive edge waves activities. *Oltman-Shay et al.* [1989], *Dodd et al.* [1992], *Ozkan-Haller and Kirby* [1999], using the data collected during the SUPERDUCK field experiment [*Crowson et al.*, 1988], applied the k-f aiming at studying the shear instabilities of the longshore current. *Holland and Holman* [1999] used this technique on 26 swash time series (spaced every 10 m in the longshore direction) obtained by sampling video recordings of swash motion on a natural beach.
We apply the k-f to the laboratory experiments described in chapters 3 and 4 [*Di Risio et al.*, 2009b; *Molfetta et al.*, 2010]. Note that only the experimental data collected by using LS1 have been used for the k-f. As shown later, this analysis needs high space-resolution data. Since a great number of measurements, with a proper spatial-resolution, are available for the LS1 model only, this implies that only this data are suitable to be processed by this kind of technique. In order to identify the dispersion relation followed by the waves that, travelling around the island, inundate the coast, the one-dimensional k-f has been applied to the shoreline run-up time series, collected by *Di Risio et al.* [2009b] along the coast of the island. The analysis has been applied to the records, and the comparison of the results with theoretical frequency dispersion relations allows to understand what are the dominant propagation mechanisms. Furthermore a comparison between theoretical and experimental phase and group celerity of the waves travelling around the island has been carried out.
Moreover the two-dimensional k-f has been applied to the experimental data described in the chapter 4 [*Molfetta et al.*, 2010]. *Molfetta et al.* [2010], by using the same experimental set-up of *Di Risio et al.* [2009b], performed a new set of experiments. As shown in chapters 3 and 4 a new acquisition technique allowed to obtain a very high-space resolution dataset. Thus a great number of free surface elevation time series collected around the island have been used to gain insight on the trapping mechanisms of the tsunamis.
The chapter is structured as follows. After this introduction, the next section describes in depth the basics of the k-f. Then results and discussions are presented. Concluding remarks close the chapter.

5.2 Wavenumber-frequency analysis (k-f)

The k-f has been widely used in geophysics. It can be applied to any geophysical signal measured by a spatial array of sensors (one-, two- or three-dimensional). The accuracy of the results depends on the spatial structure

of the array (e.g. shape and extension of the array, minimum and maximum distance between two sensors, etc.) related to the properties of the measured signals.
This analysis is often conceptually divided into two types or techniques: the high-resolution method [*Capon*, 1969], and frequency-domain beamforming method [*Lacoss et al.*, 1969]. In this work the frequency domain beamforming method has been used. A brief description of this method is given in the following; the reader is referred to *Yoon* [2005] for further details.
The purpose of the k-f is to estimate the wavenumber-frequency spectral density $P(\mathbf{k}, f)$ (i.e. the *steered response power spectrum*). Given the time series acquired by a spatial array of M sensors, placed at known positions $\mathbf{x_m} = [x_m, y_m]$ (where $m = 1, ..., M$) in a two-dimensional space, the steered response power spectrum (hereinafter SRPS), for a specific frequency $f = f_0$, is given by the following relationship

$$P(\mathbf{k}, f_0) = \mathbf{e}^H \mathbf{W} \mathbf{R} \mathbf{W}^H \mathbf{e}. \tag{5.1}$$

$\mathbf{e}$ is a *steering vector*, function of the wavenumbers vector $\mathbf{k} = (k_x, k_y)$, $\mathbf{W}$ is a diagonal matrix that contains the *shading weights* w_m, $\mathbf{R}$ is the *spatio-spectral correlation matrix* and $(\cdot)^H$ denotes the Hermitian transpose operator. It is possible to define the steering vector as follows

$$\mathbf{e}(\mathbf{k}) = [\exp(-i\mathbf{k} \cdot \mathbf{x_1}), ..., \exp(-i\mathbf{k} \cdot \mathbf{x_M})], \tag{5.2}$$

while the diagonal matrix $\mathbf{W}$ can be expressed as

$$\mathbf{W} = \begin{bmatrix} w_1 & ... & 0 \\ \vdots & \ddots & \vdots \\ 0 & ... & w_M \end{bmatrix}, \tag{5.3}$$

where each term w_m represents the shading weight for the generic m^{th} sensor. In this work the shading weights are set equal to 1 (as suggested by *Zywicki and Rix* [2005]). The spatio-spectral correlation matrix $\mathbf{R}(f_0)$, for a given frequency, is given by the following relationship

$$\mathbf{R}(f_0) = \begin{bmatrix} G_{11}(f_0) & ... & G_{1M}(f_0) \\ \vdots & \ddots & \vdots \\ G_{M1}(f_0) & ... & G_{MM}(f_0) \end{bmatrix}, \tag{5.4}$$

where each element $G_{ij}(f_0)$ represents the *cross-power spectrum* between the sensors i and j (where $i, j = 1, ..., M$). The cross-power spectrum is defined as

$$G_{ij}(f_0) = S^*(\mathbf{x_i}, f_0) S(\mathbf{x_j}, f_0), \tag{5.5}$$

where the generic element $S(\mathbf{x_m}, f_0)$, contained in the following column vector

$$S(f_0) = [S(\mathbf{x_1}, f_0), ..., S(\mathbf{x_M}, f_0)] \,, \tag{5.6}$$

represents the element corresponding to the frequency $f = f_0$ of the Fourier Transform of the signal measured at the mth sensor and $(\cdot)^*$ denotes its complex conjugate.
The accuracy on estimating the wavenumber-frequency spectral density depends on the spatial structure of the array, compared to the properties of the signal. It is possible to define a wavenumber resolution Δk for a linear array as

$$\Delta k = \frac{2\pi}{D}, \tag{5.7}$$

where D is the extension (or aperture) of the array. Of course a high wavenumber resolution allows to isolate accurately two waves with adjacent wavenumbers. Furthermore spatial aliasing phenomena may occur. In order to avoid it the minimum spatial lag $d_{\min}$ between two adjacent sensors has to be smaller than a half of the smallest wavelength of the measured signal. Thus it is possible to define the largest wavenumber that can be measured without spatial aliasing. This is the Nyquist wavenumber k_N, defined for linear array as follows

$$k_N = \frac{\pi}{d_{\min}}. \tag{5.8}$$

For a fixed number of sensors there is a trade-off between spatial aliasing and wavenumber resolution, that (in this case) are substantially competing objectives. Anyway the use of linear array with irregularly spaced sensors is one means of achieving a good balance between these two sampling issues. Although the technique is strictly valid for stationary processes, it has been applied to transient signals (e.g., *Capon* [1969], *Gupta et al.* [1990a, b]), similarly to those considered in this work.

5.3 Description of the k-f features

As earlier mentioned, the k-f is based on spatial measurements of propagating wave signals collected at some specific locations. As far as spatial sampling techniques are concerned, similarly to the standard time sampling ones, several issues can arise. In this section a brief overview of the so-called "spatial sampling issues" is given. A more detailed and exhaustive description can be found in the work of *Yoon* [2005], to which we refer to describe some of the main spatial sampling issues.

In principle a perfect spatial sampling of propagating wave signal implies continuous spatial measurements; but in practice, only a finite number of sensors is used at specific locations. This section aims at evaluate the effects that finite sampling in space causes on the k-f results. As shown in this section, the properties of the sensors array, compared with the features of the wave signal to be measured (e.g., wavelenght, wave period, etc.), influences the k-f results in terms of identification of the signal properties themselves. In order to better comprehend the so-called spatial sampling issues it is useful to show the following dissertation (see pp. 56-57 of the work of *Yoon* [2005] for an exhaustive description). If a one dimensional signal $\eta(x,t)$ that propagate along x direction is considered, it is possible to describe the spatial sampling with the following function

$$z(x,t) = w(x)\eta(x,t), \tag{5.9}$$

where $w(x)$ is a function that described the spatial array of sensors in x direction, which can be defined as follows

$$w(x) = \begin{cases} 1 & \text{if } 0 \leq x \leq D \\ 0 & \text{otherwise} \end{cases}. \tag{5.10}$$

Thus it is possible to define the Fourier Transform of $z(x,t)$ as the convolution between the new functions $W(k)$ and $S(k,t)$ that represent the spatial Fourier Transfoms of $w(x)$ and $\eta(x,t)$, respectively. This new quantity is defined as follows

$$Z(k,t) = W(k) * S(k,t). \tag{5.11}$$

In spatial signal processing, the Fourier Transfom $W(k)$ of the spatial array $w(x)$ is called the "array smoothing function" (hereinafter ASF). It is demonstrated (see *Yoon* [2005]) that as the array aperture D increases, $W(k)$ becomes similar to the impulse function $\delta(k)$ and $Z(k,t)$ approximates adequately the transform of the original signal $S(k,t)$. In other words the ASF is a filter that magnifies the transform of a signal which is measured by a spatial array of sensors .
The ASF $W(k)$, by following the approach of [*Johnson and Dudgeon*, 1993], is defined as follows

$$W(k) = \sum_{m=1}^{M} w_m e^{ikx_m}, \tag{5.12}$$

where M is the number of sensors in the array and w_m is the shading weight for the mth receiver. Thus, as earlier shown, the ASF represents the Fourier Transform of a discrete spatial window. If a perfect sampling is desidered

the array smoothing function should be an impulse function. In practice the spatial data collection is performed in a finite manner; thus the effects of finite spatial sampling have to be considered in order to evaluate the performance of the k-f. The array smoothing function $W(k)$, along with the wavenumber resolution Δk and the Nyquist wavenumber k_N, which is related to the "spatial aliasing", can be intended as parameters that are suitable to characterize the effectiveness of the array in measuring the signal. Consequently these quantities allow to estimate the robustness of the k-f. As shown in detail in the following, the shape of the ASF allows to evaluate the effectiveness of the spatial sampling. The array aperture influences the value of the wavenumber resolution Δk (see the equation (5.7)), which is equal to the half of the mainlobe width of the ASF. Furthermore, the so-called spatial aliasing, that depends on the minimum spatial lag d_{min} (see the equation (5.8)) between adjacent sensors of the array, can be referred to the sidelobes height of the ASF.
In the following, several explaining examples are considered in order to investigate the spatial sampling issues, and the k-f behaviour.

5.3.1 Spatial sampling issues: 1D k-f

In this section the spatial sampling issues, related to the one-dimensional k-f analysis, are shown. The properties of the ASF (i.e., the so-called mainlobe width and sidelobe height), along with the capability of the one-dimensional k-f in identifying the dispersion relation followed by the propagating waves, are shown in the following.

ASF: mainlobe width

As previously described, the wavenumber resolution Δk is related to the array aperture D (i.e., the extension of the sensors array), and it is defined as the half of the mainlobe width of the array smoothing function $W(k)$. In Figure 5.1 an example of one-dimensional k-f analysis is provided. A one-dimensional array, that is made-up of a fixed number M of equally spaced sensors (i.e., $M = 30$), is used to measure an ideal wave signal that propagate in space along the x axis. The wave signal $\eta(x, t)$ is defined as follows

$$\eta(x, t) = a \cos(kx - \omega t + \phi), \tag{5.13}$$

where the angular frequency ω is 2.0944 rad/s, the amplitude a is 0.01 m, and the phase ϕ has a constant value equal to 0. It is assumed that the waves are propagating on a constant depth $h = 100$ m, and follow the dispersion

relation as for the linear wave theory:

$$\omega^2 = g\,k \tanh(kh)\,. \tag{5.14}$$

Thus the wavenumber k used in the (5.13) is 0.4471 rad/m.
In this example the influence of the array aperture D is evaluated. As mentioned, the number of sensors has been kept fixed, while the array aperture has been varied (D = 50, 100, 200, 400 m; see the legend of Figure 5.1). It is shown that as the array aperture increases, then the mainlobe width of the ASF becomes closer. This implies an improvement of the wavenumber resolution Δk. However, considering that the number of sensors is fixed, it is clear that as D increases, the spatial lag d_{min} between two adjacent sensors increases as well. This allows to obtain a smaller Nyquist wavenumber k_N; thus also the features of the spatial aliasing (i.e., occurrence of sidelobe

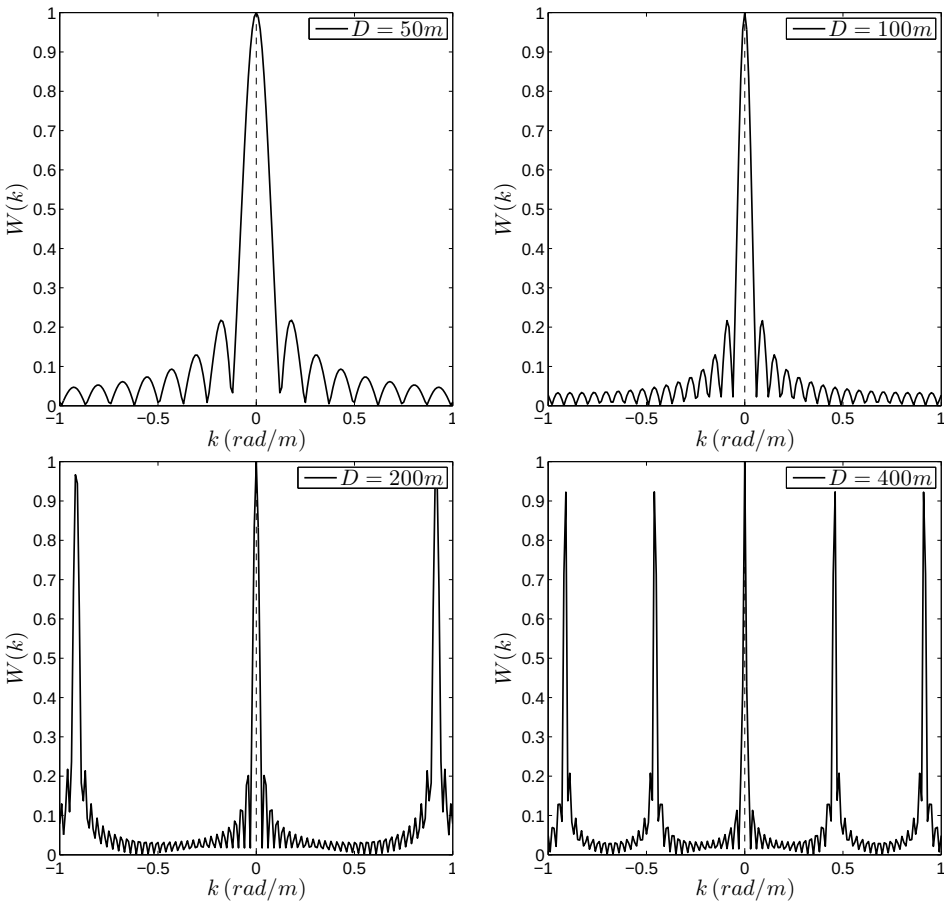

Figure 5.1: Array smoothing functions for four array apertures D. Note: the number of sensors is fixed and equal to 30.

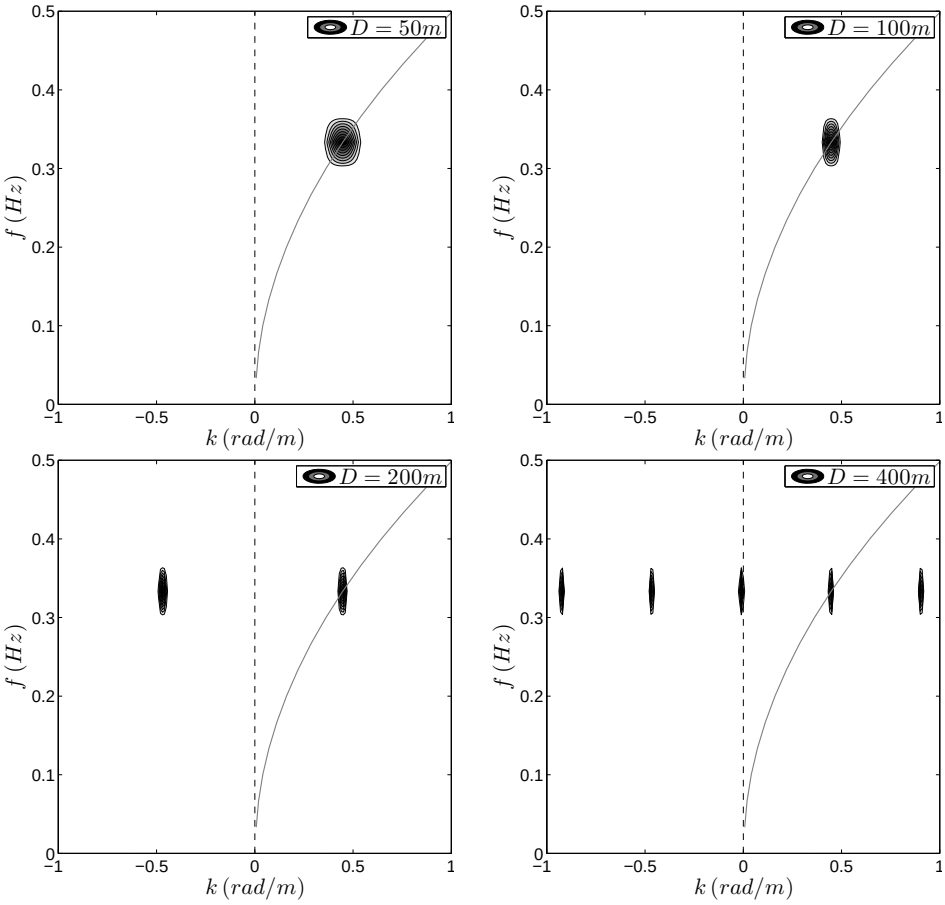

Figure 5.2: Steered response power spectra. The gray line identifies the linear waves dispersion relation. Note: the number of sensors is fixed and equal to 30.

peaks) can be seen in Figure 5.1. As D is equal to 200 m, spurious peaks occur in the wavenumber domain of the ASF (see lower panels of Figure 5.1).

Figure 5.2 shows the SRPS, which is the result of the k-f, obtained for each of the four investigated arrays. If the array aperture increases, then the horizontal spreading (in the wavenumbers domain) of the SRPS drescreases around the exact wavenumber k of the signal, i.e. the k-f identifies more precisely the proper pair wavenumber-frequency that characterizes the propagating signal. Accordingly to this, the dispersion relation followed by the waves is univoquely identified. Of course when D is equal, or greater, to 200 m, spatial aliasing occurs; spurious peaks, related to those of the array smoothing functions, occur in the SRPS. In this example, the best

trade-off between wavenumber resolution (i.e., mainlobe width) and Nyquist wavenumber (i.e., lack of spatial aliasing) is reached if the array aperture D is 100 m.

ASF: sidelobe height

Other important issues to evaluate the effectiveness of the k-f are related to the occurrence and the magnitude of sidelobes in the ASF. These spurious peaks imply the occurrence of spatial aliasing. In order to comprehend this feature the following example is provided. In this case the same wave signal described in the equation (5.13) is measured by four array of sensors. Each array is characterized by the same array aperture ($D = 100$ m). A different number of sensors has been employed for each array; more specifically: 5,

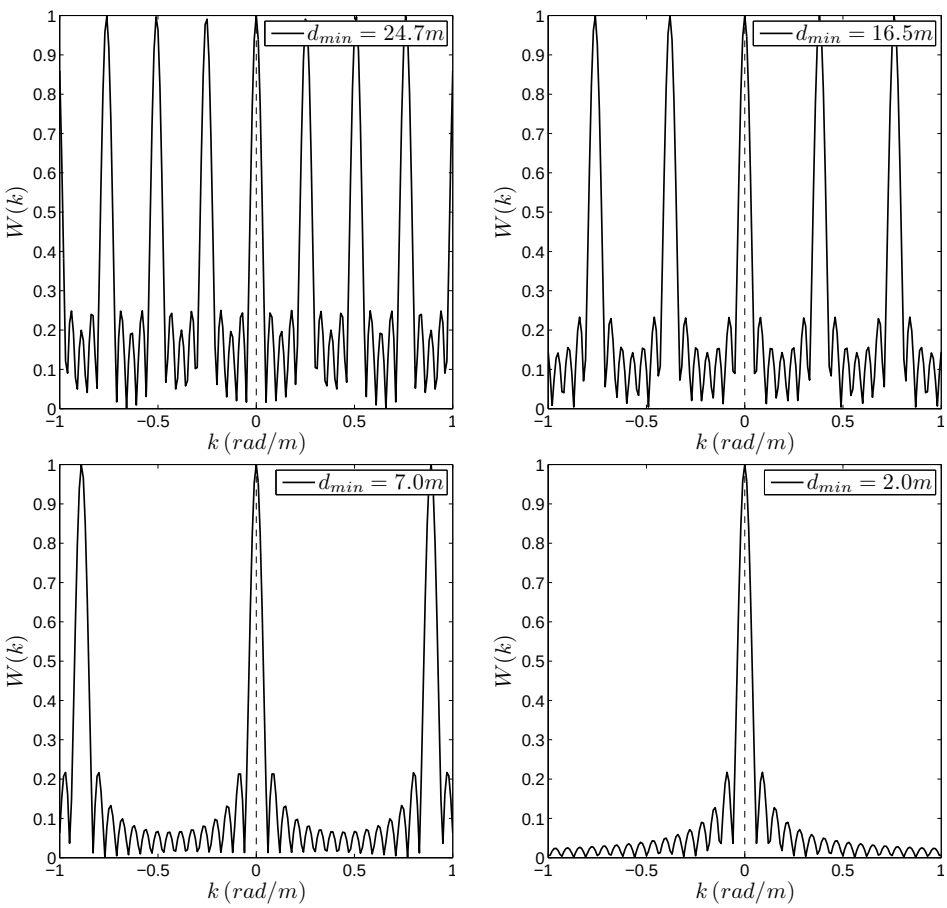

Figure 5.3: Array smoothing function for four arrays made-up of different numbers of sensors (i.e., several spatial lag d_{min}). Note: the aperture of the array D is fixed.

7, 15, 50. Thus, the wavenumber resolution Δk is constant. Conversely, the Nyquist wavenumber k_N varies, given that the spatial lag d_{min} decreases as the number of sensors increases. Figure 5.3 shows the ASF of the mentioned arrays. As the spatial lag is too coarse (see upper panels and lower left panel of the Figure 5.3) spurious peaks (i.e., sidelobes that have height comparable with that of the mainlobe) occur in the ASF. Instead, if the spatial lag is adequately small the ASF is characterized by small sidelobes (lower right panel of the Figure 5.3). In order to minimize the sidelobe height, the optimal spatial lag d_{min} has to be equal or smaller than the half of the smallest measured wavelength, and can be defined as follows

$$d_{min}^{opt} \leq \frac{L_{min}}{2}. \tag{5.15}$$

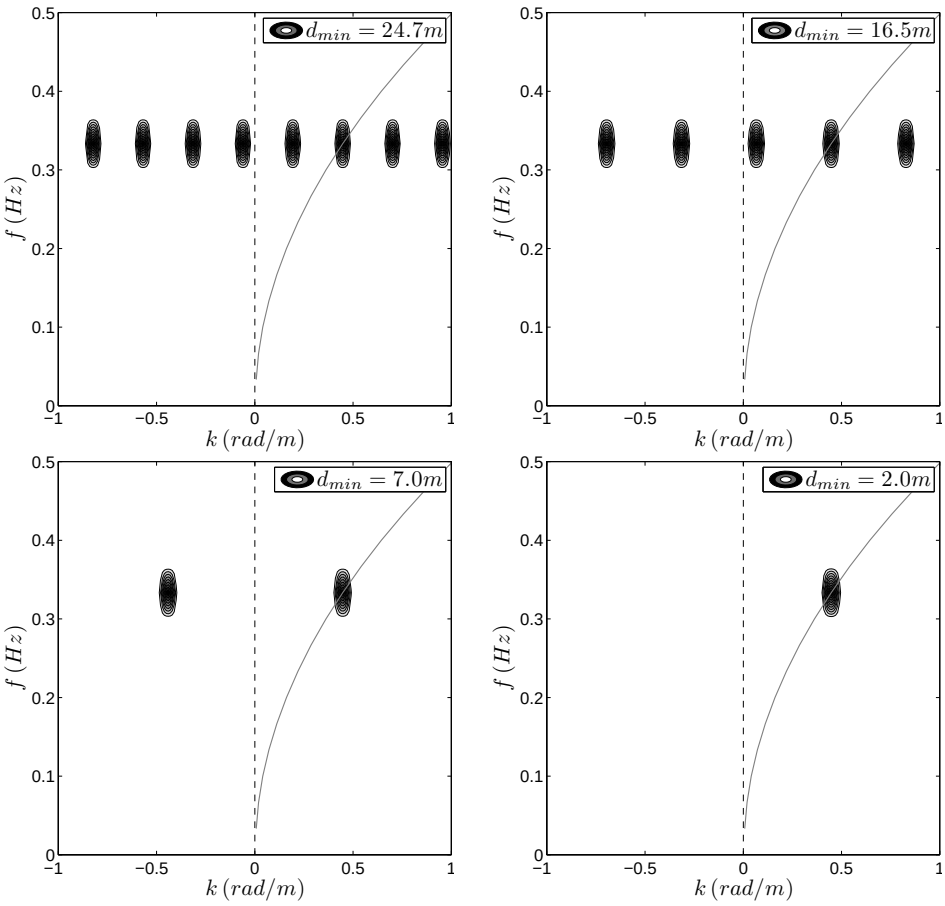

Figure 5.4: Steered response power spectra. Note: the aperture of the array D is fixed.

Figure 5.4 shows the SRPS obtained by applying the k-f to the signals measured by the four mentioned arrays. It is clear that only the fourth sensors array provides an accurated identification of the wave properties (lower right panel of the Figure 5.4), in terms of both frequency and wavenumber. Finally, as previously stated, it useful to recall that if a fixed number of sensors is given it is essential to find a trade-off between the wavenumber resolution and the Nyquist wavenumber.

Dispersion relation detection

This section aims at explaining the potentialities of the k-f in detecting the dispersion relation followed by the measured wave signals. To better comprehend this features, several ideal wave signals have been processed with the one-dimensional k-f. The detection of the dispersion relation followed by the measured waves is straightforward in the k-f plane. By observing the SRPS distribution in the k-f plane the dispersion relation is univoquely determined. In the following four examples are shown. To show the detection procedure, a sensors arrays with aperture $D = 100$ m, made-up of 50 sensors, has been used to measure four ideal wave signals; more specifically:

- wave signal characterized by one frequency component that travel toward the positive x direction following the linear wave dispersion relation;

- wave signal characterized by two frequency components that travel toward the positive x direction following the linear wave dispersion relation;

- wave signal characterized by three frequency components. Two of these travel toward the positive x direction, and the remaining one travel in opposite direction (i.e., negative x direction). All the components follow the linear wave dispersion relation;

- solitary wave that propagate in the positive x direction.

The SRPSs obtained by the k-f are shown in Figure 5.5. For each panel the shape and the position of the SRPS allows to identify the dispersion relation followed by the propagating waves. Figure 5.5 shows that the energy densities are placed on the proper dispersion relations. Furthermore also the propagation direction of each frequency component is adequately detected.

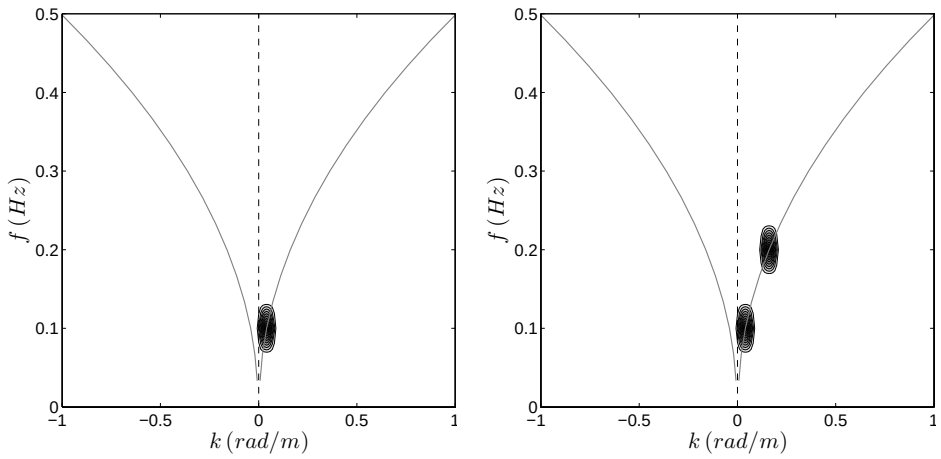

(a) *Cosine wave (1 frequency).*

(b) *Cosine wave (2 frequencies).*

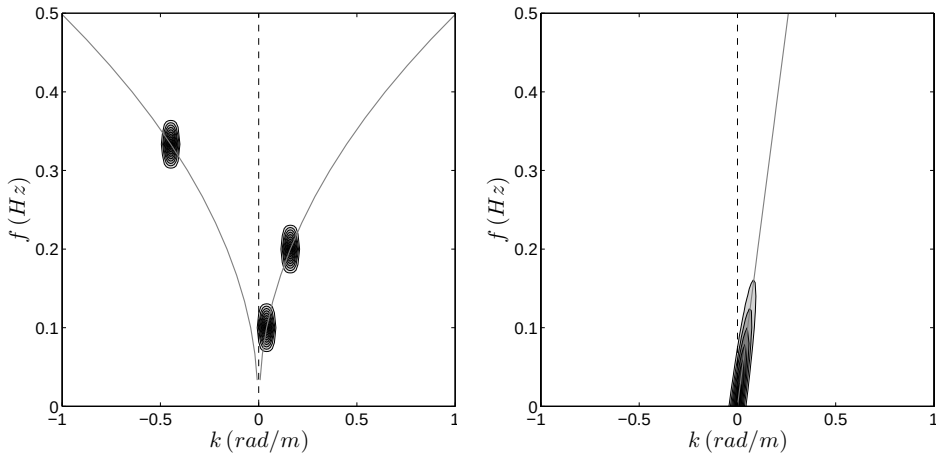

(c) *Cosine wave (3 frequencies).*

(d) *Solitary wave.*

Figure 5.5: Steered response power spectra of four test wave signals. Upper left panel: wave signal characterized by one frequency component. Upper right panel: characterized by two frequency components. Lower left panel: wave signal characterized by three frequency components. Lower right panel: solitary wave that propagate in space. Note: gray lines identify the wave dispersion relations.

5.3.2 Spatial sampling issues: 2D k-f

In this section the spatial sampling issues, related to the two-dimensional k-f analysis, are shown. When the 2D k-f is considered it is important to stress that other issues, as well as potentialities, occur with respect to those seen for the 1D k-f. Given that the degrees of freedom of the problem increase, new spatial sampling issues arise. For instance, the shape of the sensors

array can affect the ASF and, consequently, the k-f results. However, the increased complexity of the problem allows to better describe the features of the propagating wave signals. As shown in the following, the 2D k-f allows to estimate not only the global (or synthetic) SRPS of the measured signal in the k-f plane; indeed, for each frequency it is also possible to estimate the SRPS in the domain of the wavenumber scalar components (i.e., k_x-k_y). This allows to evaluate the propagation direction, along with the dispersion relation followed by the waves, of each frequency component of the measured wave signal.

Array geometry

In this section the influence of the array geometry on the 2D k-f, is investigated by means of several ideal tests. To gain insight on this aspect a theoretical wave signal, that propagate over a constant depth h of 100 m in a two-dimensional space by following the dispersion relation (5.14), is measured by four different sensors arrays. The theoretical wave signal, characterized by two frequency components, is defined as follows

$$\eta(x, y, t) = \sum_{i=1}^{2} a_i \cos\left(\mathbf{k}_i \cdot \mathbf{x} - \omega_i t + \phi_i\right), \tag{5.16}$$

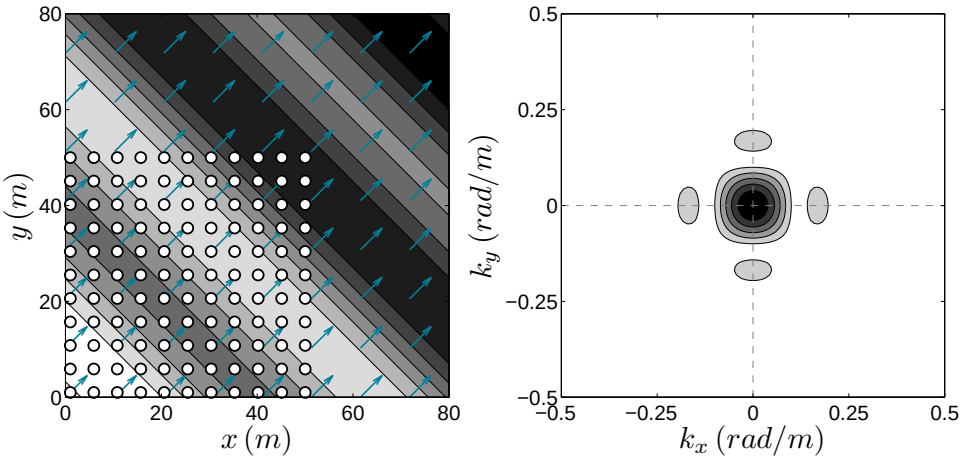

Figure 5.6: Left panel: contour plot of the free surface elevation at $t = 1.0$ s, measured by a square-shaped array; white markers identify the sensors that form the array, while blue arrows identify the propagation direction of the waves. Note: the sensors are equally-spaced. Right panel: ASF.

where the angular frequencies ω_i are 1.2566 and 0.6283 rad/s respectively, the amplitudes a_i are equal to 0.01 m, and the phases ϕ_i have a constant value equal to 0. Since the waves propagate by following the dispersion relation (5.14), the wavenumbers k_i are equal to 0.1610 and 0.0403 rad/m, in absolute value. Given that the wave propagate in a two-dimensional space, each wavenumber has two scalar components (i.e., k_x-k_y). In this test the angle δ that the wavenumber vector forms with the x axis has been fixed to 45°. Thus, the wavenumber scalar components are immediately obtained (i.e., $k_{x1} = 0.1138$ rad/m, $k_{y1} = 0.1138$ rad/m, $k_{x2} = 0.0285$ rad/m, $k_{y2} = 0.0285$ rad/m). The properties of the first sensors array are shown in Figure 5.6. Left panel of the figure shows a contour plot of the free surface elevation at a given time-step (i.e., $t = 1.0$ s); in the same plot the sensors that form the array are identified by the white markers. Furthermore, the propagation direction of the waves is identified by the blue arrows. The sensors array is square-shaped, and the sensors are equally-spaced each-other. Right panel of the Figure 5.6 shows the array smoothing function $W(k)$ of the considered array. As far as a 2D array is concerned, the ASF is a three-dimensional function. The ASF represented in the right panel of the Figure 5.6 shows quite close mainlobe, along with few and small sidelobes.
Figure 5.7 represents the SRPS, evaluated in the wavenumber scalar components domain, at the carrier frequencies of the wave signal (left panel:

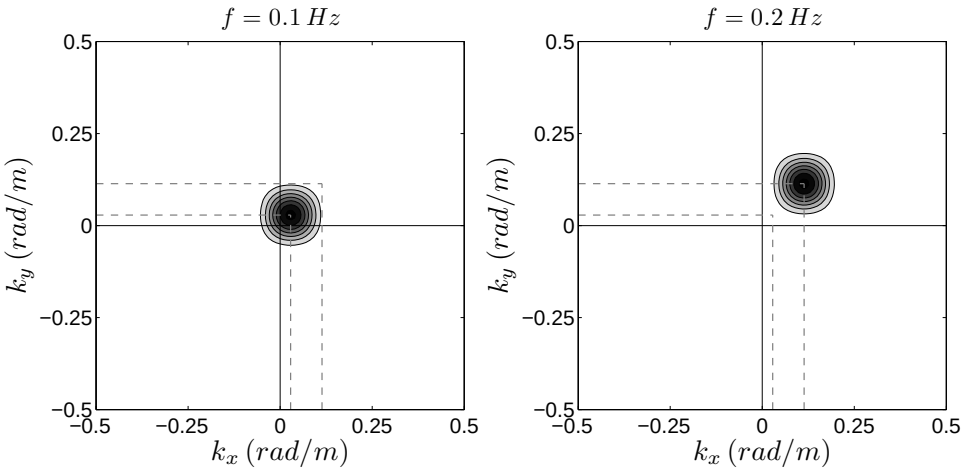

Figure 5.7: SPRS evaluated at the two carrier frequencies of the wave signal, as a function of the wavenumber scalar components. Note: gray dashed lines identify the theoretical values of the wavenumber scalar components.

$f = 0.10$ Hz; right panel: $f = 0.20$ Hz). As earlier mentioned, when a two-dimensional k-f is applied, it is possible to evaluate the energy distribution of the signal in the k-f plane, both in a global way (as shown at the end of the section), and in a detailed manner (i.e., at each solved frequency). The latter feature is quite useful, given that by identifying the energy distribution in the wavenumber scalar components domain, it allows to estimate both the value of the wavenumber (absolute value and scalar components value) at which the maximum of the energy occurs and the propagation direction of the waves for that frequency. Figure 5.7 clearly shows that the k-f adequately identifies, for each frequency, the wavenumber scalar components of the two carrier wave components. Moreover the propagation direction of each frequency component is detected as well.

In the Figure 5.8 the properties of the second sensors array are represented. Left panel of the Figure 5.8 shows the contour plot of the free surface elevation at a given time-step (i.e., $t = 1.0$ s) as from the equation (5.16), the sensors array (white markers) and the propagation direction of the waves (blue arrows). The array is square-shaped and it is made-up of the same number of sensors than that earlier described (see Figure 5.6), but it has to be stressed that in this case the sensors are not equally-spaced. Given this, the shape of the ASF (right panel of the Figure 5.8), is similar to that obtained for a equally-spaced array, but not identical. The mainlobe

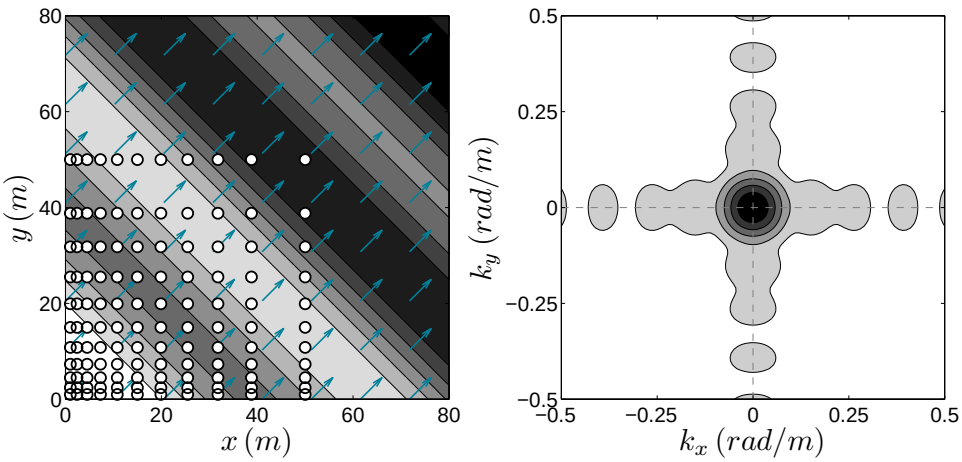

Figure 5.8: Left panel: contour plot of the free surface elevation at $t = 1.0$ s, measured by a square-shaped array; white markers identify the sensors that form the array, while blue arrows identify the propagation direction of the waves. Note: the sensors are not equally-spaced. Right panel: ASF.

is quite close; conversely, some minor sidelobes occur. Figure 5.9 represents the SRPS, evaluated in the wavenumber scalar components domain, at the carrier frequencies of the wave signal (left panel: $f = 0.10$ Hz; right panel: $f = 0.20$ Hz). The figure shows that the k-f analysis is effective in identifying the proper wavenumber scalar components as well as the direction of propagation of the waves. The different arrangement of the sensors does not seem to improve the performance of the k-f. However, it is well known that a not equally-spaced array is more powerful when a random signal (i.e., composed by a large range of frequencies and wavenumbers that are not known a priori) is measured by the array itself.

In the Figure 5.10 the properties of the third sensors array are represented. Left panel of the Figure 5.10 shows the contour plot of the free surface elevation at a given time-step (i.e., $t = 1.0$ s) as from the equation (5.16), the sensors array (white markers) and the propagation direction of the waves (blue arrows) The array is diamond-shaped and it is made-up of the same number of sensors than those earlier described (see Figure 5.6 and 5.8). In this case the sensors are again equally-spaced. The right panel of the Figure 5.10 shows the ASF obtained for this array geometry. By observing the ASF some discrepancies occur, if it is compared with those of the Figures 5.6 and 5.8. The mainlobe of the ASF is not very close. Furthermore, sidelobes (although not very large) occur. Figure 5.11 represents the SRPS, evaluated in the wavenumber scalar components domain, at the carrier frequencies of

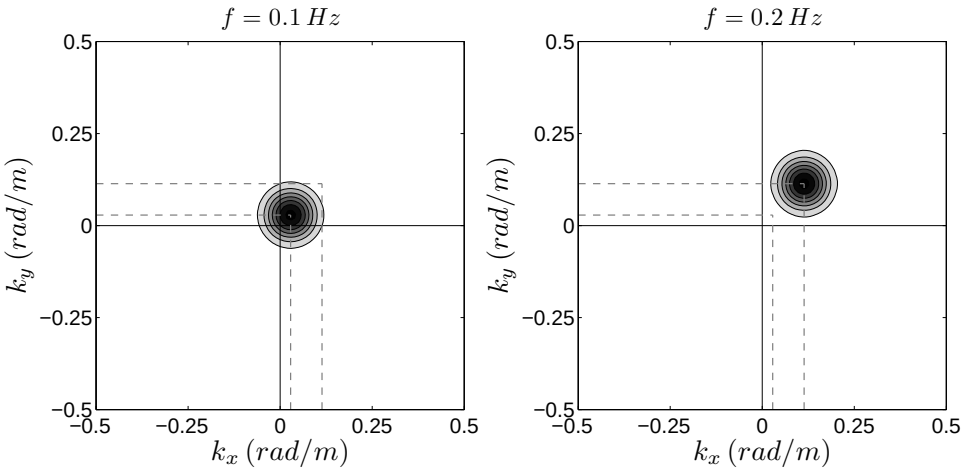

Figure 5.9: SPRS evaluated at the two carrier frequencies of the wave signal, as a function of the wavenumber scalar components. Note: gray dashed lines identify the theoretical values of the wavenumber scalar components.

the wave signal (left panel: $f = 0.10$ Hz; right panel: $f = 0.20$ Hz). It is evident that the SRPS is properly placed on the right wavenumber scalar components; furthermore, the direction of propagation of the waves is detected as well. However, as a consequence of the spreading of the ASF, the SRPS is quite spreaded. In other words, the k-f adequately estimates the properties of the wave signal, also given that the signal is quite simple, however a more complicated signal could not be properly analyzed by using this array shape.

In the Figure 5.12 the properties of the fourth sensors array are represented. Left panel of the Figure 5.12 shows the contour plot of the free surface elevation at a given time-step (i.e., $t = 1.0$ s) as from the equation (5.16), the sensors array (white markers) and the propagation direction of the waves (blue arrows). The array is circle-shaped and it is formed by means of concentric circles. It is made-up of the same number of sensors than those earlier described (see Figure 5.6, 5.8 and 5.10). In this case the sensors are not equally-spaced. The right panel of the Figure 5.12 shows the ASF obtained for this array geometry. The mainlobe of the ASF is quite close. Furthermore, it is interesting to note that small sidelobes occur at large distances, in terms of wavenumber, from the mainlobe. The latter aspect minimizes the occurrence of the so-called spatial aliasing. It is possible to state that, for the theoretical wave signal measured by means of these

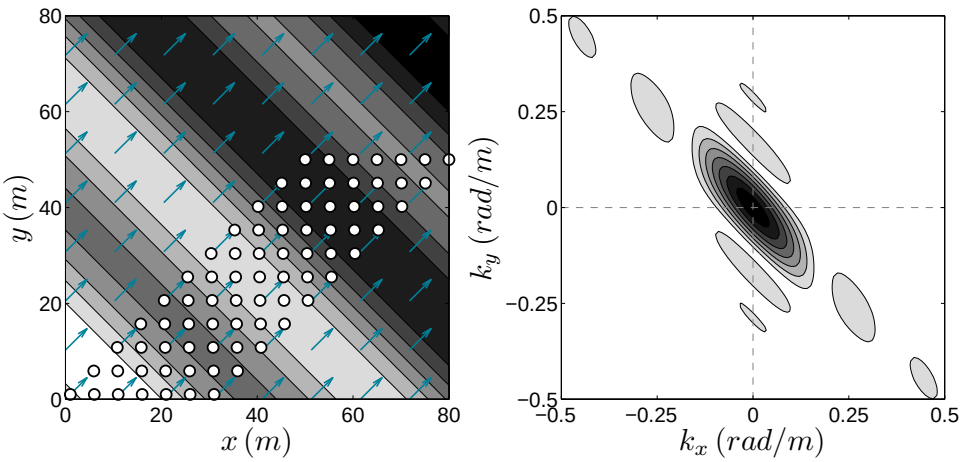

Figure 5.10: Left panel: contour plot of the free surface elevation at $t = 1.0$ s, measured by a diamond-shaped array; white markers identify the sensors that form the array, while blue arrows identify the propagation direction of the waves. Note: the sensors are equally-spaced. Right panel: ASF.

ideal sensors array, the fourt array offers the best performance in terms of ASF, i.e., in terms of spatial sampling requirements.
Figure 5.13 represents the SRPS, evaluated in the wavenumber scalar components domain, at the carrier frequencies of the wave signal (left panel: $f = 0.10$ Hz; right panel: $f = 0.20$ Hz). The k-f identifies the proper wavenumber scalar components accordingly to the propagation direction of the propagating waves .

Finally, the global, or more appropriate, the synthetic SRPS (hereinafter S-SRPS), obtained by applying the k-f to the four investigated array geometries, is represented in Figure 5.14. To provide a synthetic representation of the SRPS in the wavenumber-frequency plane, as far as a two-dimensional k-f is concerned, we consider the wavenumbers in terms of absolute values. Consequently, we represent only the absolute values of the wavenumbers to which correspond the maximum value of the SRPS for each frequency. Figure 5.14 shows that each panel, which refer to a different array shape, is in principle similar to the Figures 5.2, 5.4 and 5.5 that are related to the 1d k-f. By observing the shape of the S-SRPS, and even more important the pairs wavenumber-frequency at which the maximum values occurs, it is possible to identify the dispersion relation followed by the waves. The S-SPRS shown in the Figure5.14, are indeed properly placed on the black lines, that represent the dispersion relation (5.14), which is followed by the propagating waves. Thus, it is demonstrated how the array geometry can

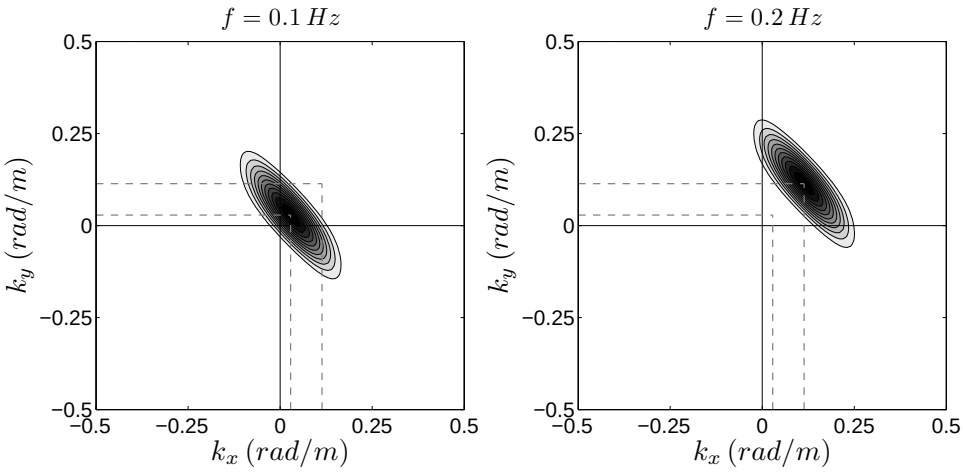

Figure 5.11: SPRS evaluated at the two carrier frequencies of the wave signal, as a function of the wavenumber scalar components. Note: gray dashed lines identify the theoretical values of the wavenumber scalar components.

influence the k-f results and how the results themselves can be interpretated.

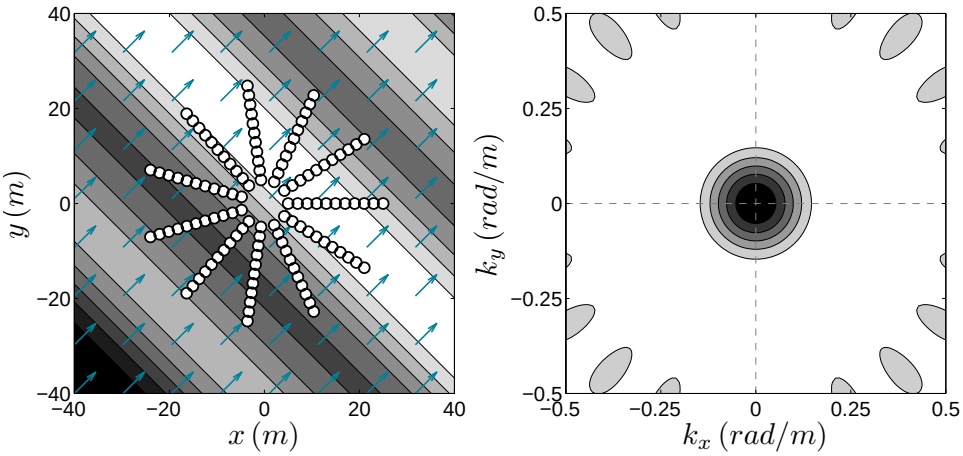

Figure 5.12: Left panel: contour plot of the free surface elevation at $t = 1.0$ s, measured by a circle-shaped array; white markers identify the sensors that form the array, while blue arrows identify the propagation direction of the waves. Note: the sensors are not equally-spaced. Right panel: ASF.

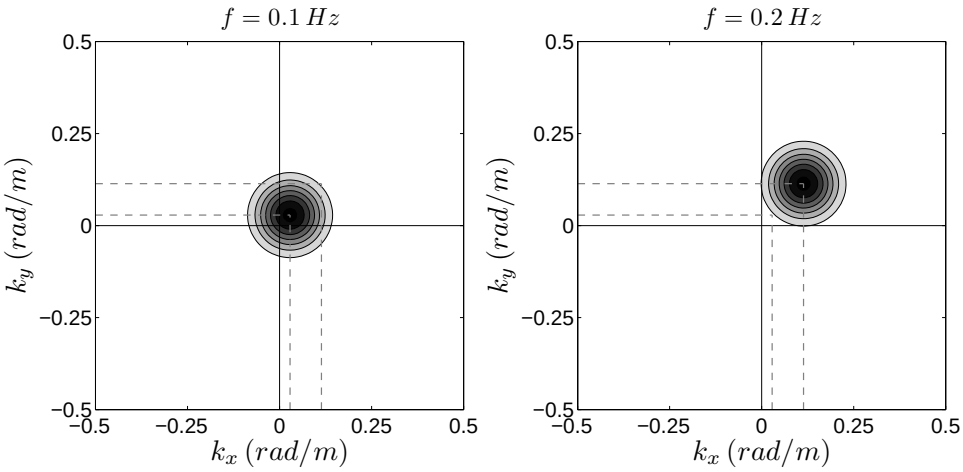

Figure 5.13: SPRS evaluated at the two carrier frequencies of the wave signal, as a function of the wavenumber scalar components. Note: gray dashed lines identify the theoretical values of the wavenumber scalar components.

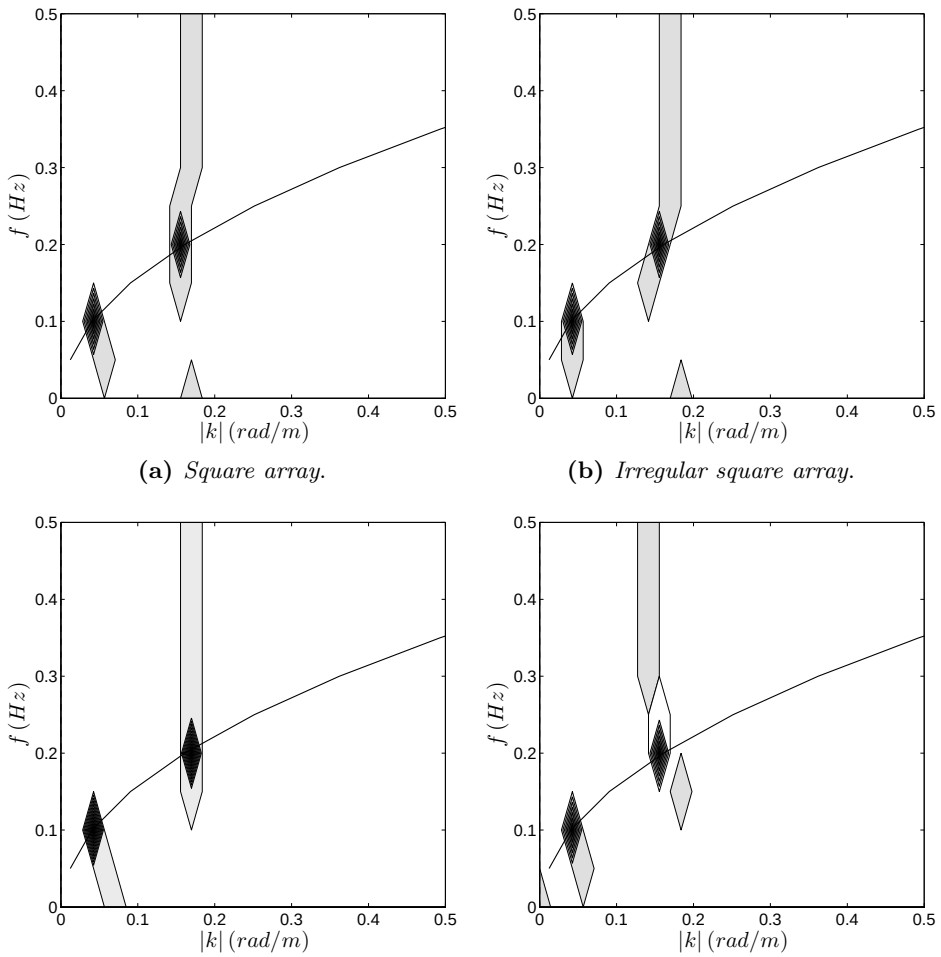

(a) *Square array.* **(b)** *Irregular square array.*

(c) *Diamond array.* **(d)** *Circular array.*

Figure 5.14: Synthetic SRPS. Note: the black lines identify the linear wave dispersion relation.

Features of circular arrays

In the previous section some spatial sampling issues of the two-dimensional k-f, related to the array geometry, have been addressed. In this section we focus on both the features and the potentialities of the circular arrays. In this case, we not consider arrays of arbitrary shape; indeed, the exact sensors array that has been used to measure the landslide-generated tsunamis around the conical island (see chapter 3) is considered. But, as shown in the previous sections, only ideal wave signals have been used to gain insight on the properties of the considered array. Furthermore, to catch in a more general way the features of the circle-shaped arrays we not consider the real bathymetry of the conical island, but a simplified one. The array is supposed to be placed on a flat sea bottom of constant depth h equal to 100 m. The array is shown in the left panel of the Figure 5.15 and it is identified by the white markers. To magnify the features of the circular arrays, three ideal wave signals are analyzed. The free surface elevation $\eta(r, \vartheta, t)s$ is described by the following equation

$$\eta(r, \vartheta, t) = a \cos\left[(k_r r + k_\vartheta \vartheta) - \omega t + \phi\right], \tag{5.17}$$

where the angular frequency ω is 6.2832 rad/s, the amplitude a is 5.0 m, the phases ϕ has a constant value equal to 0 and the wavenumbers k_r and k_ϑ are the radial and the angular wavenumber respectively.

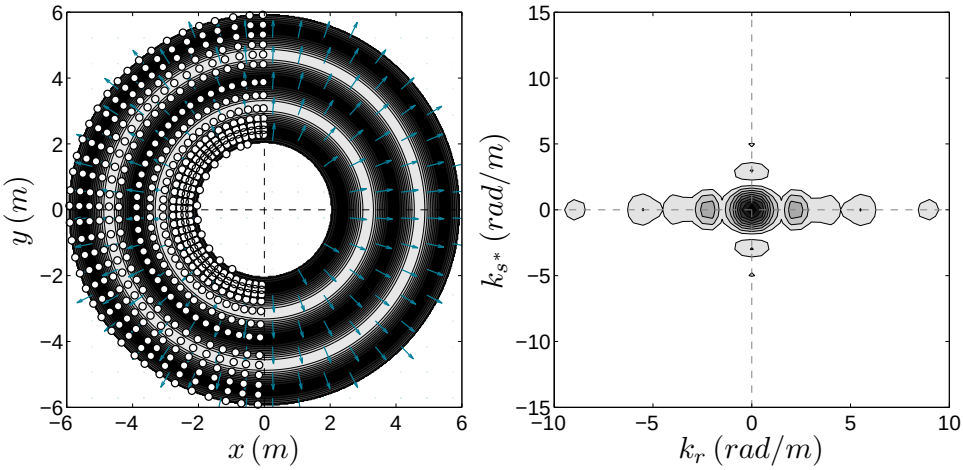

Figure 5.15: Left panel: contour plot of the free surface elevation at $t = 0.02$ s (radiated waves); white markers identify the sensors that form the array, while blue arrows identify the propagation direction of the waves. Right panel: ASF.

Given the equation (5.17) three different wave signals have been considered; more specifically:

- radiated waves (i.e., $k_r \neq 0$ and $k_\vartheta = 0$);
- trapped waves (i.e., $k_r = 0$ and $k_\vartheta \neq 0$);
- partially trapped and partially radiated waves (i.e., $k_r \neq 0$ and $k_\vartheta \neq 0$);

Furthermore, the left panel of the Figure 5.15 shows the contour plot of the free surface elevation at a given time-step (i.e., $t = 0.02$ s). The propagation direction of the waves is identified by the blue arrows. The waves propagate radially (i.e., wave fronts are locally perpendicular to the radius) from the island's center toward the open sea and follow the dispersion relation (5.14). This test aims at evaluate the features of the real sensors array used in the conical island experiments; given this only the experimental domain covered by the measurementes collected using the moving arm is considered. No measurements are available when the radius r is lower than the radius at which the undisturbed shoreline is placed (i.e., $r = 2.05$ m), or greater than the radius at which the last sensor on the moving arm is placed (i.e., $r = 5.91$ m). The right panel of the Figure 5.15 shows the ASF as a function of the radial and angular wavenumbers. The mainlobe is quite close, while few

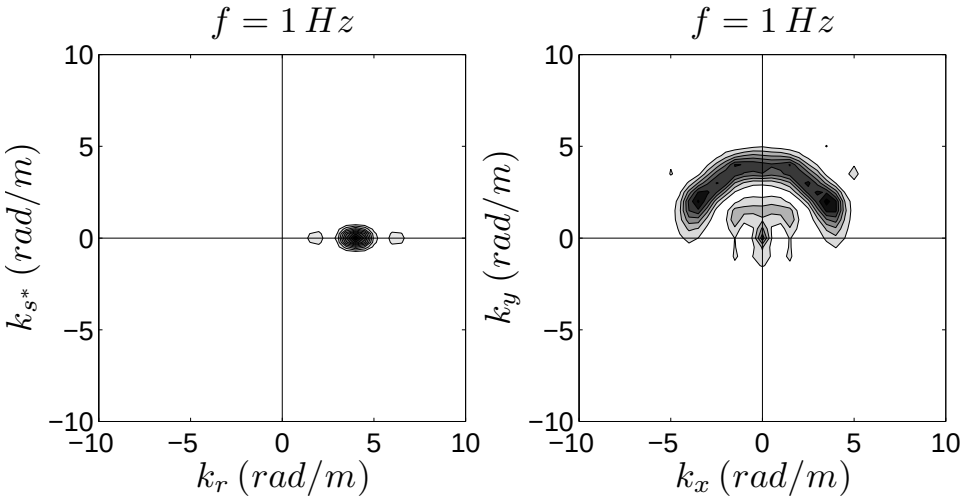

Figure 5.16: SPRS evaluated at the carrier frequency of the wave signal. Left panel: SPRS as a function of the wavenumber scalar components in cartesian coordinates. Right panel: SPRS as a function of the wavenumber scalar components in polar coordinates.

minor sidelobes occur. As later described the ASF is defined in wavenumber scalar components domain expressed in polar coordinates.
Figure 5.16 represents the SRPS, evaluated in the wavenumber scalar components domain expressed both in cartesian coordinates (left panel), and in polar ones (right panel), at the carrier frequency of the wave signal (i.e., $f = 1.0$ Hz). As far as the present problem is concerned, a reference frame expressed in polar coordinates (r,θ) appears useful to study the direction of propagation of the waves. Thus it is more convenient to express the vector wavenumber $\mathbf{k}$ not only in its scalar components expressed in cartesian coordinates ($\mathbf{k} = [k_x, k_y]$), but also in its scalar components expressed in polar coordinates ($\mathbf{k} = [k_r, k_\theta]$). In this way if, for a given frequency f_0, the SRPS is concentrated along the k_r axis, it implies that the waves, for that frequency, propagate along the radius (i.e. the wave fronts are locally perpendicular to the radius). Otherwise if the SRPS is concentrated along the k_θ axis it means that the waves, for that frequency, propagate rotating around the island (i.e. the wave fronts are locally parallel to the radius). Furthermore by dividing the angular wavenumber k_θ by a specific radius r^* (for instance the radius of the shoreline) we obtain the new wavenumbe k_s^*, defined as follows

$$k_s^* = k_\theta \frac{1}{r^*} = \frac{2\pi}{r^* \Theta}, \tag{5.18}$$

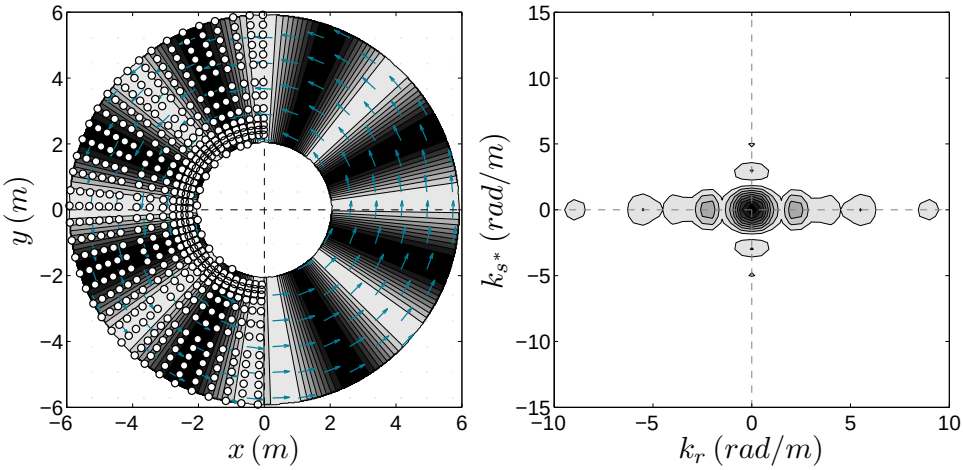

Figure 5.17: Left panel: contour plot of the free surface elevation at $t = 0.02$ s (trapped waves); white markers identify the sensors that form the array, while blue arrows identify the propagation direction of the waves. Right panel: ASF.

where Θ is an angular wavelength.
Figure 5.16 shows that the SRPS is totally arranged on the k_r axis (see left panel of the figure). The two-dimensional k-f, expressed in polar coordinates, allows not only to identify the proper wavenumber, and consequently the proper dispersion relation, but also to accurately estimate the direction of propagation of the waves for that frequency. Conversely, for that geometry the SRPS evaluated in the wavenumber domain expressed in cartesian coordinates is not straightforward to interpretate.
The left panel of the Figure 5.17 shows the contour plot of the free surface elevation of the second test wave signal at a given time-step (i.e., $t = 0.02$ s). The propagation direction of the waves is identified by the blue arrows. The waves are perfectly trapped (i.e., wave fronts are locally parallel to the radius) and propagate, by following the dispersion relation (5.14), rotating around the center of the island. Figure 5.18 represents the SRPS, evaluated in the wavenumber scalar components domain expressed both in cartesian coordinates (left panel), and in polar ones (right panel), at the carrier frequency of the wave signal (i.e., $f = 1.0$ Hz). The SRPS is totally arranged on the k_ϑ axis. The propagation direction of the waves, along with the dispersion relation followed by the propagating waves, are properly detected.
The left panel of the Figure 5.19 shows the contour plot of the free surface elevation of the third test wave signal at a given time-step (i.e., $t = 0.02$ s).

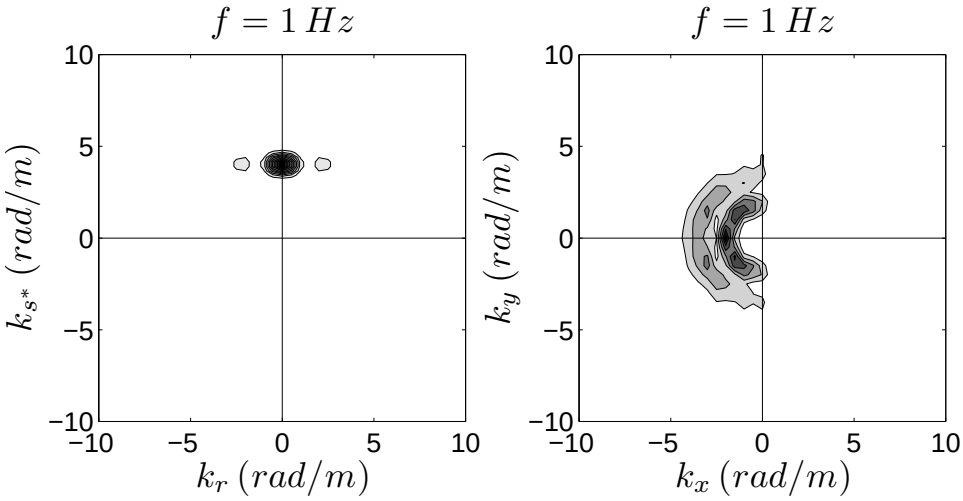

Figure 5.18: SPRS evaluated at the carrier frequency of the wave signal. Left panel: SPRS as a function of the wavenumber scalar components in cartesian coordinates. Right panel: SPRS as a function of the wavenumber scalar components in polar coordinates.

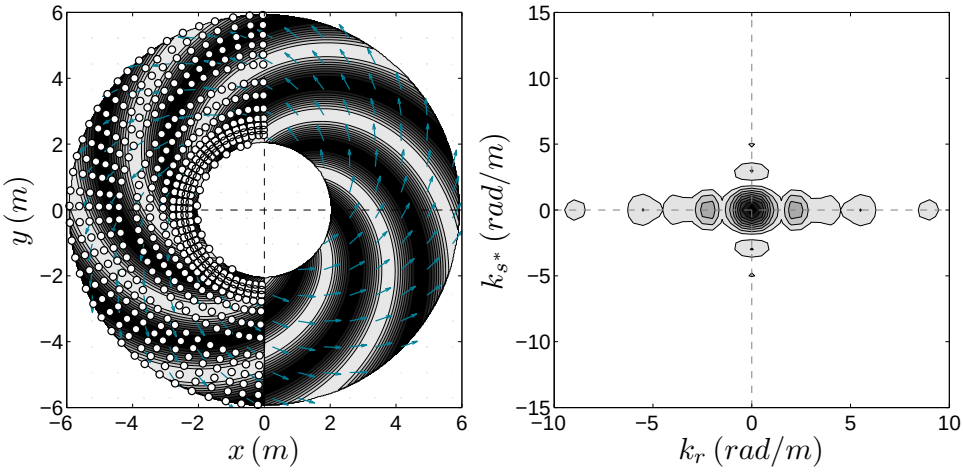

Figure 5.19: Left panel: contour plot of the free surface elevation at $t = 0.02$ s (partially radiated and partially trapped waves); white markers identify the sensors that form the array, while blue arrows identify the propagation direction of the waves. Right panel: ASF.

The propagation direction of the waves is identified by the blue arrows. In this case the waves are partially trapped and partially radiated, and propagate by following the dispersion relation (5.14). Figure 5.20 represents the

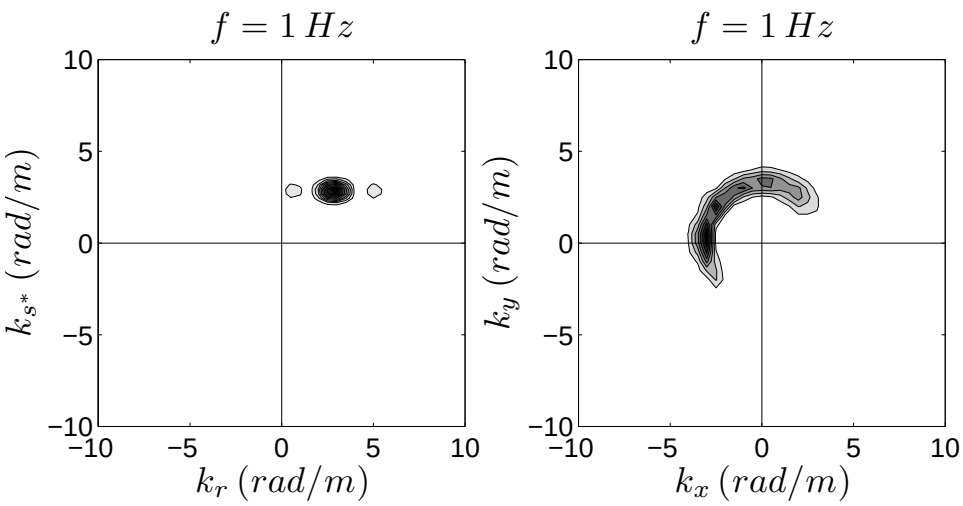

Figure 5.20: SPRS evaluated at the carrier frequency of the wave signal. Left panel: SPRS as a function of the wavenumber scalar components in cartesian coordinates. Right panel: SPRS as a function of the wavenumber scalar components in polar coordinates.

SRPS, evaluated in the wavenumber scalar components domain expressed both in cartesian coordinates (left panel), and in polar ones (right panel), at the carrier frequency of the wave signal (i.e., $f = 1.0$ Hz). The SRPS is placed in an intermediate position between the k_r axis and the k_ϑ one.
Thus, we show that if a reference frame expressed in polar coordinated is suitable (as for the physical model described in this work), it can be simple to estimate not only the dispersion relation followed by the propagating waves, but also the propagation direction of the waves evaluated with respect to the shoreline of the island itlself. This is very useful to assess if the propagating waves are radiated, trapped or both. In the following section a detailed application of the k-f is shown on the experimental data described in the chapter 4.

5.4 Results and discussion

5.4.1 The one-dimensional k-f

The one-dimensional k-f has been applied to 11 run-up time series collected by the run-up gauges during the laboratory experiments (see Figure 5.21). Since 37 repetitions of the same experiment are available, this technique has been carried out for each repetition. Given that the experiment has a good repeatibility, the results of the one-dimensional k-f are almost identical. The Table 5.1 reports the position of each sensor; the curvilinear abscissa s, is defined as follows

$$s = r\,\theta, \tag{5.19}$$

where r is the radius of the island evaluated at the undisturbed water surface ($r = 2.05$ m) and θ is an angle that, moving away from the generation area ($\theta = 0°$), is measured counterclockwise.
The k-f has been applied to a portion of each time series of duration of 15 s. This is measured with respect to the beginning (t =0 s) of each experiment (i.e. few seconds before the impact of the landslide with the water). This has reduced the possibility that the spurious waves reflected at the tank walls could contaminate the analysis. The wavenumber resolution and Nyquist wavenumber are respectively equal to $\Delta k = 1.1584$ rad/m and $k_N = 7.0810$ rad/m.
In the Figure 5.22 the results are shown. The contour lines and the color map represent the SRPS. To help the interpretation several theoretical wave dispersion relations have been plotted on the figure. The two thick black lines represent the ones of the zero and first order edge waves modes, ac-

cording to *Ursell* [1952]:

$$\omega^2 = g\,k \sin\left[(2n+1)\,\beta\right], \tag{5.20}$$

where $n = 0,\ 1$, is the order of the edge waves mode and β is the slope of the bottom. The Stokes edge waves mode corresponds to $n = 0$. It is worth to cite that (5.20) is valid if $(2n+1)\beta \leq \frac{1}{2}\pi$. The upper line represents the 1st-order, while the lower one the 0th-order. The thin black line represents the 0st-order edge waves mode, obtained by *Smith and Sprinks* [1975], when a curvilinear shoreline is considered:

$$\omega^2 = g\,k \tan\beta \left[1 - \frac{1}{4}(k\,r_s)^{-1}\right]^2, \tag{5.21}$$

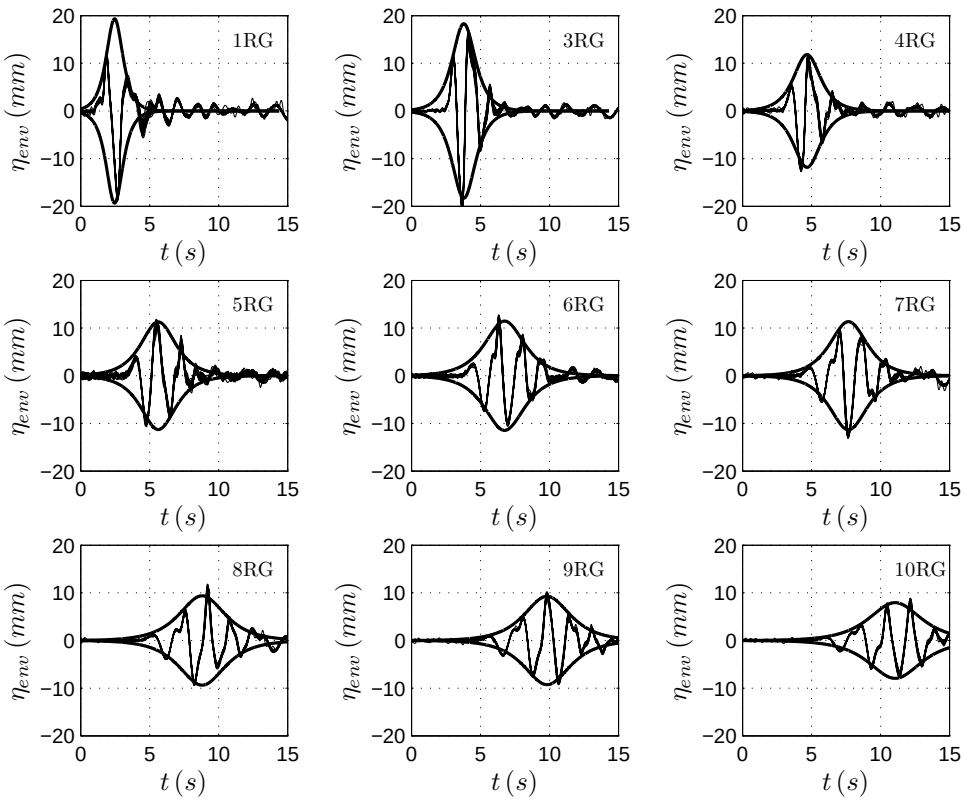

Figure 5.21: Run-up time series (thin black lines) for nine wave gauges (from the top to the bottom). Each panel contains several run-up time series (one for each repetition of the same experiment). The envelopes (thick black line), obtained for each run-up gauge, are also proposed in each plot.

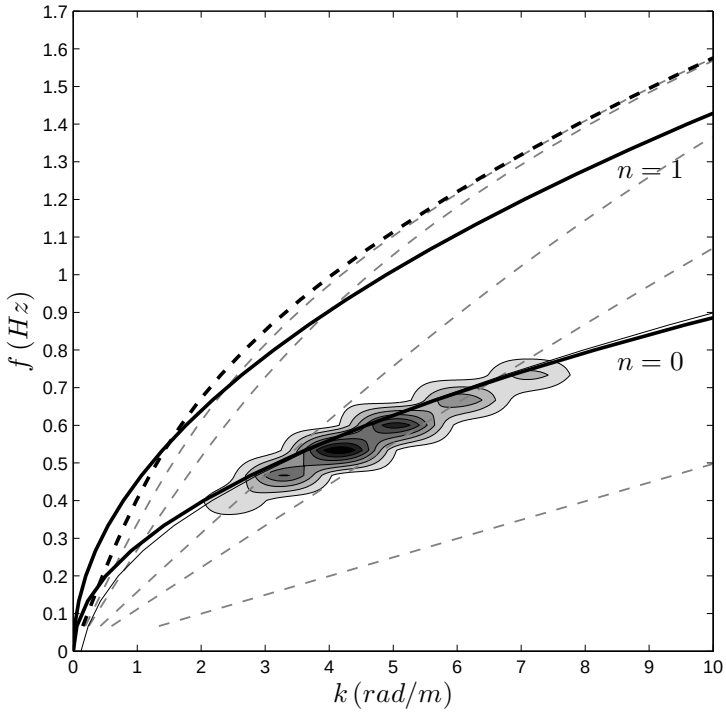

Figure 5.22: Steered response power spectrum obtained by means of the one-dimensional k-f analysis and several dispersion relations (black dashed line: linear waves for $h = 0.8$ m; upper thick black line: 1st-order edge waves; lower thick black line: 0th-order edge waves; thin black line: 0th-order edge waves for curvilinear shoreline; gray dashed lines: linear waves for different values of water depth).

where r_s is the radius of the island evaluated at the shoreline. For this experimental conditions (i.e., angle of the slope, radius of the shoreline, etc.) the (5.20) and the (5.21) provide very similar results; however, a small difference, especially for low frequencies, exists. The dashed gray lines identify the dispersion relation as from the linear wave theory:

$$\omega^2 = g\,k \tanh(kh)\,. \tag{5.22}$$

The water depth h, appearing into the (5.22), has been varied in the range between 0.01 m and 0.8 m. The dashed black line represents the limit of h = 0.8 m.

The results presented in the figure suggest that the analyzed run-up time series contain waves following the 0th-order edge waves dispersion relation. None of the other theoretical functions seem to adequately match with the experimental data. In order to explore the possibility that smaller energy

waves exist, we have also examined the small energy values of the power spectrum. However no other edge waves modes, nor waves following the (5.22) seem to exist in the records. Thus it seems reasonable to state that waves travel around the island as a 0th-order edge waves packet. This is consistent with previous researches (e.g. *Chang* [1995], *Liu et al.* [1998], *Lynett and Liu* [2005]).

The k-f allows to easily estimate the range of both wavenumbers and frequencies that dominate the measured signals. Wavenumbers appear to be in the range from 2.0 rad/m to 7.0 rad/m, while frequencies vary from 0.4 Hz to 0.7 Hz. Maximum values of energy are identified approximately at a wavenumber of 4.3 rad/m and at the frequency of 0.5 Hz. The peak wave length is therefore of 1.46 m while peak period is 2 s.

Once verified that the waves propagate around the island as a 0th-order edge waves packet, it is interesting to check if the celerity of the measured waves follows the (5.20). Both the phase and group celerities are considered. The phase celerity describes the velocity at which each single wave propagates. From a technical point of view it is useful to estimate the time taken by the tsunami to give the first inundation at any point along the coast. But the first wave, in the far field, is not the one that gives the maximum inundation, given the frequency dispersion. The waves travel as a packet (or a group), and the maximum inundation is given by the wave at the center (i.e. at the crest) of the group. The velocity at which the crest of the group propagates is the group celerity, that is therefore a quantity of special practical interest. The theoretical phase (c) and group (c_g) celerities can be obtained from the equation (5.20), considering that $c = \omega/k$, and $c_g = d\omega/dk$:

$$c = \frac{g}{\omega} \sin\left[(2n+1)\beta\right] \tag{5.23}$$

$$c_g = \frac{c}{2}. \tag{5.24}$$

In order to calculate these quantities it is fundamental to estimate the angular frequency ω of the carrier wave of the packet; this may differ from gauge to gauge. A standard spectral analysis has therefore been applied to all the run-up records to calculate the mean frequency. The spectral amplitudes are plotted against the frequency in Figure 5.23 using thin black lines. Each line refers to one single repetition of the experiment. In the same figure the averaged value (i.e., averaged over all the repetitions) of the mean frequency, has been marked for each run-up gauge using gray dashed lines, and are reported in the Table 5.1. These mean frequencies have been used to calculate one single value of ω for each run-up gauge.

In order to calculate the phase celerity from the experimental data, the run-up time series have been processed using a standard zero-up crossing method to identify each single wave. Then it has been calculated the time taken by the crest of the first three waves to propagate from gauge to gauge. Given that the distance between the gauges is known, it has been possible to calculate the phase celerity of these waves. The results are reported in the left panel of the Figure 5.24, using gray circles for the first wave, gray square markers for the second wave and gray diamonds for the third wave. Note that the estimated values of c (respectively c^*_{1w}, c^*_{2w} and c^*_{3w}) are considered to be valid between the two gauges used for the calculation, so in the figure the markers have been placed at an intermediate position of each couple of neighbouring gauges. At the first run-up gauge only two waves have been identified in the packet.

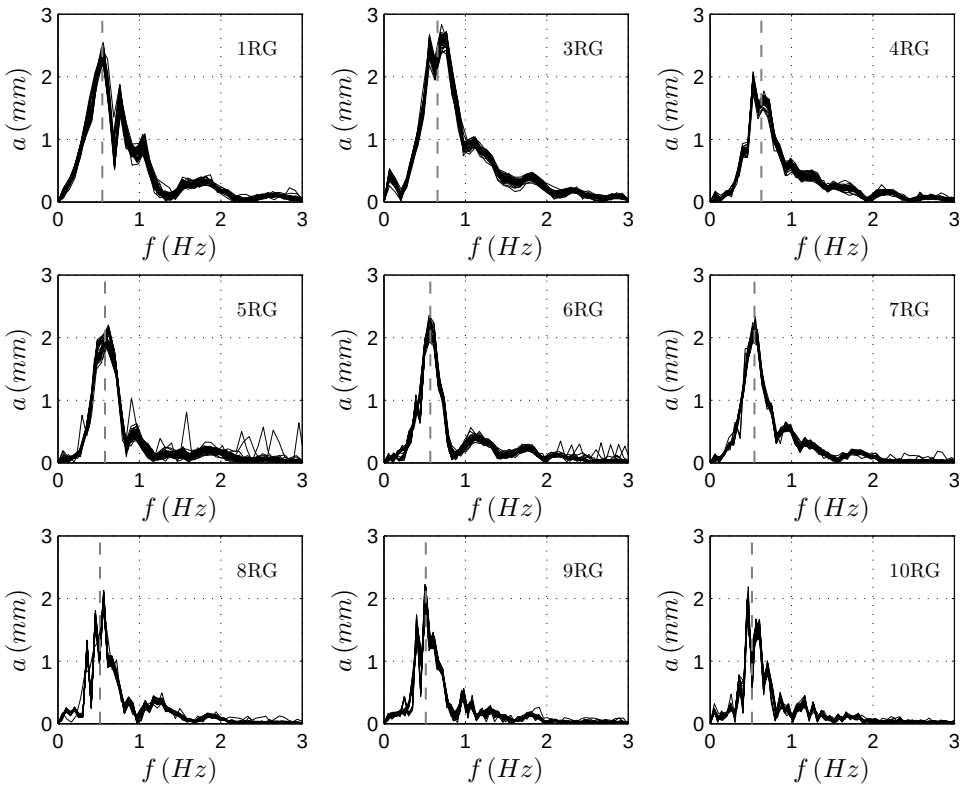

Figure 5.23: Wave spectral amplitudes (thin black lines) for nine wave gauges (from the top to the bottom). Each panel contains several spectral amplitudes (one for each repetition of the same experiment). In each panel the averaged values of the mean frequency (averaged over all the repetitions), are marked by the dashed lines.

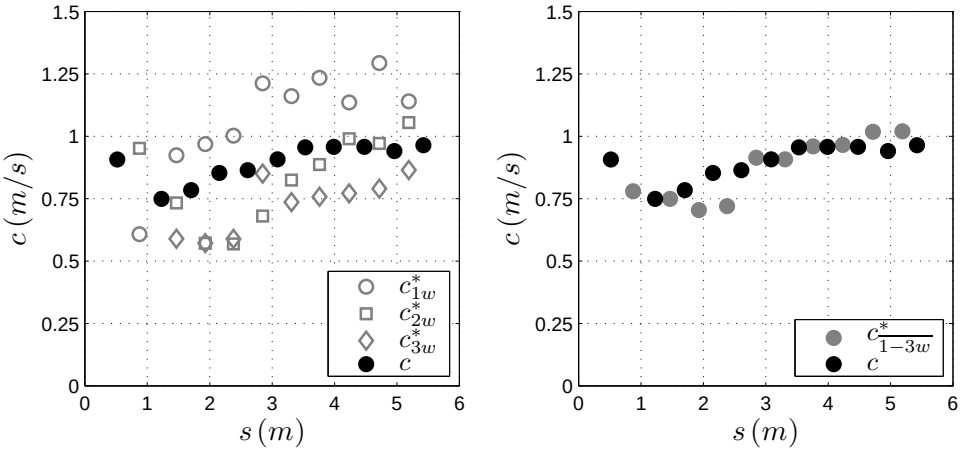

Figure 5.24: Left panel: Comparison between the theoretical phase celerities (black dot markers) and the estimated ones (gray markers) of the first three waves. Right panel: Comparison between the theoretical edge waves celerities (black dot markers) and the mean values (evaluated at an intermediate position of each couple of neighbouring gauges) of the estimated celerities of the first three waves (gray dot markers). Note: The overlined symbols in the legend are mean values.

The theoretical edge waves celerity has been calculated applying equation (5.23) at each gauge, using the value of ω calculated by using the carrier frequency f reported in the Table 5.1. It has to be mentioned that by using the peak frequencies, instead of the mean ones, similar wave celerities can be obtained. These celerities are plotted both in the left and in the right panels of the Figure 5.24 using black dot markers. Of course from the (5.23) only one single value of c is obtained for each gauge. Considering that the mean value $\overline{c}$ (averaged over the all gauges) of the theoretical phase celerities c is equal to 0.894 m/s, it appears that the equation (5.23) is able to give a reasonable estimate of the mean values (averaged over all the intermediate positions between two adjacent gauges) of the experimental phase celerities of the first three waves, since these are respectively equal to $\overline{c^*_{1w}} = 1.068$ m/s, $\overline{c^*_{2w}} = 0.823$ m/s and $\overline{c^*_{3w}} = 0.724$ m/s.
Furthermore, in order to better evaluate the agreement between the experimental and the theoretical results, the mean phase celerities $c^*_{\overline{1-3w}}$, calculated for each intermediate position between two adjacent gauges by averaging the experimental celerities of the first three waves, are plotted in the left panel of the Figure 5.24 with gray dot markers. The mean value $\overline{c^*_{\overline{1-3w}}}$ (averaged over all the intermediate positions between two adjacent gauges)

Gauge name	Angular position θ (°)	Curvilinear abscissa s (m)	a_{env} (mm)	Ω (rad/s)	t_0 (s)	Carrier freq. f (Hz)
1R	14.5	0.5188	19.34	1.83	2.46	0.544
3R	34.3	1.2272	18.31	1.32	3.79	0.658
4R	47.6	1.7031	11.83	1.13	4.67	0.629
5R	60.24	2.1539	11.29	0.88	5.62	0.578
6R	72.9	2.6083	11.46	0.77	6.74	0.570
7R	86.3	3.0877	11.34	0.82	7.68	0.544
8R	98.7	3.5314	9.37	0.67	8.80	0.517
9R	111.5	3.9894	9.27	0.67	9.83	0.515
10R	125.2	4.4796	7.94	0.59	11.06	0.515
11R	138.6	4.9590	6.56	0.41	12.19	0.524
12R	151.6	5.4241	7.34	0.47	13.43	0.512

Table 5.1: Position and wave parameters at each run-up gauge.

of the $c^*_{\frac{}{1-3w}}$ is equal to 0.8739 m/s. The right panel of the Figure 5.24, and the mean values of the two set of data ($\overline{c} = 0.894$ m/s, $c^*_{\frac{}{1-3w}} = 0.8739$ m/s), confirm that the equation (5.23) provides a good estimate of the experimental phase celerity, at least in a mean sense.
As far as the group celerity is concerned, the run-up time series have been processed in order to calculate the envelopes of the wave packets. These have been obtained using a procedure similar to that used by *Di Risio et al.* [2009b]. It is assumed that the envelopes are described by the following function

$$\eta_{\text{env}}(t) = a_{\text{env}} \operatorname{sech}\left[\Omega(t - t_0)\right], \tag{5.25}$$

where η_{env} is the time series of the wave envelope, a_{env} its amplitude, Ω is an angular frequency and t_0 the instant at which the maximum of the wave envelope occurs at each gauge. Note that also a numerical procedure, like the Hilbert transform, can be suitable to describe the wave envelopes. However, an analytical function, based on the hyperbolic secant (as described by *Di Risio et al.* [2009b] and by *Yeh* [1985]), allows to easily define the meaning and the value of the group celerity. The unknown parameters (i.e. a_{env}, Ω, t_0) have been obtained by means of the Gauss-Newton non linear optimization method, by using the whole set of experimental time series for each gauge. The results are reported in the Table 5.1 and the envelopes at each gauge have been plotted using thick solid lines in the Figure 5.21.

Once the parameter t_0 is known at each gauge, it is possible to calculate the group celerity. This is the ratio of the distance between each gauge and

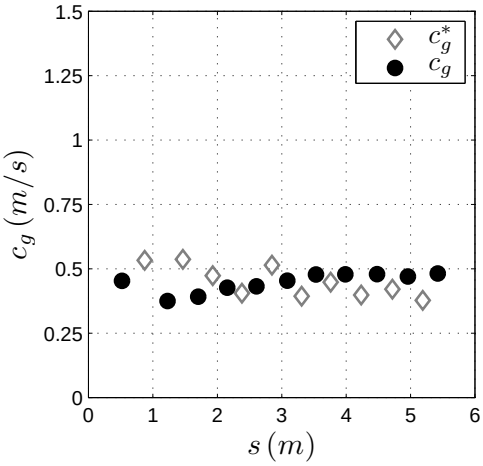

Figure 5.25: Comparison between the theoretical group celerities (black dot markers) and the estimated ones (gray diamond markers).

the time taken for the crest of the group to travel from one gauge to the next one. The results (c_g^*) are represented in the Figure 5.25 using gray diamonds. The edge waves theoretical c_g has been calculated at each gauge and the values plotted in the same figure using black dots. It appears that a very good agreement between the laboratory results and the theoretical values is obtained. It is also evident that the group celerity does not vary significantly during the propagation around the island.
It is worth to stress that also the mean values of the group celerity have been calculated. The mean value $\overline{c_g}$, averaged over all the run-up gauges, of the group celerities, obtained by the (5.20), is equal to 0.447 m/s, while the mean value $\overline{c_g^*}$ of those obtained from the experimental results is 0.450 m/s. This result implies that the knowledge of the carrier frequency f of the wave packet (and consequently of the ω) allows to calculate a quite accurate estimate of the group celerity of the packet itself by using the (5.20).

5.4.2 The two-dimensional k-f

The two-dimensional k-f has been applied four times, by using each time a different array geometry. In the Figure 5.26 the results are presented. In the left panels of the figure the four arrays of sensors used are indicated. These are identified by the black full markers, while the remaining ones (not used) are identified by the black empty markers.

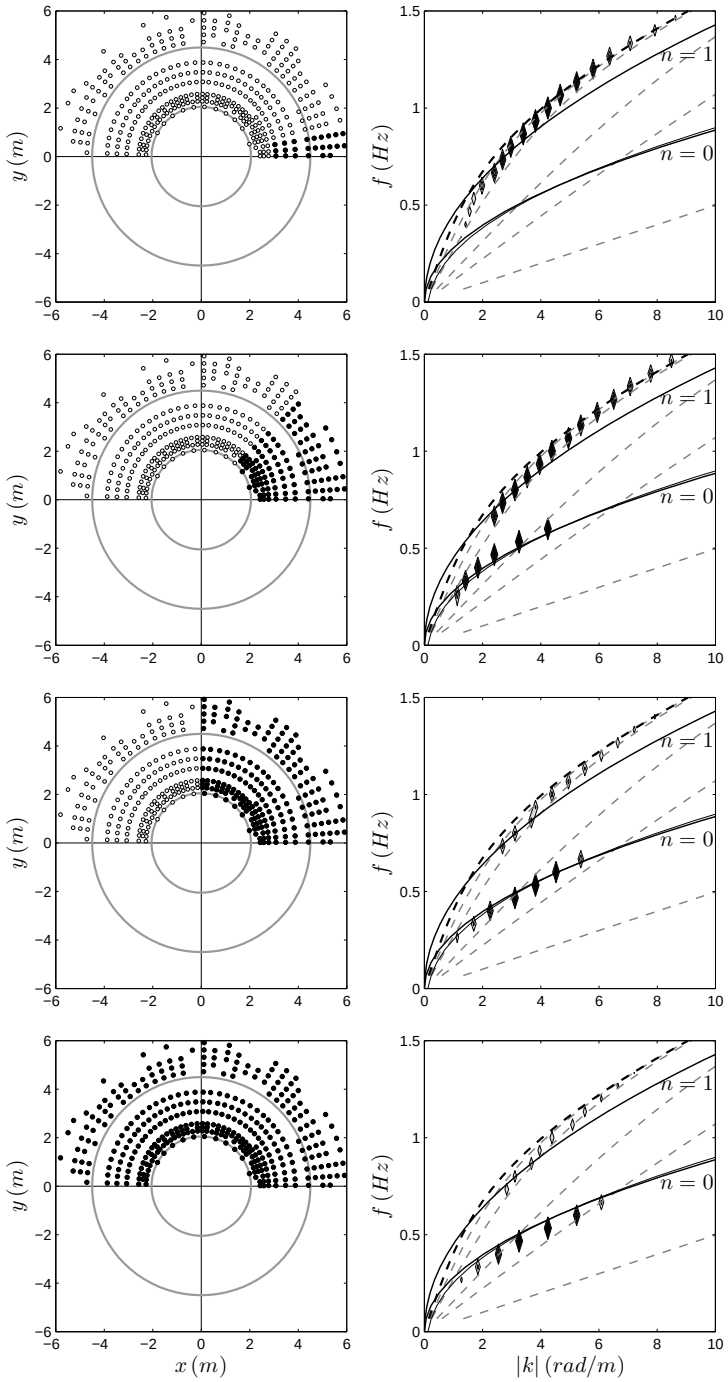

Figure 5.26: Left panels: Sketch of the used sensors for the two-dimensional k-f analysis. Right panels: Synthetic steered response power spectrum obtained for the four array geometries. Note: The line styles of the dispersion relations plotted are the same of those described in Figure 5.22.

The Figure 5.26 shows, starting from the top, that we used a larger number of sensors as moving away from the generation area (i.e. as the angle θ increases). In the right panels of the Figure 5.26 the synthetic SRPS (i.e., S-SRPS) obtained from each array geometry is represented in the k-f plane. It is important to recall that in order to provide a synthetic representation of the SRPS in the wavenumber-frequency plane, since a two-dimensional k-f has been used, we consider the wavenumbers as absolute values and, consequently, we represent only the wavenumbers to which correspond the maximum value of the SRPS for each frequency. Note that only observing the SRPS for a given frequency, as shown later, information about directionality can be provided. Furthermore in all the plots are also represented the dispersion relations such as those described in the Figure 5.22.
The S-SRPS of the first array of sensors (i.e. first line of the Figure 5.26) shows that the tsunami waves propagate as free radiating waves. Most of the energy in the k-f plane is around the frequency of 1.0 Hz and along both the limit ($h = 0.80$ m) and intermediate waters dispersion relation. Since the gauges used are placed almost directly in front of the generation area, in a sector of 10° with the direction of the landslide, this result seems to be reasonable. In fact no trapped waves are expected to exist in this area.
In the second line of the Figure 5.26 an array that includes sensors placed up to $\theta = 45°$ is considered. For this particular array the S-SRPS shows at least two different systems of waves. Around a frequency of 0.5 Hz the 0th-order edge waves mode dominates the propagation mechanisms (this confirms the one-dimensional k-f). As the frequency increases other modes occur. At a frequency of about 0.7 Hz the 1st-order edge waves mode appear to become relevant. For frequencies greater than 1.2 Hz the energy in the k-f plane is located on the limit of the deep water waves, although if this energy is small in terms of magnitude.
The third line of the Figure 5.26 considers an array of sensors that covers one quarter of the island ($\theta = 90°$). In this case most of the energy of the S-SRPS is located around 0.5 Hz and is concentrated along the 0th-order edge waves dispersion relation. As the frequency increases 1st-order edge waves mode and free radiating waves occur, but the magnitudes of the S-SRPS for these modes are smaller than the values observed for the Stokes edge waves.
A similar result is shown in the fourth line of the Figure 5.26. In this case the whole set of measurements ($\theta = 180°$) has been used. These results suggest that as the distance from the generation area increases the propagation mechanisms are dominated primarily by the 0th-order edge waves mode and then by the 1st-order edge waves mode.

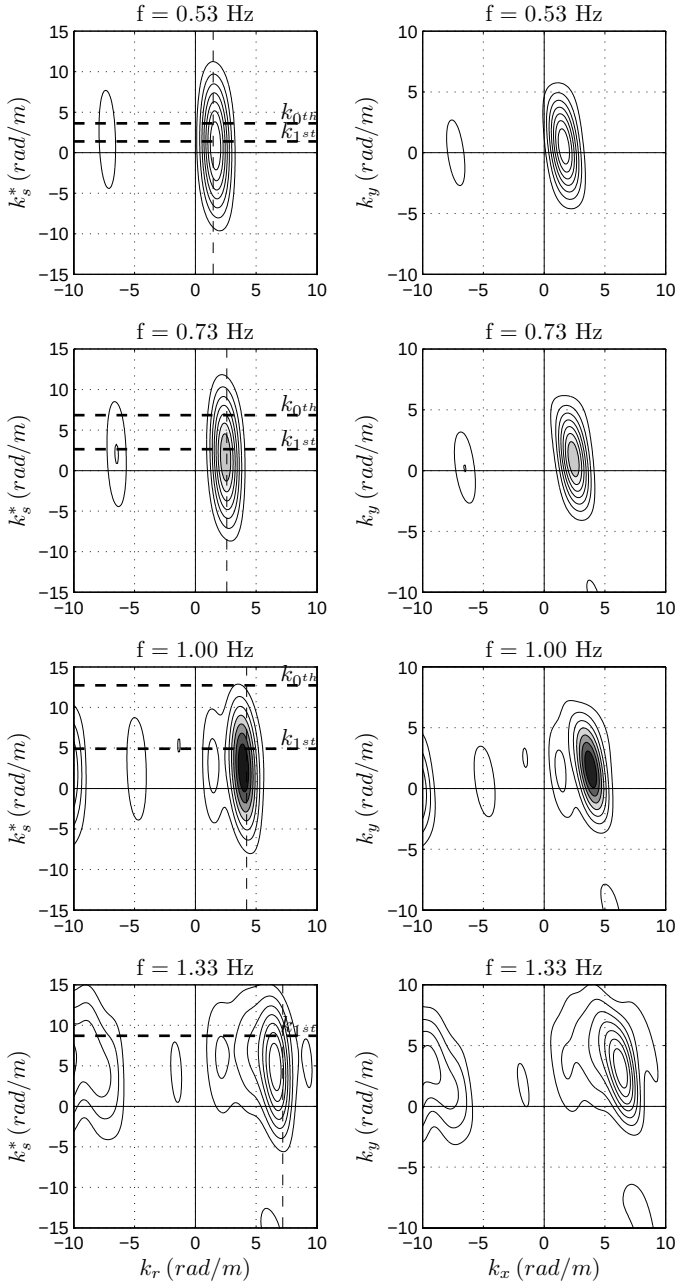

Figure 5.27: Steered response power spectra, obtained from the first array geometry, evaluated at four selected frequencies in the k_r-k_s^* plane (left panels) and in the k_x-k_y plane (right panels). Horizontal black dashed lines: alongshore wavenumbers of the 0th- and 1st-order edge waves. Vertical black thin dashed lines: radial wavenumbers as from the linear wave theory dispersion relation. Note: the same color scaling is used for all the plots.

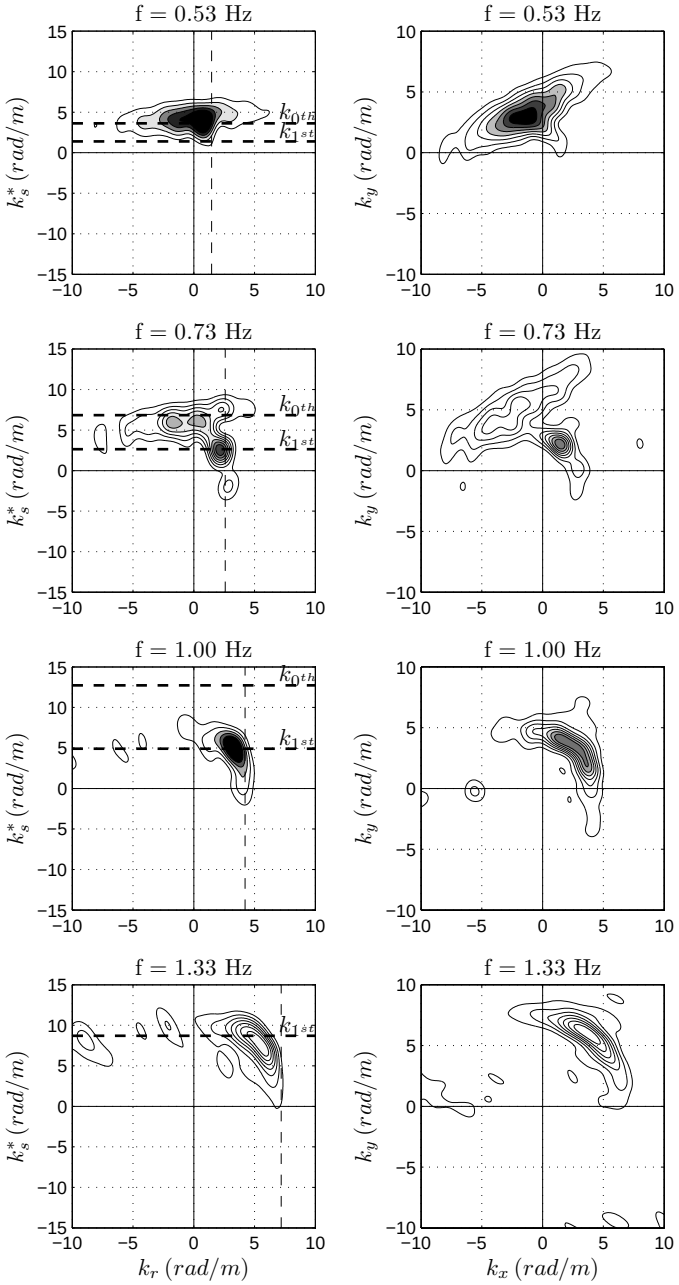

Figure 5.28: Steered response power spectra, obtained from the second array geometry, evaluated at four selected frequencies in the k_r-k_s^* plane (left panels) and in the k_x-k_y plane (right panels). Horizontal black dashed lines: alongshore wavenumbers of the 0th- and 1st-order edge waves. Vertical black thin dashed lines: radial wavenumbers as from the linear wave theory dispersion relation. Note: the same color scaling is used for all the plots.

This implies that most of the tsunami energy in proximity of the island remains trapped by the bathymetry, while free waves, radiating seaward, take place mostly in front of the generation area.
To better investigate the properties of the waves it is helpful to represent the SRPS, obtained from each specific array geometry, for some selected frequencies. For each frequency it is possible to evaluate the energy distribution, provided by the k-f, in the plane of the wavenumber scalar components (i.e. in the k_x-k_y plane if cartesian coordinates are considered or in the k_r-k_s^* plane if the polar coordinates are considered).
As discussed in Section 5.3.2, a reference frame expressed in polar coordinates (r,θ) appears useful to study the direction of propagation of the waves. Thus it is more convenient to express the vector wavenumber $\mathbf{k}$ not only in its scalar components expressed in cartesian coordinates ($\mathbf{k} = [k_x, k_y]$), but also in its scalar components expressed in polar coordinates ($\mathbf{k} = [k_r, k_\theta]$). In this way if, for a given frequency f_0, the SRPS is concentrated along the k_r axis, it implies that the waves, for that frequency, propagate along the radius (i.e. the wave fronts are locally perpendicular to the radius). Otherwise if the SRPS is concentrated along the k_θ axis it means that the waves, for that frequency, propagate rotating around the island (i.e. the wave fronts are locally parallel to the radius).
Furthermore by dividing the angular wavenumber k_θ by a specific radius r^* (for instance the radius of the shoreline) we obtain the new wavenumber k_s^*, defined as follows

$$k_s^* = k_\theta \frac{1}{r^*} = \frac{2\pi}{r^* \Theta}, \tag{5.26}$$

where Θ is an angular wavelength. This quantity is very helpful to compare the results of the k-f expressed in polar coordinates with the theoretical wavenumbers of the edge waves.
In the Figures 5.27, 5.28, 5.29 and 5.30 are represented the steered response power spectra evaluated at four selected frequencies (f = 0.53, 0.73, 1.00, 1.33 Hz), obtained from each array geometry presented in the Figure 5.26. The left panels of the figures show the SRPS in the k_r-k_s^* plane, while the right ones present the same quantity in the k_x-k_y plane.
The plots of the left panels of the Figure 5.27 show that for each frequency the energy distribution is mostly concentrated along the k_r axis. The two dimensional k-f, performed by using the sensors placed in front of the generation area, shows that the waves propagate mainly seaward. This is confirmed also by the plots of the right panels of the Figure 5.27; the SRPS is indeed located on an intermediate position between the coordinated axes.

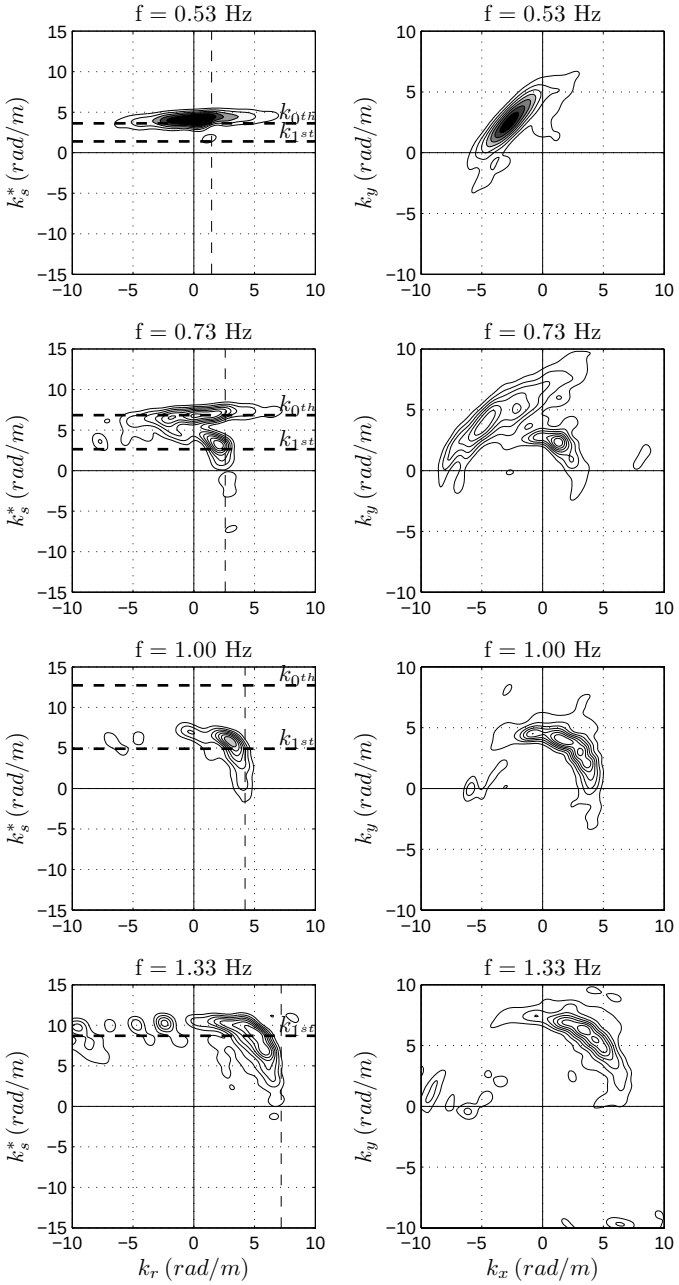

Figure 5.29: Steered response power spectra, obtained from the third array geometry, evaluated at four selected frequencies in the k_r-k_s^* plane (left panels) and in the k_x-k_y plane (right panels). Horizontal black dashed lines: alongshore wavenumbers of the 0th- and 1st-order edge waves. Vertical black thin dashed lines: radial wavenumbers as from the linear wave theory dispersion relation. Note: the same color scaling is used for all the plots.

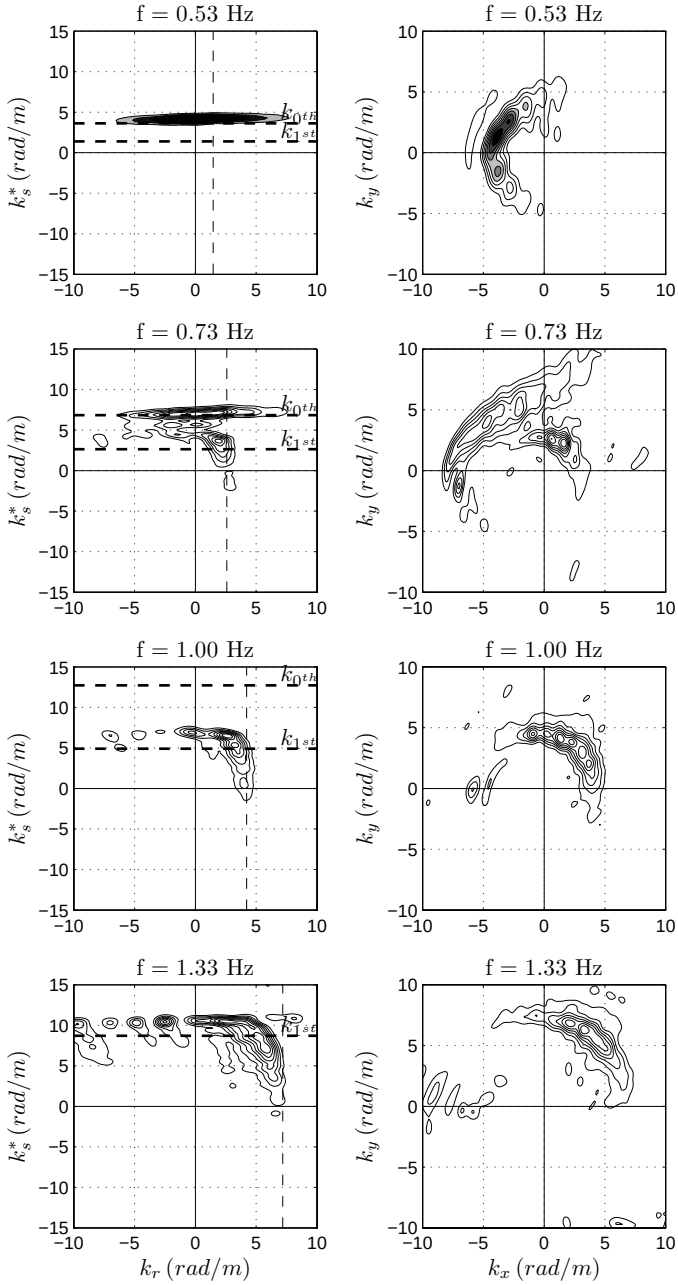

Figure 5.30: Steered response power spectra, obtained from the fourth array geometry, evaluated at four selected frequencies in the k_r-k_s^* plane (left panels) and in the k_x-k_y plane (right panels). Horizontal black dashed lines: alongshore wavenumbers of the 0th- and 1st-order edge waves. Vertical black thin dashed lines: radial wavenumbers as from the linear wave theory dispersion relation. Note: the same color scaling is used for all the plots.

Furthermore by observing the colours of the contour plot it is shown that the carrier frequency of the wave packet is about 1.0 Hz (third line of the figure). Moreover, for each represented frequency, the radial wavenumbers have been calculated by the (5.22), using a mean value of h, defined as the averaged value of the water depths related to the position of each sensor of the considered array. These are plotted in the left panels of the figure (vertical black thin dashed lines). It is worth to highlight that, for each plot of the figure, the radial wavenumber at which the maximum value of the SRPS occurs is in good agreement with the theoretical wavenumber obtained by the (5.22).
In the first line of the Figure 5.28 (left panel) the SRPS is located on the k_s^* axis. It implies that the waves, that have a carrier frequency of 0.53 Hz, propagate rotating around the island (i.e. wave fronts almost perpendicular to the shoreline). Furthermore on the same plot also the values of the theoretical alongshore wavenumber of both the 0th-order and the 1st-order edge waves modes are represented (horizontal black dashed lines). A good agreement exists between the wavenumber at which occurs the maximum value of the SRPS and the theoretical wavenumber of the 0th-order edge waves mode. In the second line of the Figure 5.28 (left panel) splitting of the SRPS occurs. The maximum value of the energy moves towards lower wavenumbers, however remains closer to the k_s^* axis than to the k_r one. Moreover the maximum of the SRPS is in good agreement with the theoretical wavenumber of the 1st-order edge waves mode for that frequency. This suggests that the waves, at a frequency of 0.73 Hz, propagate around the island mostly as a 1st-order edge waves packet. In the third line of the Figure 5.28 (left panel) the shape of the SRPS suggests a mixing of trapped and non-trapped modes. Although the maximum value of the SRPS is in good agreement with the theoretical wavenumber of the 1st-order edge waves it is reasonable to state that both trapped (i.e. 1st-order edge waves) and non-trapped modes (i.e. free radiating waves) exist. On the fourth line of the Figure 5.28 (left panel) the SRPS slowly shifts towards the k_r abscissa and its maximum value tends to not match with the 1st-order edge waves wavenumber for that frequency. The waves, which have a carrier frequency of 1.33 Hz, are not trapped by the bathymetry and propagate mainly in y direction as from the right panel of the fourth line of the Figure 5.28. Similar results are presented in the Figures 5.29 and 5.30 which show the SRPS obtained from the array geometry of the respectively third and fourth lines of the Figure 5.26. By observing the first line of both figures it is clear that the greater part of the energy is located along the k_s^* axis and the maximum values of the SRPS match very well with the theoretical wavenumbers of the

Stokes edge waves. These plots confirm that the propagation mechanisms, as the distance from the generation area increases, is dominated by the 0th-order edge waves.

Finally we present the Figure 5.31 to help the reading of the Figures 5.27, 5.28, 5.29 and 5.30, described earlier. For each frequency the maximum value of the SRPS has been identified; then by calculating the angle δ_{rs} between the scalar components (k_r-k_s^*) at which the maximum value occurs, it is possible to evaluate if that value is concentrated on the k_s^* axis or on the k_r one. If the angle δ_{rs} is equal to 0° it means that the maximum value of the SRPS for a given frequency is located on the k_r axis. Otherwise if the angle δ_{rs} is equal to 90° it implies that the maximum value of the SRPS is located on the k_s^* axis. Finally if the angle δ_{rs} takes the value of 45° it implies that the maximum value of the energy for that frequency is at an intermediate position between the two axes. By knowing the angle δ_{rs} for each frequency, and of course for each array geometry, it is possible to evaluate which spectral components of the tsunami are propagating alongshore ($\delta_{rs} = 90°$), seaward ($\delta_{rs} = 0°$) or both ($\delta_{rs} = 45°$).

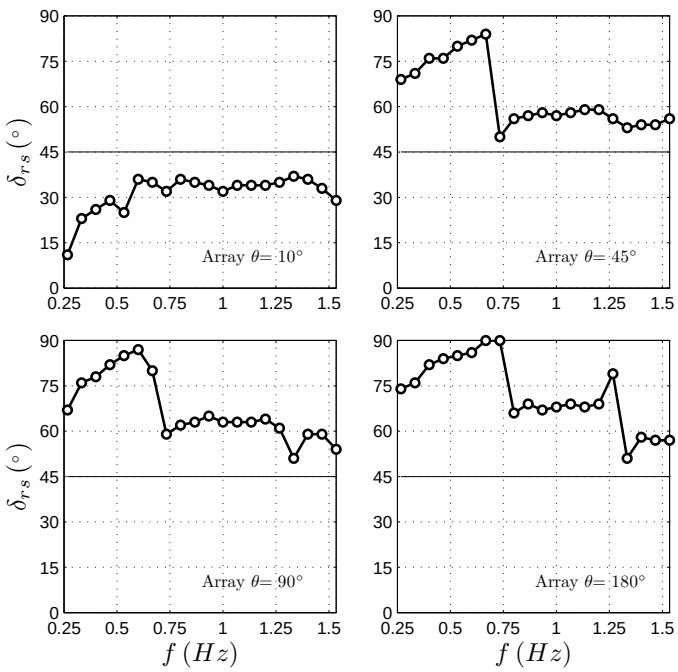

Figure 5.31: Measured angles δ_{rs}, frequency function, between the wavenumber scalar components (k_s^*-k_r) at which the maximum value of the SRPS occur at a given frequency.

5.5 Concluding remarks

The one-dimensional k-f has been applied to the run-up time series collected during the experiments by *Di Risio et al.* [2009b]. These refer to tsunamis generated by subaerial landslides along the flank of a conical island. The problem considered is similar to that involving flank instabilities at small volcanic islands like for example the Stromboli volcano, Italy [*Tinti et al.*, 2005, 2006; *Bellotti et al.*, 2009]. The k-f has revealed that the inundation of the coast is dominated by a 0th-order edge waves packet. This appears consistent with previous numerical results [*Lynett and Liu*, 2005], theoretical models [*Sammarco and Renzi*, 2008; *Tinti and Vannini*, 1995] and field measurements [*Gonzalez et al.*, 1995; *Neetu et al.*, 2011; *Yamazaki and Cheung*, 2011]. The maximum values of the wave energy are identified approximately at a wavenumber of 4.3 rad/m, i.e. at a wave length of 1.46 m; the peak frequency is of 0.5 Hz.
The theoretical frequency dispersion relation of the edge waves [*Ursell*, 1952] seems a reliable tool to estimate the celerity of propagation of the tsunamis along the coast. The phase and group celerity calculated using the experimental data has been compared with those from the edge waves theory. The agreement between measurements and theory is reasonable for the phase celerity. It is also to be considered that each wave of the tsunami packet propagates at its own celerity, while the dispersion relation provides one single value for the carrier wave of the group. The agreement of the group celerity appears very good. The edge waves theory can therefore be used to calculate the celerity of the waves along the coast once an estimate of the frequency of the tsunami is given. This can be done for instance by knowing the properties of the landslide (e.g. *Wiegel* [1955], *Watts* [1998], *Panizzo et al.* [2005a]) or by detecting in real-time the tsunami waves by means of a authomatic algorithms (e.g., *Beltrami and Di Risio* [2011]).
Moreover it is interesting to scale up the experimental results to one sample prototype scale. The physical model of the conical island [*Di Risio et al.*, 2009b] roughly represents, in a Froude law scale 1:1000, the Stromboly volcano cited before. This implies that in nature the tsunamis considered in the laboratory would have a wave length of about 1460 m and a wave period of 63 s; this appears consistent with the the 30 December 2002 landslide-induced tsunamis at Stromboli, as reported by *Tinti et al.* [2005]. The phase and group celerity at prototype scale would be of 28.3 m/s and 14.1 m/s respectively. At the island of Stromboli the distance, measured along the coast, between the unstable flank of the volcano and the inhabited area (considering an intermediate point in the NE coastal segment from Pizzillo

to Piscitá) is about 3.8 km. This implies that the first tsunami waves takes about 134 s to travel from the generation area to the inhabited area, while the maximum of the wave packet takes about 268 s. These results appear to be in qualitative agreement with those obtained by *Tinti et al.* [2006] on the basis of numerical computations.
Furthermore the two-dimensional k-f has been applied to the new measurements that have been collected by *Molfetta et al.* [2010]. Four different array geometries have been used to apply this technique. The results confirm that the 0th-order edge waves dominates the propagation mechanisms in a frequency range around to 0.5 Hz. The offshore gauges allow to observe that as the frequency reaches a value of about 0.7 Hz the 1st-order edge waves become relevant, and, as the frequency increases further ($f = 1.2$ Hz) non-trapped modes occur as well.
In conclusion, the k-f seems to be an helpful tool to identify the dispersion relation followed by the tsunami waves, especially when peculiar geometries of the problem are considered. The use of the one- and the two-dimensional k-f can provide a comprehensive overview of the propagation and trapping mechanisms and a quantitative estimate of both the wavenumbers and the frequencies involved.

Chapter 6

Numerical modelling of landslide-generated tsunamis: an inversion technique to improve tsunami early warning systems (TEWS)

6.1 Preface

In the previous chapters we focus our attention on the experimental study of the nearshore features of landslide-generated tsunamis that propagate around a conical island. In this chapter we focus on the numerical modelling of tsunami waves that radiate offshore and propagate for long distances.
As shown, we test a method for forecasting in real-time the properties of offshore propagating tsunami waves generated by landslides, with the aim of supporting tsunami early warning systems (TEWS). The method uses an inversion procedure, that takes as input data measurements of water surface elevation at a point close to the tsunamigenic source. The measurements are used to correct the results of precomputed numerical simulations, reproducing the wave field induced by different landslide scenarios. The accuracy of the method is evaluated using the results of laboratory experiments that are described in the work of *Di Risio et al.* [2009b]. Note that these experiments are partially the same of those described in chapters 3, 4 and 5.

In this chapter we investigate what is the optimal position where measure the tsunamis, and what are the effects, on the accuracy of the results, of uncertainties on the landslide scenarios. Finally the method is successfully tested using partial input time series, simulating the behaviour of the system in real-time when forecasts are updated, during the tsunami event, as the measurements become available. We refer to *Cecioni et al.* [2011] for further explanations.

6.2 Introduction

Tsunami inversion techniques are mainly used to reconstruct the properties of the tsunamigenic sources (i.e., coseismic displacement field, slip distribution along the seismic source, etc.) from tsunami records. Among the many previous studies it is worth to cite *Satake* [1987], *Johnson et al.* [1996], *Tinti et al.* [2006]. Most of these researches are based on numerical and analytical solutions of the linear shallow water equations, that are used to compute the propagation of the tsunami waves. To solve the inverse problem (i.e., assessing information on tsunamigenic source from tide-gauges records), different approaches, based on Green's function, have been used. Recently some successful attempts of using the inversion techniques to support in real time tsunami early warning systems have been carried out. *Wei et al.* [2003] show a method to determine the tsunami waveforms away from the generation area by processing real time water level records near the tsunamigenic source. Their method extends the previous works by using a long wave model to create a database of synthetic mareograms at a number of strategic locations. *Titov et al.* [2005] describe the tsunami forecast system adopted by Pacific Marine Environmental Laboratory. This system combines real time seismic and water level data with a forecast database of pre-computed scenarios. The method uses a set of unit sources for constructing a tsunami scenario. Both the inversion methods described earlier use of Green's function approach.
A different method for tsunami inversion has been proposed by *Bellotti et al.* [2008]. They use a numerical model based on the linearized mild-slope equation, solved in the frequency domain, able to reproduce the propagation of small amplitude tsunami waves. By using one possible scenario of the tsunamigenic source, the model solves the governing equations by providing the Fourier Transform of the free surface elevation. The inversion technique is applied when the surface elevation time series is recorded at some points of the computational domain. The comparison between the numerical pre-

computed solution and the Fourier Transform of the measured free surface elevation makes it possible to find in real-time a correction parameter in the complex plane, to be applied to each frequency component. Therefore, the method allows to compute the tsunami waveform at each point of the computational domain. By solving the model equations using a scenario of the tsunamigenic source, it is possible to obtain the solution in terms of the Fourier Transform of the free surface elevation. The comparison between the solution referring to the scenario and the Fourier Transform of the free surface elevation records, makes it possible to find in real time a complex correction term for each frequency component, and to forecast the tsunami waveform at any point of the computational domain. The procedure takes advantage of the fact that the model equations are linearized. Moreover the authors have investigated the influence of the length of the input free surface elevation time series using two-dimensional experimental data. By means of the analysis of results obtained using partial input time series, they show that the tsunami waveform forecasting is reliable when the first crest has been recorded, and that as the length of the available record increases, the results converge smoothly to the final one.

In this chapter we investigate how the model developed by *Bellotti et al.* [2008], with further improvements by *Cecioni and Bellotti* [2010a, b], can be applied to support in real-time a landslide-tsunami early warning system, aimed at protecting coasts far away from a potential landslide tsunamigenic source, i.e. the flank of an island, not focussing on the coast of the island itself. The idea of a landslide-tsunami warning system is that devices for the measurement of landslide generated tsunamis are placed close to the possible tsunamigenic area. When a landslide event occurs, records of water surface level are processed in real-time to forecast, at some offshore location, the features of the tsunami, in order to decide if the tsunami alarm has to be spread or not. To test the applicability of the model and to measure the accuracy of the procedure we use, as reference data, the experimental results of *Di Risio et al.* [2009b], who reproduced tsunamis generated by landslides at the flank of a circular island.

This chapter is structured as follows. The next two sections give a brief description of the numerical and the physical models respectively. Then the results of the inversion procedure applied on the experimental data are shown, along with an investigation on where it is better to locate the sea level recorder device, and an evaluation of the effects of uncertainties on the landslide scenario. Discussion of the results and conclusions close the chapter.

6.3 Description of the numerical model

The numerical model is that proposed by *Bellotti et al.* [2008], which solves the linearized mild-slope equation (MSE hereinafter). In the following, we quote the exhaustive description of the model equations that *Bellotti et al.* [2008] and *Cecioni and Bellotti* [2010b] have provided.
The above mentioned authors showed that the model equation can be obtained starting from the linear (small amplitude) water wave equations for an incompressible irrotational fluid on an uneven bottom

$$\nabla_h^2 \phi + \phi_{zz} = 0 \qquad -h(x,y,t) < z < 0 \tag{6.1}$$

$$\phi_z + \frac{1}{g}\phi_{tt} = 0 \qquad z = 0 \tag{6.2}$$

$$\phi_z + h_t + \nabla_h \phi \cdot \nabla_h h = 0 \qquad z = -h(x,y,t), \tag{6.3}$$

where $\phi(x,y,z,t)$ is the velocity potential in the fluid, $h(x,y,t)$ is the water depth, defined as the fixed sea floor depth minus the landslide thickness, $h(x,y,t) = h_f(x,y) - h_l(x,y,t)$. g is the gravity acceleration, while ∇_h is the differential operator which means the divergence in the horizontal coordinates (x,y) and the symbol $\cdot$ stays for the scalar product. All these variables are real and scalar. equation (6.1) is the Laplace equation, equation (6.2) includes the dynamic and kinematic boundary conditions at the free water surface, while equation (6.3) is the bottom boundary condition which reproduces the sea floor movements allowing h to varies in time. *Cecioni and Bellotti* [2010b] followed the procedure described by *Svendsen* [2006], who starts from the Laplace equation and the free surface and bottom boundary conditions to derive the MSE, with the difference that here we take into account a moving sea floor. The solution of the given problem is assumed to be of the form

$$\phi(x,y,z,t) = \varphi(x,y,t)\, f(z) \tag{6.4}$$

where $\varphi(x,y,t)$ is the velocity potential at the undisturbed free water surface $z = 0$, which can be complex and it includes the effects of reflected waves; $f(z)$ is a function that describes how the kinematic field varies along the water depth and can be chosen as that resulting from the linear wave theory valid for harmonic waves propagating in constant depth, which however still holds locally for uneven bottom, i.e.

$$f(z) = \frac{cosh\left[k\left(h_f + z\right)\right]}{cosh\left(kh_f\right)} \tag{6.5}$$

where k is the wave number, defined as $2\pi/L$ with L the wave length. In the cases of not constant depth, h_f and therefore k vary with the horizontal coordinates, therefore $f = f(x, y, z)$. However if the mild-slope assumption $\frac{\nabla_h h_f}{k h_f} << 1$ is here introduced the variation of the function f with the horizontal coordinates can be neglected if compared with the vertical one. From the assumption (6.4) it comes that

$$\phi_{zz} = k^2 \varphi \frac{cosh\left[k\left(h_f + z\right)\right]}{cosh\left(k h_f\right)} = k^2 \phi \tag{6.6}$$

therefore the Laplace equation (6.1) can be written as

$$\nabla_h^2 \phi + k^2 \phi = 0 \tag{6.7}$$

The following considerations are made:

$$f(z) = 1 \qquad at \quad z = 0 \tag{6.8}$$

$$f_z = k\ tanh\left(k h_f\right) = \frac{\omega^2}{g} \qquad at \quad z = 0; \tag{6.9}$$

$$f_z = 0 \qquad at \quad z = -h; \tag{6.10}$$

In order to depth integrate the field equation (Laplace equation 6.1), here it is made use of the Gauss's Theorem, which states for one dimensional domain

$$\int_a^b \frac{\partial \overrightarrow{v}}{\partial x} dx = \overrightarrow{v}(b) - \overrightarrow{v}(a) \tag{6.11}$$

where $\overrightarrow{v}$ is a differentiable vector field. By considering a special vector field defined as $\overrightarrow{v} = \phi_1 \nabla \phi_2$, where ϕ_1 and ϕ_2 are arbitrary differentiable scalar functions, the Gauss theorem can be written as

$$\int_a^b \left[\phi_1 \frac{\partial^2 \phi_2}{\partial x^2} + \frac{\partial \phi_1}{\partial x}\frac{\partial \phi_2}{\partial x}\right] dx = \left[\phi_1 \frac{\partial \phi_2}{\partial x}\right]_b - \left[\phi_1 \frac{\partial \phi_2}{\partial x}\right]_a \tag{6.12}$$

Equation 6.12 is known as Green's theorem. Interchanging ϕ_1 and ϕ_2 and subtracting the resulting equation from (6.12) gives

$$\int_a^b \left[\phi_1 \frac{\partial^2 \phi_2}{\partial x^2} - \phi_2 \frac{\partial^2 \phi_1}{\partial x^2}\right] dx = \left[\phi_1 \frac{\partial \phi_2}{\partial x} - \phi_2 \frac{\partial \phi_1}{\partial x}\right]_a^b \tag{6.13}$$

For the present purpose equation 6.13 is used with $x = z$, $\phi_1 = f(z)$ and $\phi_2 = \phi(x, y, z, t)$, therefore

$$\int_{-h}^{0} \left(f \frac{\partial^2 \phi}{\partial z^2} - \phi \frac{\partial^2 f}{\partial z^2} \right) dz = \left[f \frac{\partial \phi}{\partial z} - \phi \frac{\partial f}{\partial z} \right]_0 - \left[f \frac{\partial \phi}{\partial z} - \phi \frac{\partial f}{\partial z} \right]_{-h} \tag{6.14}$$

Substituting the Laplace equation (6.1) in the first term at the left hand side (LHS), and the boundary conditions at $z = 0$ and $z = -h$ (6.2 and 6.3) and using Eqs. (6.9, 6.10) in the right hand side (RHS) terms, then, after changing the sign, equation (6.14) becomes

$$\int_{-h}^{0} \left(f \nabla_h^2 \phi + k^2 f \phi \right) dz = \frac{1}{g} \varphi_{tt} + \varphi \frac{\omega^2}{g} - [f h_t]_{-h} - [f \nabla_h h \cdot \nabla_h \phi]_{-h} \tag{6.15}$$

the LHS can be seen as the integration over the depth of the field equation. Considering that

$$\nabla_h \phi = \nabla_h (\varphi f) = f \nabla_h \varphi + \varphi \nabla_h f \tag{6.16}$$

and

$$\nabla_h^2 \phi = f \nabla_h^2 \varphi + 2 \nabla_h \varphi \cdot \nabla_h f + \varphi \nabla_h^2 f \tag{6.17}$$

using the expression (6.16) for the last term of the RHS and expression (6.17) for the first term of the LHS, equation (6.15) becomes

$$\begin{aligned} &\textstyle\int_{-h}^{0} \left(f^2 \nabla_h^2 \varphi + 2 f \nabla_h f \cdot \nabla_h \varphi + f \varphi \nabla_h^2 f + k^2 f^2 \varphi \right) dz = \\ &\textstyle\frac{1}{g} \left(\varphi_{tt} + \omega^2 \varphi \right) - \frac{1}{cosh(kh_f)} h_t - [f \nabla_h h \cdot (f \nabla_h \varphi + \varphi \nabla_h f)]_{-h} \end{aligned} \tag{6.18}$$

Now incorporating the first two terms of the LHS of equation (6.18) follows

$$\begin{aligned} &\textstyle\int_{-h}^{0} \nabla_h \cdot \left(f^2 \nabla_h \varphi \right) dz + \left[f^2 \nabla_h h \cdot \nabla_h \varphi \right]_{-h} + \varphi k^2 \int_{-h}^{0} f^2 dz = \\ &\textstyle- \int_{-h}^{0} \varphi f \nabla_h^2 f dz - \frac{1}{cosh(kh_f)} h_t - \varphi \nabla_h h \cdot [f \nabla_h f]_{-h} + \frac{1}{g} \left(\varphi_{tt} + \omega^2 \varphi \right) \end{aligned} \tag{6.19}$$

Applying the Leibniz's rule for the first two terms on the LHS and knowing that

$$\int_{-h}^{0} f^2 dz = \frac{c c_g}{g} \tag{6.20}$$

where c and c_g are respectively the phase and the group velocities, by multiplying equation (6.19) for g it results

$$\begin{aligned} &\nabla_h \cdot (c c_g \nabla_h \varphi) + \varphi k^2 c c_g - \varphi_{tt} - \omega^2 \varphi + h_t \tfrac{g}{cosh(kh_f)} = \\ &- g \varphi \{ \textstyle\int_{-h}^{0} f \nabla_h^2 f dz + \nabla_h h \cdot [f \nabla_h f]_{-h} \} \end{aligned} \tag{6.21}$$

Rigorously the identity of equation (6.20) is obtained for a single frequency of the wave spectrum, consequently equation (6.21) is valid for monochromatic waves, or can be seen as representative of narrow banded spectra sea state around a carrying frequency. The RHS terms of equation (6.21) can be shown to be $O\left((\nabla_h h)^2, \nabla_h^2 h\right)$. Therefore, as *Cecioni and Bellotti* [2010b] introduced the mild slope assumption above, i.e.: by allowing equation 6.5, $\nabla_h h \ll kh$ and it can be argued that the RHS terms $\ll$ LHS terms. Similarly, $\nabla_h^2 h \ll \nabla_h h$, which is a natural additional assumption because $\nabla_h^2 h = O(\nabla_h h)$ can only occur over short distances without changing $O(\nabla_h h)$. This means that the RHS terms are $\ll$ of all the others terms, we therefore get

$$\varphi_{tt} - \nabla_h \cdot (cc_g \nabla_h \varphi) + \left(\omega^2 - k^2 cc_g\right)\varphi = -\frac{g}{cosh\,(kh_f)} h_t \tag{6.22}$$

which is the hyperbolic version of the MSE in terms of fluid velocity potential and is usually referred to as the 'time-dependent mild-slope equation', allowing the simulation in the time-domain of the wave propagation. To obtain the MSE in terms of the free surface elevation η, equation (6.25) needs to be differentiated with respect to time.

$$\varphi_{ttt} - \nabla_h \cdot (cc_g \nabla_h \varphi_t) + \left(\omega^2 - k^2 cc_g\right)\varphi_t = -\frac{g}{cosh\,(kh_f)} h_{tt} \tag{6.23}$$

and then use the dynamic boundary condition at the free surface

$$\eta = -\frac{1}{g}\varphi_t \tag{6.24}$$

from which we obtain that $\varphi_t = -g\eta$ and $\varphi_{tt} = -g\eta_t$, those expressions can be substituted into equation (6.23) to get, after dividing by g, the hyperbolic form of MSE, in time domain and in terms of free surface elevation $\eta\,(x, y, t)$:

$$-\eta_{tt} + \nabla_h \cdot (cc_g \nabla_h \eta) - \left(\omega^2 - k^2 cc_g\right)\eta = -\frac{1}{cosh\,(kh_f)} h_{tt}, \tag{6.25}$$

where c and c_g are the phase and group celerities respectively, k is the wave number and ω is the angular frequency. Note that if the phase and group velocities are evaluated in the shallow water limit as $c = c_g = \sqrt{gh}$, then equation (6.25) reduces to the governing equation for forced long waves

$$\eta_{tt} - \nabla_h \cdot (gh \nabla_h \eta) = \frac{1}{cosh\,(kh_f)} h_{tt}. \tag{6.26}$$

The MSE [*Berkhoff*, 1972] describes the small amplitude transient wave propagation on slowly varying depth. Thus it is shown as *Cecioni and*

Bellotti [2010a, b], following *Tinti et al.* [2006] and *Kervella et al.* [2007], proposed the introduction of the source term in the right hand side of equation (6.25), in order to incorporate the wave generation due to sea floor displacements. We recall that in the equation (6.25), $h(x,y,t) = h_f(x,y) - h_l(x,y,t)$ is the water depth equal to the difference between the fixed bottom depth $h_f(x,y)$ and the landslide (or seismic sea floor) elevation $h_l(x,y,t)$; its second time derivative is not zero in the area where the landslide (or the earthquake) occurs. The term $1/cosh(kh_f)$ in equation (6.25) represents a filter function, which models the transfer of the bottom movement to the free surface.
It has to be noted that c, c_g, k and ω in equation (6.25) have been traditionally computed with reference to a single wave frequency component. Therefore the time domain MSE can be solved by assuming a dominant frequency of the wave spectrum, and the result is valid only for narrow frequency spectra seas. In order to reproduce the frequency dispersion of broad banded spectra, as those of tsunamis, *Bellotti et al.* [2008], *Cecioni and Bellotti* [2010a, b] proposed to solve the MSE in the frequency domain. By taking the Fourier Transform of equation (6.25) with respect to the time, it follows

$$\nabla_h \cdot (cc_g \nabla_h N) + \omega^2 \frac{c_g}{c} N = -\frac{1}{cosh\,(kh_f)} \overline{h_{tt}}. \tag{6.27}$$

The resulting elliptic equation (6.27) describes the stationary wave field in terms of $N(x,y,\omega)$, which is the Fourier Transform of the free surface elevation, i.e. relative to a monochromatic wave of single angular frequency ω. The forcing term in the right hand side of equation (6.27) contains $\overline{h_{tt}}$, the Fourier Transform of h_{tt}. The model solves a set of equations as equation (6.27), one for each frequency ω, with the appropriate boundary conditions and the values of c, c_g, k. The free surface elevation in the time domain, $\eta(x,y,t)$, can be then calculated by taking the Inverse Fourier Transform of the superposition of all the monochromatic solutions $N(x,y,\omega)$.
As already shown in the paper of *Cecioni and Bellotti* [2010b], when the tsunami generation mechanism is known and its effects on the water are reproduced by the forcing term, the model provides accurate reconstruction of the tsunami scenario. When the model works in a tsunami early warning application, as preliminarily shown in *Bellotti et al.* [2008], it also makes use of the recording of the tsunami itself, and has to forecast the propagating waveform in real-time while the event is occurring.
A tsunami early warning application of the present model is possible if the computational procedure is split in two parts: one computationally expensive, which has to be carried out before the occurrence of the tsunami;

the other, much faster, which provides the forecasting tsunami in real-time using the recording of the tsunami itself. The pre-event computations generate a database of possible tsunami scenario, which are computed assuming a probable generating source, based on the identification of the area where the co-seismic or landslide events likely will occur. The solution of the preliminary computation is the free water surface elevation $\eta^{p-c}(x, y, t)$ (where $p - c$ stands for pre-computed) and can be stored at any point of the numerical domain.
The second part of the model application starts in real-time when a tsunami occurs and its waveform $\eta^m(x_P, y_P, t)$ is detected from the sea surface measurement at one position (x_P, y_P). At that point we can impose the following identity

$$\eta^m(x_P, y_P, t) = s(t) \cdot \eta^{p-c}(x_P, y_P, t) \tag{6.28}$$

in order to calculate the time varying correction term $s(t)$. Once the correction term is applied to the pre-computed time series, the model solution is equal to the measured one. Indeed, when $s(t)$ is obtained from equation (6.28), it is possible to adjust the pre-event simulation results at any position of the computational domain where no records are available, by using an identical correction term for all the points of the domain:

$$\eta(x, y, t) = s(t) \cdot \eta^{p-c}(x, y, t). \tag{6.29}$$

Actually, it is more convenient to apply Eqs. (6.28) and (6.29) in the frequency domain. This requires a Fourier Transform of the measured tsunami time series record, $N^m(x_P, y_P, \omega)$. The correction term can be therefore defined as follows:

$$S(\omega) = \frac{N^m(x_P, y_P, \omega)}{N^{p-c}(x_P, y_P, \omega)} \tag{6.30}$$

and the forecasted tsunami waveform at any point is computed in the frequency domain as:

$$N(x, y, \omega) = S(\omega) \cdot N^{p-c}(x, y, \omega). \tag{6.31}$$

As stated the free surface elevation in the time domain is obtained by means of the Inverse Fourier Transform of $N(x, y, \omega)$. The computation of $S(\omega)$ is carried out in the frequency domain. It has complex values, and has therefore also the effect of correcting both the amplitude and the phase of each component of the wave specrtum. When switching to the time domain, it is not necessary to synchronize the computed and the measured time series.
An important feature of the model is that the tsunami waveform can be

estimated while the tsunami is occurring, in the sense that the term $S(\omega)$ can be calculated even when sea surface elevation record does not contain the entire tsunami waveform. It results that the accuracy of the forecasting model improves with the length of the available registration of the tsunami. However, as we will show later, good estimation of the tsunami waveform can be extracted from the model even when just the first tsunami wave has been recorded.

6.3.1 Boundary conditions

Boundary conditions used in this work are the fully reflective conditions at solid boundaries and a radiation condition.
The full-reflection boundary conditions can be expressed by imposing that the fluid velocity in the direction orthogonal to the boundary is zero. By using equation (6.24) it follows that the derivative of the Fourier Transform of the free surface elevation η along the normal to the reflective boundary should be zero (see *Mei* [1989]):

$$N_n = 0. \tag{6.32}$$

The radiation boundary condition can be obtained by using a mathematical formulation that allows the waves that propagate toward the open boundaries to freely exit the computational domain. This condition can be easily formulated for progressive outgoing waves [*Sommerfeld*, 1964; *Van Dongeren and Svendsen*, 1997]:

$$\eta_t + \frac{c}{cos\,(\theta_n)}\eta_n = 0, \tag{6.33}$$

where c is the linear phase celerity and θ_n is the angle the wave direction forms with the outgoing normal to the considered boundary.
The Fourier Transform of equation (6.33) provides the radiation condition in the frequency domain (see *Beltrami et al.* [2001]; *Steward and Panchang* [2001]):

$$N_n + ikcos\,(\theta_n)N = 0. \tag{6.34}$$

Please note that the equation (6.34) is nonlinear in the sense that θ_n is not known a priori and depends on the solution itself. Iterative techniques can therefore be applied or a reasonable estimate of this parameter can be used to solve the indeterminacy.

6.4 Description of the physical model

In order to test the tsunami inversion technique described in the previous section, experimental results described by *Di Risio et al.* [2009b] have been

used. It has to be noted that these experiments are partially the same of those described in chapters 3, 4 and 5. As shown in Figures 6.1 and 6.2 the experimental facility, the physical model (i.e., truncated conical island) and the landslide model (i.e., LS1) are excaltly the same of those described in chapter 3. Nevertheless, the experiments used to test the inversion procedure are preceding to those described in this work. In particular, different acquisition techniques, and different number and placement of the instruments have been used by *Di Risio et al.* [2009b]. Indeed, observing the Figure 6.2, if one compares it with the Figures 3.2 and 3.6, it is evident that the moving arm is not installed on the island. Furtermore, the experimental results, that have been used in this chapter to test the inversion technique, refer only to the thinner landslide model (i.e., LS1). We refer to *Di Risio et al.* [2009b] for further details on the experimental set-up. However, we briefly recall that *Di Risio et al.* [2009b] have tested, in the experimental campaign, different landslide release distances and water depths. The release distance ζ is defined as the distance between the lower point of the landslide and the undisturbed shoreline measured along the inclined plane. In order to test the tsunami inversion technique, we refer to the experimental results for $\zeta = 0.30$ m and offshore water depth $h_b = 0.80$ m.
Traditional resistive gauges were employed to register the instantaneous vertical displacement of the free surface. All the signals have been acquired

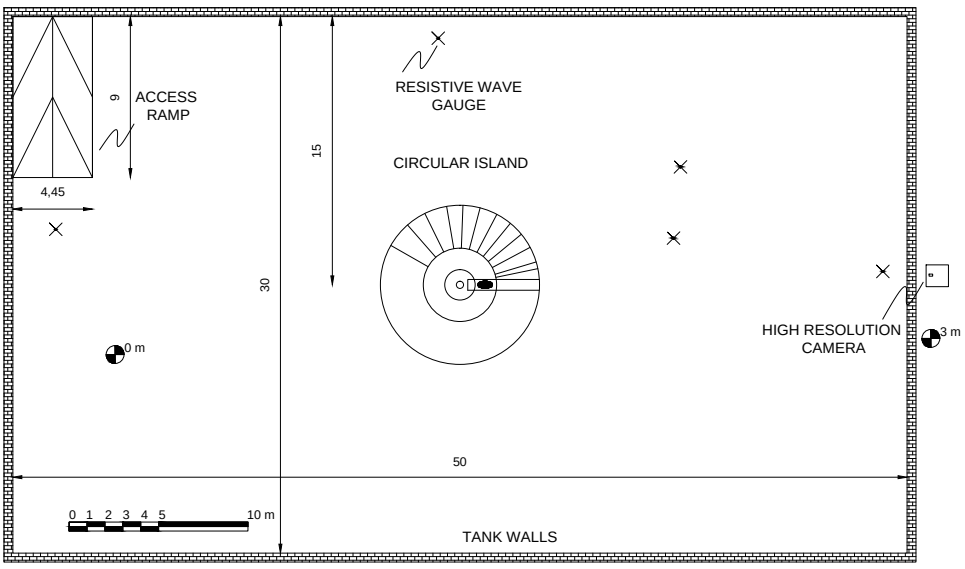

Figure 6.1: Skecth of the plan view layout of the laboratory experiments (measures in m).

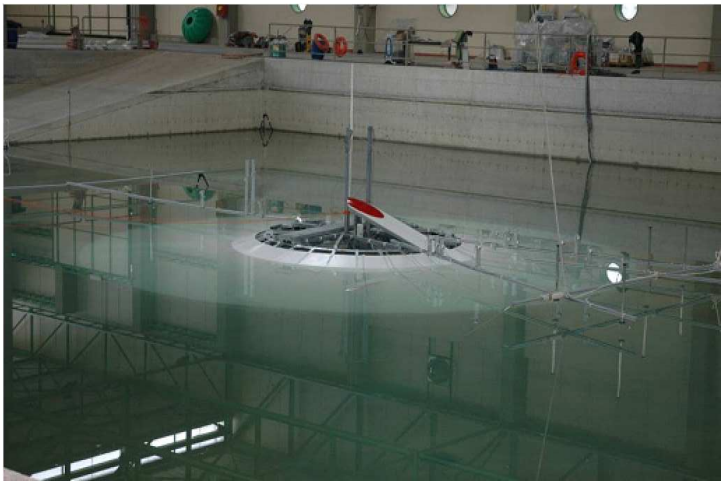

Figure 6.2: Picture of the landslide and island models.

simultaneously at a frequency of 1000 Hz. The relative position of all the gauges can be found in Figure 6.3 and in Table 6.1. The position of the gauges in Table 6.1 are expressed in polar coordinates, with the origin at the landslide-water impact point (see Figure 6.3) and the angular position measured counterclockwise from the landslide motion direction.

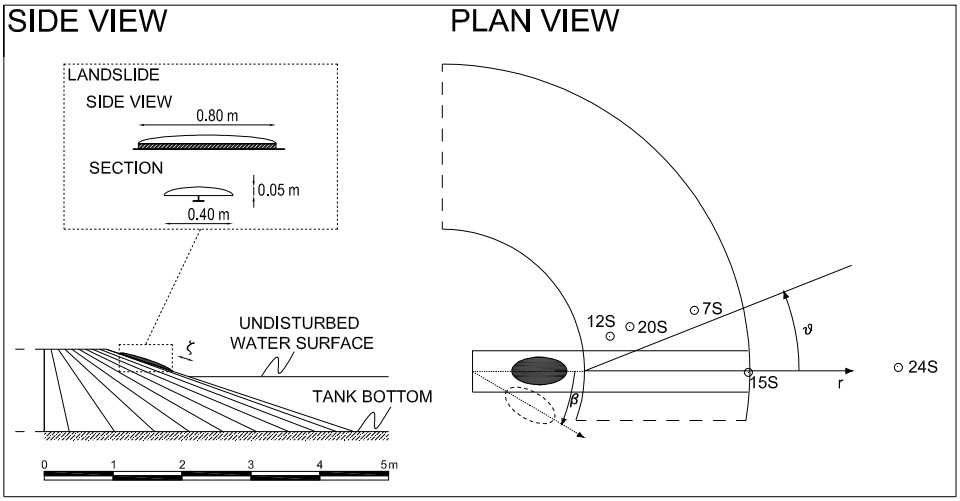

Figure 6.3: Layout of the laboratory gauges positions.

Gauge name	Angular position θ (°)	Radial position r(m)
12S	54.3	0.63
20S	44.9	0.92
7S	29.2	1.82
15S	-0.3	2.37
24S	0.8	4.55

Table 6.1: Angular and radial position of sea level gauges: the point where the landslide impacts the water is taken as the origin, and the angular position is taken counterclockwise from the landslide motion direction (see Figure 6.3).

6.5 Real-time tsunami inversion

6.5.1 Numerical simulations

The numerical simulations presented herein are aimed at reproducing the conical island experiment. The computational domain is semicircular, as shown in Figure 6.4. Taking advantage of the symmetry of the problem across the landslide motion direction, only a half of the conical island has been reproduced. The computational domain is limited at the offshore side by a semicircular boundary placed at a distance of 8 m from the centre of

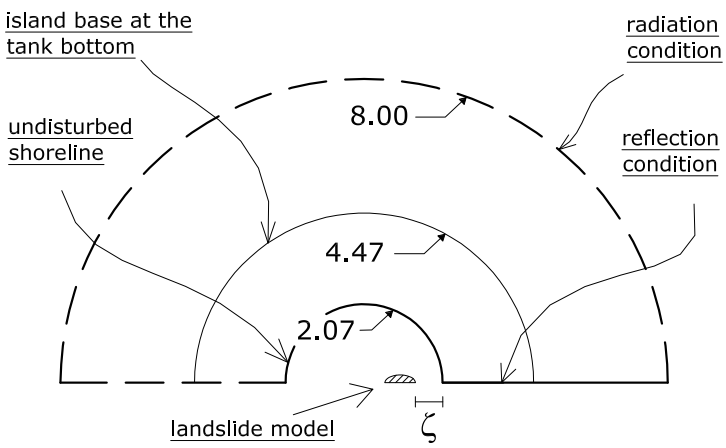

Figure 6.4: Sketch of the numerical domain from *Cecioni and Bellotti* [2010b]. The numbers 2.07, 4.47 and 8.00 express the radii in meters of the undisturbed shoreline, the island base at the tank bottom, and the external circular boundary respectively.

the island.
As sketched in the Figure 6.4, at the offshore boundary a radiation boundary condition is applied; it allows free exit of the propagating waves. At the undisturbed shoreline it is imposed a perfect reflection condition, representing a vertical impermeable wall.
The model solves the MSE (6.27) with the boundary conditions, using a Finite Element Method procedure. The time series reproduced by the model is 50 s long, with a Δt of 0.01 s, and a total of 5000 time steps. In the frequency domain, equation (6.27) has been solved for those long wave components for which relevant energy contents exist. More specifically, 100 discrete angular frequency ranging from $2\pi \cdot 0.02$ up to $2\pi \cdot 2$ rad/s have been considered for the numerical solution.
The maximum element size of the triangular mesh elements is set in order to ensure at least 10 points for the shortest wave length reproduced (0.05 m for all the performed simulations). It results in about 160,000 mesh elements and about 81,000 Degrees of Freedom of the problem. The computation time for the solution of the 100 discrete angular frequencies is about 12 minutes on an AMD Opteron 246 2GHz Computer equipped with 4 GB of RAM.

6.5.2 Inversion using the correct landslide scenario

Firstly we present results of the inversion procedure applied to the pre-event computations carried out using the correct landslide scenario. This means that the available information on the landslide volume and kinematic from the laboratory experiments are used in the numerical simulations in order to get the forcing term of the MSE (6.27).
In order to estimate the complex correction term $S(\omega)$ of equation (6.30), the numerical model results and one of the collected time series were used. We have therefore used the experimental records at one gauge, referred to as "inversion" gauge in the followings, as if it would represent the tsunami record given as input for the inversion procedure. Experimental time series at another gauge located far from the landslide area, referred to as "control gauge" in the followings, is used to validate the model prediction of the propagating waves.
The key point here is to analyze where it would be better to locate the inversion sea level gauge, which will record the tsunami and will provide in real-time the input for the inversion procedure. On one hand, in order to give early predictions, it is desirable to use gauges very close to the subaerial landslide; on the other hand, the model is expected to perform better in deep water, so in order to get accurate results it is desirable to use gauges

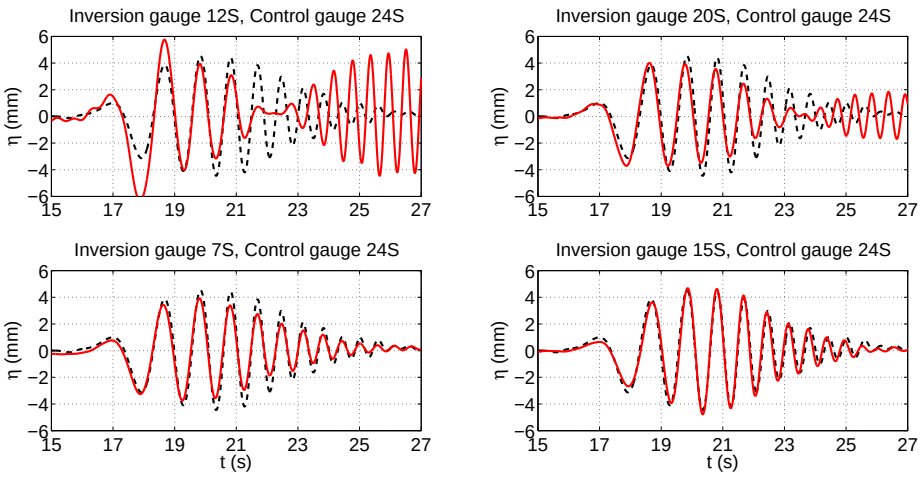

Figure 6.5: Comparison of the numerical result (red solid line) with the experimental time series (black dashed line) at the control gauge 24S. Each plot refers to a different gauge (12S, 20S, 7S and 15S) used for the inversion.

located not in the very near field.

In order to investigate what position of the inversion gauge will provide better accuracy of the tsunami prediction, Figure 6.5 reports the results of 4 different inversions, obtained using as input time series those of the gauges 12S (r=0.63 m, θ=54.3°), 20S (r=0.92 m, θ=44.9°), 7S (r=1.82 m, θ=29.2°) and 15S (r=2.37 m, θ=-0.3°). The numerical results (red solid line) are checked at the control gauge 24S (r=4.55 m, θ=0.8°) by comparison with the experimental records (black dashed line). It appears that the performances of the inversion procedure improve as the distance of the inversion gauge from the source increases. This is clearly related to the fact that in the very near field the model results are not satisfactorily, see for example the results reported on the figure 5 of *Cecioni and Bellotti* [2010b]. As shown in that paper, the accuracy of the results deteriorates in the very near field. This is mostly related to the fact that the present model does not reproduces complicated three-dimensional flows and nonlinear effects; both are expected to play a role close to the landslide and in shallow waters. Results obtained using as inversion gauge the 12S are of very poor quality. When the inversion gauge 20S is used, the results are good for the largest waves, but the following smaller waves are not correctly reproduced. The computations obtained using the gauge 7S give a good reproduction of the largest waves and of the trailing wave train. Very accurate results are obtained using the very far

gauge 15S. Note however that the instrument is on the landslide path and in the field it is not feasible to place wave gauge at that position, since they would be certainly damaged by landslides. In the following the gauge 7S is taken as the inversion one, while the gauge 24S is used as the control one, representative of waves radiating offshore.

6.5.3 Effect of uncertainties on the landslide scenario

It is now evaluated the effect of using pre-event computations carried out with wrong landslide scenarios on the accuracy of the results. Of course it is impossible to know exactly the properties of the landslide and its kinematic before the tsunami event, and it is therefore very important to assess the effects of scenario uncertainties on the method presented. The effect of uncertainty of three parameters is separately evaluated here: the volume of the landslide, its position (i.e. the axis along which it slides), and its kinematic (i.e. its velocity). Other sources of uncertainty such as the shape of the landslide and the porosity are not considered herein.

Figure 6.6 presents the results at the control gauge 24S, obtained applying the inversion from the sea level record at gauge 7S, using 4 landslide scenarios, including the correct one. These have been computed by using

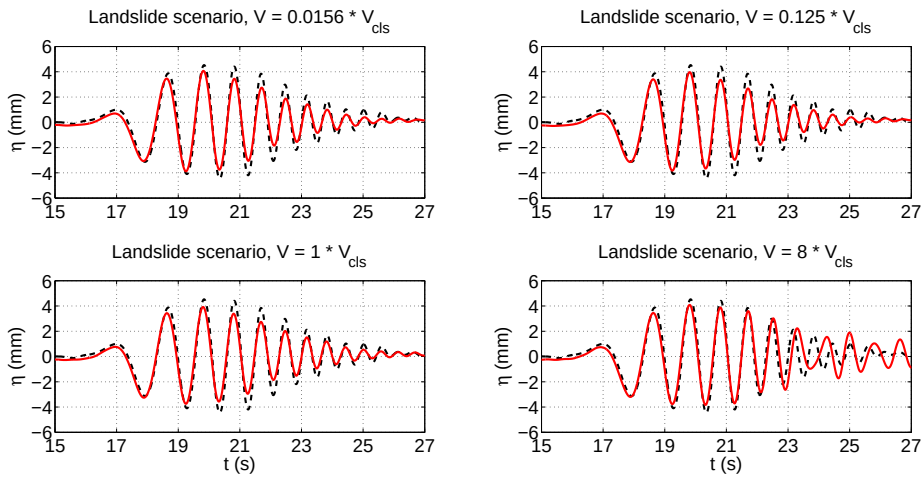

Figure 6.6: Comparison of the numerical result (red solid line) with the experimental registration (black dashed line) at the control gauge 24S. Numerical model prediction is performed adopting gauge 7S as the inversion gauge, and using pre-event numerical computations carried out with 4 tentative landslide volumes. V_{cls} is the volume of the so called correct landlide scenario.

landslides of different dimensions, but keeping the same ellipsoidal shape. The 4 landslides have been obtained by scaling the original one used in the physical model, multiplying the axes by 0.25, 0.50, 1.00 and 2.00. The resulting landslide volumes measure respectively 0.0156, 0.1250, 1.0000 and 8.0000 times the volume of the reference landslide (i.e. the one reproduced in the physical model). Again the red line reports the numerical model prediction, while the black dashed line refers to the experimental data.
The results indicate that the inversion procedure is not very much affected by the uncertainty on landslide volume. As far as the largest waves are concerned, no differences can be seen, neither a trend with the volume of the landslide. It is however pointed out that the train of small waves that follows the largest, are better reproduced by the small and the correct landslide scenarios, while increasing the dimension of the landslide a poor accuracy is obtained. Of course, as the method is aimed at predicting the largest waves, it can be concluded that the effect of uncertainties on the landslide volume can be neglected. Let us now analyze the effect of uncertainties on the landslide position, i.e. on the direction of the landslide motion on the flank of the island. The reference position is that used in the experiments (see

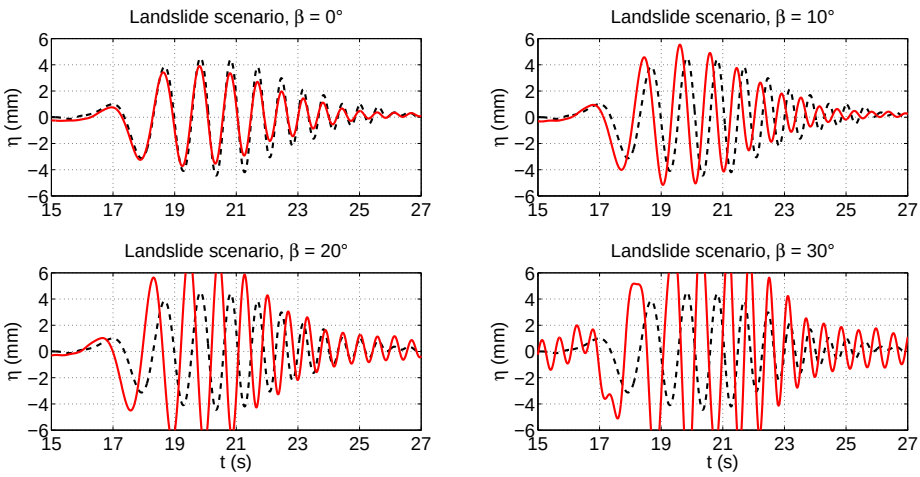

Figure 6.7: Comparison of the numerical result (red solid line) with the experimental records (black dashed line) at the control gauge 24S, using inversion gauge 7S. Numerical model prediction is performed using pre-event numerical computations carried out with 4 tentative landslide motion directions. The angle β measures the difference between the correct landslide scenario and that used in the computations. $\beta = 0^o$ represents the correct landslide scenario, i.e. that representing the experiments.

Figure 6.3). The pre-event numerical computations are created assuming landslide scenarios with the sliding axis rotated of an angle β equal to 10, 20 and 30 degrees from the reference one. Figure 6.7 presents the sea level oscillations at the control gauge 24S given by the numerical model, obtained using the inversion gauge 7S and the 4 pre-event computations with different landslide motion direction. Comparing the numerical results (red line) with the physical model records (black dashed line) it can be noted that the position of the landslide plays a very important role on the procedure. The accuracy of the results given by the method decreases as the direction of the sliding axis diverges from the correct one. An error of 10° on the landslide position gives already poor results; an error of 30° appears to produce unacceptable predictions. Finally it is investigated the effect of uncertainties on the landslide velocity. For simplicity the pre-event computations are carried out using the same kinematic law derived from the laboratory experiment, but velocities are multiplied by 0.5, 1.0, 1.5 and 2.0 respectively, thus reproducing one slower and two faster falls than the reference one. The results of the inversion procedure, again referred to the control gauge 24S and obtained from the inversion gauge 7S, are reported in Figure 6.8. The comparison with the laboratory records (black dashed line) indicates that an underestimation of the landslide velocity in the pre-event simulation still

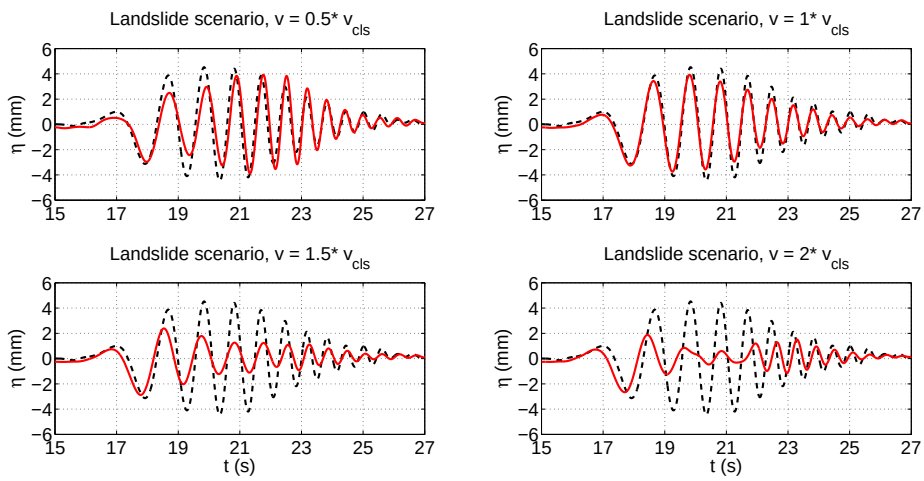

Figure 6.8: Tsunami inversion using scenarios computations with wrong landslide velocity; inversion from gauge 7S, results checked against records at gauge 24S. Red solid lines refer to numerical results, black dashed lines to experimental time series. v_{cls} is the velocity of the so called correct landslide scenario.

produces acceptable results after the inversion procedure. On the contrary, the fast landslide scenarios give poor accuracy results, and the forecasted wave packet is not able to reproduce the largest surface elevation recorded at the control gauge.
It can be concluded that the pre-event uncertainties on the landslide volume seems not affect the inversion forecasting results, while the landslide falling position appears to have strong influence upon the accuracy of the method. Also very small errors on the position of the axis along which the landslide moves, induce large errors on the results. Furthermore, it appears that it is better to reproduce slower landslides, rather than selecting too fast landslide scenarios.

6.5.4 Real-time inversion

It is now evaluated the ability of the procedure to deal with truncated input time series. Of course, when performing inversion in real-time, the data are used as they become available. Results of an example computation performed with the correct scenario are reported in Figure 6.9. Left panels refer to the time series at the inversion gauge 7S; the black dashed line refers to the full record, identical for all the plots, and the blue solid one to the part of the signal considered available for each plot. Right panels show the experimental time series at the control gauge 24S (black dashed lines) and those predicted by the model (red solid line). Each row of plots refers to a specific elapsed time, measured by the parameter t_{known}, of the input time series used for the inversion. For instance, the first row considers an input time series available up to 0 s, selected as origin of the time: no waves are measured and therefore no waves are predicted at gauge 24S. The second row refers to the computation carried out after 0.75 s, after the first wave crest has been measured: the predicted time series shows an underestimated wave train at gauge 24S. When the first wave has been completely measured, and the crest of the second wave (the largest) is included in the input time series, the predictions appear to be quite close to the reference experimental data, as shown by the plots of the third row. As the input time series becomes longer, the results converge to the measured ones. From Figure (6.9) it appears that the leading wave is well predicted already at $t_{known} =$ 1.5 s, while the following wave packet is still underestimated.

The convergence process is also shown in Figure 6.10, where it is also evaluated the effect of changing the inversion gauge. Here the maximum surface elevation predicted by the procedure at the control gauge 24S, is plot against the length of the input time series. The 4 lines refer to results

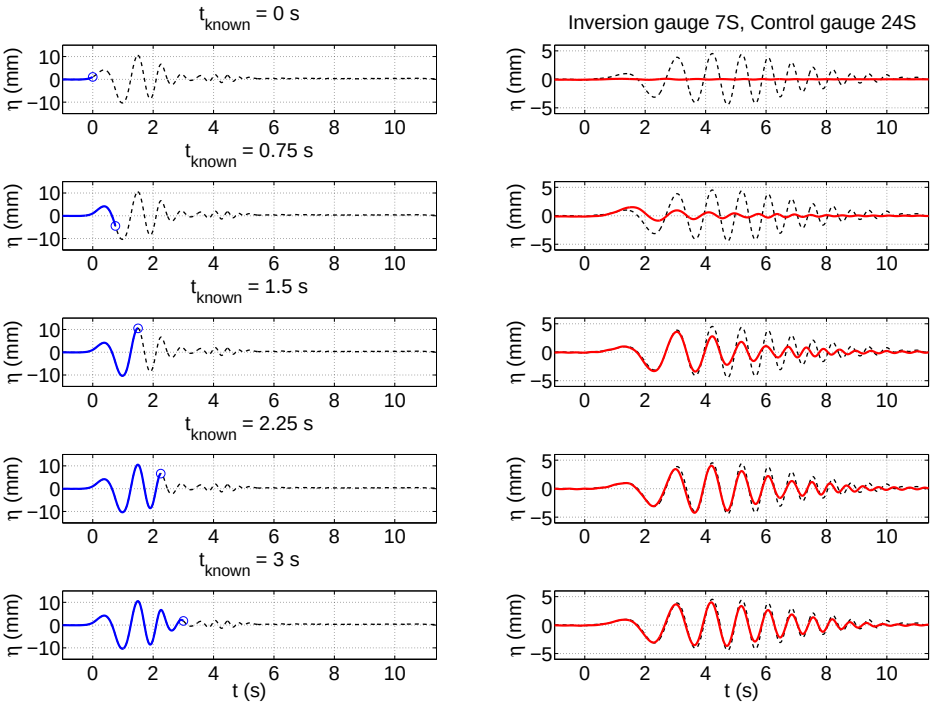

Figure 6.9: Sample computations of real-time inversion using partial input time series at gauge 7S; results checked against records at gauge 24S.

obtained using as input time series those of gauges 12S, 20S, 7S and 15S. The horizontal dashed line represents the maximum experimental surface elevation at the control gauge 24S, i.e. the correct final results. It appears that the convergence procedure is relatively smooth. Applying the inversion procedure using very near-source gauges (12S and 20S) provides a faster but less accurate estimation of the maximum sea surface elevation. The inversion carried out using the very far gauge is more accurate but gets later to the final result.

6.6 Discussion and conclusions

The inversion procedure presented in this work seems to provide forecasts of the tsunamis of good accuracy and is able to work in real time, using partial input time series. It seems therefore that it can be a useful tool to support tsunami early warning systems.

One potential drawback of the procedure is that the accuracy of the results deteriorates if the precomputed lansdlide scenario used for the inversion is

not adequate. Among the several sources of uncertainties about the scenario, it has resulted that the landslide dimension and the kinematic do not play a relevant role. On the contrary, the position of the axis along wich the landslide falls, appears to have a large effect.
A possible method for reducing the effects of scenario uncertainties is that of trying to select the most appropriate one using the measurements in real-time. The simplest approach is that of using two measurement devices of the free surface elevation. One input time series can be used to forecast, at the position of the second device, the time history of the surface elevation for each of the precomputed scenarios. Then, by comparing the results and the measurements at the second device, it may be possible to decide what is the scenario that better describes the event.
However, in the practice, monitoring systems of unstable flanks may be used to obtain reasonable estimates of the position, shape and dimension of potential subaerial landslides. These information may be used to prepare specific landslide scenarios to be included in the database. An example of such measurement technique is shown in *Casagli et al.* [2010], who have set-

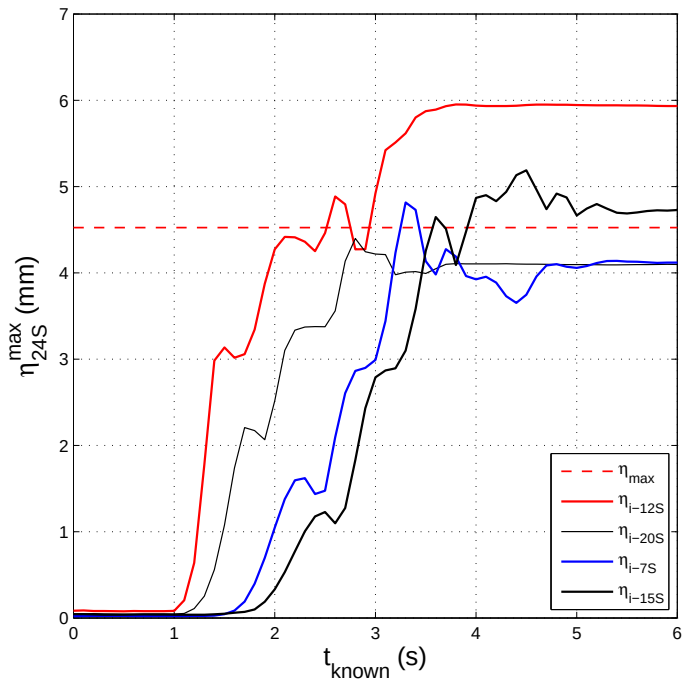

Figure 6.10: Predicted maximum surface elevation at gauge 24S, using as input partial time series of length t_{known}; horizontal dashed line represents the reference experimental result at gauge 24S.

up a ground-based radar interferometry system to monitor the Sciara Del Fuoco unstable flank at Stromboli.
Measurements of tsunamis, essential in the present technique, can be obtained using pressure transducers. Nevertheless, it has to be stressed that waves generated by landslides are not very long, and a "large portion of the wave packet energy pertains to deep water waves" [*Bellotti et al.*, 2009]. Then pressure transducers placed at the sea bottom may not be able to properly measure these tsunamis. A possible alternative is to mount the pressure transducers on poles or, for high water depths, on mooring lines of floating devices, so that the level at which measurements are carried out can be selected independently from the water depth. In the latter case, care has to be used to compensate the measurements for the possible movements of the instruments; these are expected to induce further pressure components, not related with surface waves. It is also worth to mention that the measurements have to be processed in real time, using detection algorithms [*Bressan and Tinti*, 2011; *Beltrami*, 2008], since the procedure presented in this paper expects as input purely the tsunami data. In particular, when measurement devices are placed close to the water surface, they can measure also wind-waves components, and special algorithms have to be applied [e.g. *McGehee and McKinney*, 1997; *Beltrami and Di Risio*, 2011].
This chapter has presented a brief analysis of how the position of the inversion gauge influences the accuracy of the procedure. As stated, it is desirable to measure the tsunamis close to the source, in order to increase the amount of time for the spreading of the alert. However, the propagation model used in the procedure performs better in deep waters, so the accuracy of the results can be improved by placing the inversion gauge not too close to possible landslides. In the practice it is also important to place the instruments on a stable sea bottom area, that is not expected to be reached by the landslide material.
The computations presented in this paper refer to a subaerial landslide only, as the experimental data available so far do not include submerged ones. It is certainly desirable to evaluate the performances of the method for submerged landslides, for which monitoring systems are not able to provide information and warning on flank instabilities. This is one of the points that will be addressed in our ongoing research, since new experimental data will extend the results of *Di Risio et al.* [2009b], including submerged landslides in the next future.

Chapter 7

Concluding remarks

This work aims at gaining insight on the physics of landslide-generated tsunamis that occur at the flanks of a conical island. The problem at hand has been studied by means of physical and numerical models in order to shed light on the generation and propagation mechanisms that characterize these waves. The comprehension and the modelling of the physical phenomena involved have provided tools to improve the tsunamis early warning systems (TEWS).

In this work, the results of a new set of three-dimensional experiments reproducing tsunamis generated by subaerial landslides sliding down the flank of a conical island, placed in a large wave, tank have been showed. The new experimental investigation was carried out by employing a special movable system that allows to achieve high spatial resolution, comparable to the resolution of numerical results. Thus, the experimental data are intended to be used as a benchmark for validating analytical and numerical models. A detailed analysis of landslide motion were performed and hydrodynamic coefficients were estimated on the basis of observed landslide displacements in order to provide reliable tools to define boundary conditions useful for models validation. Furthermore, given the large number of repetitions, a statistical analysis of the repeatibility of the experiments has been carried out.

Experimental analysis on free surface elevation shows that near the impact point the wave features are dependent upon the near-field wave generation process and the highest wave amplitude occurs in front of the impact point. When propagation mechanisms become the governing phenomena, the highest wave amplitudes occur at the coast. Furthermore, as previously demonstrated by *Di Risio et al.* [2009b], the new experiments confirm that frequency dispersion mechanisms play a significant role during the wave

propagation along the shoreline (i.e., run-up). It is almost clear that two different system of waves are generated. The first one propagates along the coast, the second one radiates offshore. Wave periods, celerities and wave length of the two system are rather different. Close to the coast wave periods are higher if compared to the radiating waves. The landslides volume affects significantly only wave amplitudes, whilst wave periods show little dependence upon landslide thickness.

Given the large number of measurements the wavenumber-frequency analysis has been used to identify the features of the propagating waves. The one-dimensional k-f has been applied on the run-up time series to identify the dispersion relation followed by the waves that propagate alongshore. The two-dimensional k-f has been used to study the spatial structures of the wave modes around the island. The one-dimensional k-f has revealed that the inundation of the coast is dominated by a 0th-order edge waves packet. This appears consistent with previous numerical results [*Lynett and Liu*, 2005], theoretical models [*Sammarco and Renzi*, 2008; *Tinti and Vannini*, 1995] and field measurements [*Gonzalez et al.*, 1995; *Neetu et al.*, 2011; *Yamazaki and Cheung*, 2011]. The maximum values of the wave energy are identified approximately at a wavenumber of 4.3 rad/m, i.e. at a wave length of 1.46 m; the peak frequency is of 0.5 Hz (see section 5.5 for further considerations at the prototype scale).

The theoretical frequency dispersion relation of the edge waves [*Ursell*, 1952] seems a reliable tool to estimate the celerity of propagation of the tsunamis along the coast. The phase and group celerity calculated using the experimental data has been compared with those from the edge waves theory. The agreement between measurements and theory is reasonable for the phase celerity. The agreement of the group celerity appears very good. The edge waves theory can therefore be used to calculate the celerity of the waves along the coast once an estimate of the frequency of the tsunami is given.

The two-dimensional k-f has been applied to the new measurements that have been collected around the island. The results confirm that the 0th-order edge waves dominates the propagation mechanisms in a frequency range around to 0.5 Hz. The offshore gauges allow to observe that as the frequency reaches a value of about 0.7 Hz the 1st-order edge waves become relevant, and, as the frequency increases further ($f = 1.2$ Hz) non-trapped modes occur as well.

Furthermore, aiming at providing tools to improve the tsunamis early warning systems (TEWS), a numerical model based on the MSE has been presented in this work. The model is effective in reconstructing in real time the landslide-generated tsunamis wave form in the far-field. The method

discussed herein is based on an inversion procedure that operates in the frequency domain, and makes use of precomputed tsunami scenarios (based on landslide scenarios defined a priori) to be compared with real time measurements. The inversion procedure presented in this work seems to provide forecasts of the tsunamis of good accuracy and is able to work in real time, using partial input time series. It seems therefore that it can be a useful tool to support tsunami early warning systems.
One potential drawback of the procedure is that the accuracy of the results deteriorates if the precomputed lansdlide scenario used for the inversion is not adequate. Among the several sources of uncertainties about the scenario, it has resulted that the landslide dimension and the kinematic do not play a relevant role. On the contrary, the position of the axis along wich the landslide falls, appears to have a large effect.
However, in the practice, monitoring systems of unstable flanks may be used to obtain reasonable estimates of the position, shape and dimension of potential subaerial landslides. These information may be used to prepare specific landslide scenarios to be included in a database. Moreover, the present work has presented a brief analysis of how the position of the inversion sensor influences the accuracy of the procedure. As stated, it is desirable to measure the tsunamis as close as possible to the source, in order to increase the amount of time for the spreading of the alert. However, the propagation model used in the procedure performs better in deep waters, so the accuracy of the results can be improved by placing the inversion gauge not too close to possible landslides (see section 6.6 for further considerations).
Finally, it could be useful to mention possible future research activities. Indeed, other experiments on tsunamis generated by submerged landslides that occur at a conical island have been recently carried out with the aim of providing further developments of the topic described in this work. The same acquisition techniques, as those described in this work, have been used; thus, these experiments are intended to provide a benchmark for validating theoretical models. Furthermore, a special electric engine has been used to move the landslide models. This allows to fix the law of motion of the landslide models. Thus, it is possible to assess the influence of the law of motion in terms of generated waves. Moreover, given the large number of free surface elevation time series it is possible to study the spatial structure of the waves that are generated by the landslide along with the relevance of the propagating wave modes as a function of the generation mechanisms.

Appendix A

Laboratory generation of solitary waves: an inversion technique to improve available methods

A.1 Preface

As described in chapter 2 the earthquake-generated tsunamis differ from those generated by landslides, especially for what concerns the generation and propagation mechanisms. In this Appendix it is shown a simple approach to improve the generation technique of solitary waves in experimental tests. Indeed, solitary waves are often used in laboratory experiments to study the propagation and the interaction with the coasts of tsunamis. However the experimental shape of the waves may differ from the theoretical one. Thus, a correction technique is herein presented. It aims at minimizing the discrepancies between the two profiles. Laboratory experiments revealed that it is effective to correct the experimental shape of the solitary waves, mainly for low nonlinearities. Further details can be foud in the work of *Romano et al.* [2013].

A.2 Introduction

Tsunami are transient perturbations of the water free surface elevation that propagate with high celerities for long distances. These waves, mainly generated by earthquakes or landslides, are characterized by large periods and,

consequently, large wavelengths. It is of scientific and technical interest to understand the generation, propagation and interaction with the coast mechanisms. Several experimental studies have been carried out to gain insight into these phenomena. However, when aiming at reproducing in a wave tank or in a wave flume tsunamis a theoretical wave form has to be chosen. Long waves theories have been often employed for this purpose. Depending on the magnitude of the Ursell parameter these theories may lead to the solitary waves solution [*Russell*, 1844]. Solitary waves have a theoretically infinite wavelength and constant celerity for all the spectral components; are often used to study, in a simple manner, both tsunamis propagation and interaction with the coast.

The use of solitary waves in laboratory experiments aiming at reproducing the features of the tsunamis is due to the works of *Hammack* [1972] and *Hammack and Segur* [1974, 1978a, b]. They addressed the generation and propagation of tsunamis in an ocean of uniform depth, and studied experimentally the impact of an impulsively raised or lowered portion of the sea bottom. They found that a positive initial surface disturbance of arbitrary shape, will indeed eventually lead to the formation of solitons or solitary waves. *Synolakis* [1987] proposed an approximate theory to estimate the run-up of a solitary wave on a plane beach. *Briggs et al.* [1995] performed laboratory experiments aiming at studying the run-up of a tsunami that inundates a conical island coming from offshore; a solitary wave was used as input wave profile.

Recently many authors have criticized the use of solitary waves for tsunamis experiments. *Tadepalli and Synolakis* [1994] suggested that N-waves can be more appropriate in most cases. It is known that real tsunamis often have a leading depression, preceding one or more crests (indeed this property depends on the generation mechanism). According to *Madsen et al.* [2008] rarely a real tsunami can be represented as a solitary wave. This finding was also supported by *Chan and Liu* [2012], which have recently shown that the 2011 Japan Tohoku tsunami can hardly be represented as a solitary wave.

Nevertheless solitary waves remain a tool that is still commonly used in laboratory experiments. To generate these waves in experimental facilities many techniques have been developed. The choice of the generation technique mainly depends on the type of wave maker (i.e. piston-type, flap-type, etc.). A brief description of the available techniques will be given in the next section. However, regardless of the wave maker employed the experimental measured solitary wave shape may deviate from the theoretical one. Various discrepancies between the two profiles may occur due to several reasons.

In this Appendix we present a correction technique, based on an inversion

procedure in the frequency domain, that aims at improving the profile of the experimental solitary waves. The technique, described in detail in the following sections, consists of several steps. In the first step the solitary wave is generated by using a given standard generation technique, once the wave height H and the water depth h in the flume, and consequently the nonlinearity ε, have been fixed. The experimental free surface elevation is measured by means of a wave gauge placed along the flume and is compared with the theoretical free surface elevation. The difference between the two profiles, evaluated in the frequency domain, is then used to correct the wave maker motion. Thus the corrected time series of the wave maker is then used to generate a new solitary waves that is in a better agreement with the theoretical shape. This technique has successfully been tested in the experimental wave flume of the University of Roma Tre.
The Appendix is structured as follows. After this introduction, the next section gives a brief review of the state of the art. The following section describes the basics of the correction technique. Then a brief description of the experimental set-up and the main results are presented. Concluding remarks close the Appendix.

A.3 Solitary waves generation techniques: a brief overview

Many techniques are available to generate solitary waves in experimental facilities. *Russell* [1844] was the first to observe a solitary wave and describe the generation procedure. This consists in dropping a solid box in the wave flume. *Russell* [1844] showed by means of experimental tests that a solitary wave of a certain wave height H that propagates on a constant depth h travels with constant celerity $c = \sqrt{g(H+h)}$. This technique is still used, however other methods valid for piston-type wave maker have been developed. It is worth to mention that when one considers long waves, a uniform depth-averaged horizontal velocity of the water particles is assumed. This suggests that a piston-type wave maker is a suitable tool for generating long waves in general, and solitary waves in particular. The general procedure to generate long waves and solitary waves is extensively described in the work of *Guizien and Barthélemy* [2002]. It is based on the following equation

$$\frac{dX}{dt} = \overline{u}(X,t), \tag{A.1}$$

where X is the instantaneous position of the paddle and $\overline{u}$ is the depth-averaged horizontal velocity, i.e. matching the paddle velocity at each po-

sition in time with the vertically averaged horizontal velocity of the wave. Based on this assumption several theories have been developed. Starting from the chosen solution of the solitary waves [*Boussinesq*, 1871; *Rayleigh*, 1876] a paddle time series can be obtained and appears as follows:

$$X(t) = \frac{2H}{h\beta} tanh\left(\frac{\beta}{2}\theta\right), \tag{A.2}$$

where $\theta = ct - X(t)$ is the phase function, H is the wave height, β is a decay coefficient, c is the phase celerity and h is the water depth. The stroke of the paddle is equal to $S = 4H/h\beta$ and the duration τ of the paddle motion can be determined as follows

$$\tau = \frac{4}{\beta c}\left(tanh^{-1}(0.999) + \frac{H}{h}\right). \tag{A.3}$$

Goring [1978] proposed a theory to generate long waves (i.e. cnoidal and solitary waves) in laboratory experiments by using a piston-type wave maker. In this work the Boussinesq's solution of the solitary waves [*Boussinesq*, 1871] is used and the parameter S, c and β are also provided. However by using this method spurious trailing waves can occur. *Guizien and Barthélemy* [2002] started from the Rayleigh's solution for solitary waves [*Rayleigh*, 1876]. The paddle time series is assumed to be

$$X(t) = \frac{2H}{h\beta}\left(\frac{h\, tanh\left(\frac{\beta ct}{2}\right)}{h + H\left[1 - tanh^2\left(\frac{\beta ct}{2}\right)\right]}\right), \tag{A.4}$$

where $\beta/2 = \sqrt{3H/4h^2(H+h)}$. This technique aims at minimizing the spurious trailing waves. According to the method of *Guizien and Barthélemy* [2002] in the right panel of the Figure A.1 several paddle time series , depending on the wave nonlinearity ε, are represented. When this technique is used the paddle is assumed to be at its rest position during the generation process. *Malek-Mohammadi and Testik* [2010] developed a method that considers that the paddle is moving while the waves are generating. Finally it is worth to mention that other generation techniques, in which the wave maker is not a piston-type one, have been developed. *Rossetto et al.* [2011] have presented an innovative procedure to generate long waves (i.e. solitary waves and N-waves) by using a pneumatic wave maker. However in the present Appendix only the techniques available for piston-type wave makers are treated.

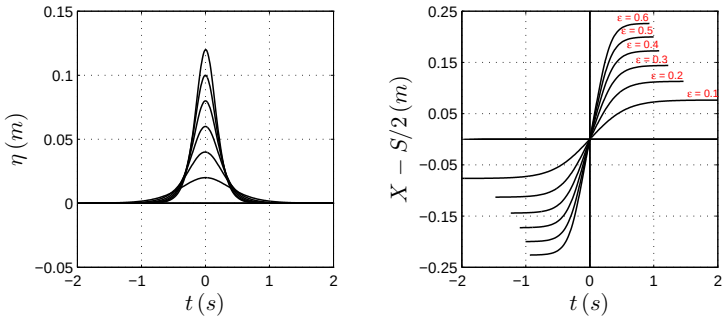

Figure A.1: Left panel: solitary waves profile for several wave nonlinearities and for a given water depth. Right panel: paddle law of motion according to the method developed by *Guizien and Barthélemy* [2002].

A.4 The correction technique

In this section the correction technique is described. We recall that this method aims at improving the shape of the experimental solitary waves with respect to the desired theoretical profile. The method is made up of several steps. The first step consists in generating a solitary wave by using a paddle law of motion $X^0(t)$ provided by an existing generation technique, as those described in the previous section. A comparison between the free surface time series $\eta_e(t)$ and the theoretical one $\eta_t(t)$ at one wave gauge follows. The difference between the two profiles is processed by an inversion technique that allows to obtain a corrected paddle law of motion. This procedure is fairly general and we applied it to improve the solitary wave profiles obtained from the generation technique described in the work of *Guizien and Barthélemy* [2002] because the latter allows to obtain very accurate initial wave profiles.

Our procedure is based on the comparison between the experimental free surface elevation of the solitary wave, measured by a wave gauge placed at known distance $x = X_s$ from the paddle, and the theoretical one. The Fourier transform $(N_e(f)|_{x=X_s}, N_t(f)|_{x=X_s})$ of these two time series is given by the following relations

$$N_e(f)|_{x=X_s} = \int_{-\infty}^{+\infty} \eta_e(x = X_s, t) \cdot e^{-i2\pi ft} dt \tag{A.5}$$

$$N_t(f)|_{x=X_s} = \int_{-\infty}^{+\infty} \eta_t(x = X_s, t) \cdot e^{-i2\pi ft} dt \tag{A.6}$$

where $\eta_e(x = X_s, t)$ and $\eta_t(x = X_s, t)$ are respectively the experimental and the theoretical free surface elevation time series, evaluated at a distance $x = X_s$ from the paddle. By subtracting the two Fourier transform as follows

$$\Delta N(f)|_{x=X_s} = N_t(f)|_{x=X_s} - N_e(f)|_{x=X_s} \tag{A.7}$$

it is possible to obtain $\Delta N(f)|_{x=X_s}$ that takes into account the differences in terms of spectral components between the two time series. It is important to stress that this comparison is made within a time window that has a duration τ, calculated by the equation (A.3). Thus the correction technique is applied in a time range between $(t^* - \tau/2)$ and $(t^* + \tau/2)$, where t^* is the time at which the maximum free surface elevation occurs. Moreover it is worth to highlight that equations (A.5), (A.6) and (A.7) provide complex quantities. Then each spectral components given by (A.7) is shifted in space to the paddle rest position. This step is carried out as follows

$$\Delta N_S(f)|_{x=0} = \Delta N(f)|_{x=X_s} \cdot e^{ik_c(f)X_S}, \tag{A.8}$$

where $k_c(f)$ is the wavenumber defined as

$$k_c(f) = \frac{2\pi f}{c}, \tag{A.9}$$

where c is the solitary waves phase celerity. Each spectral components is here shifted to the paddle's position travelling at the celerity of the solitary wave. Nevertheless this hypothesis is acceptable if solitary waves are considered (i.e. waves that propagate with constant shape), however, when other types of waves are considered, the appropriate frequency dispersion relation can be applied to calculate c for each frequency f. The term provided by (A.8) is thus converted in a correction of the paddle law of motion through the Biésel transfer function [*Biésel*, 1951]

$$\Delta N_X(f)|_{x=0} = \Delta N_S(f)|_{x=0} \cdot e^{-i\frac{\pi}{2}} \cdot F_B(f) \tag{A.10}$$

where $F_B(f)$ is the Biésel transfer function that depends only on the frequency, once the water depth is given. So it is now possible to correct, in the frequency domain, the paddle law of motion by adding the term provided by (A.10) to the Fourier transform of the initial paddle law of motion. This is obtained as follows

$$N_{\widetilde{X}}(f)|_{x=0} = N_{X^0}(f)|_{x=0} + \Delta N_X(f)|_{x=0}, \tag{A.11}$$

where $N_{X^0}(f)|_{x=0}$ is the Fourier transform of the initial paddle law of motion. Thus by means of an inverse Fourier transform it is possible to obtain a

corrected paddle law of motion that, if used to generate a solitary wave, will provide an experimental profile $\widetilde{\eta}(t)$ closer to the theoretical one. Indeed, as it will be showed in the next section, this procedure is supposed to be a convergent one. Thus by applying in an iterative manner the correction technique a better agreement between the experimental and theoretical free surface elevation time series can be reached.

A.5 Experimental set-up

Laboratory experiments have been carried out in the Hydraulic and Maritime Laboratory of the University of Roma Tre (Italy) to test the proposed technique. The laboratory is equipped with a small wave flume made of plexiglass panels and a steel frame. It is 9.0 m long, 0.27 m wide and 0.50 m high (see Figure A.2). The waves are generated by means of a piston-type wave maker. At the other side a vertical fully reflective wall is placed. The wave maker is moved by an electric engine controlled by a computer. The total stroke of the paddle is 1.0 m. A Matlab code is used to generate the waves; the experimental data are collected by means of a National Instruments 6229 A-C board. The instantaneous free surface elevation in the flume is measured by four resistive wave gauges placed along the channel. The positions of the wave gauges, evaluated with respect to the paddle rest position, are respectively $x_{WG1} = 1.96$ m, $x_{WG2} = 3.00$ m, $x_{WG3} = 4.00$ m, $x_{WG4} = 4.96$ m. The sampling frequency is 1000 Hz.

A.6 Results and discussion

Parametric laboratory experiments have been carried out. The water depth has been set constant ($h = 0.10$ m) while the nonlinearity ε of the waves has been varied in a range from 0.10 to 0.60. In Figure A.3 the results of

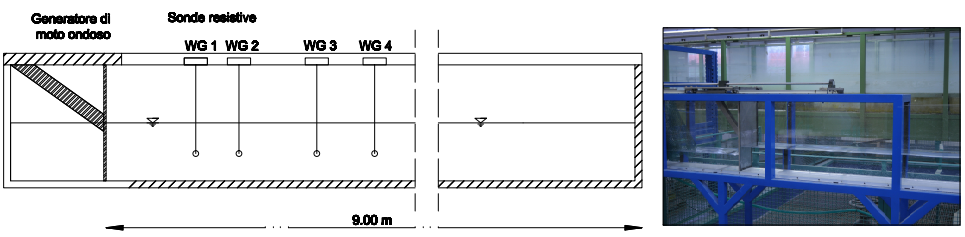

Figure A.2: Sketch of the experimental set-up (left panel) and picture of the wave maker installed on the wave flume (right).

the correction technique for three nonlinearities (ε = 0.10, 0.30, 0.50) are represented. In the left panels the paddle laws of motion are showed (grey lines: initial time series; red lines: corrected ones). In the right panels the free surface elevation time series are plotted (black lines: theoretical profiles of the solitary wave; grey lines: initial experimental profiles; red dots: corrected profiles). The experimental free surface elevation time series used in the correction technique have been measured at the wave gauge n. 3 (i.e., x_{WG3} = 4.00 m). The initial free surface elevation time series deviate from the theoretical ones. Both the maximum value and the wave "tails" disagree with the theoretical profile of the solitary wave. It is also clear that, for all the nonlinearities, the correction technique improves the agreement between the experimental profile and the theoretical one. The maximum values of the free surface elevation are also improved. The tail profiles are improved for the lower nonlinearity (ε = 0.10) while for the larger ones it remains substantially unchanged. Laboratory experiments show that this drawback of the method grows as the nonlinearity of the waves increases. In Figure A.4 the spectral components of the time series represented in Figure A.3 are plotted. The left panels reports the frequency spectra of the free surface elevations (black lines: spectrum of the theoretical profiles of the solitary wave; grey lines: spectrum of the initial experimental profiles; red dots: spectrum of the corrected profiles). In the right panels the differences between the spectra of the experimental and the theoretical solitary waves are plotted, for all the nonlinearities. Figure A.4 shows that for the lower nonlinearity the correction technique is effective for all the frequencies. When the larger nonlinearities are considered it turns out that the correction technique is effective for the high frequencies, while fails in correcting the low ones. As observed in Figure A.3 the low frequencies influence the shape of the tails.
In order to evaluate quantitatively the effectiveness of the correction procedure, several coefficients aiming at estimating the agreement between the experimental solitary waves and the theoretical ones have been defined. The first coefficient C_H, aims at evaluating the difference between the experimental wave height and the theoretical one. This coefficient is defined as follows

$$C_H = 1 - \left| 1 - \frac{H_e}{H_t} \right|, \tag{A.12}$$

where H_t and H_e are the theoretical and the experimental wave height, respectively. The second coefficient σ_f assesses the discrepancies in terms of shape between the two profile within the time window used to correct the initial solitary wave.

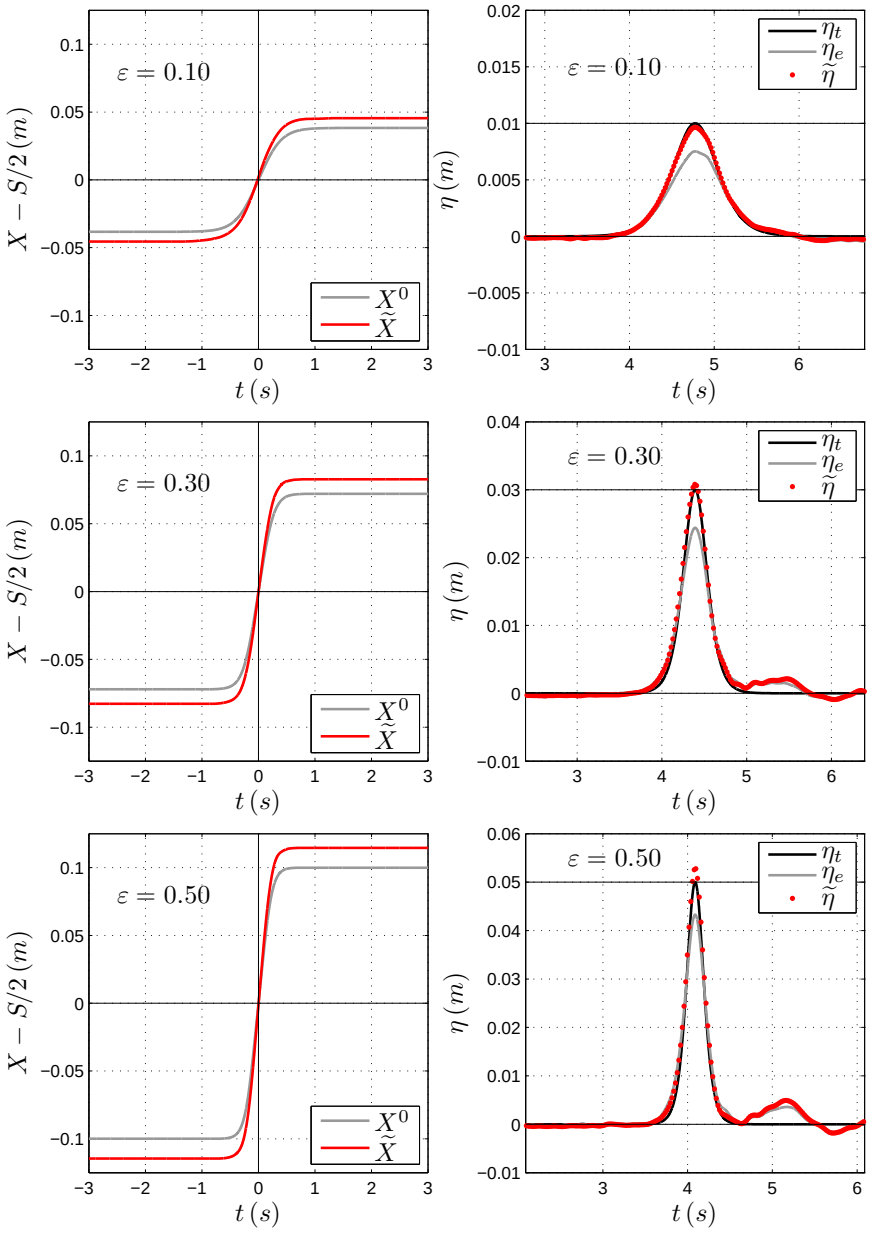

Figure A.3: Left panel: comparison between the paddle laws of motion for three wave nonlinearities (grey lines: initial law of motion; red lines: corrected law of motion). Right panel: comparison between the water free surface elevation (black lines: theoretical profile; grey lines: initial profile; red dots: corrected profile). Note: the experimental free surface elevation time series used in the correction technique have been measured at the wave gauge n. 3 (i.e., $x_{WG3} = 4.00$ m).

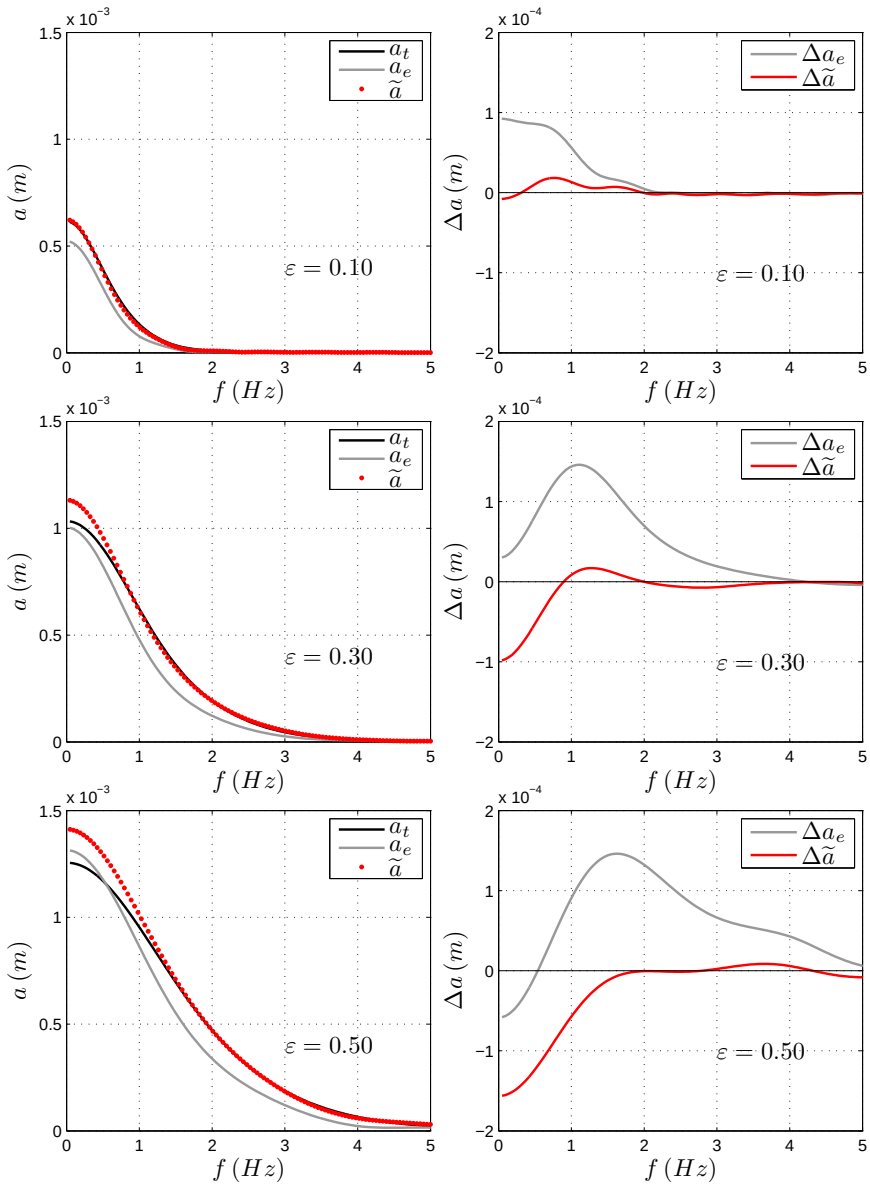

Figure A.4: Left panel: comparison between the spectral amplitudes for three wave nonlinearities (black lines: spectrum of the theoretical profile; grey lines: spectrum of the initial profile; red dots: spectrum of the corrected profile). Right panel: comparison between the spectral differences (grey lines: spectral difference between the theoretical profile and the initial one; red lines:spectral difference between the theoretical profile and the icorrected one). Note: the experimental free surface elevation time series used for the correction technique have been measured at the wave gauge n. 3 (i.e., $x_{WG3} = 4.00$ m).

We recall that the time window has a duration of τ, as defined in equation (A.3). This coefficient is defined by the following

$$\sigma_f = 1 - \frac{\sqrt{\frac{1}{N_\tau}\sum_{i=1}^{N_\tau}\left[\eta_e(t_i) - \eta_t(t_i)\right]^2}}{H_t}, \tag{A.13}$$

where N_τ is the number of elements in the time window and t^* is the time at which the maximum of the profile occurs. Of course this coefficient has to be calculated in the same time window used to correct the initial profile of the solitary wave. The last coefficient K is defined as the product of the previous ones:

$$K = C_H \cdot \sigma_f. \tag{A.14}$$

Each coefficient varies between 0 and 1. When all the coefficients are equal to 1, then a perfect agreement between the experimental and theoretical profile is reached. In Figure A.5 the three coefficient are plotted against the nonlinearity ε. They are calculated for both the initial experimental profile (round markers) and the corrected one (diamond markers). If nonlinearity is lower than 0.4, the procedure yields a relevant improvement, i.e. for low values of nonlinearity the corrected solitary waves are in a very good agreement with the theoretical profile of the waves. Instead, as the nonlinearity increases, the correction procedure does not give a larger significant improvement.

Finally it is interesting to evaluate whether the described procedure is convergent or not. The procedure has been applied five times ($N = 5$) in an

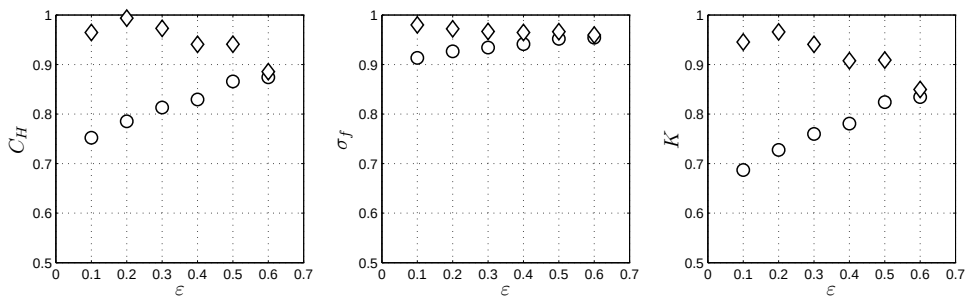

Figure A.5: Left panel: peak coefficient. Middle panel: shape coefficient. Right panel: global coefficient. Note: circle markers identify the coefficient calculated for the initial profiles, while the diamond markers are those calculated for the corrected ones. Note: the experimental free surface elevation time series used in the correction technique have been measured at the wave gauge n. 3 (i.e., $x_{WG3} = 4.00$ m).

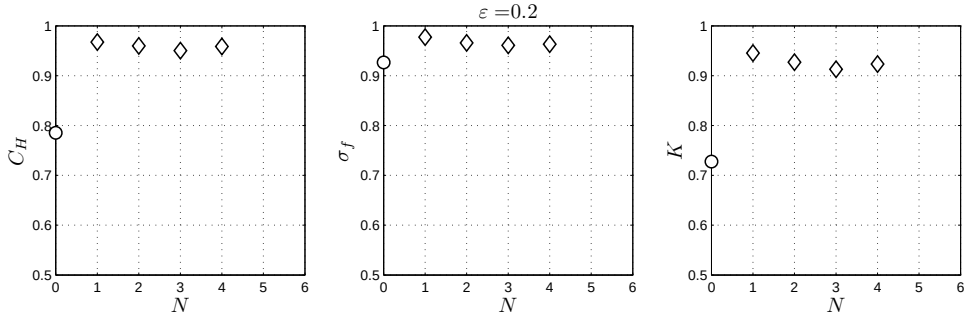

Figure A.6: Peak coefficient (left panel), shape coefficient (middle panel), global coefficient (right panel) against the number of iteration N, for a given wave nonlinearity. Note: circle markers identify the coefficient calculated for the initial profiles, while the diamond markers are those calculated for the corrected ones. The experimental free surface elevation time series used in the correction technique have been measured at the wave gauge n. 3 (i.e., $x_{WG3} = 4.00$ m).

iterative manner for a given wave nonlinearity ($\varepsilon = 0.20$). Results are represented in Figure A.6. In this figure the coefficients, described in equations (A.12), (A.13), and (A.14) are plotted against the number of iterations for which the technique has been applied. When N is equal to 0 we refer to those coefficient calculated for the initial wave profile (round markers). When N is greater than 0 we refer to those coefficients evaluated for the Nth iteration. It can be seen that the largest improvement is obtained between the 0th and the 1st iteration. After the 1st iteration the value of the coefficients remains almost constant. Similar behaviour has been observed for the others nonlinearities investigated, also for the highest ones (i.e., $\varepsilon = 0.50, 0.60$). Hence, we can conclude that there is no evident improvement in applying the method more than once.

A.7 Concluding remarks

In this Appendix a correction technique to improve the agreement between the experimental and the theoretical solitary waves profile is proposed. The technique aims at correcting the paddle law of motion by comparing, in the frequency domain, the experimental profile of solitary waves with the theoretical one. The differences in terms of spectral components between the two profile are used to correct the paddle law of motion. We test the technique with focused laboratory experiments in a small wave flume. They indicated that the correction technique allows to improve the experimental

solitary waves shape, especially for low nonlinearities ($0.10 \leq \varepsilon \leq 0.40$). As the nonlinearity of the waves increases ($\varepsilon > 0.50$) a minor improvement is provided. Furthermore experimental tests showed that although the technique is convergent and may be applied more times for each experiment, the largest improvement is achieved at the first iteration.

Bibliography

Ataie-Ashtiani, B., and A. Nik-Khah, Impulsive waves caused by subaerial landslides, *Environmental Fluid Mechanics*, *8*(3), 263–280, 2008.

Bellotti, G., C. Cecioni, and P. De Girolamo, Simulation of small-amplitude frequency-dispersive transient waves by means of the mild-slope equation, *Coastal Engineering*, *55*(6), 447–458, 2008.

Bellotti, G., M. Di Risio, and P. De Girolamo, Feasibility of tsunami early warning systems for small volcanic islands, *Natural Hazards and Earth System Sciences*, *9*(6), 1911–1919, 2009.

Beltrami, G., An ann algorithm for automatic, real-time tsunami detection in deep-sea level measurements, *Ocean Engineering*, *35*(5), 572–587, 2008.

Beltrami, G. M., and M. Di Risio, Algorithms for automatic, real-time tsunami detection in wind-wave measurements part i: Implementation strategies and basic tests, *Coastal Engineering*, *58*(11), 1062–1071, doi: 10.1016/j.coastaleng.2011.06.004, 2011.

Beltrami, G. M., G. Bellotti, P. De Girolamo, and P. Sammarco, Treatment of wave breaking and total absorption in a mild-slope equation fem model, *Journal of waterway, port, coastal, and ocean engineering*, *127*(5), 263–271, 2001.

Berkhoff, J. C. W., Computation of combined refraction-diffraction, in *Proceedings of the 13th International Conference On Coastal Engineering-ASCE, Vancouver, Canada*, 1972.

Biésel, F., Les Apparails Generateurs de Houle en Laboratorie, *La Houille Blanche*, *6*, 2–5, 1951.

Boussinesq, J., Théorie de lintumescence liquide appelée onde solitaire ou de translation se propageant dans un canal rectangulaire, *Comptes Rendus Acad. Sci (Paris)*, *72*, 755–759, 1871.

Bressan, L., and S. Tinti, Structure and performance of a real-time algorithm to detect tsunami or tsunami-like alert conditions based on sea-level records analysis, *Nat. Hazards Earth Syst. Sci*, *11*, 1499–1521, 2011.

Briggs, M., C. Synolakis, G. Harkins, and D. Green, Laboratory experiments of tsunami runup on a circular island, *Pure And Applied Geophysics*, *144*(3-4), 569–593, doi:10.1007/BF00874384, 1995.

Capon, J., High-resolution frequency-wavenumber spectrum analysis, *Proceedings of the IEEE*, *57*(8), 1408–1418, doi:10.1109/PROC.1969.7278, 1969.

Casagli, N., F. Catani, C. Del Ventisette, and G. Luzi, Monitoring, prediction, and early warning using ground-based radar interferometry, *Landslides*, *7*(3), 291–301, 2010.

Cecioni, C., and G. Bellotti, Modeling tsunamis generated by submerged landslides using depth integrated equations, *Applied Ocean Research*, *32*(3), 343–350, 2010a.

Cecioni, C., and G. Bellotti, Inclusion of landslide tsunamis generation into a depth integrated wave model, *Nat. Hazards Earth Syst. Sci*, *10*, 2259–2268, 2010b.

Cecioni, C., A. Romano, G. Bellotti, M. Di Risio, and P. de Girolamo, Real-time inversion of tsunamis generated by landslides, *Nat. Hazards Earth Syst. Sci*, *11*, 2511–2520, 2011.

Chan, I., and P. Liu, On the runup of long waves on a plane beach, *Journal of Geophysical Research*, *117*(C8), C08,006, 2012.

Chang, K. T., Evolution of landslide-generated edge wave packet, Ph.D. thesis, University of Washington, 1995.

Cho, Y.-S., and P. L.-F. Liu, Crest-length effects in nearshore tsunami runup around islands, *Journal of Geophysical Research*, *104*(C4), 7907–7913, 1999.

Crowson, R., W. Birkemeier, H. Klein, and H. Miller, *SUPERDUCK Nearshore Processes Experiment: Summary of Studies, CERC (Coastal Engineering Research Facility) Field Research Facility*, Tech. Rep., Coastal Engineering Research Center, Vicksburg, MS, 1988.

Di Risio, M., and P. Sammarco, Analytical modeling of landslide-generated waves, *Journal of waterway, port, coastal, and ocean engineering*, *134*(1), 53–60, 2008.

Di Risio, M., G. Bellotti, A. Panizzo, and P. De Girolamo, Three-dimensional experiments on landslide generated waves at a sloping coast, *Coastal Engineering*, *56*(5-6), 659–671, doi:10.1016/j.coastaleng.2009.01.009, 2009a.

Di Risio, M., P. De Girolamo, G. Bellotti, A. Panizzo, F. Aristodemo, M. G. Molfetta, and A. F. Petrillo, Landslide-generated tsunamis runup at the coast of a conical island: New physical model experiments, *Journal of Geophysical Research-Oceans*, *114*, doi:10.1029/2008JC004858, 2009b.

Di Risio, M., P. De Girolamo, and G. Beltrami, *Forecasting landslide generated tsunamis: a review*, Tsunami, Research and Technologies, 2010.

Dodd, N., J. Oltman-Shay, and E. B. Thornton, Shear instabilities in the longshore current: A comparison of observation and theory, *J. Phys. Oceanogr.*, *22*(1), 62–82, 1992.

Enet, F., and S. T. Grilli, Experimental study of tsunami generation by three-dimensional rigid underwater landslides, *Journal Of Waterway Port Coastal And Ocean Engineering-ASCE*, *133*(6), 442–454, doi:10.1061/(ASCE)0733-950X(2007)133:6(442), 2007.

Fujima, K., R. Dozono, and T. Shigemura, Generation and propagation of tsunami accompanying edge waves on a uniform sloping shelf, *Coastal Engineering Journal*, *42*(2), 211–236, doi:10.1142/S0578563400000109, 2000.

Giachetti, T., R. Paris, K. Kelfoun, and F. J. Pérez-Torrado, Numerical modelling of the tsunami triggered by the güìmar debris avalanche, tenerife (canary islands): Comparison with field-based data, *Marine Geology*, *284*(14), 189 – 202, 2011.

Gonzalez, F., K. Satake, E. Boss, and H. Mofjeld, Edge wave and non-trapped modes of the 25 april 1992 cape-mendocino tsunami, *Pure And Applied Geophysics*, *144*(3-4), 409–426, doi:10.1007/BF00874375, 1995.

Goring, D., Tsunamis: The propagation of long waves onto a shelf, Ph.D. thesis, California Institute of Technology, 1978.

Grilli, S. T., and P. Watts, Underwater landslide shape, motion, deformation, and tsunami generation, in *EGS - AGU - EUG Joint Assembly*, p. 13216, 2003.

Guizien, K., and E. Barthélemy, Accuracy of solitary wave generation by a piston wave maker., *journal of hydraulic research*, *40*(3), 321–331, 2002.

Gupta, I., C. Lynnes, T. McElfresh, and R. Wagner, Fk analysis of noress array and single station data to identify sources of near-receiver and near-source scattering, *Bulletin of the Seismological Society of America*, *80*(6B), 2227–2241, 1990b.

Gupta, I. N., C. S. Lynnes, and R. A. Wagner, Broadband f-k analysis of array data to identify sources of local scattering, *Geophysical Research Letters*, *17*(2), 183–186, doi:10.1029/GL017i002p00183, 1990a.

Hammack, J., and H. Segur, The korteweg-de vries equation and water waves. part 2. comparison with experiments, *Journal of Fluid mechanics*, *65*(02), 289–314, 1974.

Hammack, J., and H. Segur, The korteweg-de vries equation and water waves. part 3. oscillatory waves, *Journal of Fluid Mechanics*, *84*(02), 337–358, 1978a.

Hammack, J., and H. Segur, Modelling criteria for long water waves, *Journal of Fluid Mechanics*, *84*(02), 359–373, 1978b.

Hammack, J. L., 'tsunamis: A model of their generation and propagation', Ph.D. thesis, California Institute of Technology, 1972.

Holland, K., and R. Holman, Wavenumber-frequency structure of infragravity swash motions, *Journal Of Geophysical Research-Oceans*, *104*(C6), 13,479–13,488, doi:10.1029/1999JC900075, 1999.

Huntley, D. A., R. T. Guza, and E. B. Thornton, Field observations of surf beat 1. progressive edge waves, *Journal Of Geophysical Research-Oceans*, *86*(C7), 6451–6466, 1981.

Johnson, D. H., and D. Dudgeon, Array signal processing: Concepts and techniques, *PRT Prentice Hall, Englewood Cliffs, NJ*, 1993.

Johnson, J., K. Satake, S. Holdahl, and J. Sauber, The 1964 prince william sound earthquake: Joint inversion of tsunami and geodetic data, *Journal of Geophysical Research*, *101*(B1), 523–532, 1996.

Johnson, R. S., Edge waves: theories past and present, *Philosophical Transactions Of The Royal Society A-Mathematical Physical And Engineering Sciences*, *365*(1858), 2359–2376, doi:10.1098/rsta.2007.2013, 2007.

Kamphuis, J., and R. Bowering, Impulse waves generated by landslides, in *Proceedings of the International Conference on Coastal Engineering*, 1970.

Kervella, Y., D. Dutykh, and F. Dias, Comparison between three-dimensional linear and nonlinear tsunami generation models, *Theoretical and computational fluid dynamics*, *21*(4), 245–269, 2007.

La Rocca, M., D. Galluzzo, G. Saccorotti, S. Tinti, G. B. Cimini, and E. Del Pezzo, Seismic signals associated with landslides and with a tsunami at stromboli volcano, italy, *Bulletin of the Seismological Society of America*, *94*(5), 1850–1867, doi:10.1785/012003238, 2004.

Lacoss, R. T., E. J. Kelly, and M. N. Toksoz, Estimation of seismic noise structure using arrays, *Geophysics*, *34*(1), 21–36, doi:10.1190/1.1439995, 1969.

Liu, P., and H. Yeh, The generation of edge waves by a wave-maker, *Physics Of Fluids*, *8*(8), 2060–2065, doi:10.1063/1.869008, 1996.

Liu, P., H. Yeh, P. Lin, K. Chang, and Y. Cho, Generation and evolution of edge-wave packets, *Physics Of Fluids*, *10*(7), 1635–1657, doi:10.1063/1.869682, 1998.

Liu, P., T. Wu, F. Raichlen, C. Synolakis, and J. Borrero, Runup and rundown generated by three-dimensional sliding masses, *Journal of fluid Mechanics*, *536*(1), 107–144, 2005.

Lynett, P., and P. Liu, A numerical study of the run-up generated by three-dimensional landslides, *Journal of Geophysical Research-Oceans*, *110*(C3), doi:10.1029/2004JC002443, 2005.

Madsen, P., D. Fuhrman, and H. Schäffer, On the solitary wave paradigm for tsunamis, *Journal of Geophysical Research*, *113*(C12), C12,012, 2008.

Malek-Mohammadi, S., and F. Testik, New methodology for laboratory generation of solitary waves, *Journal of Waterway, Port, Coastal, and Ocean Engineering*, *136*(5), 286–294, 2010.

Mallet, R., and J. W. Mallet, Fourth report upon the facts and theory of earthquake phenomena, in *Report of 28th Meeting of British Association for the Advancement of Science*, pp. 1–136, 1858.

McGehee, D., and J. McKinney, Tsunami detection and warning capability using nearshore submerged pressure transducers-case study of the 4

october 1994 shikotan tsunami, *ADVANCES IN NATURAL AND TECHNOLOGICAL HAZARDS RESEARCH*, *9*, 133–144, 1997.

Mei, C. C., *The applied dynamics of ocean surface waves*, vol. 1, World Scientific Publishing Company Incorporated, 1989.

Miller, D., *Giant Waves in Lituya Bay, Alaska: A Timely Account of the Nature and Possible Causes of Certain Giant Waves, with Eyewitness Reports of Their Destructive Capacity*, Professional paper, U.S. Government Printing Office, 1960.

Miller, R. L., Prediction curves for waves near the source of an impulse, in *Proceedings of the International Conference on Coastal Engineering*, vol. 1, 1970.

Molfetta, M., M. Di Risio, A. Romano, G. Bellotti, L. Pratola, P. De Girolamo, and L. Damiani, Tsunamis generated by subaerial landslides at the coast of conical islands: a new set of high resolution experimental dataset, in *Proceedings of the Third International Conference on the Application of Physical Modelling to Port and Coastal Protection: Coastlab 10, Barcelona, Spain*, pp. 1–10, International Coastal Resources Research Centre (CIIRC), 2010.

Montagna, F., G. Bellotti, and M. Di Risio, 3d numerical modeling of landslide-generated tsunamis around a conical island, *Natural hazards*, *58*(1), 591–608, 2011.

Neetu, S., I. Suresh, R. Shankar, B. Nagarajan, R. Sharma, S. S. C. Shenoi, A. S. Unnikrishnan, and D. Sundar, Trapped waves of the 27 november 1945 makran tsunami: observations and numerical modeling, *Natural Hazards*, *59*(3), 1609–1618, doi:10.1007/s11069-011-9854-0, 2011.

Newman, J. N., *Marine hydrodynamics*, MIT Press, Cambridge, Mass., 1989.

Noda, E., Water waves generated by landslides, *Journal of the Waterways, Harbors and Coastal Engineering Division*, *96*(4), 835–855, 1970.

Oltman-Shay, J., P. A. Howd, and W. A. Birkemeier, Shear instabilities of the mean longshore current, 2, field observations, *J. Geophys. Res.*, *94*, 18,031–18,042, 1989.

Ozkan-Haller, H., and J. Kirby, Nonlinear evolution of shear instabilities of the longshore current: A comparison of observations and computations, *Journal Of Geophysical Research-Oceans*, *104*(C11), 25,953–25,984, doi: 10.1029/1999JC900104, 1999.

Panizzo, A., G. Bellotti, and P. De Girolamo, Application of wavelet transform analysis to landslide generated waves, *Coastal engineering*, *44*(4), 321–338, 2002.

Panizzo, A., P. De Girolamo, and A. Petaccia, Forecasting impulse waves generated by subaerial landslides, *Journal of geophysical research*, *110*(C12), C12,025, 2005a.

Panizzo, A., P. De Girolamo, M. Di Risio, A. Maistri, and A. Petaccia, Great landslide events in italian artificial reservoirs, *Natural Hazards and Earth System Science*, *5*(5), 733–740, doi:10.5194/nhess-5-733-2005, 2005b.

Pelinovsky, E., and A. Poplavsky, Simplified model of tsunami generation by submarine landslides, *Physics and Chemistry of The Earth*, *21*(1 - 2), 13 – 17, 1996.

Rayleigh, L., On waves, *Phil. Mag*, *1*(5), 257–279, 1876.

Renzi, E., and P. Sammarco, Landslide tsunamis propagating around a conical island, *Journal of Fluid Mechanics*, *650*, 251–285, doi:10.1017/S0022112009993582, 2010.

Renzi, E., and P. Sammarco, The influence of landslide shape and continental shelf on landslide generated tsunamis along a plane beach, *Nat. Hazards Earth Syst. Sci*, *12*(5), 1503–1520, 2012.

Roeber, V., Y. Yamazaki, and K. F. Cheung, Resonance and impact of the 2009 samoa tsunami around tutuila, american samoa, *Geophysical Research Letters*, *37*, doi:10.1029/2010GL044419, 2010.

Romano, A., M. Guerrini, G. Bellotti, and J. Lie-hong, Laboratory generation of solitary waves: an inversion technique to improve available methods, *Submitted for publication to China Ocean Engineering*, 2013.

Rossetto, T., W. Allsop, I. Charvet, and D. Robinson, Physical modelling of tsunami using a new pneumatic wave generator, *Coastal Engineering*, *58*(6), 517–527, 2011.

Russell, J., Report on waves, in *14th meeting of the British Association for the Advancement of Science*, pp. 311–390, 1844.

Russell, J. S., Report on waves, in *14th meeting of the British Association for the Advancement of Science*, pp. 311–390, 1845.

Sammarco, P., and E. Renzi, Landslide tsunamis propagating along a plane beach, *Journal of Fluid Mechanics*, *598*, 107–119, doi:10.1017/S0022112007009731, 2008.

Satake, K., Inversion of tsunami waveforms for the estimation of a fault heterogeneity: method and numerical experiments, *Journal of Physics of the Earth*, *35*(3), 241–254, 1987.

Seo, S.-N., and P. L.-F. Liu, Edge waves generated by the landslide on a sloping beach, *Coastal Engineering*, *73*, 133–150, 2013.

Smith, R., Edge waves on a beach of mild slope, *The Quarterly Journal of Mechanics and Applied Mathematics*, *27*(1), 101–110, doi:10.1093/qjmam/27.1.101, 1974.

Smith, R., and T. Sprinks, Scattering of surface waves by a conical island, *J. Fluid Mech.*, *72*, 373, 1975.

Sommerfeld, A., *Lectures on theoretical physics*, vol. 3, Academic Press New York, 1964.

Steward, D. R., and V. G. Panchang, Improved coastal boundary condition for surface water waves, *Ocean engineering*, *28*(1), 139–157, 2001.

Svendsen, I. A., *Introduction to nearshore hydrodynamics*, vol. 24, World Scientific Publishing Company Incorporated, 2006.

Synolakis, C., The runup of solitary waves, *J. Fluid Mech*, *185*(523-545), 1, 1987.

Synolakis, C., J. Bardet, J. Borrero, H. Davies, E. Okal, E. Silver, S. Sweet, and D. Tappin, The slump origin of the 1998 papua new guinea tsunami, *Proceedings of the Royal Society of London. Series A: Mathematical, Physical and Engineering Sciences*, *458*, 763–789, 2002.

Synolakis, C. E., Generation of long waves in laboratory, *Journal of waterway, port, coastal, and ocean engineering*, *116*(2), 252–266, 1990.

Tadepalli, S., and C. E. Synolakis, The run-up of n-waves on sloping beaches, *Proceedings of the Royal Society of London. Series A: Mathematical and Physical Sciences*, *445*(1923), 99–112, 1994.

Tinti, S., and C. Vannini, Theoretical investigation on tsunamis induced by seismic faults near ocean islands, *Marine Geodesy*, *17*(3), 193–212, doi:10.1080/15210609409379727, 1994.

Tinti, S., and C. Vannini, Tsunami trapping near-circular islands, *Pure And Applied Geophysics*, *144*(3-4), 595–619, doi:10.1007/BF00874385, 1995.

Tinti, S., A. Manucci, G. Pagnoni, A. Armigliato, and F. Zaniboni, The 30 december 2002 landslide-induced tsunamis in stromboli: sequence of the events reconstructed from the eyewitness accounts, *Natural Hazards and Earth System Science*, *5*(6), 763–775, 2005.

Tinti, S., G. Pagnoni, and F. Zaniboni, The landslides and tsunamis of the 30th of december 2002 in stromboli analysed through numerical simulations, *Bulletin of Volcanology*, *68*, 462–479, 10.1007/s00445-005-0022-9, 2006.

Titov, V., F. Gonzalez, E. Bernard, M. Eble, H. Mofjeld, J. Newman, and A. Venturato, Real-time tsunami forecasting: Challenges and solutions, *Natural Hazards*, *35*(1), 35–41, 2005.

Ursell, F., Edge waves on a sloping beach, *Proceedings of the Royal Society of London. Series A. Mathematical and Physical Sciences*, *214*(1116), 79–97, doi:10.1098/rspa.1952.0152, 1952.

Van Dongeren, A., and I. A. Svendsen, Absorbing-generating boundary condition for shallow water models, *Journal of waterway, port, coastal, and ocean engineering*, *123*(6), 303–313, 1997.

Walder, J. S., P. Watts, O. E. Sorensen, and K. Janssen, Tsunamis generated by subaerial mass flows, *Journal of geophysical research*, *108*(B5), 2236, 2003.

Watts, P., Wavemaker curves for tsunamis generated by underwater landslides, *Journal Of Waterway Port Coastal And Ocean Engineering-ASCE*, *124*(3), 127–137, doi:10.1061/(ASCE)0733-950X(1998)124:3(127), 1998.

Watts, P., Tsunami features of solid block underwater landslides, *Journal Of Waterway Port Coastal And Ocean Engineering-ASCE*, *126*(3), 144–152, doi:10.1061/(ASCE)0733-950X(2000)126:3(144), 2000.

Watts, P., F. Imamura, and S. Grilli, Comparing model simulations of three benchmark tsunami generation cases, *Sci. Tsunami Hazards*, *18*(2), 107–124, 2000.

Watts, P., S. Grilli, D. Tappin, and G. Fryer, Tsunami generation by submarine mass failure. ii: Predictive equations and case studies, *Journal of Waterway, Port, Coastal, and Ocean Engineering*, *131*(6), 298–310, doi:10.1061/(ASCE)0733-950X(2005)131:6(298), 2005.

Wei, Y., K. Cheung, G. Curtis, and C. McCreery, Inverse algorithm for tsunami forecasts, *Journal of waterway, port, coastal, and ocean engineering*, *129*(2), 60–69, 2003.

Wiegel, R. L., Laboratory studies of gravity waves generated by the movement of a submarine body, *Transactions of the American Geophysical Union*, *36*(5), 759–774, 1955.

Wiegel, R. L., E. K. Noda, E. M. Kuba, D. M. Gee, and G. F. Tornberg, Water waves generated by landslides in reservoirs, *Journal of the Waterways, Harbors and Coastal Engineering Division*, *96*(2), 307–333, 1970.

Yamazaki, Y., and K. F. Cheung, Shelf resonance and impact of near-field tsunami generated by the 2010 chile earthquake, *Geophysical Research Letters*, *38*, doi:10.1029/2011GL047508, 2011.

Yeh, H., Nonlinear progressive edge waves - their instability and evolution, *Journal of Fluid Mechanics*, *152*(MAR), 479–499, doi:10.1017/S0022112085000799, 1985.

Yeh, H., A note on edge waves, in *Proceedings of Coastal Hydrodynamics, ASCE*, pp. 256–269, 1987.

Yeh, H., P. Liu, M. Briggs, and C. Synolakis, Propagation and amplification of tsunamis at coastal boundaries, *Nature*, *372*(6504), 353–355, 1994.

Yoon, S., Array-based measurements of surface wave dispersion and attenuation using frequency-wavenumber analysis, Ph.D. thesis, Georgia Institute of Technology, 2005.

Zywicki, D., and G. Rix, Mitigation of near-field effects for seismic surface wave velocity estimation with cylindrical beamformers, *Journal Of Geotechnical And Geoenvironmental Engineering*, *131*(8), 970–977, doi:10.1061/(ASCE)1090-0241(2005)131:8(970), 2005.